

On the experimental simulation of atmospheric-like
disturbances near the surface

Thesis by
Christopher Dougherty

In Partial Fulfillment of the Requirements for the
Degree of
Doctor of Philosophy

Caltech

CALIFORNIA INSTITUTE OF TECHNOLOGY
Pasadena, California

2022
Defended December 8, 2021

© 2022

Christopher Dougherty
ORCID: 0000-0002-0974-5696

All rights reserved.

ACKNOWLEDGEMENTS

Where one ought to start when the immensity of the task precludes specific recognition of all those that environ this very moment in time? Not unlike the physical systems considered herein, our lives represent in some reduced capacity an amalgamation of intertwined, integrated, and only rarely isolated events that serve to reveal portions of a trajectory that we may reflect back upon only after sufficiently established. When considered over an appreciable timeframe, some guiding trend may appear, but that discovery can likely never be apparent in the complex instantaneous moment it is occurring nor could we experience enough realizations in a lifetime to prove its relevance with requisite certainty. Acknowledgements, in most ways then, act as a reflection of past experiences filtered through a selection criteria affording more weight to the most memorable and therefore first to mind. It is here that heaps of subjectivity emerge, connections once obvious fade with time, remembrances falter and unintentional exclusions are all but guaranteed — artefacts of our humanness. I suspect some solace can be found if we presume the qualitative aspects of recognition-giving bridge to the quantitative when considering context, however limited, such that many would find reassurance in an expression honoring the individual value of the person while upholding the primacy of their role.

Toward that end: To my spouse (a steadfast and intimate partner), I am forever beholden. To my children (joyful and dependable perspective), I remain devoted. To my parents (who have supported these endeavors in the most basic and tangible ways), I am perpetually grateful. To those seemingly intangible few (who defy definition but continue to both simultaneously initialize and bound this journey), many continued thanks. To the colonelcy and chiefs of staff (whose stalwart support, resolve, and commitment to duty inspire and instruct), my deepest gratitude and respect. To family, close friends, colleagues, mentees, and all others on whom I depend (the support system), I am indebted. To committee members, contributors, and my advisor (whose expertise paved a path to completion), I am graciously appreciative. And to all those less heralded (the engine), I hope soon to resource you in ways long overdue.

If in any regard, upon reading this, a resonance occurs, it is likely that you are entangled somewhere along this journey. To you, whoever you may be, I am personally grateful.

ABSTRACT

Any and every ‘decision-maker’ gravity-bound to the planetary surface (or very nearly so) must contend with the frictional complexities confined to its relatively small surface layer. From the perspective of the near-surface-bound small autonomous flyer, it is the microclimatic local set of atmospheric conditions (i.e. the weather), characterized by moisture, temperature, and the parameters describing wind, that determines the baseline flowfields within which these flyers must navigate and negotiate. Unlike their human-on-board counterparts, mission parameters relegate small (nearly) massless autonomous flyers to the lower regions of the atmospheric boundary layer, where they may not be fortunate enough to soar above the effects of friction or wait for clearer skies. Relatively little focus has been placed on the experimental strategies of how these machines might *learn* to function in challenging scenarios *well-before* encountering them in the real-world. To address such shortcomings, this work focuses on the experimental simulation of flight-relevant environments through the development of multi-source wind-generating apparatuses (i.e. fan arrays) that can initialize velocity distributions discretely-individually or in-concert to produce appropriate mean and fluctuating velocities through an ample open-air test envelope that enables full-scale conventional statically-mounted aerodynamic-characterizations up through free-flight autonomous vehicle testing. Though outside the scope of current experimental work, as full of an environmental description (i.e. moisture, temperature, and wind) is given as possible, prior to ultimately reducing the scope to a neutrally stable atmosphere devoid of any major weather events other than a reasonably strong prevailing wind. Nearly always set amongst the backdrop of a high Reynolds number turbulent flowfield, two primary prototypical flowfields (continuous-gust and discrete-gust) are identified as meriting consideration for mainstay experimental simulation. The core features within the spectral overlap of these windy disturbance environments with the response characteristics of flyers of interest ensure that the turbulence of consideration is nearly always of the mechanical-type. Unlike air motions far above local effects in the inertial sublayer (ISL), the dominant flow mechanism within regions of interest near canopied surfaces is augmented by the presence of coherent structures due to the prevalence of locally initiated mixing layers and wakes such that the task becomes one of simulation of suitable forcing spectra in the physical domain for the regions of interest during anticipated times-of-flight.

Likely to prove challenging to the small autonomous flyer are encounters of a change in wind state that occur upon piercing the dividing streamline of air masses of two different velocities. From the view of the flyer navigating the built-up environment, intermittent free shear layers due to wind-interactions with surface roughness elements are unavoidable and are experienced discretely when the flyer and shear layer dynamics are decoupled. Fan array techniques for the generation of mixing layers, the basic building block of any such free shear layer, is explored as a candidate flowfield for the experimental simulation of a discrete gust forcing input for the flyer near the surface. Both initialized dual-stream and triple-stream mixing layers at flight-relevant freestream velocity differences are explored and found to principally behave like the mixing layers developed in a more conventional splitterplate experiment. The Reynolds number Re_{δ_ω} based on the velocity difference ΔU and vorticity thickness δ_ω (both outer scale parameters) is shown to linearly increase with downstream development as the vorticity thickness increases commensurately. The spectral analysis along the centerline confirms local isotropy for every tested case.

The continuous-gust flowfield (simply referred to as ‘turbulence’) is prevalent throughout the atmospheric boundary layer as are quasi-coherent flowfields of superimposed wakes within canopied environments. Because velocity fluctuations manifest as (predominantly) random deviations at any given instant, these flowfields are good candidates for statistical analysis. Generation techniques to produce such turbulent flowfields are introduced and compared against the uniform flow modality (i.e. all fan units set to produce nominally the same initial velocity condition to develop a well-mixed turbulent flowfield beyond $x/L \sim 0.5$ with $Re_{\lambda_T} = 135$). The random-phase (R-P) perturbation technique proves useful in increasing Re_{λ_T} upwards of nearly sevenfold with only a slight further-loss-of-uniformity (to within 3.7% of the mean). The uniform flow modality with the (R-P) perturbation activated is shown, through the presence of a -5/3 slope power law region, to be locally isotropic at relevant freestream velocities. Significant increases in Re_{λ_T} are made through a static-reconfiguring of the discrete source fan-units into a so called quasi-grid (Q-G) configuration. The highest recorded Taylor microscale Reynolds number was found to be $Re_{\lambda_T} = 2700$, likely accompanied by a non-negligible loss of uniformity at the fixed measurement location, though traverses were not undertaken during this campaign so no direct statement of homogeneity is put forth.

For all the flow modalities presented (i.e uniform, pseudo-random, quasi-coherent,

and mixing layer), the high-Re number criteria ($Re_{\delta_\omega} \approx 10^4$, $Re_{\lambda_T} \approx 10^2$) has been met. This serves, then, as a necessary minimum benchmark in the development of multi-source wind tunnels with intended use as environmental simulators for flyers near the surface and also provides the basis for a spectral framework of comparison to enable systematic development of flowfields in future work. Characteristics of the evolving flowfields can further be tuned through the introduction of perturbation techniques applied as initial conditions to both increase the standard deviation of the fluctuating velocities about a desired mean as well as to initiate, evolve, and combine flowfields in representative ways. A preliminary example of one such combination of flow modalities (pseudo-random and mixing layer) indicates significant alteration of flow development compared to a nominal mixing layer case.

TABLE OF CONTENTS

Acknowledgements	iii
Abstract	iv
Table of Contents	vii
List of Illustrations	ix
List of Tables	xx
Chapter I: Resolving a Worldview	4
1.1 Introduction - the atmospheric boundary layer	5
1.2 The physical processes themselves - micrometeorology	5
1.3 More layers, thinner slices – a resolution problem	8
1.4 Touring the various microclimates	12
1.5 Wind near the surface	17
1.6 Treatment of flows near the surface: a simplified view	25
1.7 The free shear layer: a change in wind state	31
1.8 The regions of interest and approach methodology	36
1.9 Objectives: the winds ahead	38
Chapter II: Methodology: multi-sourcedness	40
2.1 Experimental premise: multi-sourcedness	40
2.2 Types of flow generation	46
2.3 Summary	52
Chapter III: The discrete gust velocity field	53
3.1 Dynamic ‘couplings’ within a free shear layer	54
3.2 Turbulent free shear flows - the mixing layer	56
3.3 Experimental mixing layers	59
3.4 Fully-developed turbulence - local isotropy	87
3.5 Summary	89
Chapter IV: The continuous-gust and quasi-coherent turbulent velocity field	91
4.1 Turbulence-generation techniques in wind tunnels	91
4.2 Analysis techniques	94
4.3 Experimental simulation results and discussion	95
4.4 Summary	100
Chapter V: Summary of Results and a Way Forward	101
5.1 A framework for comparison	102
5.2 Comparisons	110
5.3 Concluding remarks	113
5.4 Looking forward - research potential	114
Bibliography	116
Appendix A: Fan Array Wind Tunnels	123
A.1 Design Intent	123
A.2 Schematic Overview	124

A.3 Flow Quality	127
A.4 Main facilities with FAWT implementations	139
Appendix B: Considerations for flow development of a module with non-negligible inlet geometry	142
Appendix C: Turbulence on-demand (TOD)	145
C.1 Fluctuations about a desired mean - random-phase (R-P) mode	145
C.2 TOD Considerations: single vs. dual-layer FAWT	147
Appendix D: A combination of flow modalities: a discussion of the application of perturbation techniques	150
D.1 The application of software-enabled perturbation techniques	150

LIST OF ILLUSTRATIONS

<i>Number</i>	<i>Page</i>
1.1 A conceptual view of a horizontal layer within a turbulent atmosphere characterized by superimposed quasi-coherent structures below and wave-like streamwise unsteadiness above.	9
1.2 A view of the atmospheric boundary layer with its various sublayers established in (a) the daytime and (b) the nighttime. Figure reproduced from Timothy R Oke et al. (2017) with permission of Cambridge University Press through PLSclear.	11
1.3 The local cityscape of 53rd and Park Avenue in New York City, NY, centered upon Seagram building and plaza. Not only must a flyer contend with the effect that heterogeneity of the manmade-building cityscape has on local winds, but also on the environmentally-driven factors of its location in Midtown Manhattan, an island bounded by the Hudson river to the west and the East and Harlem rivers to the east.	13
1.4 A gridded agricultural canopy of date palm trees (Thermal, CA). In this view, relatively slender trunks uphold rather large canopy crowns that demarcate the atmosphere above from the under-canopy below.	15
1.5 Hillside outcrop within Murray Buttes region, lower Mount Sharp. Images taken by MASTCAM onboard NASA's Mars rover Curiosity on Sol 1419 and processed further by Seán Doran (NASA et al., 2016), use under: CC BY-NC-ND 2.0.	16
1.6 Wind profile with the log-law (eq. (1.9)) and exp-law (eq. (1.10)) included for comparison against the demarcated surface layer of fig. 1.2a. Figure reproduced from Timothy R Oke et al. (2017) with permission of Cambridge University Press through PLSclear.	20
1.7 Evidence of the spectral gap from the Van der Hoven spectrum at the Brookhaven site from two occasions, one in nominal conditions ('breeze') and the other purposefully tested during hurricane Connie ('storm'). Figure republished with permission of Springer, from Stathopoulos and Baniotopoulos (2007), after Van der Hoven (1957); permission conveyed through Copyright Clearance Center, Inc.	21

- 1.8 The conventional atmospheric length scales of macro-, meso-, local-, and micro- are defined atop and put into urban cityscape reference elements below. Characteristic time scales are given at left and put into colloquial divisions at right. It is interesting to note the separation of scales between the flyers (UAVs, birds, bats, insects) and the majority of likely urban atmospheric fluid events. Overlap in the dashed region 1 corresponds to mechanical eddies shed by obstacles. 2 - cross-canyon vortex; 3 - individual building wake; 4 - chimney stack plume; 5 - urban park breeze circulation 6 - urban-rural breeze system; 7 - uplift in city ‘plume’. Figure republished and modified with permission of Springer Nature BV, from Tim R Oke (2006); permission conveyed through Copyright Clearance Center, Inc. 24
- 1.9 In the phenomenological model of Poggi et al. (2004), the size of vortices distribute into three categories. Far above local effects, the displaced rough wall boundary layer vortices extend up into the ISL ($z \gg 2H$). Within the canopy, local canopy geometric considerations determine the nature of the vortices. The vortices in the region at and just above the canopy top are of the mixing layer type. Figure republished and modified with permission of Springer, from Poggi et al. (2004); permission conveyed through Copyright Clearance Center, Inc. 30
- 1.10 The hatched areas highlight the growth of the shear layer in the jet, wake, step, and simple building configurations. Figure republished with permission of Springer, from Heinrich E. Fiedler (1998); permission conveyed through Copyright Clearance Center, Inc. 31
- 1.11 Gust types within the selected view. 32

1.12	The surface roughness density determines two types of flow behaviors in the idealized uniform-height roughness configurations typically tested in wind tunnel studies. Denser configurations result in a sheltered skimming flow that decrease the effect of roughness in upper layers whereas sparser configurations increase the reach of roughness proportional to the frontal surface of the roughness elements. Meandering ‘superstructures’, representing the most energetic structures in the energy spectrum of the surface layer, reach up into the logarithmic region and scale with the boundary layer thickness δ , an outer variable length scale (e.g., see Hutchins and Marusic, 2007). Figure republished with permission of Springer Nature BV, from Perret et al. (2019); permission conveyed through Copyright Clearance Center, Inc.	34
1.13	The fluctuating wind vectors over a regular array of cubic obstacles from the numeric study of Coceal et al. (2007).	35
1.14	Approximate frequency regimes of overlap for flyer-specific and atmospheric disturbance features, from MIL-STD-1797A.	38
2.1	Schematic of the basic type fan unit typically used in FAWT. The part highlighted in blue represents the annular flow output area. Arrays built from the fan unit as diagrammed constitute a single-layer fan array. A dual-layer fan array is comprised of counter-rotating pairs of stacked single fan units that do not change the overall footprint but increase the depth by one stacked layer. These dual-layer fan arrays can be coupled front-and-back layer or remain individually controllable.	41
2.2	Control volume schematic for FAWT analysis.	43
2.3	Response characteristics to sinusoidal forcing.	45

- 2.4 Development of a steady uniform flow measured for a $d/L = 0.33$ resolution dual-layer array ($d = 0.080$ m) with minimal mounting structure at fan unit intake. The streamwise (x-z plane) cut corresponds to the centerline plane ($y = 0$) and the positions of the spanwise (z-y plane) distributions are dashed for all three locations. To the right of each spanwise cut is a corresponding velocity profile at the centerline ($y = 0$) for that respective view. The core flow homogenizes first from discrete source units to a nearly uniform square cross section of size $L \times L$ and then spatially reduces with downstream distance as the core flow smoothes to a rounder cross-section as the boundary shear layers entrain and grow. The colorbar corresponds to \bar{u}/\bar{u}_{max} 47
- 2.5 Spanwise (z-y plane) distribution of a steady uniform flow measured at the downstream location $x/L = 0.35$ for a $d/L = 0.03$ resolution dual-layer array. This particular fan array has outer dimensions $L = nd = 2.88$ m ($n = 36$, $d = 0.080$ m) with $36 \times 36 \times 2 = 2592$ individual fan units stacked in two layers and arranged into 144 total modules. It is evident in this view that a funneling effect of the module geometry is still present. The dashed line corresponds to the location $z/L = 0.3$ of the extracted velocity profile above. The colorbar corresponds to \bar{u}/\bar{u}_{max} 48
- 2.6 Streamwise (z-x plane) distribution along the centerline plane ($y = 0$) of a steady uniform flow for a $d/L = 0.03$ resolution dual-layer array. Velocity profiles in the middle portion of the array between $-0.27 < z/L < 0.27$ are extracted at three downstream locations $x/L = 0.17, 0.35$, and 1.00 . The standard deviation of each profile is 3.6%, 2.9%, and 1.3%, respectively. The colorbar corresponds to \bar{u}/\bar{u}_{max} 49
- 2.7 A velocity trace from a handheld wind anemometer recording of an instantaneous prevailing wind of a small uninhabited island in the Caribbean is mapped into the FAWT software environment to generate an input distribution that attempts to playback the simulated output. Prevailing winds in the region are directional and constant, averaging to be 8 – 10 m/s at all times of the year, but their instantaneous nature is gusty, fluctuating as high as 11.5 m/s and as low as 2.5 m/s. 50

2.8	Example analyses afforded by the triple decomposition. Filtering out the forced frequency ($f_p = 0.1$ Hz) periodic sinusoidal portion of the signal \tilde{u} isolates the stochastic fluctuating content u'	51
3.1	Diagram for the evolution of the mean velocity profile for a dual-stream planar mixing layer.	57
3.2	Developmental stages of a shear layer rollup.	58
3.3	Visual properties of a large-scale coherent structure. Diagram reproduced from Bernal (1981).	59
3.4	Mean velocity profiles in dimensional y -coordinate system, $r = 0.4$ (left) and $r = 0.2$ (right).	62
3.5	The maximum percentage velocity overshoot of the high and low side for dual-stream mixing layers generated from a modular multi-source wind tunnel.	63
3.6	The dependence of vorticity-thickness spreading rate on the parameter $\lambda = \Delta U / 2\bar{U}$ for uniform density mixing layers, as adapted from Brown and Roshko (1974) with present results added.	64
3.7	Diagram for the evolution of the mean velocity profile for a triple-stream planar mixing layer.	66
3.8	Mean velocity profiles in dimensional y -coordinate system, $r_{outer} = 0.2$, for inter-shear spacing of 6.3 inches (left) and 12.6 inches (right).	67
3.9	Spreading diagram for dual-stream mixing layer with $r = 0.4$	70
3.10	Spreading diagram for dual-stream mixing layer with $r = 0.2$	71
3.11	Spreading diagram for $r_{outer} = 0.2$ with a $2d$ initial separation at fan inlet plane.	72
3.12	Spreading diagram for triple-stream mixing layer with a $4d$ initial separation at fan inlet plane.	73
3.13	Spreading diagram for a geometrically reduced inter-shear spacing of $l_{4d}/2 = l_{2d_{art}}$	74
3.14	Spreading diagram for the triple-stream cases with virtual origin brought up to the line $y = 0$ inches and rotated such that every centerline point falls along the line $y = 0$ inches. The rightmost plot is a zoomed in view of the development in physical space ($x > 0$ inches). The color and line-type are as in fig. 3.11 and fig. 3.12.	75
3.15	Mean velocity profiles of the dual-stream mixing layer in η -similarity coordinates, $r = 0.4$	76

3.16	Mean velocity profiles of the dual-stream mixing layer in η -similarity coordinates, $r = 0.2$	76
3.17	Mean velocity profiles of the triple-stream mixing layer with initial separation of $ss = 4d$ in η -similarity coordinates. The top row presents data from $x = 28$ inches and the bottom row from $x = 58$ inches. Red denotes the upper mixing layer and blue denotes the lower mixing layer. Here, the upper and lower mixing layers are distinct (region I) enough to be treated separately.	77
3.18	Mean velocity profiles of the triple-stream mixing layer with initial separation of $ss = 4d$ in η -similarity coordinates at downstream locations $x = 88$ inches and $x = 118$ inches. Here, the upper and lower mixing layers are transitioning towards merging (region II). . .	78
3.19	Mean velocity profiles of the triple-stream mixing layer with initial separation of $ss = 2d$ in η -similarity coordinates at. Beyond $x > 28$ inches, the upper and lower mixing layers have merged (region III) and can be treated as a dual-stream mixing layer.	78
3.20	Distribution of streamwise normal stress for $r = 0.4$	80
3.21	Distribution of streamwise normal stress for $r = 0.2$	80
3.22	Fluctuating velocity profiles of the triple-stream mixing layer with initial separation of $ss = 4d$ in η -similarity coordinates. The top row presents data from $x = 28$ inches and the bottom row from $x = 58$ inches. Red denotes the upper mixing layer and blue denotes the lower mixing layer. Here, the upper and lower mixing layers are distinct (region I) enough to be treated separately.	81
3.23	Fluctuating velocity profiles of the triple-stream mixing layer with initial separation of $ss = 4d$ in η -similarity coordinates at downstream locations $x = 88$ inches and $x = 118$ inches. Here, the upper and lower mixing layers are transitioning towards merging (region II). . .	82
3.24	Fluctuating velocity profiles of the triple-stream mixing layer with initial separation of $ss = 2d$ in η -similarity coordinates at. Beyond $x > 28$ inches, the upper and lower mixing layers have merged (region III) and can be treated as a dual-stream mixing layer.	83
3.25	Distribution of skewness for $r = 0.4$	84
3.26	Distribution of skewness for $r = 0.2$	84
3.27	Distribution of kurtosis for $r = 0.4$	84
3.28	Distribution of kurtosis for $r = 0.2$	84

3.29	Energy spectrum for the dual-stream mixing layer, $r = 0.2$, along the centerline at distances of (a) $x = 7$ inches, (b) $x = 28$ inches, (c) $x = 88$ inches, (d) $x = 118$ inches from the fan array outlet plane. A reference line of slope $-5/3$ indicates a fully developed inertial cascade.	85
3.30	Energy spectrum for the triple-stream mixing layer, $ss = 4d$, along the centerline at distances of (a) $x = 28$ inches, (b) $x = 58$ inches, (c) $x = 88$ inches, (d) $x = 118$ inches from the fan array outlet plane. A reference line of slope $-5/3$ indicates a fully developed inertial cascade. Red denotes the upper mixing layer and blue denotes the lower mixing layer.	86
3.31	Energy spectrum for the triple-stream mixing layer, $ss = 2d$, along the centerline at distances of (a) $x = 28$ inches, (b) $x = 58$ inches, (c) $x = 88$ inches, (d) $x = 118$ inches from the fan array outlet plane. A reference line of slope $-5/3$ indicates a fully developed inertial cascade.	86
3.32	Energy spectrum for the dual-stream mixing layer, $r = 0.2$ along the high-speed stream edge at $\eta - \eta^* \sim -1/8$ at $x = 28$ inches distance downstream. A major peak at $f = 12.7$ Hz corresponds to an inverse wave number of 6.3 inches, roughly the non-uniform transverse distance between crests of the spatial wavefront developed from the non-uniform initial conditions of the discrete side-by-side modules.	87
3.33	The Reynolds number as a function of downstream distance for fully-developed, non-merging mixing layers. The black line is the dual-stream case of $r = 0.2$, the gray line is the post-merged triple stream case with $ss = 2d$ and the red and blue lines are the upper and lower pre-merged mixing layers of the triple-stream case $ss = 4d$	88
3.34	Profiles of the nondimensional mean velocity for each fully-developed, non-merging mixing layer.	90
4.1	Conceptual drawing of shearing velocities initiated at the fan array exit plane.	93
4.2	Fluctuating component time series and corresponding u -spectra in the frequency domain for the measured turbulent flowfields.	96

4.3	The longitudinal velocity (u) spectra with various scalings. The topmost-left is the dimensional u -spectra in the wavenumber domain. The topmost right u -spectra is compensated (pre-multiplied) using the dissipative (Kolmogorov) scales. The bottommost u -spectra is compensated (pre-multiplied) using inertial subrange scales. The Taylor Reynolds number ranges from $Re_{\lambda_T} = 135$ (the baseline uniform case, dashed, with $U = 8.0$ m/s, $TI = 2.7\%$) to $Re_{\lambda_T} = 2707$ (quasi-grid with $U = 9.1$ m/s, $TI = 26.9\%$).	99
5.1	Normalized energy spectrum plotted in an area-preserved manner highlighting two separate and non-overlapping regions. The leftmost region demarcates the frequencies that contribute 90% of the total fluctuation energy (from $f \rightarrow 0$ to f_{90}) and the rightmost region reflects the frequencies that account for 90% of the energetic contribution to dissipative processes (from df_{10} to $f_s/2$, where f_s is the sampling rate).	107
5.2	Normalized energy spectrum for $r = 0.2$ along the centerline at $x = 118$ inches. The dashed vertical line marks the frequency of validity according to Lin's criteria. The left-most solid vertical line marks the Raichlen criteria of f_{50} and gives a reasonable estimate of the beginning of the $-5/3$ roll-off. The right-most solid vertical line marks df_{10} and reasonably divides the frequency at which the slope steepens away in the dissipative range. The theoretical fit is of a form proposed by Dryden.	110
5.3	Normalized energy spectrum for the uniform flow modality (top), the quasi-grid modality (middle), and dual-stream shear layer $r = 0.2$ along the centerline (below), each at $x/L \sim 0.75$. The solid vertical line corresponds to the wavenumber based on f_{50} . The dashed vertical line of the dual shear layer normalized energy spectrum corresponds to Lin's criteria.	111
A.1	Annotated hardware overview of FAWT.	125
A.2	Flow of information from module to micro-controller to computer through a network.	127
A.3	Three identifiable regions of the simplest square array configuration. The "fan-centered" and "fan-array-centered" locations represent a stagnation condition whereas the "duct-centered" represents an accelerated inlet condition.	128

A.4	The downstream convergence of the measured values of turbulence and freestream velocity indicate that the flow has fully mixed and is invariant to the measurement location beyond $x/L \approx 0.5$	129
A.5	Centerline homogeneous turbulence decay for three different sized fan units configured into arrays. The $d = 0.080$ m fan unit corresponds to a 36×36 dual-layer array, the $d = 0.092$ m fan unit corresponds to a 11×11 single-layer array, and the $d = 0.120$ m fan unit corresponds to a 10×10 single-layer array.	131
A.6	Diagram view of flow manipulator (FM) placement at set downstream locations ($l_{1,2,\dots,5}$) relative to the fan array.	132
A.7	Effect of honeycomb on downstream development of uniform flow.	133
A.8	Effectiveness of various flow manipulator configurations at reducing turbulence intensity.	134
A.9	Types of flows able to be generated by FAWT.	135
A.10	The turbulence intensity distribution of a $d/L = 0.03$ resolution dual-layer array at nominal freestream velocities.	137
A.11	Spatial development of a gentle vertical gradient shear flow. Contour shear velocity profiles (above) with corresponding velocity profiles (below) for a centerline streamwise measurement plane of a $d/L = 0.03$ resolution array. The maximum velocity is 7.5 m/s incremented piecewise per fan down to the idle velocities of the fan units, 2 m/s.	138
A.12	Spanwise vorticity plots derived from particle image velocimetry measurements at $x/L = 2.0$ with varying side fan velocities \bar{u}_s	138
A.13	FAWT within the 25-ft Space Simulator chamber at the Jet Propulsion Laboratory (JPL). A full-scale model of Ingenuity is seen fix-mounted (upside-down) in front of a bank of $21 \times 21 \times 2 = 882$ individual fan units stacked in two layers with a metallic honeycomb affixed to the outlet plane.	139
A.14	A bipedal walker in the foreground interacting with a flock of flyers in the surround against the backdrop of the CAST fan array.	140
A.15	FAWT within the Aerodrome in CAST.	141

B.1	Development of a steady uniform flow measured for a $d/L = 0.33$ resolution array ($d = 0.080$ m) with a diverging duct mounting structure at fan unit intake. The streamwise (x-z plane) cut corresponds to the centerline ($y = 0$) and the positions of the spanwise (z-y plane) distributions are dashed for all three locations. The core flow homogenizes first from discrete source units to a nearly uniform square cross section of size $\sim L \times L$ and then spatially reduces with downstream distance as the core flow smoothes to a rounder cross-section as the boundary shear layers entrain and grow. The colorbar corresponds to \bar{u}/\bar{u}_{max}	143
B.2	Streamwise (x-z plane) visualization of a $d/L = 0.33$ resolution array ($d = 0.080$ m) with a diverging duct highlighting the core convergence of a single 3×3 module for a commanded constant RPM input condition. The colorbar corresponds to $\Delta\bar{u}_T/\bar{u}_{max}$, where $\Delta\bar{u}_T$ is the difference between the mean velocity \bar{u} and a certain threshold value \bar{u}_T	144
B.3	Spanwise (z-y plane) visualization of a $d/L = 0.11$ resolution array ($d = 0.080$ m) comprised of nine total (3×3) modules assembled into a 9×9 array. The colorbar corresponds to $\bar{u}/\bar{u}_{0,0}$, where $\bar{u}_{0,0}$ is the center velocity at $z/L = y/L = 0$	144
C.1	Example of varying turbulence intensity about a desired mean. The above row shows the effect when the algorithm is active compared to the bottom row where it is initialized as spatially random but not active.	146
C.2	Comparisons of the TOD algorithm on a single- and dual-layer FAWT.	147
C.3	Comparisons of the energy spectra of the TOD algorithm implemented on a single- and dual-layer FAWT.	148
C.4	The energy spectra for the TOD algorithm applied to the backmost layer of a decoupled dual-layer fan array showcases that the increase of the total fluctuation energy is broadly distributed across all relevant scales as the maximum allowed percentage deviation range in the TOD algorithm is consistently increased.	149
D.1	The stabilizing effect on coherent structures through forcing, from Koepp et al. (1991).	152

- D.2 Mean velocity profile (above) and fluctuating velocity profile (below) for the perturbed triple-stream mixing layer with initial separation of $ss = 4d$. The baseline (non-perturbed case) is denoted by the (\square) marker. Random-phase perturbations are denoted by ($*$) when applied to the whole array, ($+$) the center segment, and the (\leftarrow) upper segment. Sinusoidal periodic perturbations of $f_f = 1$ Hz is applied to the whole array (\cdot) and the upper segment (\triangleright), $f_f = 2$ Hz is applied to the whole array (x) and the upper segment (∇). 155

LIST OF TABLES

<i>Number</i>	<i>Page</i>
1.1 Selected scaling parameters	7
3.1 Summary of results for the dual-stream mixing layer experiments. . .	65
3.2 Selected parameters of comparable mixing layer experiments.	65
3.3 Comparison of nominal mixing layer with velocity ratio $r = 0.2$ to velocity ratio $r_{outer} = 0.2$ initially separated by $ss = 2d$	69
3.4 Summary of results for triple-stream mixing layer experiments. The two mixing layers are initially separated by $ss = 4d$ at the fan outlet plane.	69
5.1 Summary of results tabulated using Raichlen's criteria for three dif- ferent flow modalities at approximately the same measurement location.	112
5.2 Summary of results tabulated using Raichlen's criteria for a dual- stream and triple-stream mixing layer.	113
A.1 Fan RPM distributions for example implementations for FAWT. . . .	125
A.2 Flow manipulator configurations. <i>honeycomb</i> : HC, <i>perforated plate</i> : PP, <i>screen</i> : S.	133
A.3 Turbulence intensity and velocity reduction for various flow manipu- lator configurations. Dimensional units for $l_{1,2,\dots,5}$ are in inches. . . .	134
A.4 Description of techniques and analysis for flow characterization. . . .	135

PROLOGUE

The real world is a messy place — not exactly in the untidy sense, but moreso in its interwoven tangled-ness. Higher order problems may be its most defining feature, salient across all disciplines, and steadfast through the ages — a complex, intricate, mixed-up system spanning extraordinary scales. The qualitative descriptors humankind has assigned the messiness nearly always precede our ability to quantify its measurables. One may casually ask, “how’s the weather today?” ...to be met with “a bit windy with a dry heat.”, or something of the sort. Local weather patterns have always driven our day-to-day decision-making and this may never change; in present times we may assign a magnitude and direction to that ‘windiness’, a temperature to its ‘heat’, and a relative humidity to its ‘dryness’, but the principle question remains the same: is the weather close enough to matter and if so, how long must it be dealt with?

In more ways than one is this not unique to our human experience. Any and every ‘decision-maker’ gravity-bound to the terrestrial surface (or very nearly so) must contend with the frictional complexities confined to its relatively small surface layer. Geostrophic forces in the macroclimatic systems well-aloft and well-beyond our control set into motion processes in the planetary boundary layer that are characteristically complex and reside over many length and time scales. Chiefly because the diversity of life, with rare exception, spends most of its existence within this narrow band as a means to survive should we provide it overdue attention, lest, to borrow some from Sutton (1953), “the complete omission of viscosity [be] fatal”.

Indeed there continues to exist a need to rigorously develop relevant simulated environments to better understand and help inform the ‘decision-maker’ operating near the surface. At resolutions of interest, virtual representations of these environments oftentimes discard or wash-out the temporally-dynamic and spatially-varying frictional complexities. The fan array technologies developed herein represent a toolset that can simulate, in the confines of a laboratory setting, elements of the real world that more accurately model the complex realities of environments of interest. Observations made in the real world are mapped to the virtual one as a means to set forth initial conditions. These prescriptions initiate flowfields in the physical domain that are reproducible in a manner conducive to observation. Iterative comparison of the real world observation to the lab-generated one provides the modeling framework for a given environment.

This dissertation, written from the perspective of the small autonomous flyer not fortunate enough to soar above the friction, sets down a path of study of the micrometeorological and microclimatic processes (i.e. weather) that govern the atmospheric boundary layer, with primary focus ultimately relegated to the nature of the winds and their subsequent effects adjacent to the surface. Roughness elements like buildings and trees dot the topography, as do carve-outs and canyons, in domains of interest.

Aligning our view with a prevailing wind in Chapter I allows for some progress to be made in describing the characteristic fluid features that emerge on account of the wind-wind and wind-surface-element interactions. Descriptions of the upper reaches of the atmospheric boundary layer are briefly mentioned followed by a descension into the so-called canopy layer, the primary layer of interest in this study. The prototypical flowfields likely to be encountered by the flyer near the surface in the presence of a reasonably strong wind are considered candidates for experimental simulation. The core features of the spectral overlap of the flyer dynamics and windy disturbance environment ensure that the turbulence of consideration is nearly always of the mechanical-type and is initiated from a turbulence mechanism that departs from the zoomed-out view of the canonical turbulent boundary. Instead, the dominant flow mechanism in regions of interest near canopied surfaces is augmented by the presence of coherent structures from the prevalence of locally initiated mixing layers and wakes. The task, then, becomes one of simulation of suitable forcing spectra in the physical domain for the regions of interest during anticipated times-of-flight.

In Chapter II, a conceptual framework for multi-source wind tunnels is given. The unsteady equation governing the motion along a streamline is derived and then extended to the case of a uniformly oscillating flowfield, where it is shown that fan arrays behave as low-pass filters. Visualizations of prototypical flow modalities are presented, with much of the discussion specific to fan array wind tunnels left to appendix A. The funneling influence of the module geometry and perturbation techniques driven solely by software augmentations are also left to appendices (appendix B and appendix C, respectively).

In Chapter III, the prototypical turbulent free shear flow that serves as the basic building block of turbulence generation of multi-source wind tunnels through shearing velocities initiated at the fan array outlet plane is introduced. The planar dual-stream mixing layer is further explored as a candidate flowfield to simulate a discrete gust

forcing input to the flyer passing through. This well-studied class of flows provides a basis to see how well shear layers generated by fan array wind tunnels comport to the classical cases. Baseline dual-stream mixing layers are compared to the so-called triple-stream mixing layer to better understand the merging behaviors in the downstream development.

Chapter IV represents a first attempt at simulating the continuously turbulent flowfields of the atmospheric boundary layer far from local topographical effects as well as the quasi-coherent flowfields within canopied environments. It is shown, through pseudo-random modulation techniques and static reconfiguration of the multitude of fan units, that a random-phase (R-P) and quasi-grid (Q-G) configuration generates an energetic turbulence cascade well-described by a theoretical $-5/3$ region of the u -spectra in the inertial subrange. In general, increasing turbulence intensities through shearing velocity distributions at the fan array exit plane proves an effective means of increasing Re_{λ_T} .

A framework of comparison between the uniform, quasi-grid, and mixing layer flow modalities is formally presented in Chapter V based on the premise that every experimental flowfield presented meets the mixing criteria of a high Reynolds number turbulent flowfield. Conclusions are drawn and potential research directions are discussed, with strategies regarding perturbation techniques for future work preliminarily considered in appendix D.

Chapter 1

RESOLVING A WORLDVIEW

Any and every ‘decision-maker’ gravity-bound to the planetary surface (or very nearly so) must contend with the frictional complexities confined to its relatively small surface layer. Geostrophic forces in the macroclimatic systems well aloft set into motion processes in the planetary boundary layer that are characteristically complex and reside over many length and time scales. From the perspective of the surface-bound small autonomous flyer, however, it is the microclimatic local set of atmospheric conditions (i.e. the weather) that determines the baseline flowfields within which these flyers must navigate and negotiate.

At least qualitative consideration of local weather conditions under the banner of flight safety informs human-in-the-loop-piloted (manned and remote-controlled) aircraft. For instance, human-on-board aircraft are routinely rerouted mid-flight as weather patterns evolve and if conditions are particularly austere from the onset, flights may be grounded altogether. Once nominal weather conditions are restored, these massive vehicles take to the inviscid free atmosphere to further avoid any surface friction effects. But what, then, of the small autonomous flyer¹ not fortunate enough to soar above the friction or wait for clearer skies? That is to ask what becomes of the (nearly) massless flyer confined to the atmospheric boundary layer that can neither avoid the weather nor wait for it to pass? Must it either do nothing or doom itself to failure?

The principle question of how might the weather affect a vehicles’ capacity to function garners much attention early in the design cycle and again as issues (sometimes tragically) arise, but relatively little attention has been placed on the experimental strategies of how these flyers might *learn* to function in challenging scenarios *well-before* encountering them in the real-world. It therefore seems prudent to understand the fundamental fluid processes active in the high Reynolds number turbulent atmospheric boundary layer to elucidate the types of scenarios worth simulating.

¹be it manmade (e.g. drone) or natural (e.g. birds/insects/seeds).

1.1 Introduction - the atmospheric boundary layer

The turbulent exchange between a planetary surface and its atmosphere defines the atmospheric boundary layer (ABL), a transitional domain whereby the inviscid conditions of the free atmosphere graduate in some fashion to satisfy the boundary conditions at the surface. Indeed, all the kinetic energy of flowing air (i.e. wind) is transformed to thermal energy (i.e. heat) when its motion is terminated at the surface. Aside from the very thinnest layer immediately adjacent to the surface where molecular physics dominate, eddy diffusion (i.e. mixing due to eddy motions) in the ABL occurs due to a combination of frictional and convective exchanges of energy, mass, and momentum.

For a given domain of interest, the topography, distribution of roughness elements (e.g. height, fetch), and local weather conditions prevalent in that area for a given time of day (i.e. microclimates) all contribute to the complex nature of the gradation from free atmosphere to the surface. When averaged over some appreciable unit of length, say a large-area horizontal distance, and time (e.g. a day), transitions between sublayers appear gradual; fluid events near the surface, however, are characteristically intermittent (i.e. neither continuous nor steady) and agitated (i.e. exchanging/mixing). Due to the presence of both thermal kinetic energy processes (from surface heating) and mechanical kinetic energy processes (from frictional elements), the wind motions relegated to the ABL are nearly always turbulent and characterized by irregular motions containing all possible frequencies. When air motions are oriented in different directions and/or at different speeds, internal forces due to shearing can initiate dynamic instabilities that ultimately convert the mechanical kinetic energy of that collection of particles to thermal kinetic energy through the cascading nature of turbulence. These processes do occur aloft between layers of air, but are far more commonplace where air is locally slowed by a roughness element. As we continue to zoom into the various characteristic features that may come to define zones of influence within our view of the physical processes found in the innermost sublayers of a planetary atmosphere, a gradient-like partitioning is employed to better represent the length scales that emerge from the geometric dimensions of the elements within, the thicknesses of the boundary layers upon them, and the wakes of various sizes produced behind them.

1.2 The physical processes themselves - micrometeorology

In general, the effect of the Coriolis force cannot be ignored in the study of the physical processes of a planetary atmosphere, but its effect is not felt in the flux

gradient relationship of the surface layer. From the fundamental principles of conservation of mass, momentum, and energy, equations used to model the forces and budget the energy in the ABL are made possible. At scales of interest, though some six orders of magnitude smaller than the largest-scale atmospheric processes, a macroscopic description of the fluid can still be justified². Though a Lagrangian view is better aligned with the notion of a fluid consisting of a swarm of molecules, following the many parcels of fluid that make up a volume of interest is impractical, so for practical applications, descriptions of the fluid motion employ an Eulerian viewpoint, as is ultimately done herein.

Fundamentals

The continuity equation can be stated generally in convective form as:

$$\frac{D\rho}{Dt} + \rho \nabla \cdot \underline{u} = 0 \quad (1.1)$$

where the fluid is assumed a continuum. When taken to be incompressible but heterogeneous, that is, the density of the fluid as a whole may change one point to another but the density of a given element does not as it moves, the continuity equation reduces to:

$$\frac{D\rho}{Dt} = 0; \quad \nabla \cdot \underline{u} = 0 \quad (1.2)$$

Then for an ideal Newtonian fluid³, the momentum equation at any instant can be written as:

$$\rho \frac{D\underline{u}}{Dt} = -\nabla p + \rho \underline{B} + \mu \nabla^2 \underline{u} \quad (1.3)$$

where the Coriolis force is neglected and in the most general sense, every macroscopic variable can be a function of location (x, y, z) and time t , where ρ , \underline{u} , p , μ , and \underline{B} represent density, velocity, pressure, shear viscosity, and specific body force, respectively. Pressure, temperature, and density are related to one another through an equation of state. For an ideal gas,

$$p = \rho RT \quad (1.4)$$

can be used satisfactorily, R being the gas constant. This is a reasonable approximation for both Earth and Mars atmospheres. For a stationary atmosphere, the vertical

²the Knudsen number — a comparison of the characteristic physical length scale of the fluid to that of the molecular mean free path — is typically used to determine when the treatment of the fluid as a continuous distribution of mass in space is valid. It is worth mentioning that the treatment of a fluid as a set of continuous fields (macroscopic viewpoint), though useful, does not illuminate the true particulate nature of the fluid (microscopic viewpoint) itself.

momentum component of eq. (1.3) yields $dp/dz = -\rho g$, which, through use of eq. (1.4), can be used to test the stability of an atmospheric parcel by studying the isentropic motion of a fluid particle on account of the temperature gradient as:

$$\left(\frac{dT}{dz}\right)_{ad} = -\frac{g}{c_p} \quad (1.5)$$

which is known as the adiabatic lapse rate and describes a *neutrally stable* atmosphere when $dT/dz = (dT/dz)_{ad}$. If the vertical temperature gradient is greater than the adiabatic lapse rate, $dT/dz > (dT/dz)_{ad}$, then the fluid particle put into rising motion maintains a density greater than its surroundings and the atmosphere is described as *unstable*. If the fluid particle sinks, $dT/dz < (dT/dz)_{ad}$, then the reverse holds and the atmosphere is described as *stable*. Due to the significant heating from surface radiation near the surface, which changes dramatically night-to-day, air motions can be initiated even when the atmosphere is at rest (i.e. $\underline{u} = 0$).

Scaling considerations

Upon expanding into its differential form, and adopting these scalings:

Table 1.1: Selected scaling parameters

Scaling parameter	Description	Scaling Substitution
L	Characteristic length	$\underline{x} = L\underline{x}^*$
U	Characteristic velocity	$\underline{u} = U\underline{u}^*$
f	Characteristic frequency	$t = t^*/f$
Δp_0	Reference pressure difference	$p = \Delta p_0 p^*$
g	Gravitational acceleration	$\underline{B} = g\underline{g}^*$

the momentum equation (1.3) can be transformed, after rearrangement, into nondimensional form as:

$$\frac{fL}{U} \frac{\partial \underline{u}^*}{\partial t^*} + (\underline{u}^* \cdot \nabla^*) \underline{u}^* = -\frac{\Delta p_0}{\rho U^2} \nabla^* p^* + \frac{gL}{U^2} \underline{g}^* + \frac{\mu}{\rho UL} \nabla^{*2} \underline{u}^* \quad (1.6)$$

where the operator $\nabla = \nabla^*/L$ is used throughout and the body force term is scaled by the acceleration due to gravity. Selection of the characteristic scaling parameters is a bit of an art, but with care for a given scenario, if the scaling substitutions are $\mathcal{O}(1)$ (i.e. normalized), then the relative weights of the terms can be analyzed directly through comparison of the relative magnitudes of the nondimensional parameters St , Eu , Fr , and Re :

³The viscous stress tensor, τ , is hypothesized to depend on changes of velocity, whereby $\nabla \cdot \tau = \mu(\nabla \underline{u} + \nabla \underline{u}^T) = \mu \nabla^2 \underline{u}$, with the volume viscosity taken as null.

$$[St] \frac{\partial \underline{u}^*}{\partial t^*} + (\underline{u}^* \cdot \nabla^*) \underline{u}^* = -[Eu] \nabla^* p^* + \left[\frac{1}{Fr^2} \right] \underline{g}^* + \left[\frac{1}{Re} \right] \nabla^{*2} \underline{u}^* \quad (1.7)$$

Viewed in this way, ‘localness’ can be determined in reference to the ∇^* operator. If changes in space of the field are on the order of the characteristic length of interest, then its effect is taken to be a local one. When the viscous forces of a given flow are much smaller than the inertial ones, the Reynolds number, Re , is large (i.e. $Re \gg 1$), such that its reciprocal is small enough so as to neglect the final term of equation (1.7) outright. Where oscillating flow mechanisms are encountered, unsteadiness can be evaluated by the Strouhal number, St . When $St < 10^{-4}$, the contributions of the local accelerations are small and the fluid can be analyzed behaving as a steady flow. Corresponding considerations can be given to the Euler number, Eu , and the Froude number, Fr , for a particular scenario of interest.

1.3 More layers, thinner slices – a resolution problem

The physical processes of the lower strata which give rise to the microclimates therein are complex chiefly because the mixedness of the variables that characterize the system. Short and long wave radiation that determines surface heating distributions across domains of interest drive temperature gradients along the surface itself and the air above that may influence the relative humidity which, altogether, govern the average characteristics of a parcel of air swept away in a prevailing wind, issuing, say, from the mouth of a volcano, made visual to an observer by the mixed water vapor of the exhaust. In scenarios such as these, retaining a sense of scale is only made possible when held in reference to the subject of study. That is to say that the characteristics of the flyer (or particulate) and the objectives of the study themselves determine the scales that are appropriate to consider. Influences to the vicinity of the subject (i.e. its "local neighborhood") may of course derive from a scale much larger and slower, but the perceivable effects, from the view of the flyer, manifest only in an instantaneous and local sense. Thus, careful consideration is given to both the typical scales of the atmospheric processes in concert with the typical scales of the flyers themselves. Descriptions of the atmosphere over many horizontally extensive surfaces are oftentimes presented as spatial averages of vertical layers where sets of average properties are assigned to each layer division. Notions of layers and scaling are explored next.

What are layers?

The physical processes of transition from one state to another take place in layers. Horizontal layers, as adopted in this view, represent the transition from one state of a measurable set of parameters to another across sheets of material, with the flux across the boundaries oriented more or less vertically. The perception of change of a given domain demarcates the abutting boundary and the sharpness/gentleness of the transition determines the layer thickness. At the scales of interest here, regions [1] and [2] of fig. 1.1 will represent significant changes within and/or between microclimates, with special focus given to changes in wind. A microclimate as the term is used simply represents a local set of atmospheric conditions near the surface, characterized by moisture, temperature, and the parameters describing wind.

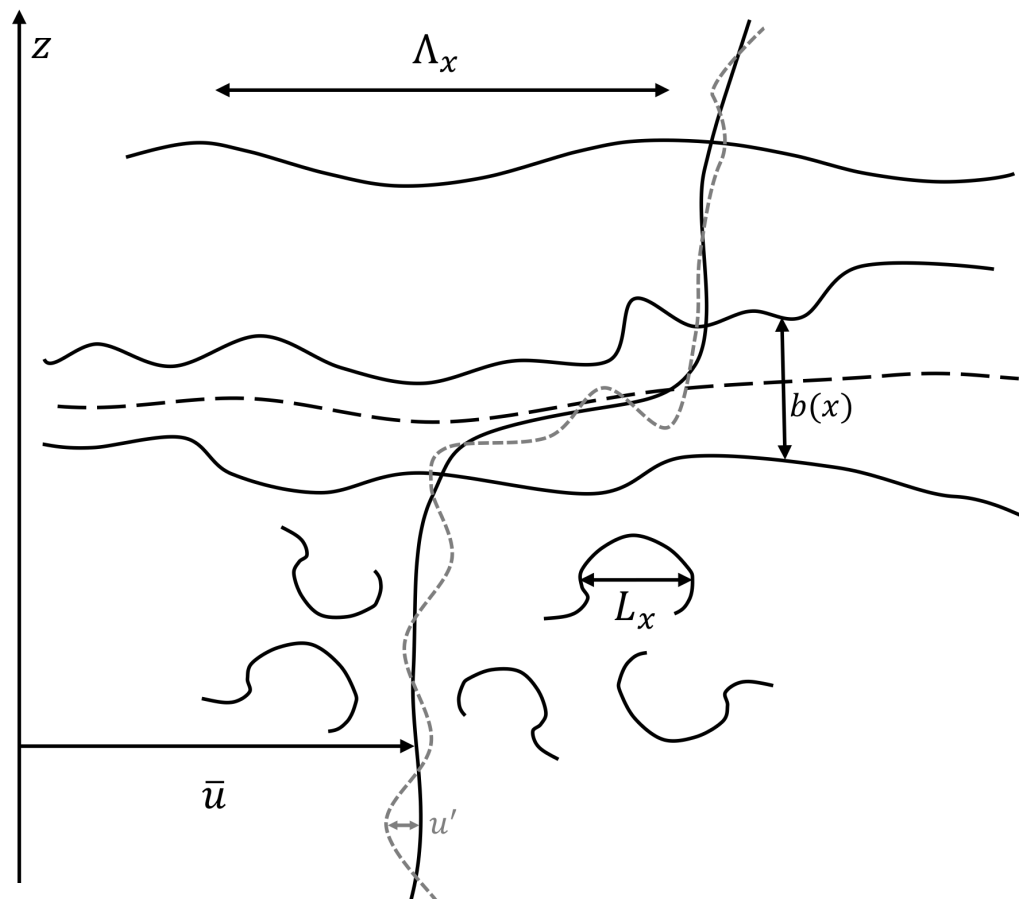


Figure 1.1: A conceptual view of a horizontal layer within a turbulent atmosphere characterized by superimposed quasi-coherent structures below and wave-like streamwise unsteadiness above.

Layers in atmospheric boundary layer (ABL)

Layers in the upper ABL establish differently in the daytime versus nighttime, on account of the drastic change in surface radiation, a consequence of the stability of the atmosphere to be discussed in more detail in a subsequent section. Figure 1.2 identifies the horizontal layers that comprise the ABL over an urban setting in day and night, a useful example that highlights the salient features of the more general ABL of any setting with relatively notable surface topography. The upper layers, denoted here as the mixed layer (ML) and entrainment zone (EZ), can be thought of as the initial gradation from free atmosphere down to the surface. In this region, which can occupy up to 90% of the ABL, atmospheric flux properties (e.g. momentum, sensible heat, water vapor) are nearly homogeneous with height due to the mixing effect of entraining less turbulent air down from the free atmosphere through the entrainment zone. Subgeostrophic wind in the middle portion of the mixed layer is nearly constant in speed and direction with turbulence in the region that is typically convectively-driven, though wind shear at the top of the mixed layer does contribute at times. The lowest $\sim 10\%$ of the ABL is considered to be the surface layer (SL), which represents the most accessible region for measurements of all the atmospheric layers. The surface layer is comprised of an inertial sublayer (ISL) (present under specific conditions) and a roughness sublayer (RSL). Winds within the ISL at any instant vary randomly in space and are often described as stochastic- or continuous-gust velocity fields with an average wind speed profile observed to decrease with height nearly logarithmically to satisfy the no-slip condition at the surface. The RSL is the region where the flow is unequivocally influenced by the surface and the roughness elements upon it (if any). It is the RSL that is given special attention herein.

Subdividing further, but this time with vertical demarcations in either or both of the remaining directions, narrows the domain down to a column of air that may or may not vary in its thickness and/or extent. Such an abstraction, known as a control volume, may be arbitrarily assigned, or selected to contour about a given physical surface. Parameters fluxing across the boundaries of these defined spaces, when observable and repeatable, promote discovery of the physical laws that govern that particular volume of interest. The selected volume may represent a smaller part of a greater system or at most be the size of the greater system, but not any larger. This control volume view better emphasizes the so-called canopy layer (CL) as it cuts through a variety of microclimate domains, representative of a further horizontal subdivision of the RSL which generally connects the topmost features of roughness

elements to their nearest neighbors, as illustrated in fig. 1.2. The salient features of three such representative microclimates will be highlighted next.

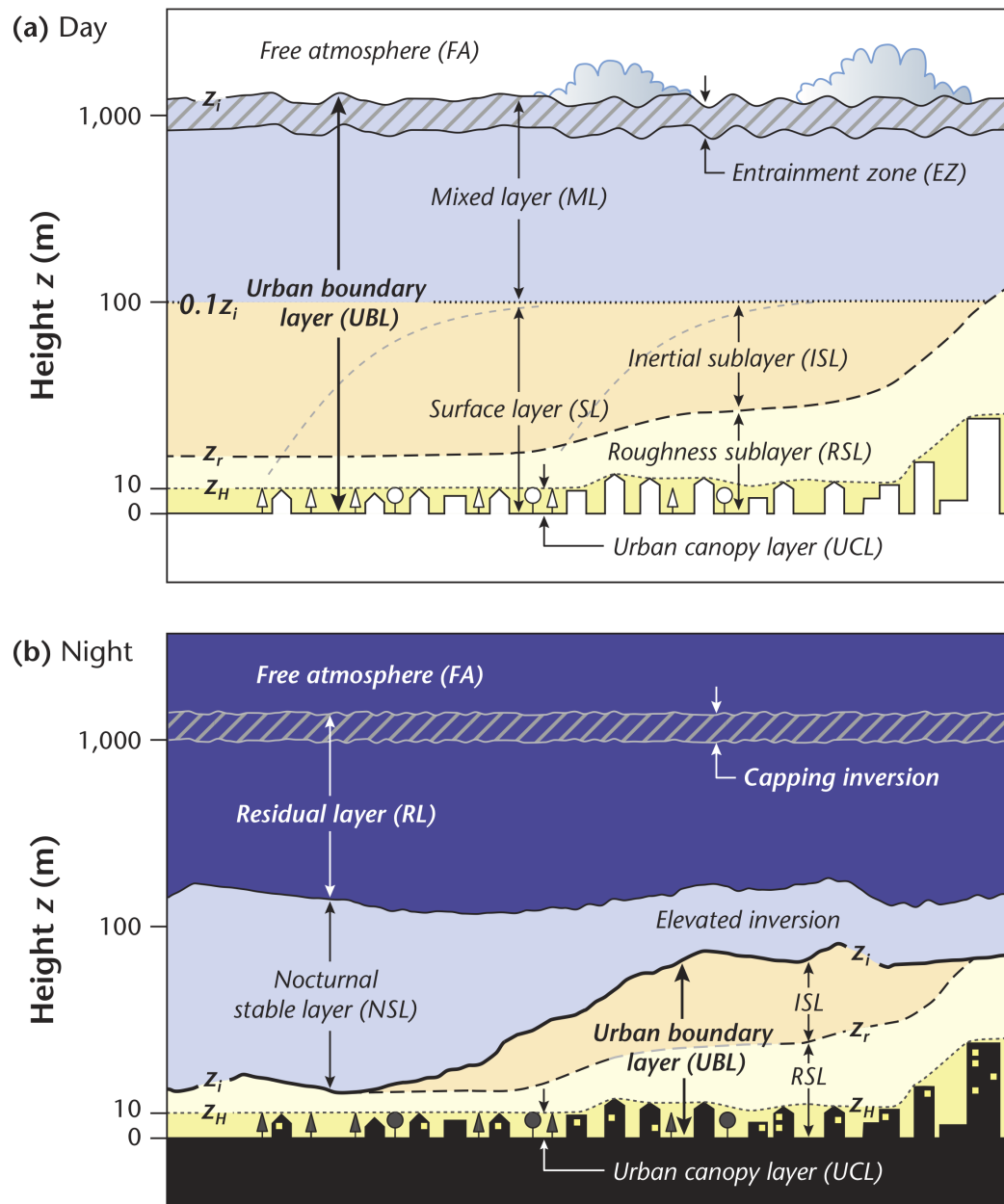


Figure 1.2: A view of the atmospheric boundary layer with its various sublayers established in (a) the daytime and (b) the nighttime. Figure reproduced from Timothy R Oke et al. (2017) with permission of Cambridge University Press through PLSclear.

1.4 Touring the various microclimates

With a better understanding of the physical mechanisms that drive the complex dynamics of the ABL now established, three representative microclimates will be explored to further elucidate the relevant fluid events a flyer may experience near the surface. Though outside the scope of current experimental work, as full of an environmental description (i.e. moisture, temperature, and wind) is given as possible, prior to ultimately reducing the scope to a neutrally stable atmosphere above a canopied surface devoid of any major weather events other than a reasonably strong prevailing wind. Building an intuition for the environmental domains of interest will serve as a reminder of the interconnectedness of the local set of atmospheric conditions that ultimately contribute to shaping the local nature of the wind and how it behaves upon encountering surface roughness elements.

The urban microclimate

Built-up manmade structures of various heights clustered pseudo-randomly upon a location of mixed surface cover where heat, water, and various pollutants are exchanged into the atmosphere well-describes an urban microclimate. Flow among and between buildings and the subsequent turbulent wakes produced are prevalent and generate eddy sizes dependent on the geometry of the roughness element, angle of incidence, and its shedding process. The urban canopy layer (UCL) is defined by the ground below and a contoured boundary connecting building tops above, as drawn in fig. 1.2. The effects of the presence of the UCL can be felt upwards of two to three times the average building height, featuring large variability in the mean and turbulence flowfield properties. Turbulence within this region is characterized by increased vertical momentum flux on account of the increased mechanical turbulent mixing from obstacle wakes. A maximum value of turbulence kinetic energy is found to occur somewhere between just above roof height and twice the building height. Due to the intense mixing right above and the wake production amongst and between buildings, typical similarity scaling methods⁴ used in the upper portions of the ABL do not apply in the urban canopy layer (Christen et al., 2007; Roth, 2000).

⁴For example, the Monin-Obukhov similarity theory (MOST) for the subinertial range of the ABL assumes an approximately constant turbulent flux density of heat, mass, and momentum with height as well as the typical assumptions of homogeneity and stationarity of turbulence for closure of the turbulent boundary layer equations.



Figure 1.3: The local cityscape of 53rd and Park Avenue in New York City, NY, centered upon Seagram building and plaza. Not only must a flyer contend with the effect that heterogeneity of the manmade-building cityscape has on local winds, but also on the environmentally-driven factors of its location in Midtown Manhattan, an island bounded by the Hudson river to the west and the East and Harlem rivers to the east.

The vegetation microclimate

Consider next a plant cover, like a forest, that occupies space between the surface and the atmosphere. Radiative processes are absorbed and reflected like solid boundaries on the various leaf, branch, trunk surfaces but the remainder light can pass through and air motions can circulate beneath and within. The finite thickness layer formed that divides the under-canopy from the above-canopy of tall vegetation represents a permeable and living layer that photosynthesizes, respire, sheds, and grows with the shifting seasons. Temperature differentials from sun to shade and water vapor distributions can both change on account of the winds. Gusts or sweeps can usher in sudden inflows of the atmosphere above to the understory below whereas bursts or ejections have the opposite effect. In a forest with profuse foliage but a clear trunk space free of thickets and sapling growth, wind speeds in the under-canopy may exceed those of the crown, but do not (typically) exceed wind speeds in the above-canopy on account of the aerodynamic drag on the plants. An inflection point in the mean velocity profile is oftentimes observed at the top of the plant canopy layer (PCL) (Raupach et al., 1996), initiating the eddy diffusion processes that more efficiently exchange air masses. Canopy turbulence intensities are far higher than anywhere else in the surface layer on account of energy production in the intense shear layer at the plant tops, though smaller scale turbulence produced from plant wakes contribute too. Due to the spatio-temporal complexity of turbulence in the PCL, combined with the sinks-and-sources of momentum and scalars alike, typical similarity scaling methods used in the upper portions of the ABL do not apply in the PCL (Kaimal and J. J. Finnigan, 1994).



Figure 1.4: A gridded agricultural canopy of date palm trees (Thermal, CA). In this view, relatively slender trunks uphold rather large canopy crowns that demarcate the atmosphere above from the under-canopy below.

The mountain cliffside - Mars

Finally, consider exploration of the Red Planet through the eyes of the Rover. No buildings or trees to be spotted, but cliffscapes can be made out when the dust settles. Daytime is stark in comparison to night. Along the Rover wheels, the ground temperature may be 15K higher than at its tallest mast, a mere six feet above, only to plummet an extra 100K when night arrives to switch the gradient direction. Both the short wave radiation of the sun and the long wave absorption by the CO₂ contribute to large horizontal temperature gradients from mountains to plains to craters that drive topographically-induced thermal circulations during the day. The resulting convective motions may swirl up a dry and wandering dust devil (Schofield et al., 1997) or katabatic winds down the crater slopes and into the dune fields. The atmosphere is thin, about 1/100th the density that its earthly twin and water is scarce, thousands of times less precipitable than an equivalent Earth atmospheric column (Jakosky and Phillips, 2001; Smith et al., 2001). Due to the intense radiative heating-cooling cycle, typical similarity scaling methods used in the upper portions of the ABL do not apply in the Mars planetary boundary layer (PBL) near the surface.



Figure 1.5: Hillside outcrop within Murray Buttes region, lower Mount Sharp. Images taken by MASTCAM onboard NASA's Mars rover Curiosity on Sol 1419 and processed further by Seán Doran (NASA et al., 2016), use under: CC BY-NC-ND 2.0.

1.5 Wind near the surface

In general, air motions observed to vary randomly in space and time subject to the stability characteristics of the atmosphere at a given location, when averaged, are reported as a horizontal wind speed $u_h = \sqrt{\bar{u}^2 + \bar{v}^2}$ oriented in a certain compass-based direction, a safe assumption when the average vertical wind component \bar{w} is much smaller than the horizontal wind components \bar{u} and \bar{v} , as is often the case in the surface layer. By aligning our view with this prevailing wind, and when averaging over homogeneous horizontal layers, conceptually, a two- or potentially three-dimensional mean velocity field can be evaluated as a one-dimensional (assuming divergence is small) horizontal wind that varies with height z . Winds "near the surface", which is oftentimes meant synonymously to flowfields within the RSL in this dissertation, can be made more explicit by considering a bounding height parameter beneath which dynamic turbulence (i.e. mechanically-driven) dominates, a concept explored next.

Stability of winds - time of flight

A measure of the stability of the atmosphere in relation to the isentropic motion of a fluid particle due to the temperature gradient in a stationary atmosphere was previously discussed but can further be identified circumstantially by the characteristics of air motions during specific times-of-day. For instance, at night as the surface radiatively cools outward toward space, lighter-warmer air from above moves downward toward the surface, tending to suppress the vertical displacements of fluid elements. This negative buoyancy flux associated with the positive temperature gradient describes a stable atmosphere and if winds in the region are particularly weak, one may add select descriptors to mark its relative stillness. Classifications of stability, when reported, are often done so rather qualitatively (e.g. "strong", "moderate", "weak", "very weak" in the Turner Classes Turner, 1964), in large part because meteorologists rarely know the actual local gradients⁵ called for in the turbulence kinetic energy equation. For the purposes herein, measures of stability (i.e. how a fluid particle may behave when put into vertical motion against the backdrop of time-averaged local conditions) simply act as broad indicators of the likelihood and prevalence of turbulence in a region at a given altitude for a given time-of-day, couched in the understanding that even statically stable air can be made to create turbulence dynamically through wind shear in the surface layer. As such, because the energetic overlaps of the forcing spectrum and the natural modes of the flyers predominantly occur in the high-frequency turbulent fluctuations portion of

the spectrum, the turbulence of note when testing the response characteristics of flyers of interest will almost always be mechanically-driven.

The Richardson number (Ri), a measure of the relative magnitudes of shear (mechanical) production to buoyant consumption in the turbulence kinetic energy equations, can be used to signal when a flow may become dynamically unstable. For example, when $Ri > 0$, layer stratification is stable and the development of turbulence is hindered⁶. When the $Ri < 0$, with temperature gradients superadiabatic, layer stratification is unstable and the intensity of turbulence increases. At $Ri = 0$, temperature distribution with height is adiabatic, the layers are neutrally-stratified and the turbulent processes occurring within are strictly mechanically-driven. Though useful in its various forms in meteorology, the Richardson number says nothing to the intensity of turbulence likely to be experienced by a flyer flying through, and only expresses the tendency of a flow to become or remain turbulent (or become and remain laminar). Because the value of Ri approaches zero near ground level (no-slip), evidently a sub-layer exists where the influence of stratification due to a given temperature distribution in an inhomogeneous atmosphere (whether stable or unstable) is small enough to neglect, and a *near-neutral* stability condition is reasonably met. By extending criterion to diabatic (non-neutral) environments through a correction factor that accounts for the buoyancy contributions, Obukhov derived a conditional length characteristic L_O he called "the height of the sub-layer of dynamic turbulence", which is typically on the order of tens to hundreds of meters and varies diurnally, even in fair weather conditions (e.g., see Stull, 1988, Fig. 5.21), given here as

$$L_O = \frac{-u_*^3 \bar{\theta}_v}{\kappa g (\overline{w'\theta'_v})_o} \quad (1.8)$$

where $\bar{\theta}_v$ is the mean virtual potential temperature and $(\overline{w'\theta'_v})_o$ is the virtual potential temperature flux at the surface. The physical interpretation of the Obukhov length as a height *proportional* to which the buoyant production of turbulence dominates the mechanical production of turbulence is a useful bounding parameter for the purposes herein. For instance, when $L_O < 0$ (indicating an unstable atmosphere, typical on sunny days due to convective heating), $|L_O|/10$ can be taken as the height that

⁵Approximations of these gradients via more readily available observations do provide more quantitative metrics, such as the NOAA GOES-R Series Advanced Baseline Imager (ABI) Level 2 Derived Stability Indices (DSI).

⁶In theory, beyond a certain critical Ri , turbulence can be suppressed outright.

separates the predominantly mechanical from predominantly convective turbulence (Panofsky, 1984). A dimensionless height ξ^7 based on the Obukhov length provides the most utility, as the sign of $\xi = z/L_O$ implies the stability of the atmosphere in the surface layer and the magnitude of L_O determines the altitudes z at which dynamic turbulence is expected to dominate. Though we acknowledge the effects of atmospheric stability in the upper layers of the ABL, winds near the surface characterized by predominant mechanical turbulence will be treated as satisfying (even if approximate) a near-neutral condition. This focus on reasonably strong winds ensures near-neutral conditions are essentially always met so that $L_O \rightarrow \infty$.

Wind profiles

In the upper regions of the surface layer, the influence of individual surface features reduces to the point where their roughness can be accounted for in an integral sense. That is to say that when considering *mean* characteristics of the velocity field in the inertial sublayer (ISL) in a neutrally-stratified atmosphere, the spatial variability of atmospheric properties introduced at or near the surface are sufficiently homogenized so as to be considered akin to a sandpaper roughness in the canonical turbulent boundary layer studies of flows over smooth and rough surfaces, as first suggested by Prandtl (1932). The logarithmic law of the wall, put forth by Kármán (1931), and adjusted for surface roughness can be given as:

$$\frac{\bar{u}_h(z)}{u_*} = \frac{1}{\kappa} \ln\left(\frac{z - z_d}{z_0}\right) \quad (1.9)$$

where u_* is the friction velocity ($\sqrt{\tau/\rho}$), z_d is the zero-plane displacement thickness that moves up the height of the effective uniformly-rough surface 'felt' by the flow, z_0 is the roughness length typically found through extrapolation of \bar{u}_h to zero, and $\kappa \approx 0.4$ is von Kármán's constant. The zero-plane displacement thickness included in eq. (1.9) reflects the reality that momentum is absorbed predominantly by the upper portion of the canopy roughness elements. A so-called exponential wind law was formulated by Cionco (1965) for flow within an 'ideal' vegetation canopy (i.e. uniform geometry and distribution) and was later modified by Macdonald (2000) in wind tunnel studies of arrays of bluff elements (cubes with height H) to more closely represent the features of an urban-type surface. Through an empirically-determined attenuation coefficient (that can be related to the turbulence length scale), spatially

⁷A functional dependence on this dimensionless height forms the premise of the so-called Monin-Obukhov similarity theory (MOST), applicable to the profile equations in the constant-flux portion of the surface layer, valid $|\xi| < 1 - 2$. Foken (2006) notes that even in ideal conditions over homogeneous surfaces, MOST is only about 10-20% accurate.

averaged velocity profiles within the canopy ($z < z_H$) were modeled as:

$$\frac{\langle \bar{u}_h(z) \rangle}{\langle \bar{u}_h(z_H) \rangle} = \exp \left[a \left(\frac{z}{z_c} - 1 \right) \right] \quad (1.10)$$

where z_H represents the measurement location at $z = H$ and a is the attenuation coefficient found to be $a = 9.6$ for in-line and staggered arrays of cubes of uniform height. Christen (2005) found adequate agreement for the exponential decay law of eq. (1.10) within the upper portion of an urban canopy layer based on extensive field site testing, whereas Castro et al. (2006) noted its deficiency in higher density roughness cube distributions in wind tunnel studies. Florens et al. (2013) suggest a linear in-canopy velocity profile from measurements with a high resolution PIV system. More to the point, whatever shape the velocity profile within the canopy layer may take, an inflection point of the mean velocity profile is noted to occur near canopy height z_H in every study of wind flowing across the face of roughness elements (the implications of which will be discussed in a subsequent section). When taken together, wind profiles in the surface layer above distinct canopies can be roughly represented as in fig. 1.6, with the discrepancies of in-canopy velocity profiles noted as above.

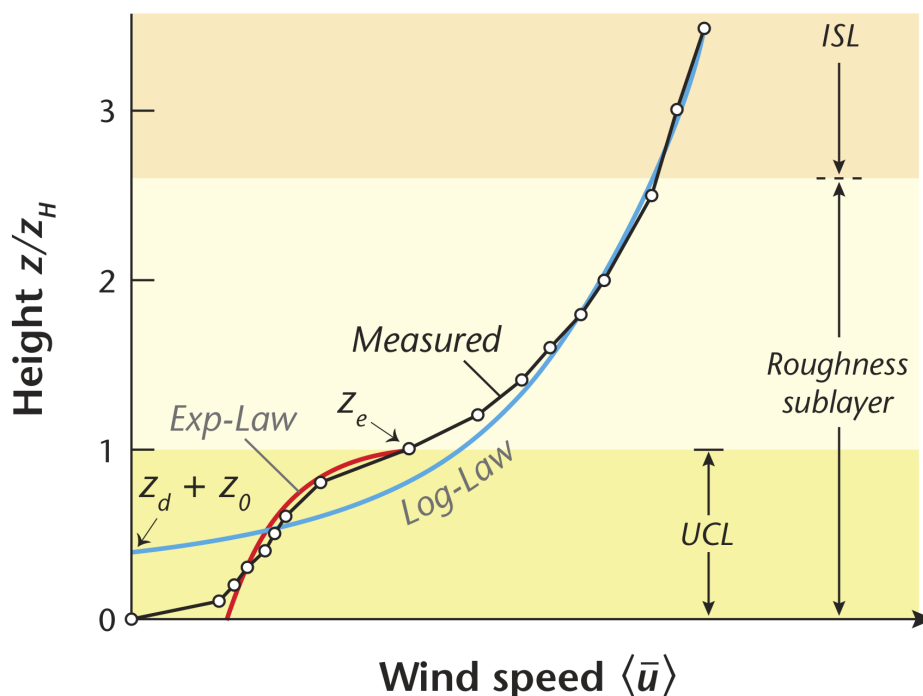


Figure 1.6: Wind profile with the log-law (eq. (1.9)) and exp-law (eq. (1.10)) included for comparison against the demarcated surface layer of fig. 1.2a. Figure reproduced from Timothy R Oke et al. (2017) with permission of Cambridge University Press through PLSclear.

The nature of the winds near the surface

The wind profiles presented in the previous section, though useful mathematical constructs, obscure the true instantaneous nature of winds which are nearly always turbulent and unsteady. Because atmospheric motions occur over a huge range of temporal and spatial scales, it is useful to know how the energy of the atmosphere at a location distributes amongst those scales. Perhaps the most direct view is that of the spectrum. In general, a spectrum plotted for an atmospheric quantity measures the distribution of the variance of that given variable in relation to frequencies or eddy sizes. When the variable in question is a time record of a velocity component, the spectrum then describes directly the distribution of (kinetic) energy with respect to frequency. The kinetic energy of horizontal air motions within the atmospheric boundary layer under certain conditions is observed through field experiments (see Davenport, 1961; Van der Hoven, 1957) to distribute into two distinct energy bands with a gap in between.

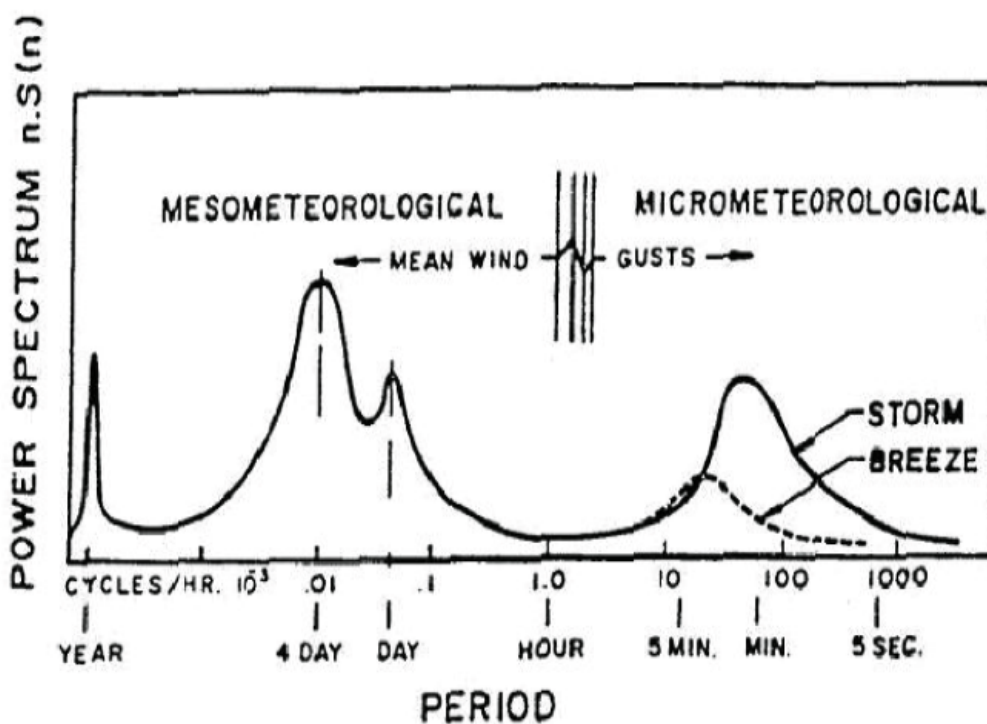


Figure 1.7: Evidence of the spectral gap from the Van der Hoven spectrum at the Brookhaven site from two occasions, one in nominal conditions ('breeze') and the other purposefully tested during hurricane Connie ('storm'). Figure republished with permission of Springer, from Stathopoulos and Baniotopoulos (2007), after Van der Hoven (1957); permission conveyed through Copyright Clearance Center, Inc.

Synoptic scale instabilities associated with horizontal wind gradients create large-scale (horizontal) atmospheric motions on the order of several thousand kilometers, representative of the types of macroscale atmospheric flow systems that can be resolved on weather maps. In contrast, microscale motions representing fluctuations with periods less than about one hour occur predominantly due to heating and the frictional motions of air near the surface. Sitting inbetween are the mesoscale motions that account for strong diurnal variations such as sea breezes and gravity waves.

When energy distributes amongst specific energetic bands, advantages in analysis emerge; chief among those are the treatment of those particular frequency bands as statistically independent of estimates in other frequency bands. Power-spectrum analysis of horizontal winds in the ABL suggests a major energetic peak at a period of nearly four days (corresponding to fluctuations in wind-speed driven by the passage of large pressure systems) and a second discernible spectral peak at a period of about one minute (the average time from one gust to the next on account of the convective and mechanical turbulent fluctuations). Separating the two is a broad and, at times, consistently low-amplitude energetic lull centered upon periods approximately ranging from ten minutes to an hour. J. Lumley et al. (1964) suggest that in order to discuss the statistical properties of microscale turbulence in the ABL in isolation from the larger scale turbulence it is embedded in, a spectral gap is necessary. When held in reference to the flyers of interest, the existence of a statistically significant spectral gap is of secondary importance compared to the energetic bands overlapping the representative time and length scales of the flyers themselves, as will be discussed in section 1.5. However, justification in the analysis of winds in the ABL through a decomposition of the instantaneous velocity field hinges upon the suitable separation of such scales, where the synoptic scale peak is said to be associated with the *mean* flow and the microscale peak associated with *stochastic gusts*. The stability of the atmosphere at a particular location ultimately determines the nature of the microscale motions (i.e. the size and frequency) likely to be encountered by the near-surface flyer but because the mechanical turbulence tends to increase with the square of wind speed, the contribution of convective turbulence will always be comparatively small in the presence of a reasonably strong wind, validating the likelihood of a spectral gap in strong wind conditions and further diminishing the influence of stratification in these studies.

The scales of and within the surface layer

Response characteristics of a flyer flying through the surface layer depend directly on the forcing spectrum of the environment, and a particularly strong amplitudinal-response would occur at frequencies where energy in the forcing spectrum coincides with flight dynamic natural modes⁸. For the flyers of interest herein, natural modes are typically on the order of 10^0 cycles per second (Hz) (and sometimes even upwards of order 10^2 Hz), such that overlap in the forcing spectrum would nearly always occur in the microscale portion of the spectrum. As such, the mean wind motions in the surface layer averaged over 30-minute time histories or modeled by eq. (1.9) and eq. (1.10) and assigned as descriptors of the synoptic scale motions are of secondary importance when held in comparison to the fluctuations of and about the prevailing winds of the region where the flyer will fly, as it is flying. This pushes towards a more intimate understanding of the microclimatology of the region (as was explored previously) at a given time-of-day amongst the backdrop of the local terrain, because ultimately the statistical structure of the microscale motions is determined by the wind speed, the atmospheric stability, and the terrain characteristics. Coupled with the variability in flyer design, it is rather unlikely to account for every scenario in a single diagram. Instead we choose **an urban cityscape as a model environment** as it represents some of the tallest, bluffest, and most heterogeneous of the canopied topographies, further enriched and complicated by the imprint of humankind. Figure 1.8 showcases the order of magnitude overlay of characteristic flyer time and length scales compared to example urban (micro)climate phenomena in a standard time-space plot. Length and time scales of interest are defined and noted as intuitively as possible. Consistent with the bulk of literature in the atmospheric sciences, micro- here does not indicate scales of the order 10^{-6} , but rather a smaller complement of a broader, more macro- view. For instance, as put forward by Sutton (1953) micrometeorology denotes “the intimate study of physical phenomena taking place over limited regions of the surface..., and usually within the lowest layers of the atmosphere”, which is held in contrast to the synoptic-scale weather systems that involve large regions of great depths. The same applies in the microclimate and (macro-)climate complement. Many such naming conventions exist, highlighting the difficulty in grouping processes that at any instant or at a particular place may not actually conform to its assigned subdivision. For

⁸It is customary when modeling the effects of turbulence in design studies for manmade flyers to summarize the effects of system dynamics by treating the (linearized) spectral response of a flyer as a product of the forcing spectrum and its transfer function.

this reason, where possible, ellipsoids are drawn to better represent the variability inherent to the domains of interest as they present across broadly-encompassed fields of study.

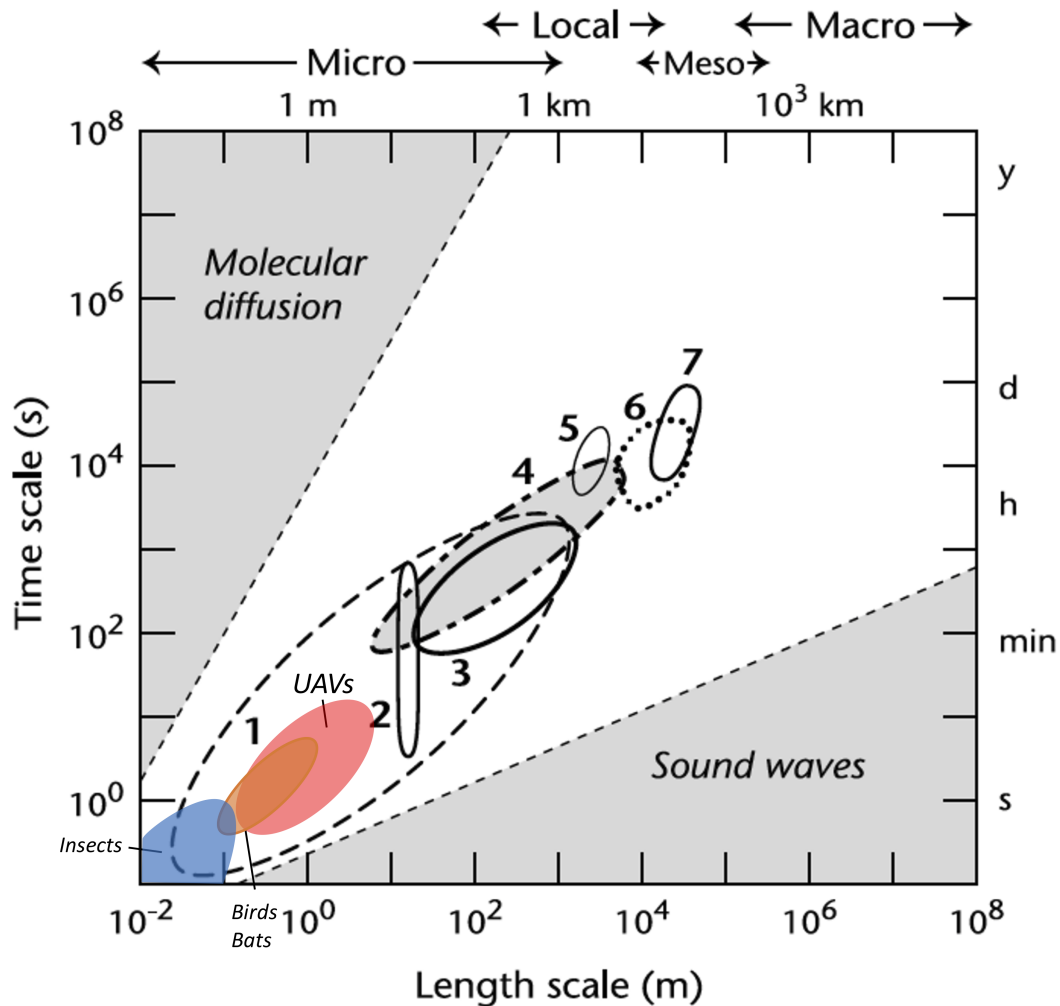


Figure 1.8: The conventional atmospheric length scales of macro-, meso-, local-, and micro- are defined atop and put into urban cityscape reference elements below. Characteristic time scales are given at left and put into colloquial divisions at right. It is interesting to note the separation of scales between the flyers (UAVs, birds, bats, insects) and the majority of likely urban atmospheric fluid events. Overlap in the dashed region 1 corresponds to mechanical eddies shed by obstacles; 2 - cross-canyon vortex; 3 - individual building wake; 4 - chimney stack plume; 5 - urban park breeze circulation 6 - urban-rural breeze system; 7 - uplift in city 'plume'. Figure republished and modified with permission of Springer Nature BV, from Tim R Oke (2006); permission conveyed through Copyright Clearance Center, Inc.

1.6 Treatment of flows near the surface: a simplified view

Though the focus of this dissertation remains extensively on the exposition into simulation techniques for the three flow regimes directly above, at, and within the canopy layer (CL) embedded within the roughness sublayer (RSL), a quick departure up to the inertial sublayer (ISL) is warranted, if nothing more, by the simple fact that the majority of available field study data and the bulk of modeling efforts has focused on treatment of roughness at the surface as a homogenous porous medium. With but few exceptions, many of the tower measurements to be referenced subsequently would describe the terrain of measurement as an open field (e.g. farmland, grassland, desert) broken only by a few trees, some hedgerow, or distant structures, each in their own way far from the environment of the built-up urban cityscape selected as a model for consideration herein. The modeling of atmospheric turbulence far above cities or near airports (or any other take-off and landing locations), however, is well-established and an important consideration for the handling characteristics and structural integrity of the larger-faster flyers that ascend/descend through the surface layer up-to/down-from cruising altitudes far outside the local microclimate views considered thus far. Even though peak energies in the forcing spectrum of the disturbance environment far from local effects do not overlap the frequency regimes of the smaller surface-bound flyers of interest herein, a discussion and simulation technique for the microscale motions in the ISL is included for completeness to complement the more local considerations in the RSL to follow.

Treatment of flows within the inertial sublayer (ISL)

The universality of wind motions in the inertial subrange over ‘rough’ walls is well-established provided the surface roughness height remains below a certain threshold relative to the boundary layer thickness. Jiménez (2004) suggests that if the height of the roughness element at the surface does not exceed 2-3%⁹ of the boundary layer depth δ_{BL} (typically cited as $\sim 500\text{m}$ for the near-neutral atmospheric boundary layer), the most important effect of roughness is the change of mean velocity profile near the surface. Time-averaged statistics in the atmospheric surface layer far from local effects can generally be accounted for by the Monin-Obukhov similarity theory (MOST), which proposes universal functions that scale height z with the Obukhov length L_O . In the presence of strong winds in a neutrally-stratified atmosphere ($L_O \rightarrow \infty$), the mean velocity profile in the windward direction reduces to the familiar logarithmic law of the wall of the canonical turbulent boundary layer,

presented in section 1.5, so that when adopting a more global view and considering flight within the ISL (say, $z \approx 3H$) above short roughness elements with average geometric height H that do not constitute a canopy, differences in terrain roughness can safely be accounted for by use of a bulk surface roughness parameter, such as the roughness height z_0 .

To center the conversation, consider a flyer attempting to maintain its hover position in the presence of a continuously-gusting velocity field high above a city or somewhere in an open field. In this coordinate system (averaged over homogenous horizontal layers), since the flyer neither appreciably gains nor loses altitude, the velocity field experienced will change in time but not in space, with peak spectral energy of the environmental disturbances occurring typically with a period of one minute or so, in accordance with observation such as in fig. 1.7. For typical gusting velocities approaching 10^1 m/s, associated longitudinal distances between wavefronts in a horizontal wind would then be of order 10^2 m for a spectral peak at a period of one minute, about one or two orders of magnitude greater than any typical geometric dimension of the flyers of interest, according to fig. 1.8. It does not appear, then, that any specific length-coupling in the longitudinal direction emerges when considering stochastic gusts in the surface layer far enough from the specific wavelengths introduced by the geometries of the roughness elements at the surface, such that the flowfield is experienced globally from the perspective of the flyer. Atmospheric turbulence in the inertial sublayer (ISL) is observed to essentially behave isotropically, analogous to the inertial subrange in the canonical turbulent boundary layer of smooth and rough walls, where eddies with no obvious direction-preference transfer energy without loss from the larger scales down to the smaller scales.

Modeling the form of the spectrum far from local effects

Davenport (1961) compiled horizontal wind velocity records when mean velocities exceeded 9 m/s, all measured below $z = 150$ m at three different tower sites. He proposed a form of the spectrum¹⁰ to fit observation based on the assumption that the energy of the eddies should be proportional to surface drag (and therefore the square of the mean velocity) measured at some reference point near the ground. The drag coefficient is more commonly used in the wind loading of structures but can be related to the roughness height z_0 (see Wieringa, 1992). Though empirical fits to observed data can be useful for some engineering models, the lack of theoretical basis

⁹Amir and Castro (2011) and Florens et al. (2013) provide some evidence that number may be closer to 7%.

limits its scope, particularly for analyses that depend on the shape of the spectrum. On strictly theoretical grounds, Kármán and Howarth (1938) calculated correlation coefficients for two arbitrary velocity components for isotropic turbulence. By considering the Fourier transform of these correlation functions, Kármán (1948) showed that, for large Reynolds numbers, the shape of the spectral function would be proportional to $k^{-5/3}$ when k is large, and behaves according to k^4 for small values of k , where $k = 2\pi f/\bar{u}$ is the wave number of the fluctuation and \bar{u} is the mean horizontal wind speed. The interpolation formula that was proposed by von Kármán was adapted for the case of fixed-wing airplane response to continuous random atmospheric turbulence in Diederich and Drischler (1957). Its use in flight applications is well summarized in Etkin (1981), and for helicopters specifically in Gaonkar (2008). The power spectral density of the longitudinal component of the velocity field, based on von Kármán's atmospheric turbulence formulation, is then written as:

$$\Phi_u(\omega) = \frac{2\sigma_u^2 L_u}{\pi V} \frac{1}{(1 + (1.339 \frac{L_u \omega}{V})^2)^{5/6}} \quad (1.11)$$

where $\omega = 2\pi f$ and V is the simulated flyer speed. Two parameterizations are required in this formulation, namely the turbulence scale length L_u (assumed to be ~ 750 m when unknown) and the root-mean-square (R.M.S) of the fluctuations $\sigma_u = (\overline{u'^2})^{1/2}$, which can be derived from the intensity of the random turbulent motions in the ABL (i.e. $TI_u = u'/\bar{u}$) known to vary with altitude and range from 5 – 30%. Measurements taken in the ABL near the surface away from local topographical effects during convectively stable and mixed atmospheres suggest integral length scales L_u to be on the order of the flyer altitude (Witte et al., 2017; Yeung et al., 2018), though calculations for this particular turbulence length scale have long been challenging and should be interpreted with caution due to the non-stationary behavior of winds near the surface. Here, Taylor's frozen turbulence hypothesis used

¹⁰Because there appeared to be only slight variation in the strong horizontal wind spectrums with height, no characteristic length for the horizontal components of gustiness that depended on altitude or surface roughness length could be identified, and was instead taken as constant to render an (empirical) expression for the spectrum of gustiness in strong winds in the lower layers near the surface but far from local effects to be:

$$\frac{f \cdot E_{11}(f)}{\kappa U_{10}^2} = 4.0 \frac{s^2}{(1 + s^2)^{4/3}}$$

where U_{10} is the reference mean velocity measured at $z = 10$ m, κ is the drag coefficient, and $s = 1200 \cdot f/U_{10}$.

in conversion from the frequency domain to the wavenumber domain is doubtful to apply, since a single constant convective velocity describing all frequency scales is not readily apparent as mean wind speeds change over time. Due to the potential of ‘smearing’ in the spectral analysis in wavenumber space, it is recommended that classification of large-scale structures in the atmospheric surface layer be carried out in the frequency domain when mean wind speeds change appreciably according to measured temporal wind records (Guala et al., 2011). Velocity fields with significant non-stationary behavior will be presented in the frequency domain only. When comparing to Kármán’s form of the spectrum, L_u will be assumed order of magnitude of the altitude at which the turbulence intensity is specified.

The theoretically-derived $-5/3$ power law behavior of the microscale structure of turbulence is observed to occur in the inertial sublayer (ISL) both from measurements on instrumented aircraft (Sheih et al., 1971; Witte et al., 2017) as well as from tower measurements far from topographical influences (Pond et al., 1963; Watkins et al., 2010). This region typically spans three decades of frequencies in a neutrally-stable atmosphere with the Reynolds number based on the root-mean-square of the fluctuating component u' and λ_T (i.e. $Re_{\lambda_T} = u'\lambda_T/\nu$) ranging from 2880 to 5330. The so-called Taylor microscale λ_T is a characteristic length scale commonly used in isotropic turbulence to denote an intermediate size eddy that is smaller than the larger energy-accepting eddies but larger than the dissipative eddy scales. This forms the basis of the preferred atmospheric disturbance model required by the military (MIL-STD-1797A) and the Federal Aviation Administration (FAA, part 25, appendix G) to model the flying qualities of a piloted fixed-wing aircraft in the ABL because it properly resolves the effects of structural modes at higher frequencies. The model relies on airplane motion through the spatially-varying continuous gust field to generate temporal variations in wind velocity (‘frozen in time’) and thus excludes its use in hover applications.

Treatment of flows within the roughness sublayer (RSL)

Close to rough surfaces, the Monin-Obukhov similarity theory (MOST) no longer holds. Turbulent fluxes near plant canopies or urban areas are nearly always greater than is predicted by MOST from observed mean gradients on account of the change in the dominant flow mechanism of turbulence generation due to the presence of coherent structures. Consider a prevailing wind flowing left to right relative to the viewer for each of the frames of figs. 1.3 to 1.5, with a control volume fitted exactly to the frame. Due to the occurrence of intermittent coherent structures within the

specified control volume, traditional boundary layer scaling techniques ultimately fail. These coherent structures are initiated by Kelvin-Helmholtz instabilities, that unlike their gentler counterparts (e.g. gravity-waves on a cool night) roll up into coherent vortices before ultimately breaking down into turbulence. This process initiates vigorous turbulent exchange of the properties of the air masses above-and-below or from within-and-without. Conceptually, moving across the interface of the dividing streamline (be it urban, vegetation, or cliffside) is characterized by notable velocity gradients, the steepness of which coupled with the angle of entry determining the closest analogous forcing input experienced by the flyer passing through. The region into which the flyer enters would vary dependent upon the morphology of the roughness, thus further shaping the forcing input experienced by the flyer.

The roughness sublayer immediately above and below the canopy eddies

Recognizing that there is at least one more relevant length scale within the roughness sublayer, a simple coupled canopy-surface layer model analogous to MOST that scales additionally with δ_ω was developed by Harman and J. J. Finnigan (2007) and for neutral-conditions by Poggi et al. (2004) scaled with the geometric roughness element width d_r . Poggi et al. (2004) notes that for a regular array of vertical rods, at least near $z \approx H$, dense canopies share many attributes with perturbed mixing layers. At an altitude within the roughness sublayer (say, $z \approx 1.25H$) above the location of the inflection point near the canopy top ($z \approx H$), a longitudinal length scale associated with the dominant flow mechanism of the coherent structures must also be considered. One candidate is the streamwise separation Λ_x of the coherent structures themselves, observed to be approximately four times the shear layer width δ_ω at plant canopy tops (Raupach et al., 1996), well within the range observed for planar mixing layers generated in the lab (see Dimotakis and Brown, 1976). The specific details of the coherent structures at the canopy top (i.e. δ_ω at $z \approx H$) are rarely reported and the longitudinal length scale from correlation data L_x measured away from the canopy eddies is often given in ratio to the more readily available geometric roughness element height H .

¹⁰Orographically-induced turbulence (e.g. gravity-waves) wouldn't be fast enough ($St \sim 10^{-2}$) to compete with the quasi-periodic eddies ($St \sim 10^0$) at the canopy layer boundary.

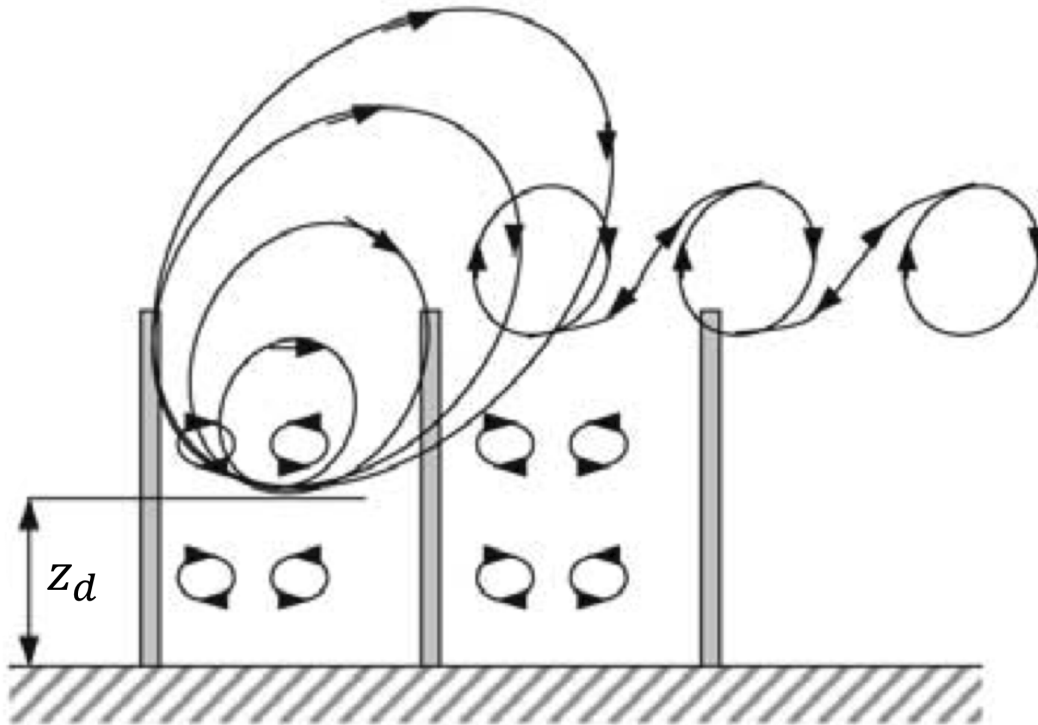


Figure 1.9: In the phenomenological model of Poggi et al. (2004), the size of vortices distribute into three categories. Far above local effects, the displaced rough wall boundary layer vortices extend up into the ISL ($z \gg 2H$). Within the canopy, local canopy geometric considerations determine the nature of the vortices. The vortices in the region at and just above the canopy top are of the mixing layer type. Figure republished and modified with permission of Springer, from Poggi et al. (2004); permission conveyed through Copyright Clearance Center, Inc.

From single-point measurements above (sparse) plant canopies, Brunet et al. (1994), J. Finnigan (2000), and Raupach et al. (1996) note that $L_x \sim H$. Shaw et al. (1995) citing limitations in Taylor's hypothesis with use of the mean velocity as a proxy for the convection velocity near canopy top suggested from spatial two-point measurements that $L_x \sim (2 - 3) \cdot H$, further supported by the work of Castro et al. (2006) over urban-type roughness (a staggered cube array). Particle image velocimetry (PIV) and laser Doppler anemometry measurements over that same staggered cube array were carried out by Reynolds and Castro (2008) to identify the dominant features above, at, and within the canopy layer. They suggest a "two-scale" behavior below $z = 1.5H$ for their wind tunnel experiments that yield a nearly four-fold difference between a large longitudinal separation trend more closely linked with outer scales and a smaller longitudinal separation trend associated with canopy-produced turbulence reported at $L_x = (0.8 - 1.5) \cdot H$, depending on

lateral measurement location relative to the cubes. Within the canopy (below the active turbulence of the canopy eddies), the geometric constraints of the roughness elements reportedly reduce longitudinal motions to a near constant $L_x = 0.15H$ for $z < 0.8H$, an $\approx 85\%$ reduction of L_x compared to measurements at $z = 1.2H$. At every measurement location $z < 1.2H$, the ratio of longitudinal length scale L_x to the vertical length scale L_z always ranged between 0.5 and 2, suggestive that eddies behave more isotropically above and within the canopy.

1.7 The free shear layer: a change in wind state

Any flow free from solid boundaries exhibiting a mean velocity gradient is considered a free shear flow. Both jets and wakes are classically-abstracted examples, but it is the mixing layer that undergirds the initial development of either flow and in this sense is considered a basic building block of any free shear flow (Heinrich E. Fiedler, 1998).

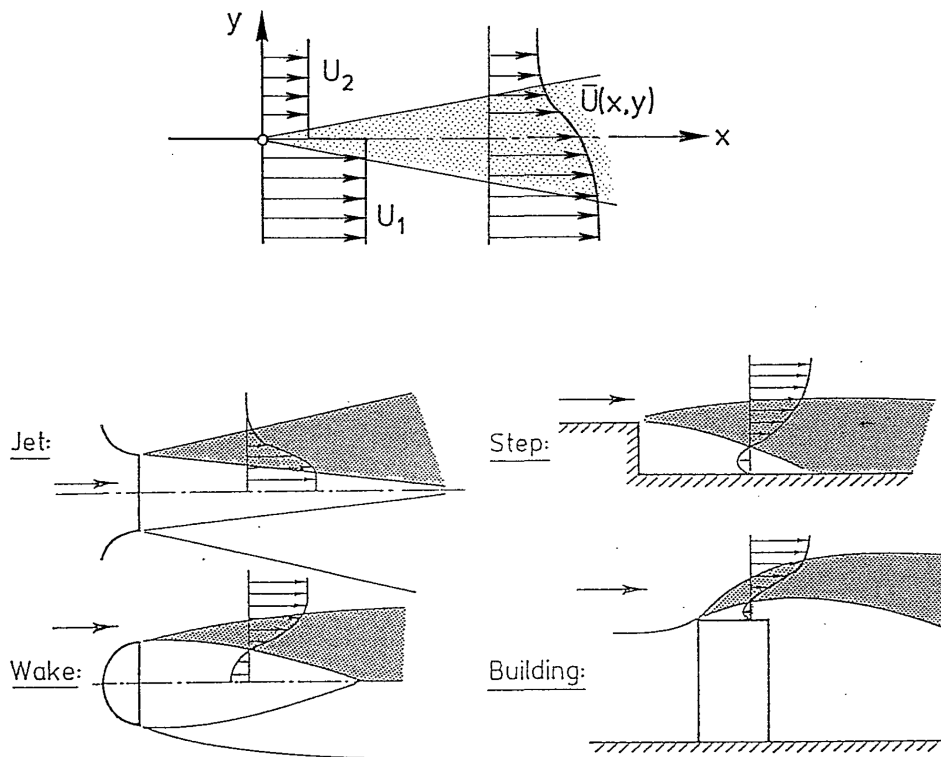


Figure 1.10: The hatched areas highlight the growth of the shear layer in the jet, wake, step, and simple building configurations. Figure republished with permission of Springer, from Heinrich E. Fiedler (1998); permission conveyed through Copyright Clearance Center, Inc.

When viewed two-dimensionally, each of the examples of fig. 1.10 conceptually initialize the wind conditions as a step input with corresponding output being that of a growing free shear layer. When the dynamics of the flyer are decoupled from the dynamics of the shear layer, passage through the shear layer can be treated as a quasi-steady gradation serving as a finite thickness division (that grows downstream) between two wind states. Then, from the point-of-view of the flyer, a discrete gust, of some obliqueness determined by the entry/exit angle of the flyer, is experienced.

What is meant by ‘discrete gust’?

A discrete gust refers to a noticeable change in wind state encountered briefly by a flyer. It is discrete insomuch as the wind event is individually separate and distinct from an otherwise baseline flowfield and is brief in that the wind event is transitory.

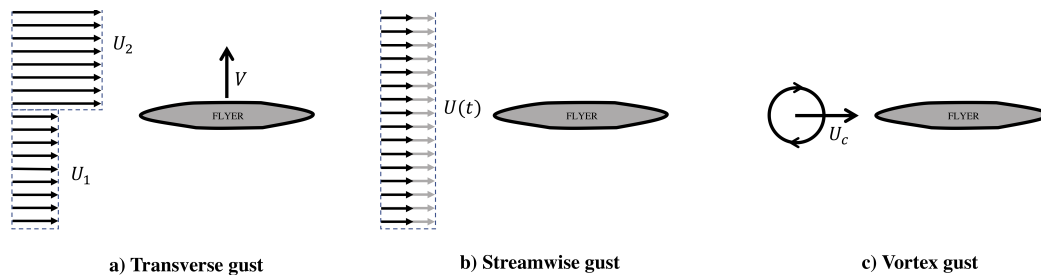


Figure 1.11: Gust types within the selected view.

Three such discrete gust abstractions are typically considered, diagrammed in fig. 1.11. *Transverse* gusts, such as updrafts in forward flight or cross-flows when ascending/descending, are characterized by their angle of incidence (i.e. direction of shearing wind relative to the flyer is taken as normal to the direction of flight) and relative magnitude of wind speed. *Streamwise* gusts that represent the instantaneous nature of changing winds near the surface, manifest as time variations in the streamwise flow, relative to the flyer; when steep, the flyer experiences a gust front. A transience (or residence time) is implied with discrete gusts, and a flyer can be thought to fly into or out of the gust encounter. Either direction can represent a significant change of state of wind speed, depending on the steepness of the gradient. Oblique flight through strong shear layers, in the two-dimensional view, represents a combination of the transverse and streamwise gust encounters. *Vortex* gust encounters are transient events that occur between gust shear layers that bound a wake, for instance, where coherent structures are shed from the surface roughness elements and are perceived by the flyer discretely.

The domains entered

Certain classical abstractions of fig. 1.10 translate to reality better than others. For instance, it is not difficult to see the similarities between the selected view of the mountain cliffside microclimate and the geometrically idealized step configuration; based on our general understanding of step flows we may even be able to intuit the nature of the recirculation zone that would likely form in the sheltered cliffside. Further, we may convince ourselves that the shear layer developed above the tallest building in a cityscape may resemble in some way the simple building configuration, but the ideal view quickly fades when descending further into the canopy layer (CL). Within, the flowfield consists predominantly of wakes, not unlike the wake configuration of fig. 1.10, but initiated and superimposed from the many individual bluff roughness elements. Interaction with such turbulence would depend largely on the morphology of the roughness and the specific point in space considered. Though the flowfield domains into which the flyer enters and exits will vary from microclimate-to-microclimate, day-to-night, based on the roughness and with height, careful consideration elucidates a set of locally energetic and prevalent flow features (in the presence of a reasonably strong wind) warranting a closer look as candidates for experimental simulation. From this point forward, to promote a more focused conversation, canopied flows over roughness elements whose average height far exceeds the applicability of traditional boundary layer scaling techniques will be considered. To enter or leave the domains demarcated by the canopy layer boundary requires passage through the canopy-scale eddies that are active in the presence of a prevailing wind. Once within the canopy, lateral shear at the interface between superposed interacting wake and non-wake regions behind the bluff bodies accounts for lesser energetic and less coherent shear-induced finer-scale turbulence. Above the canopy layer, where the freestream velocity begins to recover, the presence of the shear layer is still felt, but not discretely as when passing through.

Canopy shear layers - mixing layers and wakes

It is precisely the change in velocity profile coupled with the discreteness and distribution of the roughness elements that, when adopting a more local view, prompted researchers to explore the physical consequences of the observed mean velocity inflection point above vegetation canopies (e.g. Raupach et al. (1996) and J. Finnigan (2000) through field observation and J. J. Finnigan et al. (2009) through simulation) and subsequently extended to bluffer configurations in a wind tunnel (e.g., see Böhm et al., 2013; Reynolds and Castro, 2008).

If the roughness elements are tall enough and distributed so as to support a canopy flow regime, then the flow retains few of the mechanisms of wall turbulence and is better described as a flowfield over distributed obstacles. Notions of universality based on height above the surface have no bearing in this local view, as the presence of coherent structures near the canopy top supplants as a dominant flow mechanism. The surface density ultimately determines the thickness of the roughness sublayer (RSL), the region of transition between eddies linked to a height-independent length scale and eddies in the ISL that grow with distance from the displacement plane z_d (i.e. height-dependent).

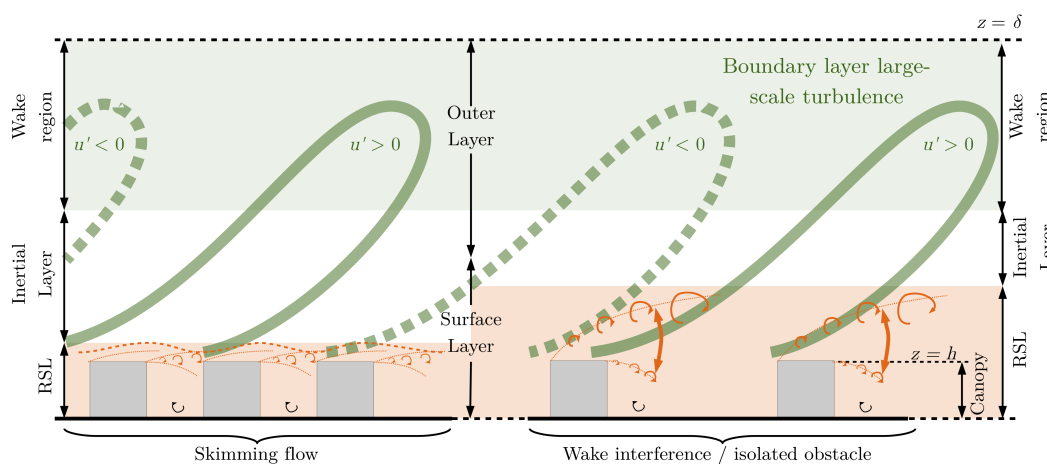


Figure 1.12: The surface roughness density determines two types of flow behaviors in the idealized uniform-height roughness configurations typically tested in wind tunnel studies. Denser configurations result in a sheltered skimming flow that decrease the effect of roughness in upper layers whereas sparser configurations increase the reach of roughness proportional to the frontal surface of the roughness elements. Meandering ‘superstructures’, representing the most energetic structures in the energy spectrum of the surface layer, reach up into the logarithmic region and scale with the boundary layer thickness δ , an outer variable length scale (e.g., see Hutchins and Marusic, 2007). Figure republished with permission of Springer Nature BV, from Perret et al. (2019); permission conveyed through Copyright Clearance Center, Inc.

A simplified view of the canopy flow regime centered on the premise that the flow dynamics in the three regions immediately above, at, and within the canopy are most influenced by the presence of free shear layers with characteristic eddy length scales that are height-independent signals a major departure from traditional boundary-layer scaling techniques that focus on the energetic motions of the inertial sublayer (ISL) known to scale with height.

The instability associated with the inflection point of the mean velocity profile near canopy top, at least for winds flowing across a relatively uniform-height urban canyon (as opposed to down its streets), was observed by Christen (2005) to produce turbulence that fit well within the plane mixing layer analogy of Raupach et al. (1996) developed for vegetation canopies to explain observed differences in canopy turbulence compared to turbulence in the ISL. However illustrative, the simplified view across a dense canopy of uniform height (or of flow above or around a single obstacle in isolation) is far removed from the spatial reality of a clustered set of bluff obstacles more commonly found in the canopies of interest.

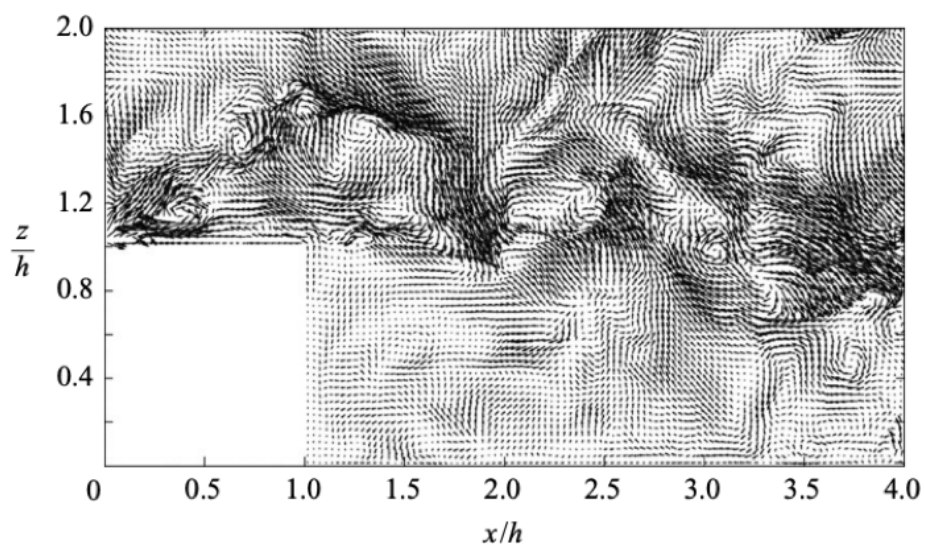


Figure 1.13: The fluctuating wind vectors over a regular array of cubic obstacles from the numeric study of Coceal et al. (2007).

A conceptual leap can be made up to a staggered or aligned array of bluff bodies as is often used in wind tunnel and numerical studies. Relatively scant data exists for within-canopy three-dimensional flows, however, Davidson et al. (1996) for a cube-obstacle array in a wind tunnel calculated turbulence statistics to compare staggered and aligned configurations and found that within the array canopy, the turbulence would be smaller scale with higher turbulence intensity, citing the reduction of Lagrangian time scales as evidence. Studies done by Böhm et al. (2013) with automotive light globes in a wind tunnel setting called into question the general dynamic significance of the mixing layer analogy applied to an urban-like environment of staggered bluff obstacles. A key difference observed was a more pronounced contribution to the energy spectrum at scales much smaller than the coherent structures

initiated at the inflection point, accounted for by the wake-introduced turbulence kinetic energy. As such, it can be expected that turbulence within the canopy layer (CL) locally has the characteristics of superimposed quasi-coherent wakes initiated from the individual roughness elements, observed to be about 1/5 the scale of the mixing layer type eddies at the canopy inflection point. This significant scale separation motivates treatment of the canopy as three distinctive flow regimes characterized by superimposed wakes within the canopy, mixing layer type coherent structures at the canopy top and a region above where the dynamics transition from a dependence on the smaller eddies at the canopy top to the larger height-dependent eddies of the ISL. It would appear, then, that to simulate idealized versions of flowfields across the canopied surfaces, the mixing layer will play a prominent role, whether initiated along a plane or shaped into the development of superposed wakes.

1.8 The regions of interest and approach methodology

For the regions of interest within the surface layer, mean vertical velocities are assumed much smaller than horizontal ones so that treatment of the problem is sufficiently one-dimensional when aligned with the prevailing wind. By rotating the view around the z-axis to always be oriented in the compass-based direction of mean motions, the velocity field is represented as:

$$\begin{aligned} u &= \bar{u}_h + u'_h \\ v &= v' \\ w &= w' \end{aligned} \tag{1.12}$$

with \bar{u}_h typically taken as the mean horizontal wind speed as measured by a probe in fixed coordinates as $\bar{u}_h = \sqrt{\bar{u}^2 + \bar{v}^2}$, with $\bar{w}^2 \approx 0$. This assumption certainly holds in the ISL and approximately holds in the RSL when far enough from local effects, particularly when roughness elements at the surface are rather short and uniformly distributed. From this point forward, the subscript "h" indicating a horizontal wind will be dropped and u, v, w will be understood to be the longitudinal, lateral, and vertical velocity components, respectively. The gap in the spectral distributions of wind, like that shown in fig. 1.7, enables the fluctuating portion of the wind spectra to be isolated from the mean motions. By taking suitably long averages (say, thirty minutes to an hour) of all terms in eq. (1.3) and then subtracting these averages from eq. (1.3) yields the Navier-Stokes equations for the gust portions of the wind spectra, which would be parameterized by mean velocity (and mean temperature) profiles with altitude. Far above the effects of roughness in the ISL, eq. (1.9) would

be one such candidate altitude-profile for mean winds and within a uniform-height, long stretching canopy, perhaps eq. (1.10) could be used with not too great a loss in accuracy. Whatever form of these mean velocity profile equations is ultimately selected, an inflection point near canopy top ensures that any similarity theory dependent solely on dynamic-scaling with height will miss the important dominant flow mechanism of the coherent structures generated within the local microclimate control volume views adopted herein.

For certain terrain-following flows when the atmosphere is particularly stable (common at night), turbulence, though continuous, is weak and waves are ubiquitous. Thus, a more encompassing decomposition for the longitudinal velocity component in this case would be $u = \bar{u} + u' + \tilde{u}$, which further parses the wave contributions \tilde{u} from the turbulent fluctuations u' in the microscale portion of the energy spectrum. A short-hand that preserves the potential for decomposing the fluctuating component between a random and deterministic periodic component as the situation calls for is given as

$$u = \bar{u} + u^* \quad (1.13)$$

where $u^* = u' + \tilde{u}$. In general, these atmospheric wave motions push energy to the mesoscale portion of the spectrum far from the spectral overlaps of interest, but eq. (2.15) is included here nonetheless because certain techniques for turbulence generation in multi-source wind tunnels leverage discrete oscillatory forcings to bump energy into specific frequency bands, and is therefore applicable in those analyses contexts.

Because traditional wind tunnel testing of fix-mounted flyers in a steady airstream with low turbulence intensity or the quasi-static dynamic modeling approach in control design is unlikely to properly account for the transient and more localized effects of gusts in the RSL, an iterative free-flight experimental approach where the flyer (e.g. machine) *learns* from exposure to the simulated environment is proposed. With a focus on flight performance during the presence of reasonably strong winds near the surface (i.e. gustiness that approaches the flight speed capabilities of the near-surface flyers), techniques for the simulation of the spectrum of horizontal winds in a laboratory setting are explored as a principal step toward that aim. A frequency-domain representation will often be employed as that will inevitably permit a direct comparison of the spectral features of a flyer of interest with the spectral content of the environmental disturbances. It is important to note that the

goal of this dissertation is not a true-to-form simulation of the spectral behavior of disturbances in the atmospheric surface layer, but rather on simulation of the most energetic disturbances within a specific spectral range likely to overlap frequency regimes important to the design, testing, and understanding of flyer-specific features, such as flight-control, actuation, and structural integrity.

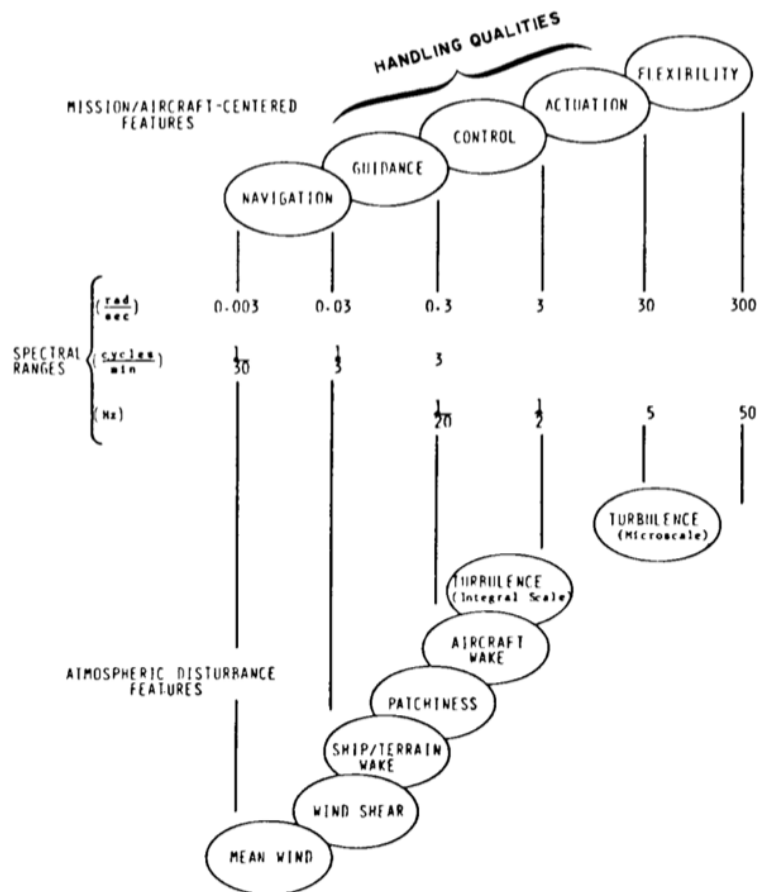


Figure 1.14: Approximate frequency regimes of overlap for flyer-specific and atmospheric disturbance features, from MIL-STD-1797A.

1.9 Objectives: the winds ahead

Though extensive variability exists within the microclimates explored, some narrowing of the view enables the development of a framework for the simulation of atmospheric-like disturbances near the surface in the confines of a laboratory setting with the goal of exposing, studying, and testing flyers of interest within physical models of the environment. By identifying the characteristic features of a given local environment most likely to impact the dynamics of a flyer of interest, an analogous flow configuration is set out to be created that *resembles* flight through the

atmosphere near the surface at relevant time and length scales. Repeated exposure to suitable forcing functions enables flyers to learn to navigate and negotiate challenging environments well-before encountering them in the real-world.

The perception of the disturbance environment by the flyer depends largely on its location in space near the surface relative to the built-up environment, when present. Far from local effects, atmospheric turbulence in the spectral overlap of interest is essentially isotropic and well-described by the theoretical model of Kármán (see eq. (1.11)). However, for control volumes zoomed in and centered at the canopy top, three identifiable flow regimes based on the relative effects and implications of an observed inflection point of the mean velocity profile were discussed. It was argued that free shear layers are prevalent in the disturbance flowfields that merit simulation in the physical laboratory environment, both for exploration of the mixing-layer type flowfields at or near the observed canopy inflection points, but also as a fundamental building block for evolved superimposed wake flowfields within the canopy.

Generation of mixing layers is given extensive treatment in Chapter III, through use of a modular, multi-source wind tunnel introduced in Chapter II and further described in appendix A. Characteristics of basic flow modalities are presented along with perturbation techniques driven solely by software toward the generation of continuous-turbulence velocity fields in Chapter IV. A framework of comparison for these high-Re flows is explored thereafter in Chapter V. A brief exploration of the effect of various perturbation techniques on core flowfields is given in appendix D. The objectives of the study are listed below:

1. Establish the conceptual framework and principal characteristics of a multi-source wind tunnel to determine its suitability for the generation of environmental disturbances (i.e. random and discrete gusts) likely to be encountered near the surface
2. Characterize the splitterplate-less dual- and triple-stream mixing layers enabled by the discrete partitioning and individual addressability of the fan units within the multi-source wind tunnel environment
3. Showcase continuous turbulence generation techniques built on the premise of shearing velocity distributions at the fan array exit plane
4. Develop a framework of comparison for the simulated flowfields of interest

Chapter 2

METHODOLOGY: MULTI-SOURCEDNESS

“The extra dimension seems to make a lot of difference. But if a little bit of gauge freedom is this good, what would a lot of it be like? Could fluid dynamics, even turbulence, appear simple when viewed in a space of (say) 26 dimensions?”

– Rick Salmon, *More Lectures on Geophysical Fluid Dynamics*

The purpose of wind tunnels, most discernibly, is to *generate wind* and their utility must then be derived from their capacity to simulate a proper environment. While even the most capable wind tunnel facilities are tunably adapted to generating high velocity flows, they are generally limited in the types of flows they can produce. In contrast, a multi-source wind tunnel is capable of generating a host of spatiotemporally-varying flows subject to the size, number, and responsiveness of the base source unit. When coupled in-phase, the multi-source wind tunnel serves equivalent to a conventional wind tunnel, provided the flow is given enough downstream distance to homogenize. For a fixed outer dimension, the design trade-off essentially amounts to one of temporal responsiveness (i.e. smaller source units would require less inertia to rotate) and overall complexity (i.e. one base unit to operate versus many). In this chapter, a mathematical framework to describe the basic characteristics of a multi-source flow-generating apparatus is introduced. Then, the downstream evolution of the baseline steady uniform flow modality is presented followed by brief discussions of the unsteady and quasi-steady counterparts.

2.1 Experimental premise: multi-sourcedness

When source units are assembled into an array, two primary benefits emerge. First, flow characteristics are initialized at the base unit scale thus reducing the overall mixing length of source-related turbulence, particularly useful in space-constrained¹ implementations. Secondly, the ability to generate spatially-varying flowfields without the need to introduce obstacle geometries downstream affords a convenience to explore greater flow varieties for a given experimental setup all the while preserving the potential for free-flight testing. The source unit of each of the multi-source wind tunnels used herein is a DC-powered off-the-shelf cooling fan that is assembled

into an array either individually or through a sub-module of nine units arranged in a square 3x3 configuration. These so-called fan array wind tunnels (FAWT) developed within the Graduate Aerospace Laboratory at Caltech (GALCIT) comprise a subclass of multi-source wind tunnels and are described in great detail in appendix A. For the purposes herein, a theoretical treatment of the source unit is provided to inform expected performance bounds when designing flowfields to be considered as candidates for environmental forcing spectra that simulate atmospheric-like disturbances in regions of interest.

The fan source unit

The most basic building block of a fan array wind tunnel is the source fan unit itself, typically described by its outer dimension, d .

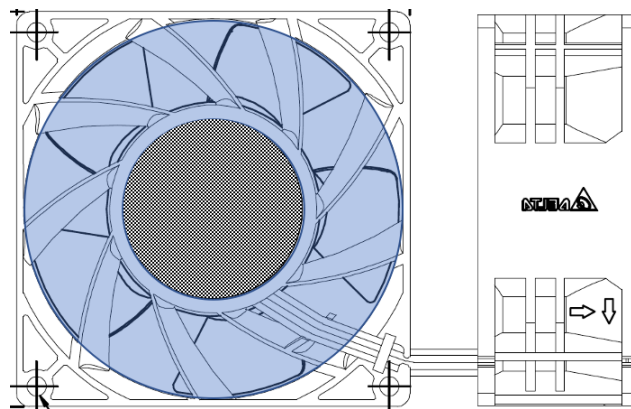


Figure 2.1: Schematic of the basic type fan unit typically used in FAWT. The part highlighted in blue represents the annular flow output area. Arrays built from the fan unit as diagrammed constitute a single-layer fan array. A dual-layer fan array is comprised of counter-rotating pairs of stacked single fan units that do not change the overall footprint but increase the depth by one stacked layer. These dual-layer fan arrays can be coupled front-and-back layer or remain individually controllable.

Flow is initiated at the scale of the fan unit, emanating out of an annular fan outlet plane, marked in blue in fig. 2.1. Measurements of the streamwise evolution of the flow suggest (see fig. A.4) that the incompressible flow is fully mixed beyond $x/d \gtrsim 20$, whereby the flow has achieved its nominal velocity expanding from an initial fan annular area, A_{ann} , to an equivalent area, A_{eq} , governed by eq. (1.2), that is roughly the size of the outer geometric dimensions of the fan unit itself (i.e. $d \times d$). The flow is driven by a pressure gradient across the fan blades that is typically

¹If there exists no space-constraint, than any single-source wind tunnel can be made proportionately bigger by adding more sources and would thus classify as a multi-source wind tunnel.

provided by a manufacturer specification sheet in the form of a ‘p-Q curve’ — a plot of the static pressure, p , as a function of volumetric flow rate, Q .

Applying the fundamentals

For an incompressible, irrotational², inviscid (i.e. $Re \rightarrow \infty$) non-steady, constant density flowfield in the absence of changing external body forces (i.e. $Fr \rightarrow \infty$), eq. (1.7) reduces to:

$$[St] \frac{\partial \underline{u}^*}{\partial t^*} + \nabla^* \left(\frac{1}{2} \underline{u}^* \cdot \underline{u}^* \right) = -[Eu] \nabla^* p^* \quad (2.1)$$

Recalling table 1.1, and taking the characteristic length as $L = ds$, where ds is an increment along a streamline, and the characteristic velocity $U = \bar{u}$ to be the mean velocity of the flowfield, eq. (2.1) can be written as:

$$\frac{1}{\bar{u}} \frac{\partial \underline{u}^*}{\partial t} ds + \frac{1}{2} \nabla (\underline{u}^* \cdot \underline{u}^*) ds = -\frac{1}{\rho \bar{u}^2} \nabla p ds \quad (2.2)$$

where the scaled instantaneous velocity remains $\underline{u}^* = \underline{u}/\bar{u}$. Restricting the view to changes that occur along a given streamline gives:

$$\frac{1}{\bar{u}} \frac{\partial \underline{u}^*}{\partial t} ds + \frac{1}{2} d(\underline{u}^{*2}) = -\frac{1}{\rho \bar{u}^2} dp \quad (2.3)$$

Integrating from the inlet (subscript i) to the test section exit plane (subscript e) yields:

$$\frac{1}{\bar{u}} \int_i^e \frac{\partial \underline{u}^*}{\partial t} ds + \frac{1}{2} (\underline{u}_e^{*2} - \underline{u}_i^{*2}) = -\frac{1}{\rho \bar{u}^2} (p_e - p_i) \quad (2.4)$$

which is a form of the unsteady Bernoulli’s equation along a streamline.

In diagram form, it is recognized that the manufacturer provided specifications are valid at the fan inlet plane; velocity calibration measurements, however, are taken (well-) beyond $x \gtrsim 20d$, denoted by subscript ∞ to imply centerline freestream measurements. For the one-dimensional flow considered here (i.e. $\underline{u} = \{u, 0, 0\}$), the volumetric flow rate across the inlet and outlet planes is:

$$Q = u_{ann} A_{ann} = u_{\infty} A_{eq} \quad (2.5)$$

which through the area ratio (A_{eq}/A_{ann}) allows for the analysis to deal solely with the freestream velocity, u_{∞} , measured beyond the initial mixing zone. Given the

²For irrotational flow, $(\nabla \times \underline{u}) = 0$, such that $(\underline{u} \cdot \nabla) \underline{u} = \frac{1}{2} \nabla (\underline{u} \cdot \underline{u})$. A swirl-free assumption for counter-rotating dual-unit fans without a honeycomb is reasonably met in some cases but is certainly applicable to both single- and dual-unit fans with a honeycomb installed for a uniform flow modality.

assumptions, for a uniform flow modality, the analysis extends to n -fan units, with proportional changes in volumetric flow rate (nQ) resulting in proportionally bigger reference areas (i.e. nA_{ann} and nA_{eq}) that ultimately reduce to eq. (2.5). The static pressure across the inlet does not change with increasing n when fan units are stacked parallel to one another.

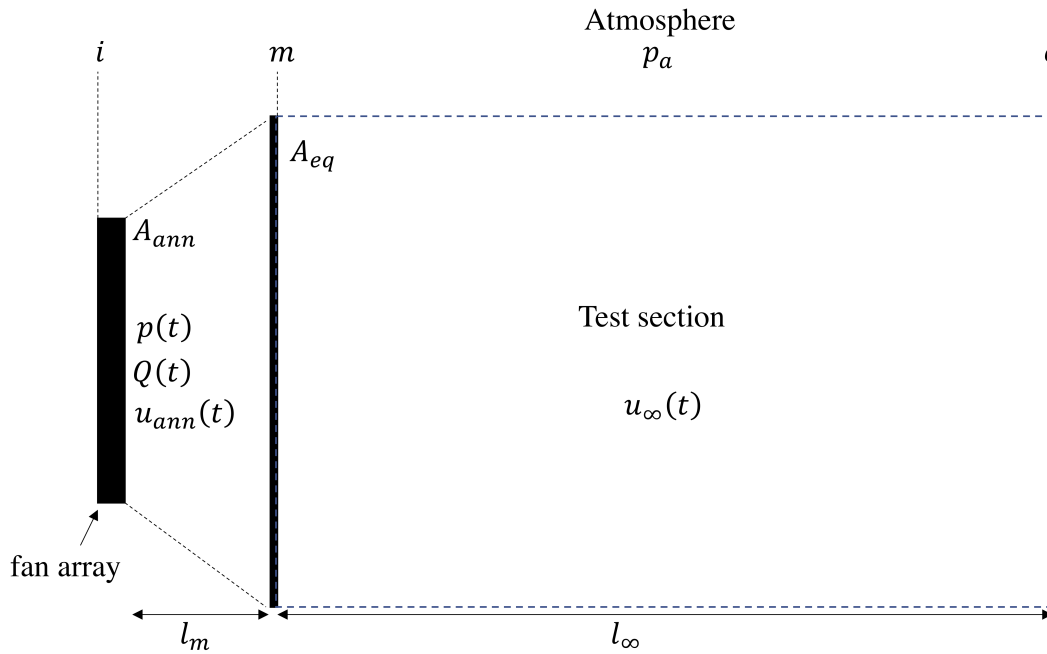


Figure 2.2: Control volume schematic for FAWT analysis.

Frequency bandwidth

The analysis can be further extended to an oscillating (or fluctuating) component of the velocity field, taken to be \tilde{u} , provided that, on average, $\bar{\tilde{u}} = 0$. The decomposition then is written as $\underline{u} = \bar{u} + \tilde{u}$, which yields:

$$\underline{u}^* = \frac{\bar{u} + \tilde{u}}{\bar{u}} = \frac{\bar{u}}{\bar{u}} + \frac{\tilde{u}}{\bar{u}} = 1 + \tilde{u}^* \quad (2.6)$$

The pressure and volumetric flow rate can likewise be decomposed into a time-averaged³ and unsteady component, as in (Greenblatt, 2016), to collectively give:

$$\underline{u}^*(t) = 1 + \tilde{u}^*(t) \quad (2.7)$$

$$p(t) = \bar{p} + \tilde{p}(t) \quad (2.8)$$

$$Q(t) = \bar{Q} + \tilde{Q}(t) \quad (2.9)$$

In accordance with fig. 2.2 (i.e. $\underline{u} = \{u_\infty, 0, 0\}$), $\underline{u}^*(t)$ is written as:

$$\underline{u}^*(t) = 1 + \frac{\tilde{u}_\infty(t)}{U_\infty} = 1 + \tilde{u}_\infty^*(t) \quad (2.10)$$

Inserting eq. (2.10) and eq. (2.8) into eq. (2.4) with the inlet velocity taken to be nearly zero (i.e. $\underline{u}_i^{*2} \approx 0$) at atmospheric pressure, p_a , and time-averaging, after rearrangement yields:

$$U_\infty = \sqrt{\frac{2\Delta p}{\rho} - \overline{\tilde{u}_\infty^2}} \quad (2.11)$$

where $\Delta p \equiv p_a - \bar{p}$. When $\overline{\tilde{u}_\infty^2} \ll U_\infty^2$, eq. (2.11) recovers the freestream velocity expression of the steady form of the Bernoulli equation.

The equation governing the motion of the fluctuating components is derived by subtracting the time-averaged form from the instantaneous form to yield:

$$\frac{L_t}{U_\infty} \frac{\partial \tilde{u}_\infty^*}{\partial t} + \tilde{u}_\infty^* = -\frac{\tilde{p}(t)}{\rho U_\infty^2} - \frac{1}{2}(\tilde{u}_\infty^{*2} - \overline{\tilde{u}_\infty^{*2}}) \quad (2.12)$$

The linearized form (i.e. ignoring the rightmost higher order terms) of eq. (2.12) gives an expression of the form $\tau \tilde{u}_\infty^{*'} + \tilde{u}_\infty^* = g(t)$, which is a forced first order linear differential equation with time constant $\tau = 1/2\pi f_c = L_t/U_\infty$. The cutoff frequency, f_c is then:

$$f_c = \frac{1}{2\pi\tau} = \frac{1}{2\pi} \frac{U_\infty}{L_t} \quad (2.13)$$

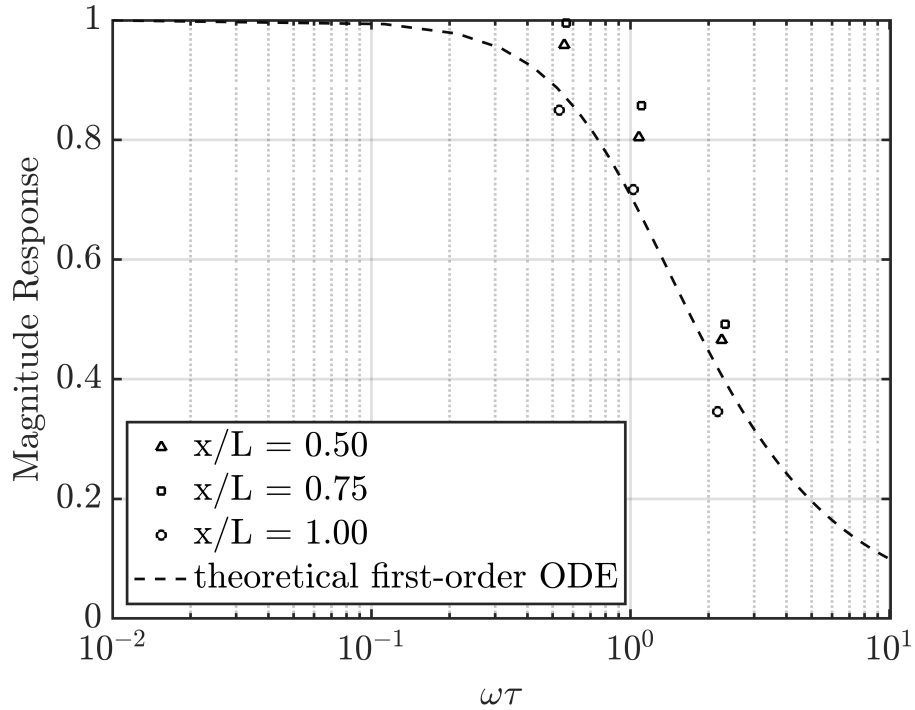
For a sinusoidal forcing function of the form $\tilde{p} = A \sin(\omega t)$, eq. (2.12) can be solved numerically. When linearized, the analytical solution is:

$$\tilde{u}_\infty^*(t) = B \sin(\omega t + \phi) \quad (2.14)$$

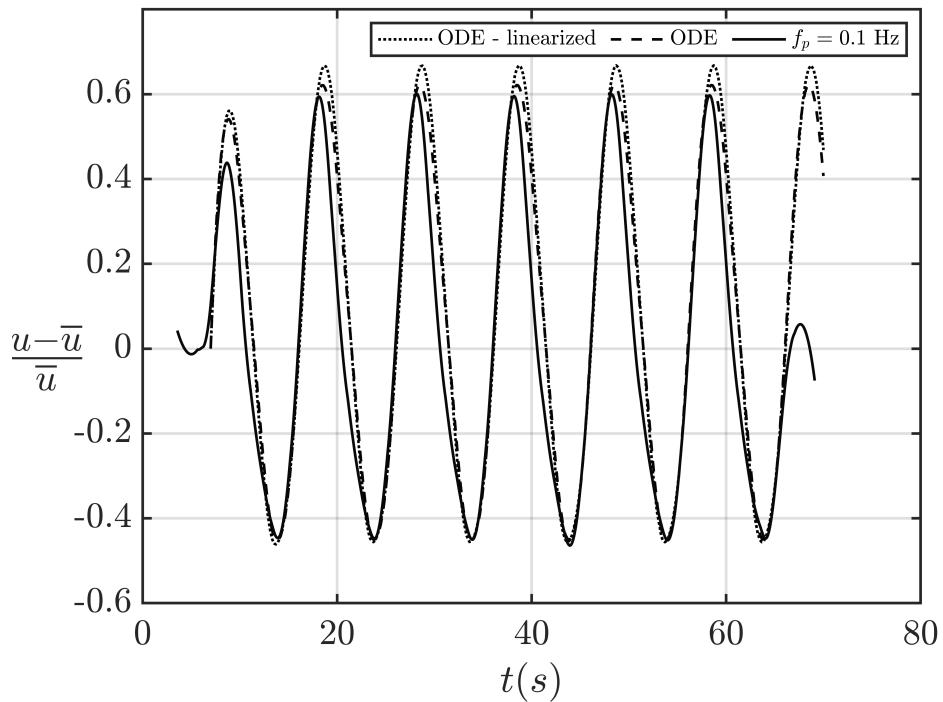
where $M = B/A = \sqrt{1 + \omega^2\tau^2}$ is the magnitude gain ratio and $\phi = -\tan^{-1} \omega\tau$ is the phase delay. Treated this way, beyond the initial mixing region, the system behaves as a low-pass filter and the air moves as a lumped mass phase-delayed by ϕ with a magnitude response governed by M for a given frequency, $\omega = 2\pi f$.

The characteristic length $L_t = L_m + L_\infty$ is not well-defined due to a lack of measurement data far downstream of open-jet wind tunnels. The theoretical treatment herein suggests L_t is of the order 10^1 , with an example given in fig. 2.3.

³in the case of an oscillation, the time-average is taken as integration over an oscillation period.



(a) Frequency response at various downstream distances. The data reasonably collapses to the theoretical fit (dashed line) $M = B/A = \sqrt{1 + \omega^2\tau^2}$ when $L_t = 14.5$ m according to eq. (2.13).



(b) Theoretical velocity time series solutions of eq. (2.12) with and without higher-order terms compared to experiment.

Figure 2.3: Response characteristics to sinusoidal forcing.

2.2 Types of flow generation

For a more detailed look into the types of flow generation possible in FAWT, the reader is referred to appendix A. Below briefly mentions some salient features worth bearing in mind for the upcoming analysis.

Flow Type #1: Steady, spatially-(non-)uniform

Using a custom-built 5-hole pressure probe and associated software both developed by Renn (2018), flow values can be spatially mapped in real time and further post-analyzed for select 2D slices of any measured steady flowfield, provided the spatial resolution is fine enough to promote reliable and accurate interpolated values. Each contour plot presented was interpolated with no greater than a thirty millimeter applicability radius. Flowfields ‘painted’ in this way give the viewer an intuitive view of the spatial distribution of the average velocity characteristics of a flowfield along planes of interest. For most cases, it is desirable to test far enough downstream so that the transient mixing behavior of each source fan mixes fully into a bulk flow. In a honeycomb-affixed-to-the-face-configuration, convergence of velocity and turbulence intensity along the centerline occurs beyond $x/L = 0.5$ (see fig. A.4). The near- and far-field flow evolution of a 3×3 ($d/L = 0.33$) dual-layer array is shown in fig. 2.4.

Selected views of a much larger and more finely-resolved 36×36 ($d/L = 0.03$) dual-layer array comprised of modules with distinct inlet geometry are given in fig. 2.5 and fig. 2.6. Unlike the open inlet design of fig. 2.4, a divergent geometry enclosing 3×3 fan units is placed upstream of the intake (see appendix B for more information). A selected mean velocity profile at $z/L = 0.3$ shows clearly a peaked behavior associated with the funneling influence of the module geometry. At $x/L = 0.35$, percentage deviation on average across the center portion of the array is 3.7% from the mean. The effect of the modules is still noticeable in visualizations at $x/L \sim 1.00$ (see fig. B.3), though the percentage deviation drops to 1.6%. Anything less than 2% is considered sufficiently uniform for the purposes herein. The variance in uniformity would be further reduced if a more traditional flow management system was installed (e.g. grids and screens). Similar treatment of the turbulence intensity distribution by hotwire traverses is given in fig. A.10. The nominal turbulence intensity values for a honeycomb only arrangement range between $\sim 3\% - 5\%$ in the regions of interest.

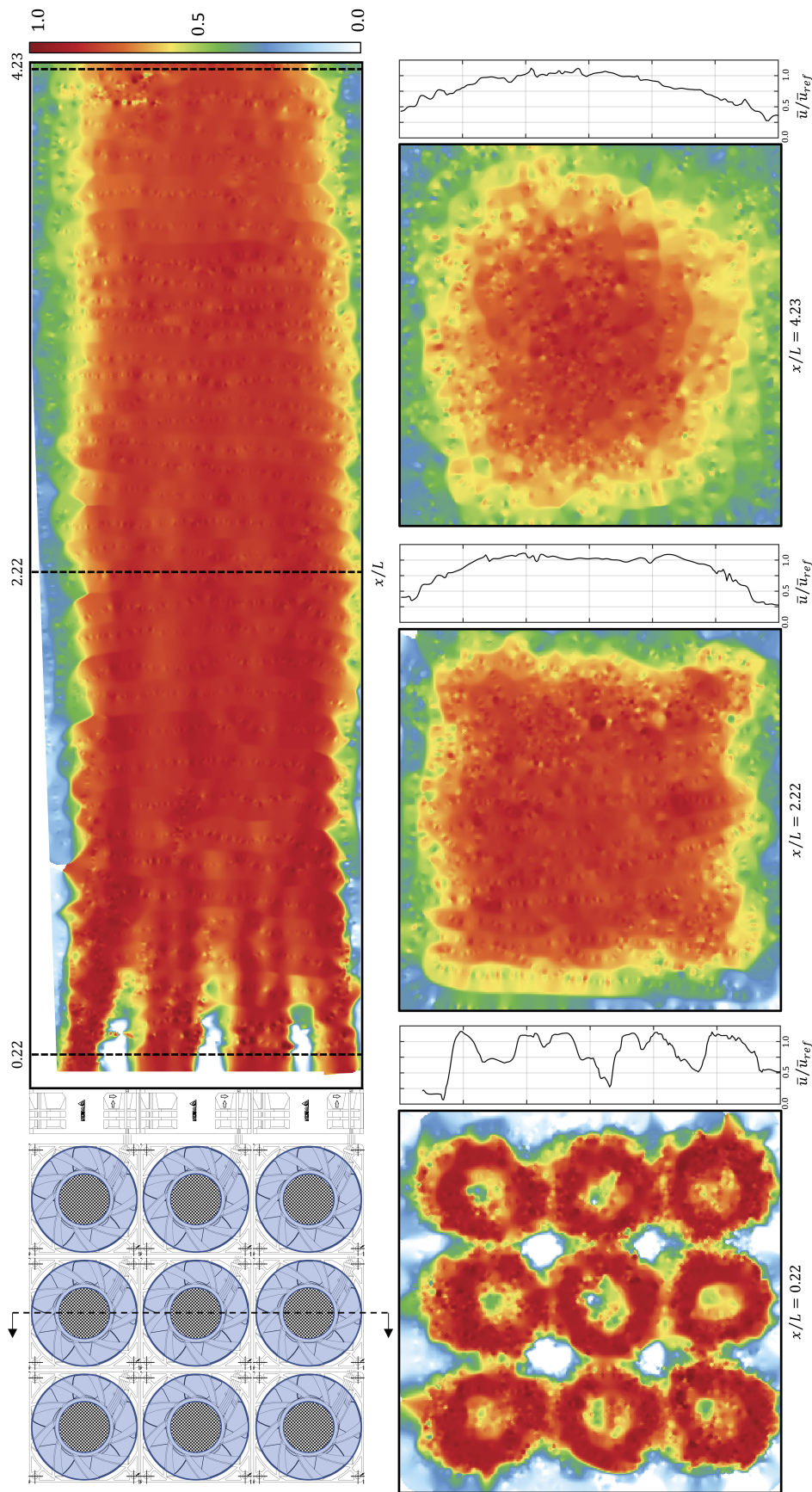


Figure 2.4: Development of a steady uniform flow measured for a $d/L = 0.33$ resolution dual-layer array ($d = 0.080$ m) with minimal mounting structure at fan unit intake. The streamwise (x - z plane) cut corresponds to the centerline plane ($y = 0$) and the positions of the spanwise (z - y plane) distributions are dashed for all three locations. To the right of each spanwise cut is a corresponding velocity profile at the centerline ($y = 0$) for that respective view. The core flow homogenizes first from discrete source units to a nearly uniform square cross section of size $L \times L$ and then spatially reduces with downstream distance as the core flow smoothes to a rounder cross-section as the boundary shear layers entrain and grow. The colorbar corresponds to \bar{u}/\bar{u}_{max} .

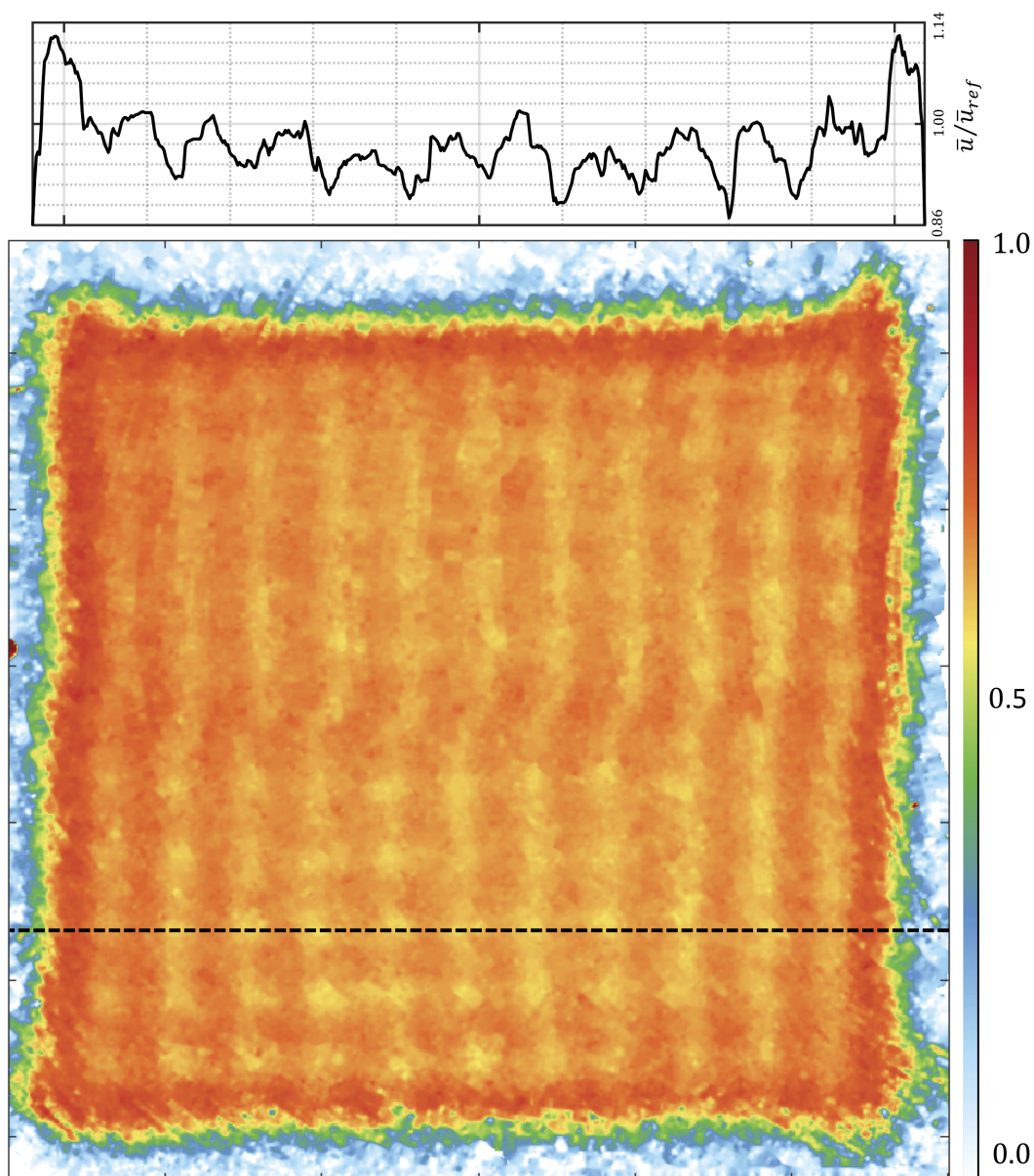


Figure 2.5: Spanwise (z - y plane) distribution of a steady uniform flow measured at the downstream location $x/L = 0.35$ for a $d/L = 0.03$ resolution dual-layer array. This particular fan array has outer dimensions $L = nd = 2.88\text{m}$ ($n = 36$, $d = 0.080$ m) with $36 \times 36 \times 2 = 2592$ individual fan units stacked in two layers and arranged into 144 total modules. It is evident in this view that a funneling effect of the module geometry is still present. The dashed line corresponds to the location $z/L = 0.3$ of the extracted velocity profile above. The colorbar corresponds to \bar{u}/\bar{u}_{max} .

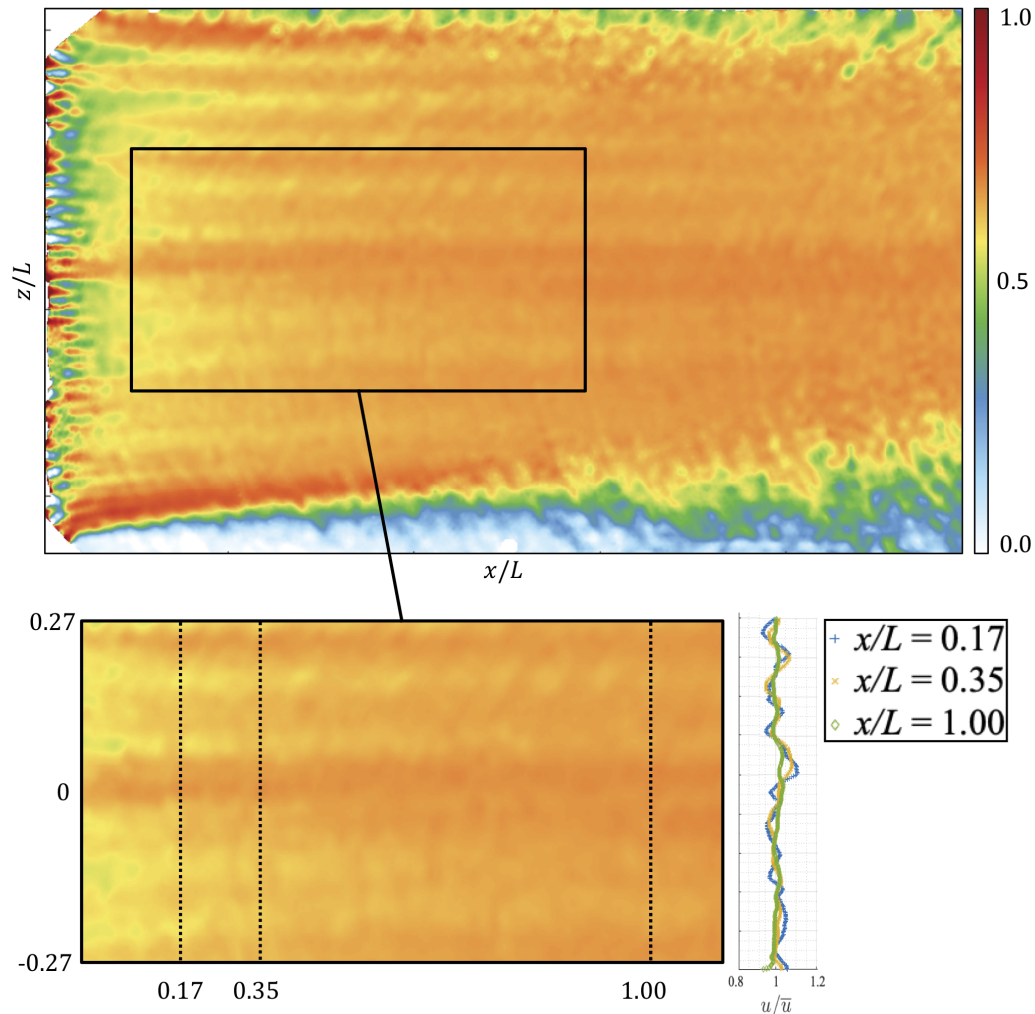


Figure 2.6: Streamwise (z - x plane) distribution along the centerline plane ($y = 0$) of a steady uniform flow for a $d/L = 0.03$ resolution dual-layer array. Velocity profiles in the middle portion of the array between $-0.27 < z/L < 0.27$ are extracted at three downstream locations $x/L = 0.17, 0.35$, and 1.00 . The standard deviation of each profile is 3.6% , 2.9% , and 1.3% , respectively. The colorbar corresponds to \bar{u}/\bar{u}_{max} .

Both uniformity and turbulence statistics converge to a quasi-steady state when measured far enough downstream. The initial fan conditions are washed out in the natural evolution of the steady, spatially-uniform flow modality starting beyond $x/L \sim 0.2$. Though the effect of each module is felt for some distance further downstream, acceptable levels of uniformity are generally found near $x/L \sim 0.5$ and beyond.

Flow Type #2: Unsteady, spatially-(non-)uniform

The discrete and individual addressing of each fan unit enables both unsteady non-uniform and uniform flow configurations. When addressed uniformly in space but varying in time as in fig. 2.7, an unsteady gust flowfield can straightforwardly be measured by standard hotwire or pitot techniques. Below is one such experimental simulation of an instantaneous unsteady velocity profile.

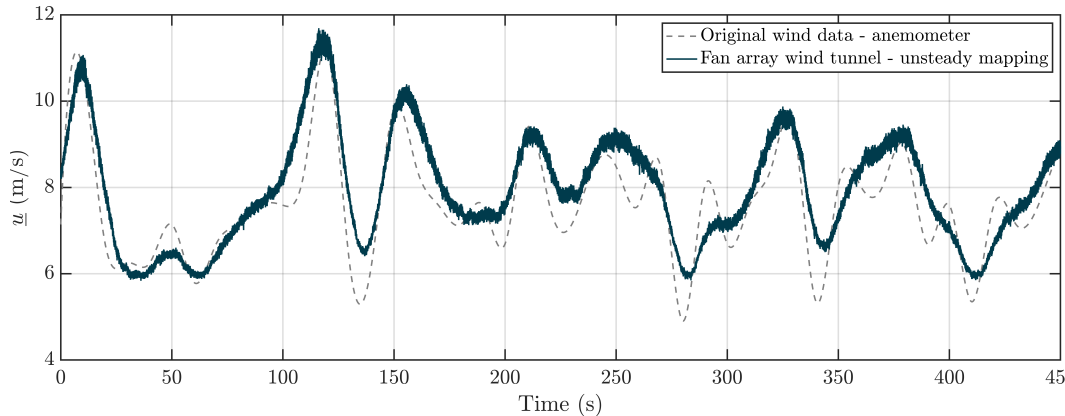


Figure 2.7: A velocity trace from a handheld wind anemometer recording of an instantaneous prevailing wind of a small uninhabited island in the Caribbean is mapped into the FAWT software environment to generate an input distribution that attempts to playback the simulated output. Prevailing winds in the region are directional and constant, averaging to be 8 – 10 m/s at all times of the year, but their instantaneous nature is gusty, fluctuating as high as 11.5 m/s and as low as 2.5 m/s.

When coupled so as not to allow any phasing between adjacent fan units, a ‘breathing’ modality of the fan array is enabled. Continuously random gusts targeting a particular frequency introduce energy at a specific wavelength. Targeting particular frequencies in a gusty environment experienced globally by the flyer is accomplished by selecting forcing frequencies within the range $0.1 < f_p < 0.5$ Hz while implemented in the ‘breathing’ modality. Amplitudinal response of the commanded input to expected output would behave according to the frequency bandwidth of the particular fan array used (see section 2.1). Measured real-world instantaneous velocity records can be mapped and simulated reproducibly by comparing the output to the original and iterated upon until satisfactory results are rendered, within the constraints of the system itself.

Flow Type #3: Quasi-steady irrotational sinusoidal

It was shown in fig. 2.3 that responses to sinusoidal inputs are sinusoidal outputs at a phase delay, with magnitude approximately determined by $\sqrt{1 + \omega^2 \tau^2}$. Where periodic external forcing is expected to play an important role, a useful alternative expression is to triply decompose the flowfield as:

$$\underline{u} = \bar{u} + u' = \bar{u} + u' + \tilde{u} \quad (2.15)$$

where u' represents the fluctuating component (i.e. background turbulence) and \tilde{u} is the forced periodic component. This is an all-encompassing prescription, particularly useful for cyclic unsteady flows.

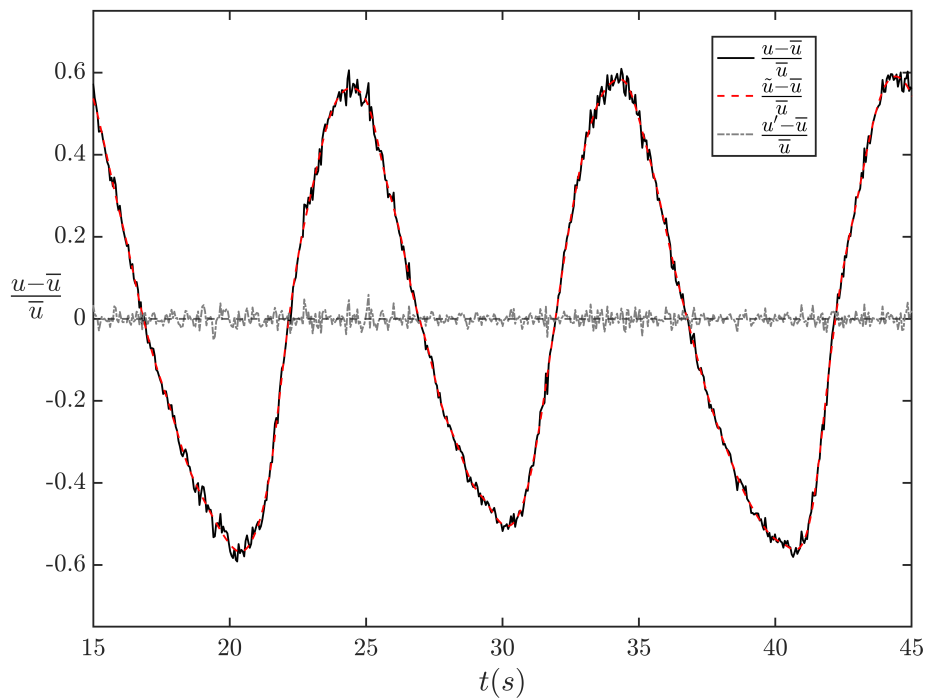


Figure 2.8: Example analyses afforded by the triple decomposition. Filtering out the forced frequency ($f_p = 0.1$ Hz) periodic sinusoidal portion of the signal \tilde{u} isolates the stochastic fluctuating content u' .

2.3 Summary

A mathematical framework applied to a typical source fan unit of outer dimension d with flow emanating from an annular area output A_{ann} was first introduced. Through fundamental treatment of the conservation of momentum for an incompressible, irrotational, inviscid, non-steady, constant density flowfield in the absence of a changing external body force, an unsteady form of Bernoulli's equation along a streamline is derived (eq. (2.4)). Through further consideration of the continuity equation, eq. (2.4) is recast in the more readily accessible test section freestream velocity u_∞ as a function, ultimately, of manufacturer provided source-fan performance input specifications and expanded to n -fan units without loss of generality for the uniform steady and 'breathing' quasi-steady flow modalities. The theoretical response to a purely oscillatory forcing function input of the 'breathing' modality is then considered and the frequency response of the flowfield (beyond the initial mixing region) was determined to behave as a low-pass filter with air moving as a phase-delayed lumped mass (fig. 2.3). Next, extensive flow visualizations of the streamwise and transverse development of the baseline steady uniform flow modality is presented, first for a $d/L = 0.33$ array (the typical 'benchtop' size array) in fig. 2.4 and then for the full-size $d/L = 0.03$ array (used predominantly throughout the rest of the dissertation) in fig. 2.5 and fig. 2.6. Finally a brief discussion of unsteady gust flowfield generation is given and an all-encompassing triple decomposition that better accounts for the, at times, discrete periodic component of flowfield generation (used extensively in perturbation techniques) is introduced in eq. (2.15).

Chapter 3

THE DISCRETE GUST VELOCITY FIELD

It was discussed in some depth in Chapter I that the response characteristics of a flyer could only be evaluated when held directly in comparison to the nature of the disturbance environment. At a glance, the energy spectrum plotted in frequency space would, for instance, alert to any potential overlaps of energy near the natural modes of the flyer, effectively bounding analysis to energetic events within a prescribed region of interest while ‘filtering’ out the rest. Furthermore, a case was made that free shear layers are prevalent at, above, and within the canopied environments of interest and that the mixing layer will play a prominent role in the simulation of such flows, whether initiated along a plane or as a fundamental building block to evolve flowfields into superimposed wakes. Consider, for example, traversal through the upper canopy layer boundary of fig. 1.3 on the scale of one or a few roughness elements. Time-averaged wind variations are observed to predominantly change only with height (i.e. $\bar{u} = \bar{u}(z)$) and wind motions relatively unencumbered by the roughness elements aloft are suddenly slowed by the momentum sink the elements represent, whereby moving from outside of the canopy layer to within (or vice versa) inflects the mean velocity profile, typically at or just above the topmost geometry of the roughness element(s). Moving from the sheltered wake of a building back into the freestream could also be described by a mean velocity profile with an inflection point. The resulting shear layer in either of these examples is the hallmark signature that a change of state in wind is occurring. Unlike the idealized step function representing the sharpest possible gradient between wind states (i.e. $\Delta z \rightarrow 0$), the friction present in the real world smoothes the gradation through the mixing process over the finite thickness of the shear layer (i.e. $\Delta z > 0$ and growing).

With the cascading nature of turbulence in mind, large energy-accepting eddies are considered coherent due to their recognizable and structured presence (i.e. able to correlated in a measured wind record) amidst an otherwise random turbulent flow field. The energy-accepting eddies of the upper atmospheric boundary layer (ABL) are not local enough (recall that $\nabla^* \sim L$ is taken as local) to directly influence the atmospheric conditions of the selected control volumes, though do indirectly contribute to the intermittency of the fluid motions as a cascaded passive background inactive turbulence. Proximate to the roughness element(s), one candidate energy-

accepting (i.e. measurable) eddy length scale persists in our view, that approximated by the shear layer thickness.

In this chapter, planar mixing layers initiated across a multi-source wind tunnel without the use of a splitterplate geometry will be explored in depth. The baseline characteristics will be compared to more conventional and canonical dual-stream mixing layer experiments. This provides the basis for use of shearing velocities at the fan array exit plane to generate relevant flowfields in physical space, including the potential for planar mixing layers to be used as a simulated environment of the free-flying flyer traversing through zones of high local shear rate. To conceptually frame traversal through a mixing layer as a physical approximation of a step-forcing-function from the perspective of the flyer, a quick commentary regarding dynamic couplings is warranted.

3.1 Dynamic ‘couplings’ within a free shear layer

Because the free shear layer is of finite thickness, the internal dynamics must be considered when passing through. Energy-accepting eddies of a measurable size are convected with regularity at a velocity proportional to the velocity difference as they emanate from a vortex-producing source. As such, a length-scale, frequency, and velocity associated with the free shear layer itself emerge and must be held in comparison to the flyer characteristic length scale, natural modes, and performance limitations. If of similar size, characteristic frequency, or velocity amplitude, certain couplings may exist and treatment of the forcing as a step-input may no longer be justified. A fuller picture emerges when considering the wave-like nature of encountered disturbances. If, for the moment, it is supposed that generic disturbances of a certain amplitude are well-described as wave-like, then a characteristic frequency (i.e. inverse period) and convective velocity are sufficient to describe a perceived wavefront separation. Flowfields well-described by Taylor’s frozen turbulence hypothesis may further be considered in the wavenumber domain and both a convective velocity and inverse wavelength associated with the flowfield more readily enter the analysis.

It is illustrative to treat each of the frequency, velocity, and length scales in turn so that metrics to evaluate performance may ultimately be established when undertaking free flight experiments within mixing layer-type disturbance environments. If, for instance, the instability frequency of the shear layer approaches the natural frequency of the flyer (i.e. frequency-coupled), a resonant response that would likely result in loss of control would be expected. A standard control dynamics

analysis typically considers this. Further complications can arise for flyers near the surface however, where gust encounters are likely to be the same order of magnitude as the flyer's maximum flight speed. Instances such as these are considered to be velocity-coupled when gust ratios (i.e. the magnitude of the gust normalized by the relative freestream velocity) are $O(1)$ and signal likely saturation of control inputs. Lastly, when coherent structures comprising a mixing layer are comparable in size to the characteristic flyer length scale, then a pseudo-type gust encounter can be experienced. When the vortex core is aligned along the lifting surface, large variations in lift would be expected. Where the coherent structures may be length-coupled to the flyer, as could happen in a vortex gust encounter, the spatial distribution of velocity across the geometric lifting surfaces would need to be considered in addition to the magnitude of the event. Geometric length-couplings like these may impact stability and handling of the flyer passing through. See fig. 1.11 for a diagrammatic overview of various gust types.

If there is no significant energetic overlap of the internal dynamics of the shear layer with the response characteristics of the flyer, then treatment of the system as a flyer moving from one wind state to another is justified (a similar argument was made in justifying use of a Reynolds decomposition of the velocity field when a spectral gap is present). As a general rule, if the eddy length scales of the shear layer itself are about an order of magnitude smaller or larger than the characteristic length scale of the flyer and if the large eddy mean deformation time scale present in the shear layer flow (i.e. the time scale that governs the linearly-unstable dynamics of the large structures of the shear layer) is much shorter or much longer than the natural period of the flyer, the dynamics of the flyer can be considered decoupled from the dynamics of the shear layer, where traversal of the shear layer by the flyer can be treated as a change in wind state that occurs upon piercing the dividing streamline of air masses of two different velocities. When the velocity gradient is large (i.e. the shear layer thickness is small relative to the flyer), a flyer passing through experiences what amounts to a gust, as discrete as nature allows. In such instances, the effect of the aerodynamic forcing of the discrete gust is a function solely of the amplitude of the gust front, as is most likely to occur in the transverse and streamwise gust encounter cases. Provided the geometry is simple and the flyer of interest is at least an order of magnitude smaller than the shear layer generating geometry, the gust front can reasonably be considered in a two-dimensional planar framework when aligned with the prevailing wind. Canonical treatment of the two-dimensional free shear layer is explored next.

3.2 Turbulent free shear flows - the mixing layer

In general, turbulent free shear flows are Re-number independent with a mean velocity profile of at least one inflection point (i.e. Rayleigh-unstable) with the primary instability mechanism by vortical induction. The basic vorticity field of the mean flow determines its expected behavior and evolution in space. Nearly all flowfields with both signs of vorticity (e.g. jets/wakes) are likely to develop into a three-dimensional global structure. Unique amongst the class of turbulent free shear flows are the one-sided vorticity-distributed flowfields (i.e. mixing layers) which recover and maintain a quasi two-dimensional global structure that persists at high Reynolds numbers even in the presence of strong initial three-dimensional disturbances (e.g., see Breidenthal, 1980). Freely evolving coherent structures organize as fairly two-dimensional "rollers" in the case of a mixing layer as a consequence of a Kelvin-Helmholtz instability. The interface between rotational and irrotational fluid is intermittent so classifying an "edge" is challenging without some level of subjectivity on account of the unsteadiness. When averaged over many instantaneous realizations, a linear growth rate of the large coherent structures has been well-established. Indeed, Brown and Roshko (2012) argue that the growth rate of the mixing layer thickness is its key defining parameter.

Anatomy of a dual-stream mixing layer

A dual-stream mixing layer consists of two streams of nonzero but different velocities. The idealized step-like separations cannot exist in the real-world since mass, momentum, and energy are exchanged across the shear layer. The shear layer width, $\delta_\omega(x)$, grows with downstream development due to entrainment and typical velocity profiles evolve like that of fig. 3.1.

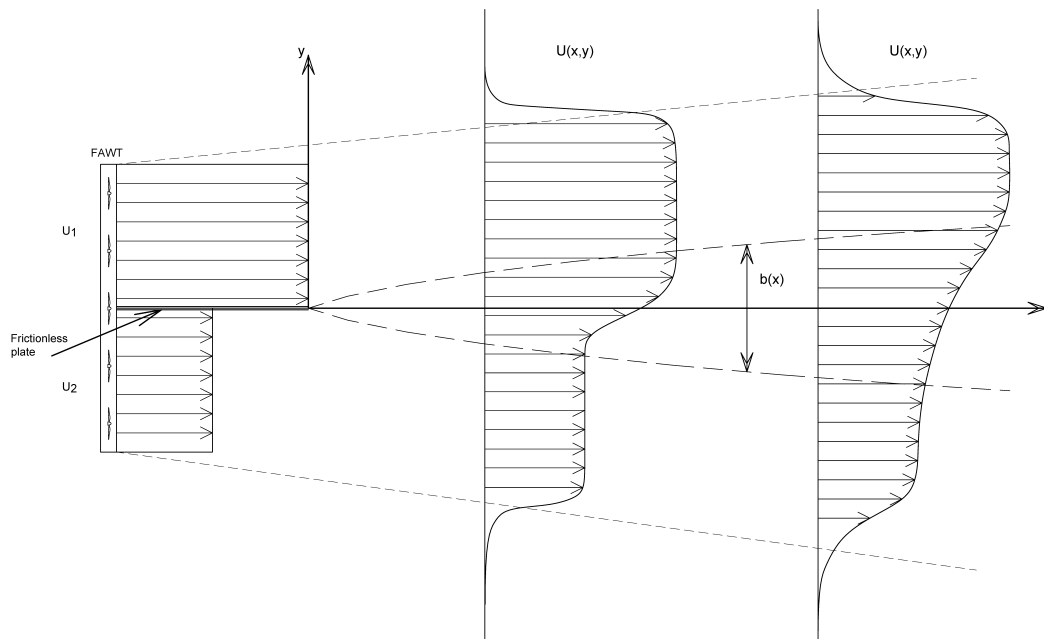


Figure 3.1: Diagram for the evolution of the mean velocity profile for a dual-stream planar mixing layer.

A mixing layer can be characterized by its velocity ratio, $r = U_2/U_1$ where U_1 is the high side freestream mean velocity and U_2 is the low side freestream mean velocity. When far enough downstream, an ideal mixing layer will reach a self-preserving state, whereby the mean velocity profiles and turbulence characteristics are self similar when scaled by a single characteristic length and velocity, typically selected to be the shear layer width $b(x)$ and the velocity difference $\Delta U = U_1 - U_2$, respectively. The mixing layer thickness is expected to grow linearly and its turbulence profiles exhibit Gaussian-like behavior, a result that can be obtained analytically from eddy-viscosity models.

Shear layer instabilities - coherent structures

The underlying structure of mixing layers was quite mysterious until the seminal work of Brown and Roshko (1974) visualized the presence of large coherent structures. These large-eddy structures were found in a turbulent dual-stream mixing layer at high Reynolds number ($Re_x = 0.5 \times 10^6$) spanning the entire mixing region, appearing to be two-dimensional in nature, persisting for longer than any appar-

ently relevant time scale. These coherent structures are found to persist even in the presence of strong external disturbances (e.g., see Wygnanski et al., 1979) and are therefore considered to be essentially two-dimensional features of a mixing layer in the range of Reynolds numbers tested ($\sim 10^4 - 10^7$). The mixing layer grows as fresh freestream fluid is entrained into the coherent structure as it convects downstream. The velocity difference puts into motion the process described below:

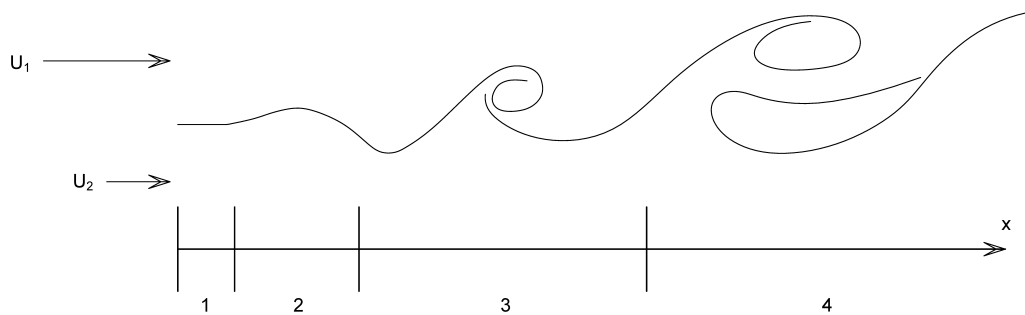


Figure 3.2: Developmental stages of a shear layer rollup.

- 1. Origin of the shear.
- 2. Fundamental Kelvin-Helmholtz instability begins to exponentially grow.
- 3. Growing disturbances cause the shear layer to roll up into discrete vortices. These spanwise rollers convect downstream and grow through entrainment.
- 4. Discrete vortices are moved from the centerline by local instabilities and begin rotating about each other, beginning to merge through a process called pairing. The amalgamation of eddies results in fewer and greater-spaced large coherent structures with downstream development.

Dimotakis and Brown (1976) showed that the entrained fluid remains discernible and practically unmixed for the lifetime of the large irrotational structure, until it rapidly mixes down to small scales. Expressed in diagram form, the coherent structures are slightly tilted downstream with a thickness, core area, and circulation that can be identified visually (e.g. from a shadowgraph or high speed video). The vorticity

thickness is an approximate¹ estimate of the size of the coherent structure, denoted D in fig. 3.3.

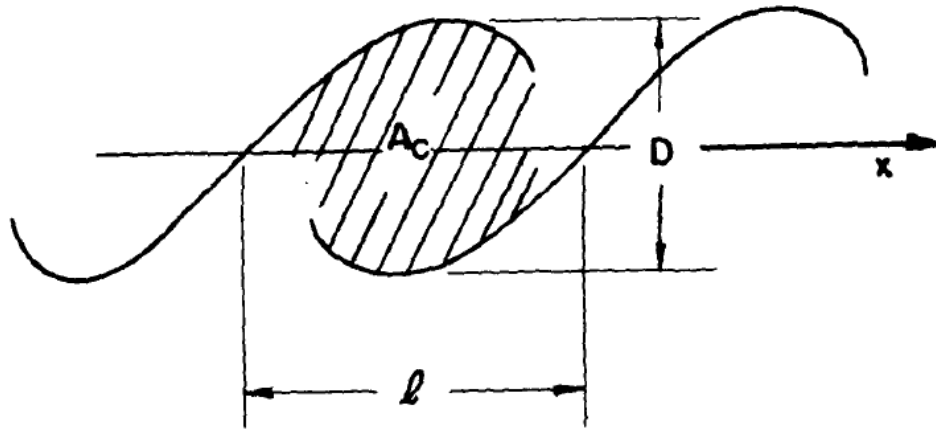


Figure 3.3: Visual properties of a large-scale coherent structure. Diagram reproduced from Bernal (1981).

3.3 Experimental mixing layers

Experimental mixing layers have traditionally been generated by single- or dual-ducted wind tunnels, separated by a splitterplate geometry with a sharp trailing edge. Much of these efforts were aimed toward establishing the self-preserving nature of these flows, understanding and subsequently amending or validating modeling efforts. This work benefits immensely from those efforts. For instance, basic criteria for describing the evolution of mixing layers is well-established and an extensive database for all such experimental shear layers (incompressible and compressible alike) can be found in the literature (e.g., see Yoder et al., 2015).

To evaluate the suitability of the experimental plane mixing layers for discrete gust testing, a shear layer characterization campaign must first be undertaken. Due to the unconventional character of the flow apparatus, in particular the absence of a splitterplate geometry coupled with a multi-source design, a rather basic analysis of the mean velocity profile characteristics is first presented followed by analysis of the turbulence characteristics to better evaluate how well multi-source generated mixing layers comport to the classical experiments.

¹approximate because the coherent structures are quasi-regularly repeated regions of discernible correlation and are not precisely defined vortex structures as is implied in diagrammatic abstractions.

Measures of shear layer width

There exist four predominant measures of shear layer width found in the literature. Here is chosen calculation of the shear layer width $b(x)$ in three different ways, consistent with the bulk of literature on the topic. First, the shear layer width is defined using the mean velocity profile maximum slope thickness:

$$\delta_\omega = \frac{U_1 - U_2}{\left(\frac{\partial U}{\partial y}\right)_{max}} \quad (3.1)$$

where δ_ω can be also interpreted as the vorticity thickness

$$\delta_\omega = |\omega|^{-1}_{max} \int_{-\infty}^{\infty} |\omega| dy \quad (3.2)$$

with $-\omega = \frac{\partial U}{\partial y}$. Secondly, a normalized form of the velocity profile, labelled herein as U^* , can be used to arbitrarily assign limits to the mixing layer:

$$U^* = \frac{U - U_2}{U_1 - U_2} \quad (3.3)$$

For instance, the location at which the normalized mean velocity profile reaches, say, $U^* = 0.05$ and $U^* = 0.95$ (i.e. 5% and 95% of its respective low and high side freestream velocities), can be denoted as $\eta_{0.05}$ and $\eta_{0.95}$, where $\eta = (y - y_0)/(x - x_0)$ is a similarity coordinate scaled using the downstream measurement location x and the coordinates of the virtual origin (x_0, y_0) . The centerline, which can be thought of as the dividing streamline between the layers, is defined to be $\eta^* = (y^* - y_0)/(x - x_0)$, the ray on which $U^*(\eta^*) = 0.5$. This methodology is most frequently employed to determine the mean velocity characteristics of a mixing layer through the construction of spread diagrams, particularly useful when probe traversals are solely used.

Thirdly, the relevant mixing layer parameters can be calculated from an error function fit to the shape of the mean profile of the form derived by Görtler (1942). Here the normalization of the mean velocity profile is collapsed by a similarity coordinate $\xi = (y - y_0)/\delta$, which is a function solely of local shear layer conditions:

$$U^*(\xi) = \frac{1}{2} \left(1 + \operatorname{erf} \left(\frac{y - y_{50}}{\delta} \right) \right) \quad (3.4)$$

where δ is used to describe the shear layer width and y_{50} , as above, is the centerline location of the flow where $\bar{U} = \frac{1}{2}(U_1 + U_2)$.

General description of the experimental setup

The precise outer geometric dimensions $L = nd$ of the CAST FAWT used herein is 113 inches \times 113 inches, though the operating envelope is conservatively taken to be 100 inches tall \times 100 inches wide \times approximately 250 inches long, given the individual fan-unit mixing that initializes near the fan outlet plane (see Chapter II and appendix A for more information). The dual-stream mixing layers are initiated across the 17th and 18th row of fans spanning the entire array (i.e. 113 inches) through discrete partitioning in software. The only flow manipulator installed is a honeycomb affixed directly to the face of the FAWT to eliminate the swirl of the individual fan units. This gives a nominal turbulence intensity of 3 \sim 5% in the regions tested (see fig. A.10 for more information regarding the turbulence intensity distribution for this particular array). The streamwise (u) components of the velocity vector were measured at four cross-sections of the flow, starting at $x = 28$ inches and moving downstream at intervals of 30 inches, corresponding to measurement locations of $x/L \sim 0.25, 0.51, 0.77, 1.04$. A 20% spatial reduction of the testing envelope with downstream development is measured at $x/L \sim 1$ (see fig. 2.6), so that at the furthest downstream location, the measurement envelope is approximately 80 inches \times 80 inches, or ± 40 inches from the tunnel centerline coordinates. Each traverse consisted of at minimum ~ 30 transverse records sampled at 1kHz for 32 seconds using one single-wire hotwire.

Dual-stream mixing layer development

The mean velocity profiles in dimensional y -coordinate space are shown in fig. 3.4 for $r = 0.4$ and $r = 0.2$, with $r = U_2/U_1$, each measured at four downstream locations. Immediately evident in the dimensional view is a series of velocity overshoots and undershoots about the average respective freestream velocities, consistent with the views of fig. 2.5 and fig. 2.6 presented in Chapter II. Similar overshoots of the mean velocity profiles in traditional splitterplate dual-stream mixing layers have been reported in the near-region development on the low velocity side on account of the wake (e.g., see Mehta, 1991), but the overshoot quickly converges to the freestream velocity further downstream. Measurements in this case were taken far enough downstream to be free of any wake deficit at flow initiation due to the annular output of the individual fan units, but still within the developing region of the roughly nine inch peaked nonuniform flow behavior of the modules at all four measurement locations. The effect diminishes further downstream, as seen by tracking the maximum overshoot and undershoot deviation, as in fig. 3.5.

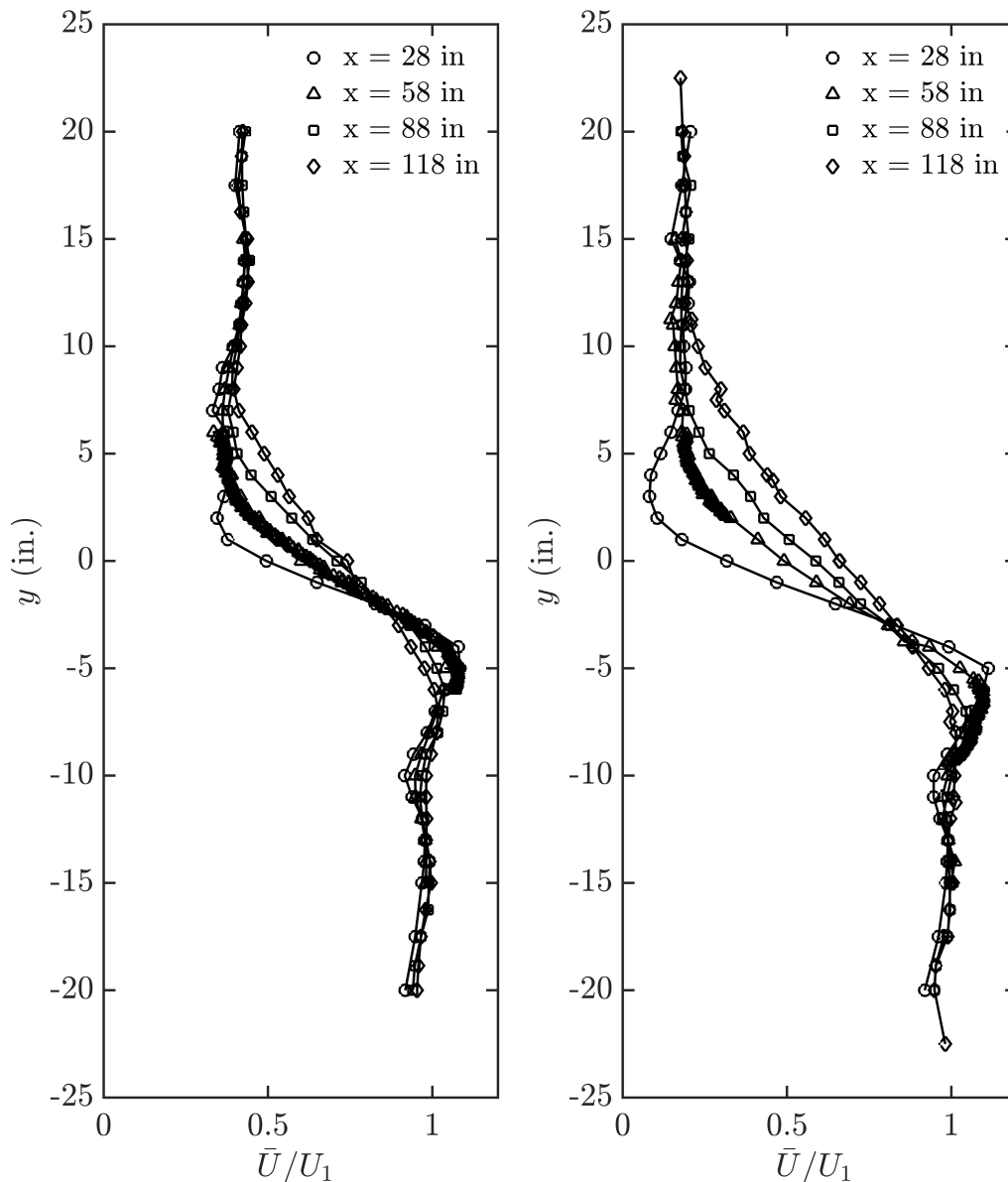


Figure 3.4: Mean velocity profiles in dimensional y -coordinate system, $r = 0.4$ (left) and $r = 0.2$ (right).

The vorticity-thickness spreading rate $\delta'_\omega = \delta_\omega/(x - x_0)$ for $r = 0.4$ and $r = 0.2$ is plotted in Figure 3.6. Due to a relationship put forth by Abramovich et al. (1984) and Sabin (1965), it is customary to plot this type of data against $\lambda = (U_1 - U_2)/(U_1 + U_2) = \sigma_0/\sigma$, rather than r . Significant scatter is noted especially for $\lambda = 1$ but also as $\lambda \rightarrow 0$. It is reasonable to posit for two streams of equal magnitude (i.e. $\lambda \rightarrow 0$) that the growth rate of the mixing layer would tend to zero. For conventional splitterplate-generated mixing layers this is not so as the effects of

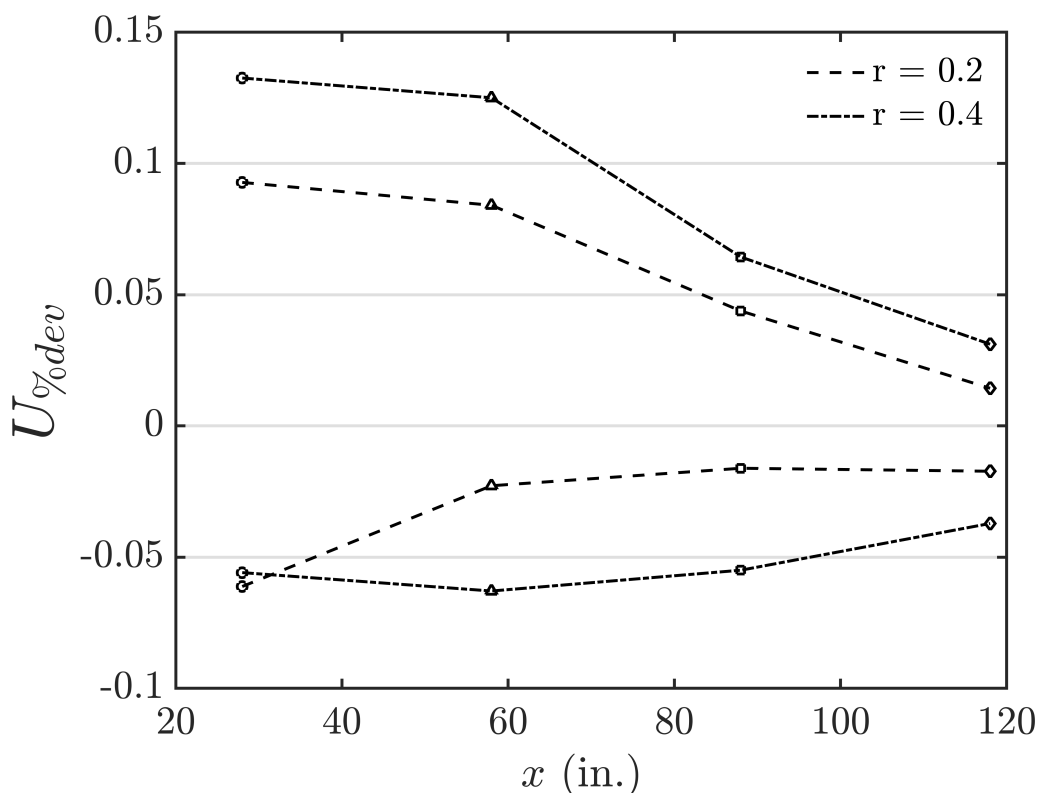


Figure 3.5: The maximum percentage velocity overshoot of the high and low side for dual-stream mixing layers generated from a modular multi-source wind tunnel.

the boundary layers developed on either side of the splitterplate persist downstream, and since the splitterplate typically spans the entirety of the test section, a wake-type flow dominates across the span of the testing domain². The scatter present at $\lambda = 1$ (i.e. $U_2 \approx 0$, a single stream mixing layer) is less understood. Difficulties measuring in the low-speed side environment may contribute, though those effects are more likely to manifest in measurement uncertainties for the turbulence characteristics and not so much in the mean velocity profiles. Brown and Roshko (2012) and Suryanarayanan and Narasimha (2017) both wonder if upstream and downstream boundary conditions contribute more than has been fully recognized. The single-stream experiments of Liepmann and Laufer (1947) are typically cited as reference, where $\delta'_{\omega_0} = 0.162$ with $Re_x > 10^5$. For a greater depth discussion regarding the various proposals for the functional dependency of the spreading rate on the velocity ratio, the reader is referred to Brown and Roshko (1974).

²A related development was observed in fig. 2.4, but because the flow separating geometries (i.e. fan housings) are not one-dimensional (cf. thin splitterplate), the global flowfield homogenizes not too far downstream (i.e. what is called the ‘uniform’ flow modality).

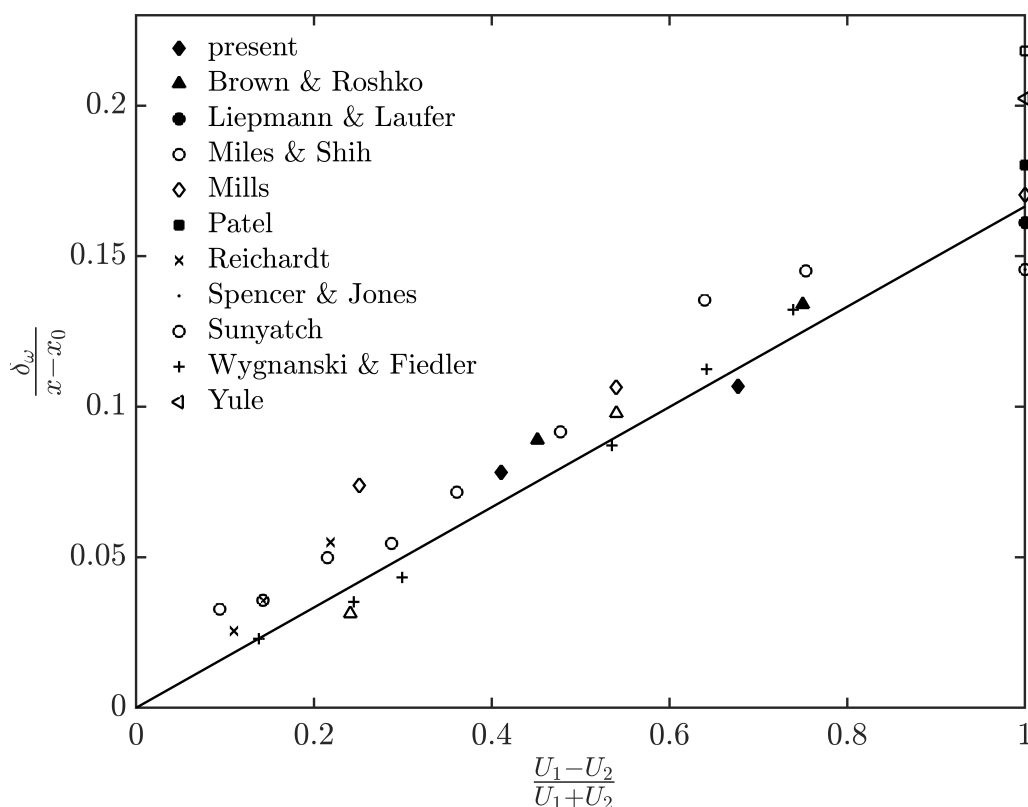


Figure 3.6: The dependence of vorticity-thickness spreading rate on the parameter $\lambda = \Delta U / 2\bar{U}$ for uniform density mixing layers, as adapted from Brown and Roshko (1974) with present results added.

Absent an obvious functional relationship, a linear fit through the origin based on the present measurements is included in fig. 3.6. The linear fit intersects $\lambda = 1$ at $\delta'_{\omega_0} = 0.167$ such that

$$\delta'_{\omega} = 0.167 \frac{U_1 - U_2}{U_1 + U_2} = 0.167 \lambda \quad (3.5)$$

with r.m.s deviation = 0.0115. These results should be interpreted with some amount of caution until measurements taken further downstream over a greater variety of velocity ratios is completed. It is still believed, though, on the basis of fig. 3.6 that the mixing layers generated by the flows of this multi-source, splitterplate-less apparatus are not principally different than more conventional flow systems. Additionally it is believed that multi-source-generated mixing layers may help further the discussion regarding the asymptotic growth rate by introducing a large, high-Re, open, splitterplate-less shear-generating apparatus amenable to lab-based observation.

Some useful comparative parameters for the dual-stream mixing layers tested are summarized in table 3.1 with comparison to a select few other investigators included for additional context in table 3.2. Here $x^* = \lambda x_{max}$ is the maximum measurement location of a given experiment scaled by its velocity ratio. For the mixing layers measured herein, the maximum measurement location downstream was $x = 118$ inches, or very nearly 3000 mm. The Reynolds number is calculated from x^* and the velocity difference ΔU . The values for σ_0 are calculated from the definition of the velocity ratio, where the dual-stream spreading parameter σ is calculated from an error function fit to the mean velocity profile to be consistent with those reported in the literature.

Table 3.1: Summary of results for the dual-stream mixing layer experiments.

r	x (in)	δ_ω (in)	δ'_ω	Re_x	Re_{δ_ω}
0.4	28	3.9	0.090	$0.4 \cdot 10^6$	$0.5 \cdot 10^5$
0.4	58	5.5	0.075	$0.8 \cdot 10^6$	$0.8 \cdot 10^5$
0.4	88	8.6	0.083	$1.1 \cdot 10^6$	$1.1 \cdot 10^5$
0.4	118	10.4	0.078	$1.4 \cdot 10^6$	$1.3 \cdot 10^5$
0.2	28	4.9	0.120	$0.5 \cdot 10^6$	$0.9 \cdot 10^5$
0.2	58	8.3	0.117	$1.1 \cdot 10^6$	$1.6 \cdot 10^5$
0.2	88	10.7	0.107	$1.6 \cdot 10^6$	$1.9 \cdot 10^5$
0.2	118	13.9	0.107	$2.0 \cdot 10^6$	$2.4 \cdot 10^5$

Table 3.2: Selected parameters of comparable mixing layer experiments.

Researcher(s)	r	λ	x^* (mm)	Re_x^*	σ_0
Liepmann and Laufer (1947)	0	1.0	900	$0.9 \cdot 10^6$	11.76
Dougherty (present)	0.2	0.67	2000	$1.4 \cdot 10^6$	12.45
Dimotakis and Brown (1976)	0.2	0.67	600	$3.0 \cdot 10^6$	9.87
Spencer and Jones (1971)	0.3	0.54	680	$1.0 \cdot 10^6$	12.31
Oster, Wygnanski, et al. (1977)	0.4	0.43	470	$0.3 \cdot 10^6$	10.81
Dougherty (present)	0.4	0.43	1200	$0.6 \cdot 10^6$	11.08
Mehta (1991)	0.5	0.33	880	$0.9 \cdot 10^6$	10.5
Spencer and Jones (1971)	0.6	0.25	320	$0.3 \cdot 10^6$	13.14

Triple-stream mixing layer development

To better understand how one-sided vorticity fields generated by this multi-source apparatus evolve, an inter-shear spacing parameter is introduced to partition the fan array into three planar segments. This flow modality, referred to as the triple-stream mixing layer herein, like all other flowfields so far discussed is initiated solely through reconfigurations of software. The thickness of the middle segment is systematically increased by an even multiple of fan rows (and the relative thicknesses of the outer segments reduced by half that multiple, respectively) to observe the behavior of initial mixing and subsequent merging of the two mixing layers when sufficiently initially separated. The mixing layer with the greater velocity difference between its faster and slower freestreams is denoted as the ‘upper’ mixing layer and the mixing layer with the lesser velocity difference as the ‘lower’ mixing layer. This is shown diagrammatically in fig. 3.7.

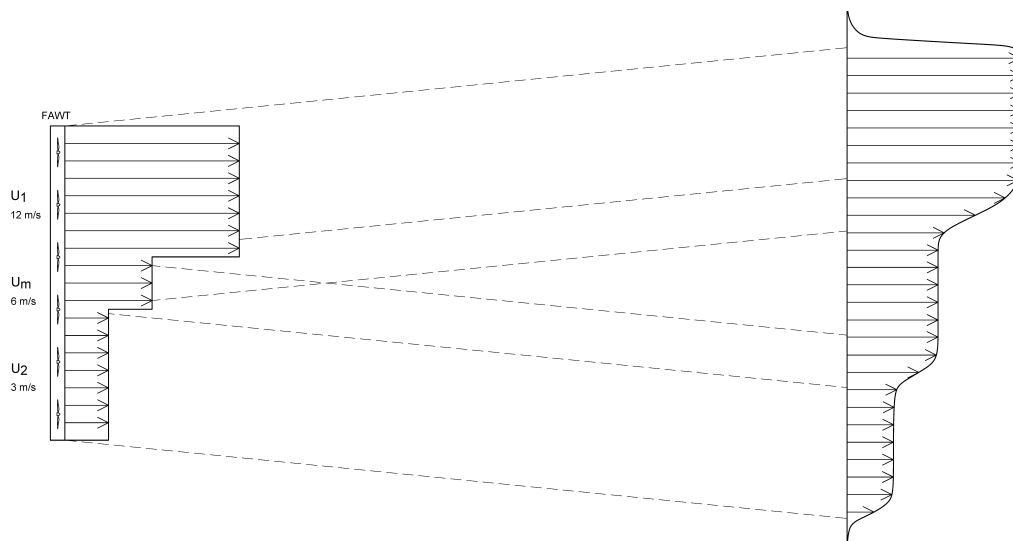


Figure 3.7: Diagram for the evolution of the mean velocity profile for a triple-stream planar mixing layer.

When the inter-shear spacing is modest, the closest analogous conventional mixing layer augmentation would be that of an increase in the splitterplate thickness, with subsequent wake dynamics shown to change the instability frequency of the flow (Dziomba and H. Fiedler, 1985). When the spacing is large enough to support two mixing layers for an appreciable distance downstream, then this is best thought of akin to a double splitterplate configuration³.

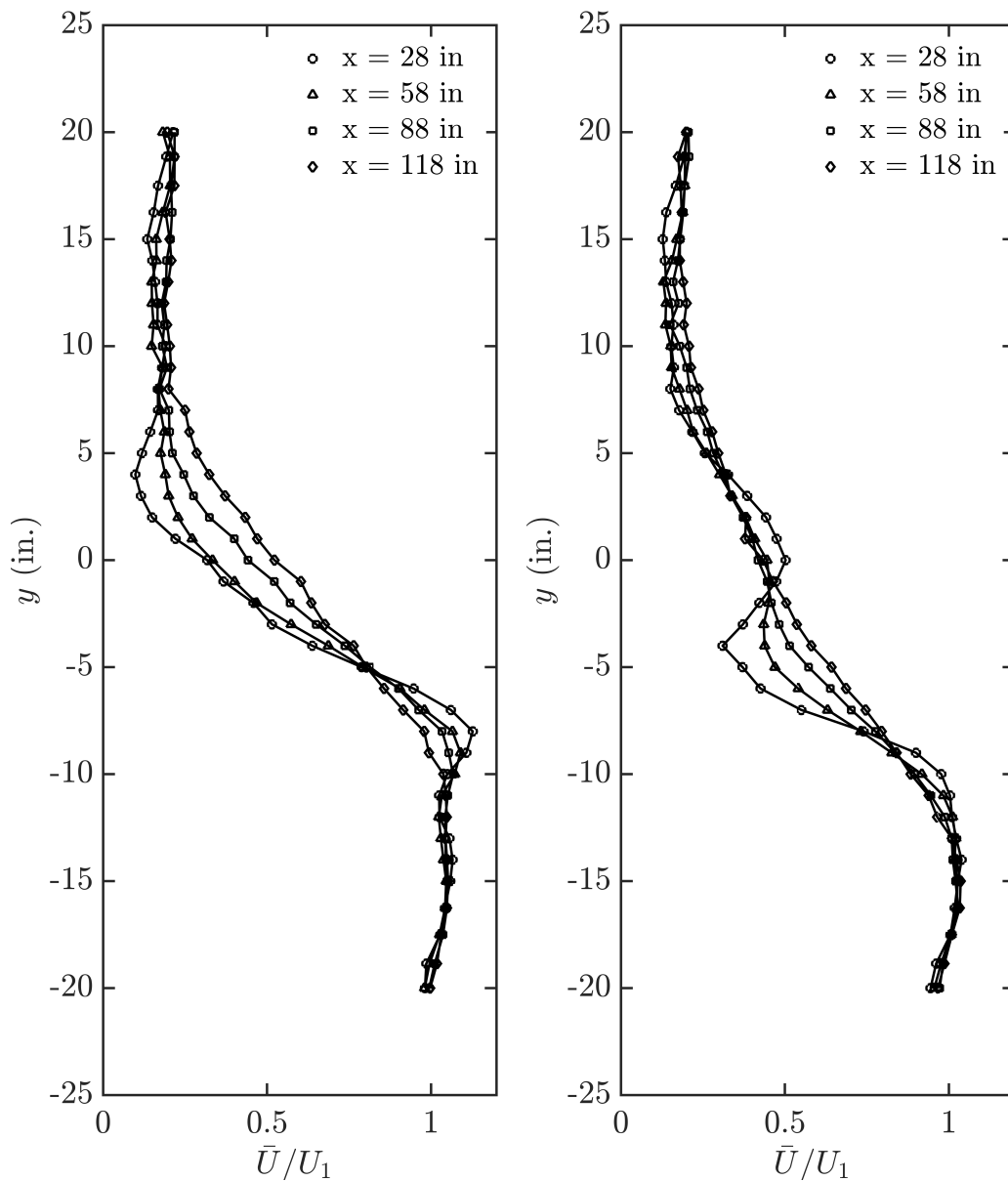


Figure 3.8: Mean velocity profiles in dimensional y -coordinate system, $r_{outer} = 0.2$, for inter-shear spacing of 6.3 inches (left) and 12.6 inches (right).

Stepping the flow in this manner may shed light on the interaction of scales within the complicated mixing layers by parsing them in a systematic way amenable to targeted studies. As a very early step toward that aim, the better-understood dual-stream mixing layer is abstracted by one dimension, introducing the aforementioned inter-shear spacing parameter as well as a merge point which describes the downstream

³To the best of this author's knowledge, no double splitterplate experiments have been reported elsewhere, though some work has been done in multi-jet configurations.

location where the three streams become two again. The velocity of the middle segment is theoretically initialized to divide the array to produce two mixing layers of the same velocity ratios (i.e. $r_{upper} = r_{lower}$), but with different respective velocity differences, ($\Delta U_{upper} \neq \Delta U_{lower}$).

In practice, verification of these upper and lower mixing layer velocity ratios is difficult when the two mixing layers are close to one another, since there is not a clear distinction between the low-speed stream of the upper mixing layer and the high-speed stream of the lower mixing layer. When the mixing layers have merged, an ‘outer’ parameterization is instead used to calculate a velocity ratio. The first triple-stream implementation presented initializes a middle segment with thickness of two rows of fan units, or $ss = 2d$, with $d = 0.080$ m being the outer dimension of the fan unit (see fig. 2.1). The velocity ratio based on the outer streams is $r_{outer} = 0.2$. The effect of the $ss = 2d$ separation is observed at the $x = 28$ inches measurement distance, whereby the vorticity thickness at that station is 55% thicker, but recovers to nominal values at subsequent measurement stations when compared to the dual-stream equivalent (i.e. $r = 0.2$ with a separation distance of $ss = 0$). These comparison results are presented in table 3.3. The x-derivative of the vorticity thickness, a measure of spreading rate, also converges to nominal values with further development downstream. The second triple-stream implementation presented increases the middle segment to $ss = 4d$. As will be more clearly evident in the geometric spreading diagrams of subsequent sections, the two mixing layers are sufficiently separated at the fan outlet plane to develop independently through much of the measurement domain. It is then possible to parse the streams and tabulate values for the upper and lower mixing layers, as has been done in table 3.4.

The goal to initialize the upper and lower mixing layers at the same velocity ratios but with nonequal velocity differences is nearly achieved up to the $x = 28$ inches measurement location. Here, $r_{upper} = 0.34$ and $r_{lower} = 0.33$, with an upper mixing layer Reynolds number based on the velocity difference and downstream location double that of the lower mixing layer (i.e. $\Delta U_{upper} = 2 \cdot \Delta U_{lower}$). Unlike the $ss = 2d$ case, the triple-stream does not recover nominally to the dual-stream characteristics within the domain tested. Indeed, the mean velocity profiles of fig. 3.8b show the tendency of the two layers to converge toward a single velocity profile maximum-slope thickness, but maintain two identifiable maximum-slope thicknesses in the $x = 118$ inches location, suggestive that the two mixing layers have yet to merge within the measurement domain.

Table 3.3: Comparison of nominal mixing layer with velocity ratio $r = 0.2$ to velocity ratio $r_{outer} = 0.2$ initially separated by $ss = 2d$.

r	x (in)	δ_ω (in)	δ'_ω	Re_x	Re_{δ_ω}
0.16	28	4.9	0.120	$0.5 \cdot 10^6$	$0.9 \cdot 10^5$
0.18	58	8.3	0.117	$1.1 \cdot 10^6$	$1.6 \cdot 10^5$
0.19	88	10.7	0.107	$1.6 \cdot 10^6$	$1.9 \cdot 10^5$
0.19	118	13.9	0.107	$2.0 \cdot 10^6$	$2.4 \cdot 10^5$
r_{outer}	x (in)	δ_ω (in)	δ'_ω	Re_x	Re_{δ_ω}
0.21	28	-	-	$0.4 \cdot 10^6$	-
0.21	58	8.3	0.123	$0.9 \cdot 10^6$	$1.2 \cdot 10^5$
0.19	88	11.0	0.113	$1.5 \cdot 10^6$	$1.9 \cdot 10^5$
0.19	118	14.3	0.113	$2.0 \cdot 10^6$	$2.4 \cdot 10^5$

Table 3.4: Summary of results for triple-stream mixing layer experiments. The two mixing layers are initially separated by $ss = 4d$ at the fan outlet plane.

r_{outer}	x (in)	δ_ω (in)	δ'_ω	Re_x	Re_{δ_ω}
0.16	28	-	-	$0.5 \cdot 10^6$	-
0.17	58	-	-	$1.0 \cdot 10^6$	-
0.19	88	-	-	$1.6 \cdot 10^6$	-
0.18	118	21.7	-	$2.2 \cdot 10^6$	$4.0 \cdot 10^5$
r_{upper}	x (in)	δ_ω (in)	δ'_ω	Re_x	Re_{δ_ω}
0.34	28	3.9	0.064	$0.4 \cdot 10^6$	$0.5 \cdot 10^5$
0.43	58	5.8	0.066	$0.7 \cdot 10^6$	$0.7 \cdot 10^5$
0.48	88	8.0	0.067	$1.0 \cdot 10^6$	$1.2 \cdot 10^5$
-	118	-	-	-	-
r_{lower}	x (in)	δ_ω (in)	δ'_ω	Re_x	Re_{δ_ω}
0.33	28	5.2	0.155	$0.2 \cdot 10^6$	$0.4 \cdot 10^5$
0.38	58	7.1	0.112	$0.3 \cdot 10^6$	$0.4 \cdot 10^5$
0.39	88	9.1	0.097	$0.6 \cdot 10^6$	$0.6 \cdot 10^5$
-	118	-	-	-	-

A longer term general objective of multi-source fan array wind tunnel research is to model initial shear conditions between each fan unit, particularly for unsteady flow generations. One can imagine the immense task ahead to understand the mixing behavior of same- and opposite-sign turbulent flows generated from some 1296 annular outputs as they change in time⁴.

⁴If one cares to indulge, this concept can be conceptually abstracted to n -dimensions, n being set by the resolution of the FAWT. Since FAWT are of finite extent, the local inter-shear spacing of each

Spreading diagrams - a geometric view

When the dual-stream mean velocity profiles are plotted in U^* coordinates, the spreading diagrams of fig. 3.9 and fig. 3.10 can straightforwardly be constructed by tracking (somewhat arbitrarily) select locations of the mixing layer. The locations at which $U^*(y_{05}) = 0.05$, $U^*(y_{50}) = 0.50$, and $U^*(y_{95}) = 0.95$ are tracked herein. The virtual origin (x_0, y_0) is determined by extrapolating the linear fits to their mutual intersection. When shifted by y_0 , the centerline of the mixing layer is seen to deflect toward the low velocity side, as to be expected from the literature.

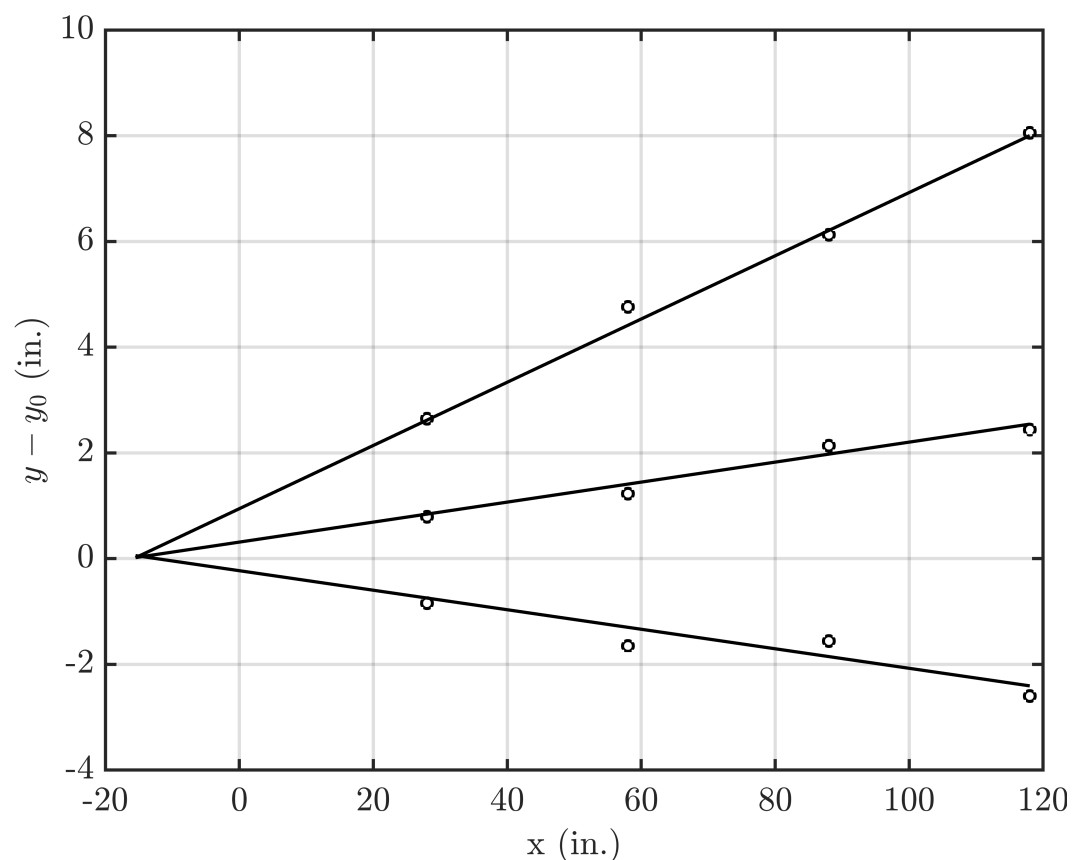


Figure 3.9: Spreading diagram for dual-stream mixing layer with $r = 0.4$.

mixing layer is reduced as more segmentations are added. If each stream was enforced to be of the same width, one can see how the max attainable inter-shear spacing would monotonically decrease with n , thereby reducing the maximum downstream location of the merge points and recovering the uniform flow modality.

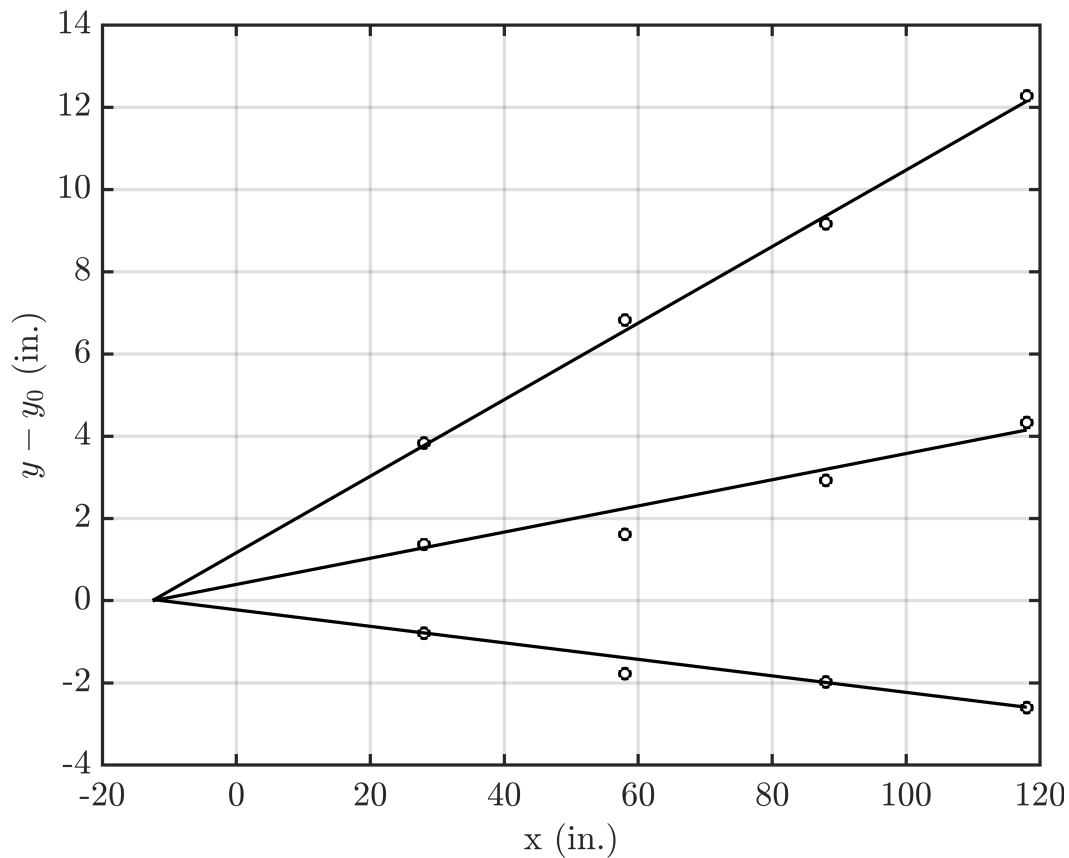


Figure 3.10: Spreading diagram for dual-stream mixing layer with $r = 0.2$.

Greater care is required for the triple-stream cases. As discussed previously, when the two mixing layers are separated enough to maintain a distinct middle stream, the upper and lower mixing layers can be evaluated separately. Cross markers (\times) denote when a given triple-stream dataset is able to be parsed as separate mixing layers. Upper mixing layer data points are given in red and lower mixing layer data points in blue. Otherwise, outer stream parameters are used, denoted by black circle markers (\circ). Two new length scales are introduced when the two mixing layers of the triple-stream case develop distinctly in physical space (i.e. $x > 0$). The inter-shear spacing parameter y_{iss} is defined as the distance between the centerlines of two neighboring, same-sign vorticity, mixing layers and a geometric merging point x_{merge} can be identified as the intersection of the lines corresponding to the low-speed stream of the upper mixing layer and the high-speed stream of the lower mixing layer. Figure 3.11 combined with the tabulated results of table 3.3 suggest that the triple-stream mixing layer with an initial separation of $ss = 2d$ recovers to the nominal $r = 0.2$ dual-stream case beyond $x > 58$ inches.

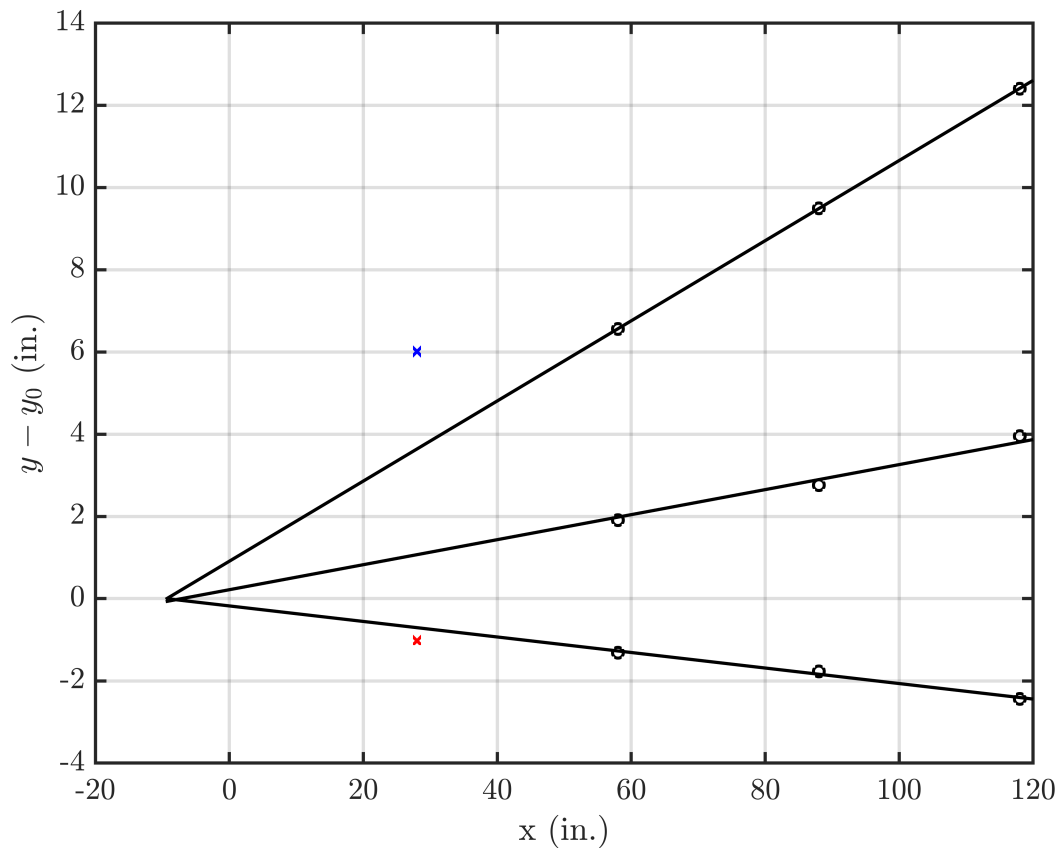


Figure 3.11: Spreading diagram for $r_{outer} = 0.2$ with a $2d$ initial separation at fan inlet plane.

Figure 3.12 suggests that full merging of the two mixing layers in the triple-stream case of $ss = 4d$ has not occurred within the measurement domain, but is likely to occur slightly beyond the measurement location $x = 118$ inches. Judicious choice of these two triple-stream mixing layers within the predetermined measurement domain effectively brackets the salient characteristics of merging same-sign vorticity mixing layers.

There are at least three identifiable regions in the development of the triple-stream mixing layers. First, when the two layers are sufficiently separated to develop nominally, an upper and lower mixing layer are established (termed Region I). Then, a region where the two mixing layers are still distinct but feel the effect of one another establishes (Region II) and begins to move the centerlines of the respective mixing layers closer to one another.

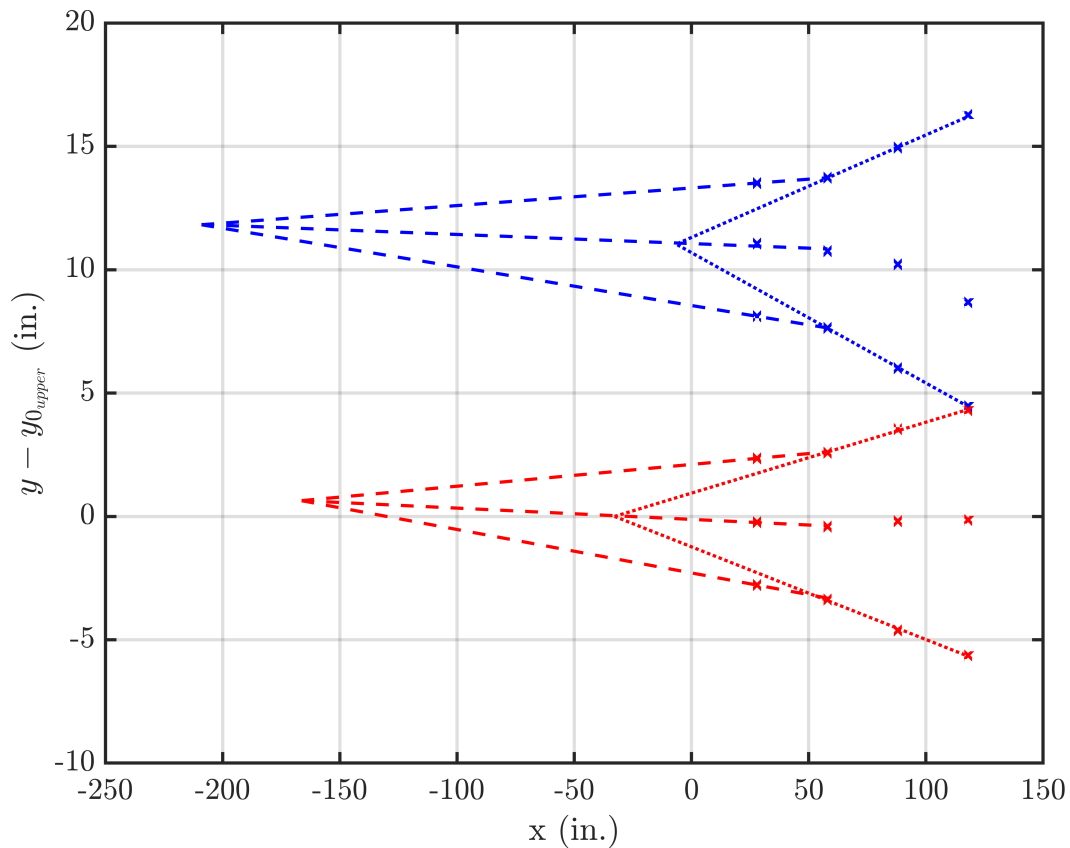


Figure 3.12: Spreading diagram for triple-stream mixing layer with a $4d$ initial separation at fan inlet plane.

The centerline of the lesser velocity difference mixing layer (lower) seemingly moves more toward the greater velocity difference mixing layer (upper), suggestive that the lower mixing layer is absorbed into the upper one. Lastly, the triple-stream mixing layer, which can begin as two distinct same-sign vorticity mixing layers, fully merges (Region III) back to a dual-stream mixing layer with outer spreading properties comparable to the nominal dual-stream case, with the exception that the vorticity thickness is necessarily increased. In fact, it is evident when comparing the outer-stream-based vorticity thickness of the $ss = 2d$ versus the $ss = 4d$ case, which has an increased initial thickness of $2d = 6.3$ inches, that the vorticity thickness at the nearly-merged furthest downstream location has essentially increased by that $2d$ amount (from $\delta_\omega = 14.3$ inches to $\delta_\omega = 20.7$ inches). The extra separation is seemingly absorbed into the dual-stream mixing layer that manifests when far enough downstream.

A geometric approximation that ignores the complexity of Region II can be a useful tool in predicting the general location at which merging is likely to occur. For instance, taking the basic structure of the initially distinct mixing layers of the $ss = 4d$ case and geometrically (artificially) moving one mixing layer closer to the other by a factor of $2d$ in fig. 3.13 gives the approximated structure of the $ss = 2d$ case of fig. 3.11 and indicates that the merging point x_{merge} would likely occur between 35 inches and 53 inches downstream.

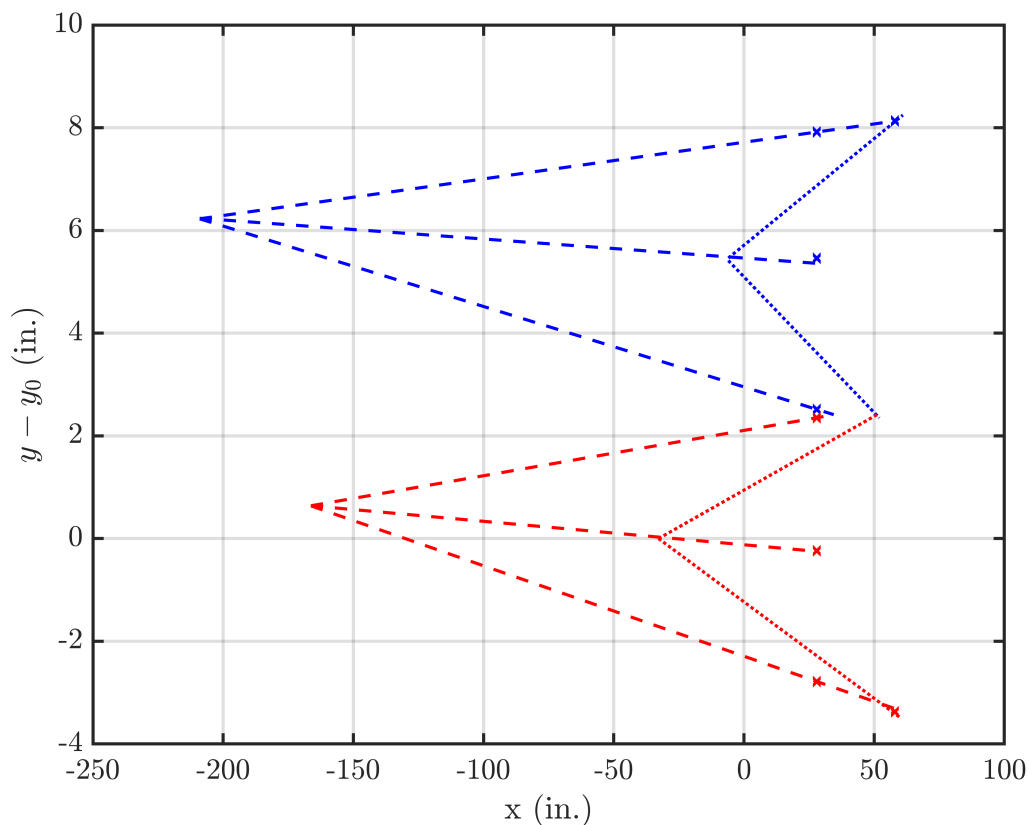


Figure 3.13: Spreading diagram for a geometrically reduced inter-shear spacing of $l_{4d}/2 = l_{2d_{art}}$.

Indeed, it can be said that for the $ss = 2d$ case, somewhere between $x = 28$ inches and $x = 58$ inches a change in spreading rate accompanies a merging point. It is reasonable to expect in the $ss = 4d$ case shortly beyond $x > 118$ inches where the triple-stream likely merges to become a dual-stream mixing layer that an increase in spreading rate would accompany the merge and begin to spread nominally. A more direct geometric comparison of the development of each mixing layer (both

initiated and evolved) can be made by pinning each respective virtual origin to $y = 0$ inches and rotating the mixing layer such that the every centerline point falls along the line $y = 0$ inches, as if the mixing layers are evolving about the same dividing streamline. This representation, given in fig. 3.14, acts then as the basis of the chosen similarity coordinates in the following section, particularly for the triple-stream cases whereby portions of the development may be distinctly separate or fully merged dependent on the downstream location, initial separation distance, and relative velocity differences.

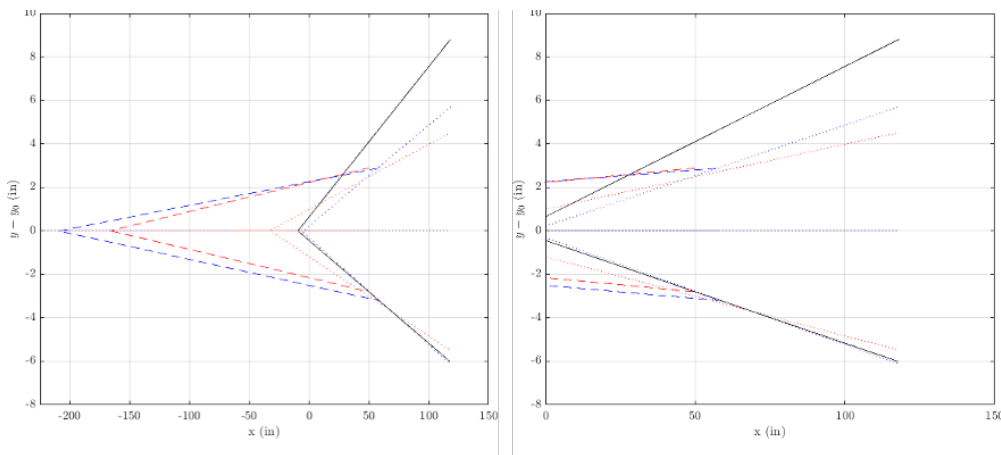


Figure 3.14: Spreading diagram for the triple-stream cases with virtual origin brought up to the line $y = 0$ inches and rotated such that every centerline point falls along the line $y = 0$ inches. The rightmost plot is a zoomed in view of the development in physical space ($x > 0$ inches). The color and line-type are as in fig. 3.11 and fig. 3.12.

Mixing layers in similarity coordinates

For a given data series, the virtual origin is determined from the spreading diagrams of the previous section. Dual-stream mixing layers have one such virtual origin so there is no ambiguity in interpretation for those datasets. Triple-stream mixing layer cases, however, manifest different spreading rates dependent on the region of development. When the triple-stream mixing layers are comprised of two distinct mixing layers (Region I), the mixing layers are analyzed separately. When the two mixing layers are beginning to merge but still maintain different maximum velocity profile slopes (Region II), upper mixing layer coordinates are arbitrarily selected for the analysis. Finally, if the two mixing layers have merged (Region III), the outer stream parameters are used. The virtual origin for the triple-stream cases can thus change for a given data series and is selected according to the appropriate ray of fig. 3.14 at each respective downstream location.

Mean velocity characteristics

Figures 3.15 to 3.19 show the normalized mean velocity profiles plotted in η coordinates, shifted by $-\eta^*$, where $\eta = (y - y_0)/(x - x_0)$ and $\eta^* \equiv (y_{50} - y_0)/(x_{50} - x_0)$. A dimensional reference is provided for the triple stream mixing layer cases. Collapse of the profiles within the mixing layer is excellent, with scatter prevalent at both low and high speed freestream sides. Since the spatial nonuniformity is roughly constant at every downstream location, normalization of the y -coordinate by any nominally increasing length parameter (downstream distance, x , in this case) will manifest as a progressive pinching of these overshoots.

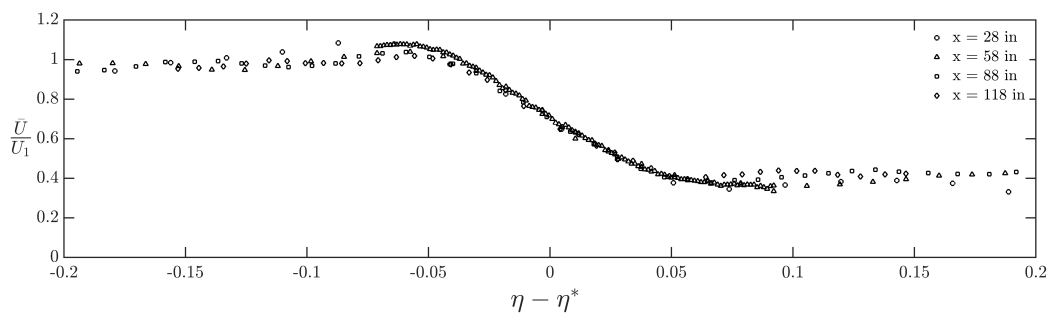


Figure 3.15: Mean velocity profiles of the dual-stream mixing layer in η -similarity coordinates, $r = 0.4$.

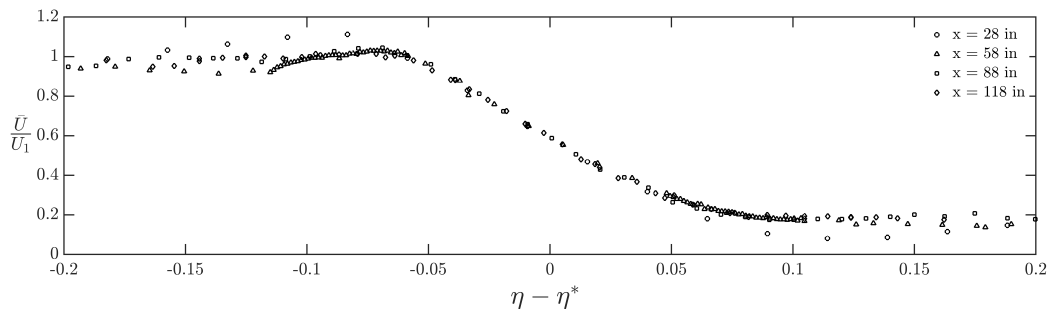


Figure 3.16: Mean velocity profiles of the dual-stream mixing layer in η -similarity coordinates, $r = 0.2$.

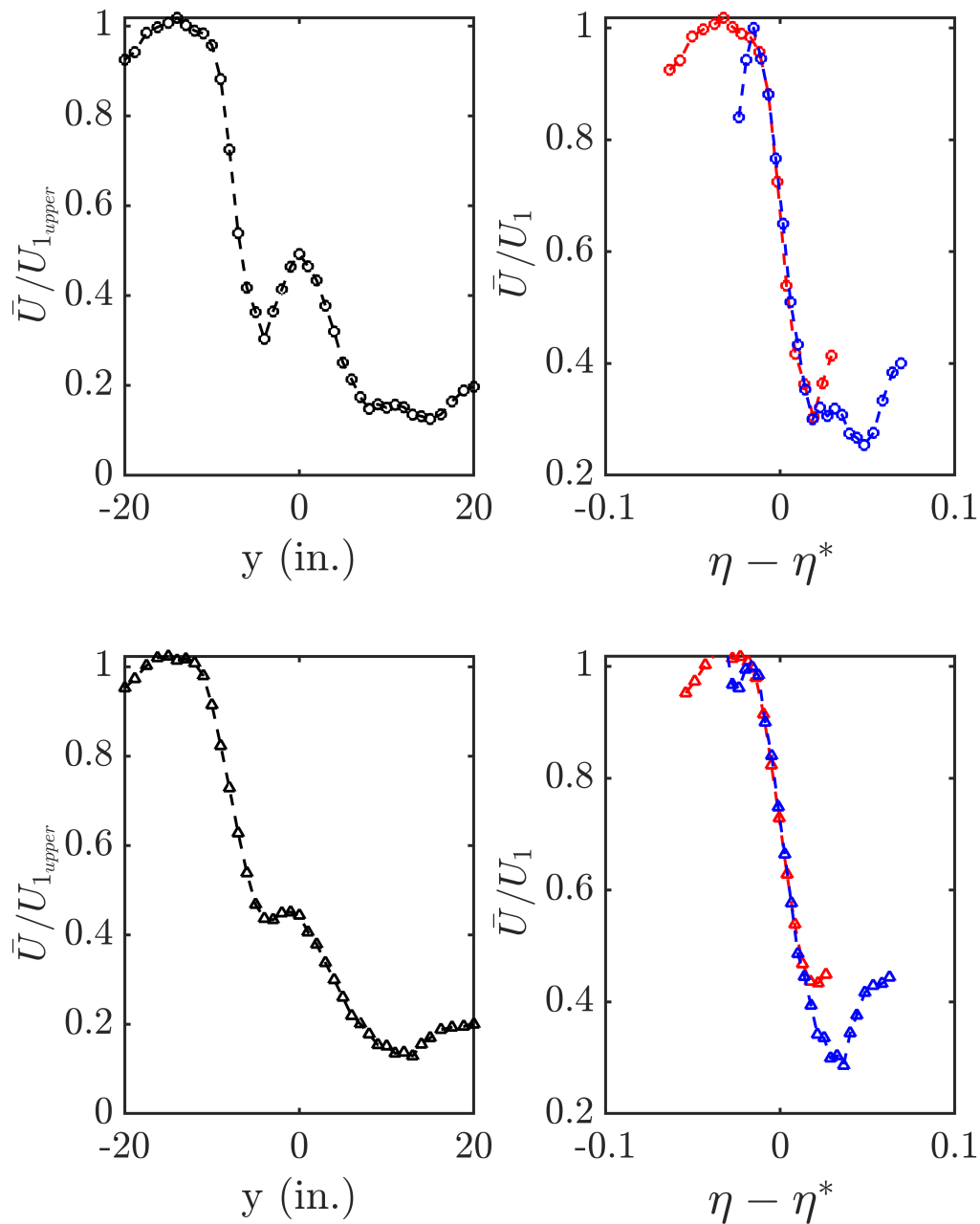


Figure 3.17: Mean velocity profiles of the triple-stream mixing layer with initial separation of $ss = 4d$ in η -similarity coordinates. The top row presents data from $x = 28$ inches and the bottom row from $x = 58$ inches. Red denotes the upper mixing layer and blue denotes the lower mixing layer. Here, the upper and lower mixing layers are distinct (region I) enough to be treated separately.

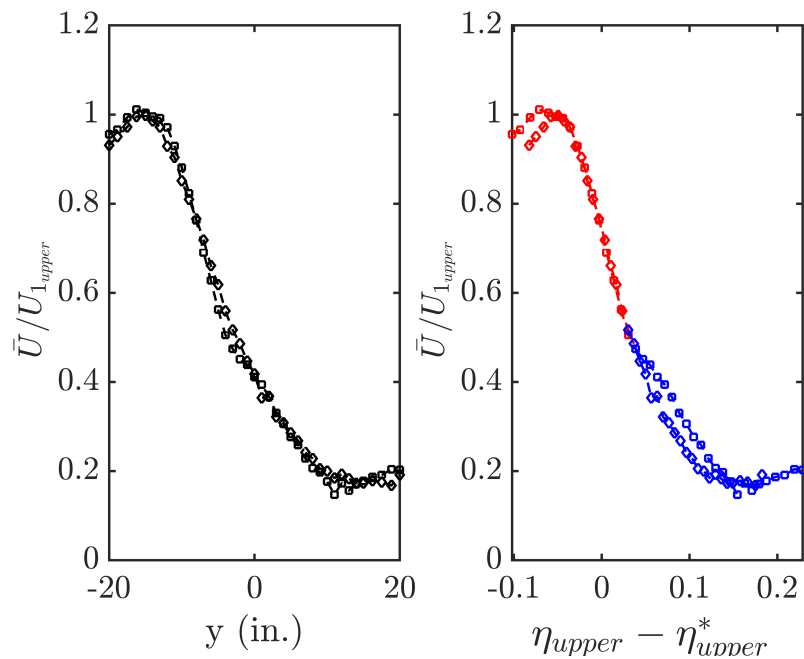


Figure 3.18: Mean velocity profiles of the triple-stream mixing layer with initial separation of $ss = 4d$ in η -similarity coordinates at downstream locations $x = 88$ inches and $x = 118$ inches. Here, the upper and lower mixing layers are transitioning towards merging (region II).

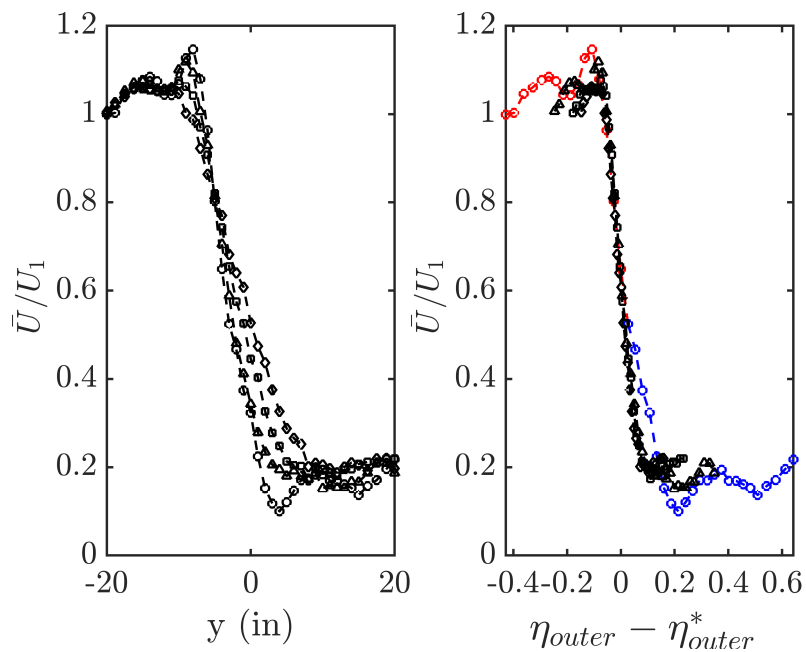


Figure 3.19: Mean velocity profiles of the triple-stream mixing layer with initial separation of $ss = 2d$ in η -similarity coordinates at. Beyond $x > 28$ inches, the upper and lower mixing layers have merged (region III) and can be treated as a dual-stream mixing layer.

Turbulence characteristics

If Re_x is sufficiently large, viscous terms in the streamwise momentum equation can be neglected to give an order of magnitude balance of the two velocity and length scales for a planar mixing layer as $u_{ML}^2/U_{ML}^2 = O(l_{ML}/L_{ML})$. Taking the representative velocity and length scale in the transverse direction to be the fluctuating velocity u' and vorticity thickness δ_ω and the representative velocity and length scale in the streamwise direction as the velocity difference ΔU and distance from the virtual origin, respectively, then:

$$u'^2/\Delta U^2 = O(\delta_\omega/(x - x_0)) = O(\delta'_\omega) \quad (3.6)$$

Thus, to achieve self-preservation, the magnitude of the ratio of the fluctuating velocity and the mean flow difference must be constant with downstream development. When the fluctuating velocity is squared and normalized by the square of the velocity difference, the distribution of the streamwise normal stress is presented. The baseline turbulence intensity of the high-speed and low-speed freestream of the present experimentation is nominally 4-5 times higher than any of the incompressible, constant density experiments with comparable Reynolds number referenced by Yoder et al. (2015). The distribution of the longitudinal component of the velocity fluctuations across the mixing layers for $r = 0.4$ and $r = 0.2$ are shown in fig. 3.20 and fig. 3.21. Peak values in the present experiments, particularly for the furthest downstream locations, reside between values of 0.035 and 0.040. Spencer and Jones (1971) report for the weaker shear case of $r = 0.6$ peak amplitudes in the fully-developed regions were $(u'/\Delta U = 0.19)^2 = 0.036$. Saiy and Peerless (1978) who introduced a static grid to increase freestream turbulence intensity upwards of 5%, found similar values in their weaker shear case of $r = 0.66$. A slight proportional increase in peak values seems attributable to initial freestream turbulence values, though the effects are thought to be secondary, affecting only the three-dimensional structures riding along the basically two-dimensional coherent structures. Though the evolution of the velocity fluctuations follows closely the mean velocity profile, some of the scatter in the data, particularly at the two closest measurement locations, could be attributable to the near-region development of the mixing layers. Spencer and Jones (1971) shows that the development of the pressure fluctuations lag behind the velocity fluctuations. Future experimentation should include a companion pressure probe to narrow the location where the mixing layer becomes fully developed.

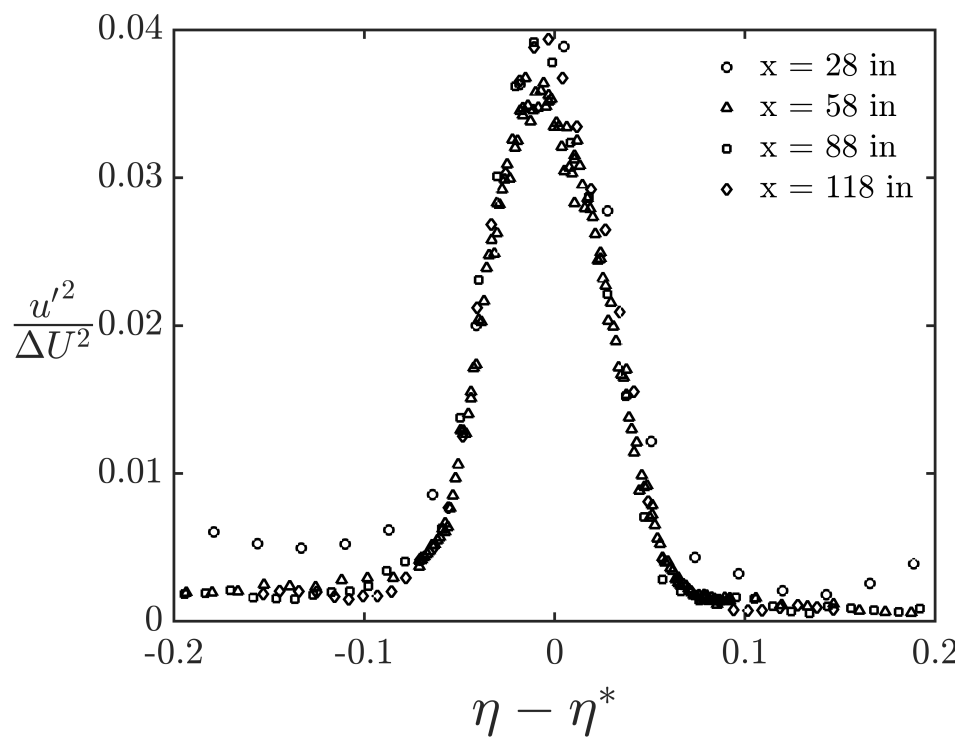


Figure 3.20: Distribution of streamwise normal stress for $r = 0.4$.

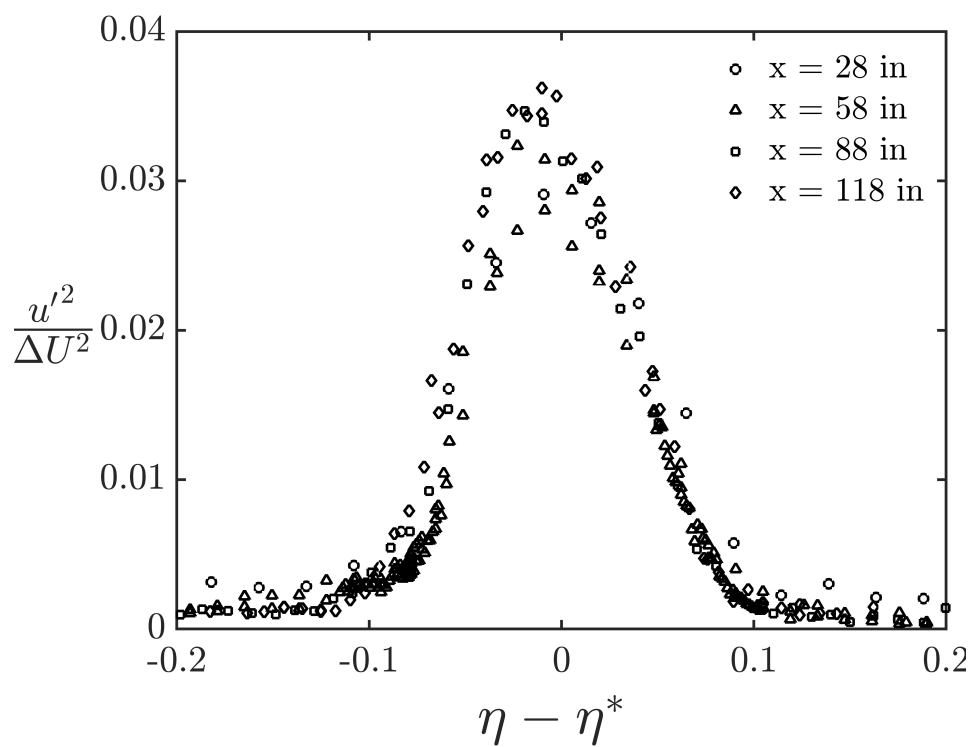


Figure 3.21: Distribution of streamwise normal stress for $r = 0.2$.

Both sets of velocity fluctuation distributions behave Gaussian-like with good collapse in the mixing layer region when plotted in similarity coordinates, which is ordinarily a good indicator of a fully-developed flowfield. According to the results summarized in table 3.1, values of δ'_ω are changing throughout the $r = 0.4$ case, but do seemingly converge to a nominally constant value of 0.107 for the $r = 0.2$ case. Tennekes et al. (1972) suggest, based on experiments up through the year 1972, that mixing layers become self-preserved when $Re_x > 4 \cdot 10^5$.

The methodologies used to analyze the mean-velocity profiles of the triple-stream cases discussed in the previous section are implemented for the fluctuating velocities of the triple-stream cases in figs. 3.22 to 3.24.

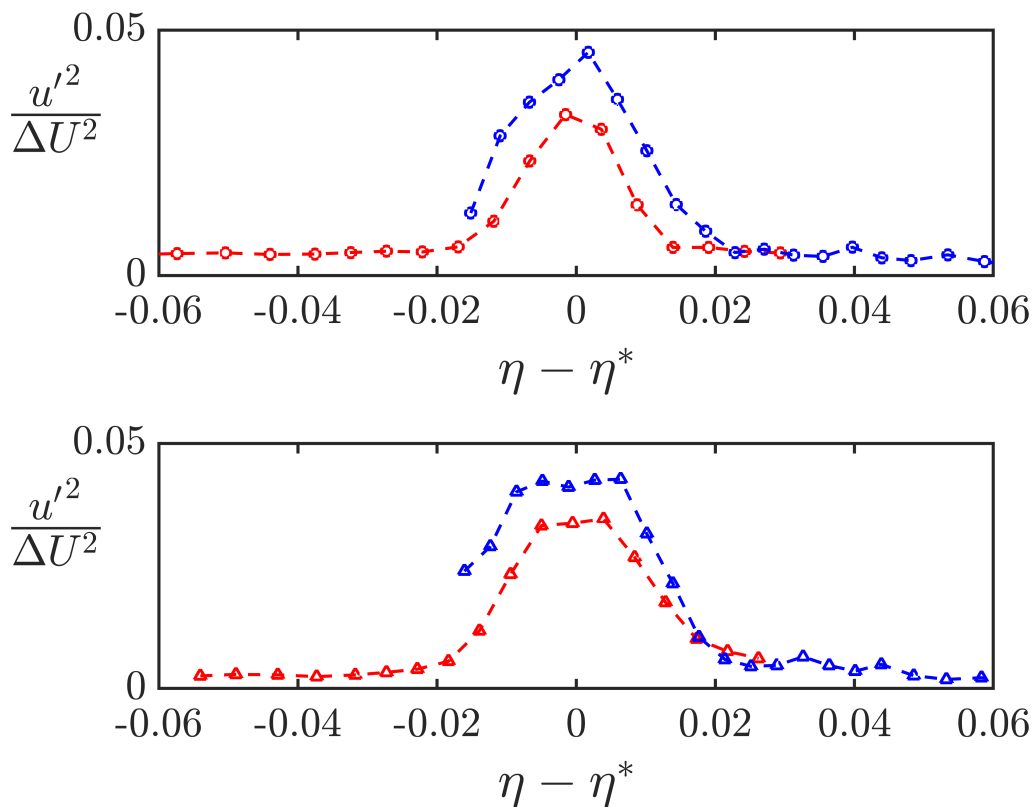


Figure 3.22: Fluctuating velocity profiles of the triple-stream mixing layer with initial separation of $ss = 4d$ in η -similarity coordinates. The top row presents data from $x = 28$ inches and the bottom row from $x = 58$ inches. Red denotes the upper mixing layer and blue denotes the lower mixing layer. Here, the upper and lower mixing layers are distinct (region I) enough to be treated separately.

Tracking the location of the peak of the fluctuating velocities sheds some light on the development of the merging triple-stream mixing layers. In the $ss = 4d$ case of fig. 3.23, where the upper mixing layer similarity coordinates are used, the upper mixing layer peak fluctuating velocity is pinned to $\eta_{upper} - \eta_{upper}^* = 0$. For $x = 88$ inches, the lower mixing layer peak fluctuating velocity is still distinct and broadly peaked about $\eta_{upper} - \eta_{upper}^* = 0.1$. However, with merging eminent just beyond $x = 118$ inches, both the lower and upper mixing layer peaks begin to move toward a new developing peak at $\eta_{upper} - \eta_{upper}^* = 0.025$. The relative movements of the peaks before and after merging are more clearly showcased in the outer similarity coordinate representation of the $ss = 2d$ case. Here, for $x = 28$ inches, the upper mixing layer peak is located at $\eta_{outer} - \eta_{outer}^* = -0.02$ and the lower mixing layer peak is located broadly about $\eta_{outer} - \eta_{outer}^* = 0.07$, suggestive that the lesser velocity difference mixing layer is absorbed into the upper mixing layer somewhere between $x = 28$ inches and $x = 58$ inches.

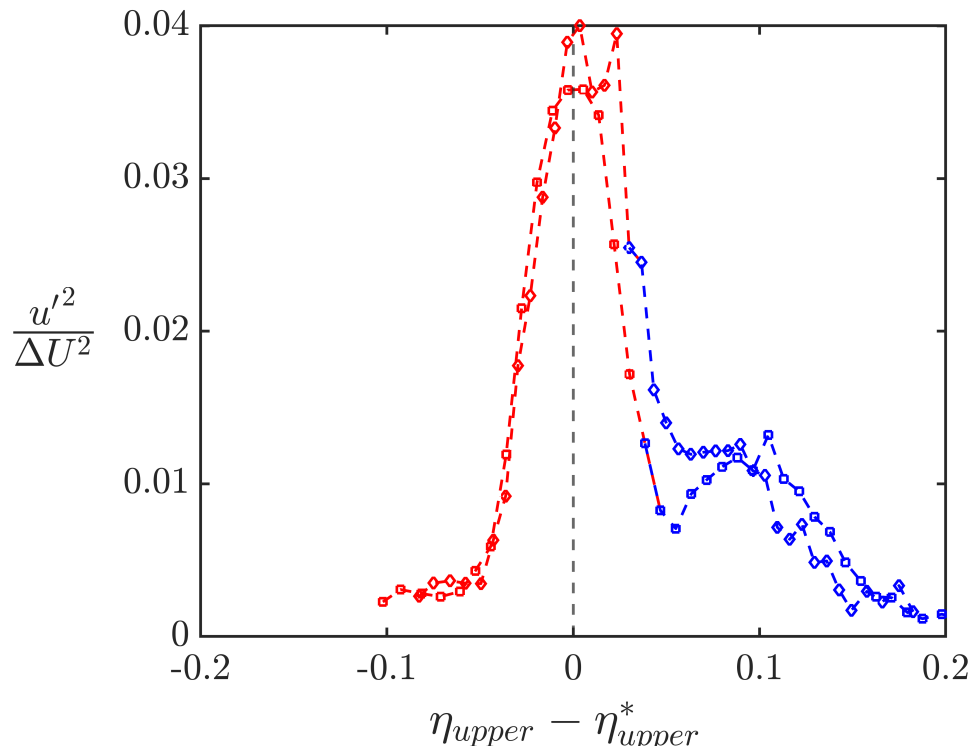


Figure 3.23: Fluctuating velocity profiles of the triple-stream mixing layer with initial separation of $ss = 4d$ in η -similarity coordinates at downstream locations $x = 88$ inches and $x = 118$ inches. Here, the upper and lower mixing layers are transitioning towards merging (region II).

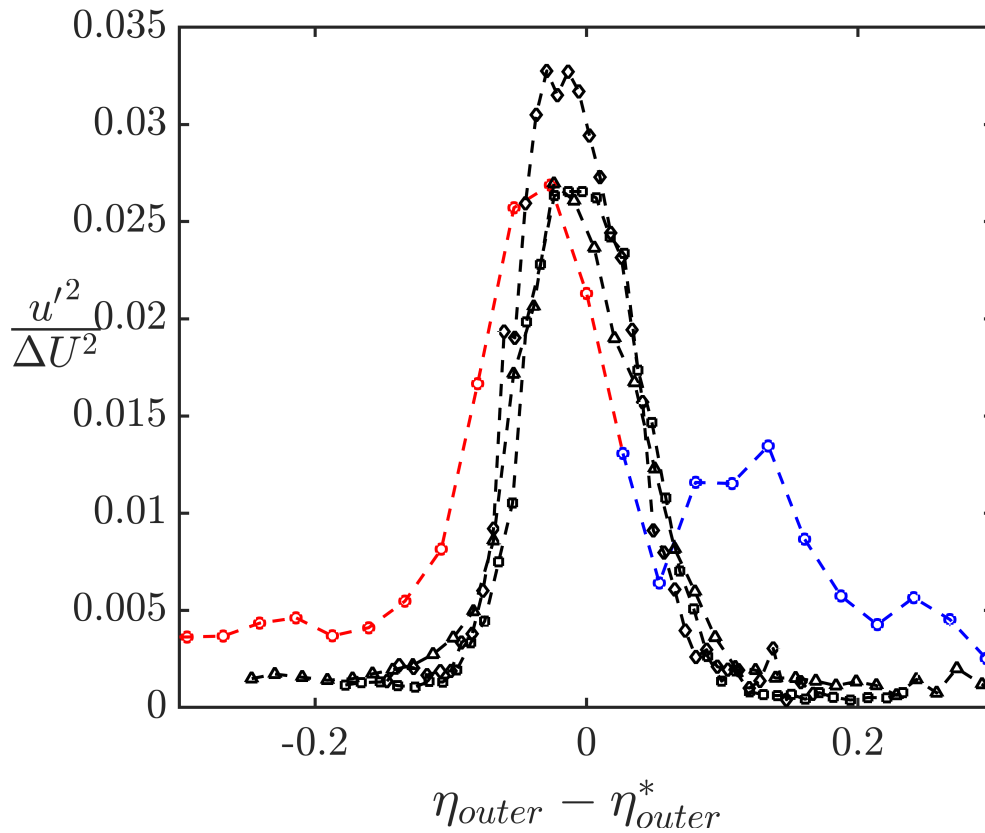


Figure 3.24: Fluctuating velocity profiles of the triple-stream mixing layer with initial separation of $ss = 2d$ in η -similarity coordinates at. Beyond $x > 28$ inches, the upper and lower mixing layers have merged (region III) and can be treated as a dual-stream mixing layer.

Measurement error - dual-stream example

The predominant source of scatter seen throughout on the low-speed velocity side of the mixing layers, but particularly for the of $r = 0.2$ cases, is believed to be measurement-based. Calibration ranging errors of the hotwire anemometer were observed to occur more frequently when the temperature dropped late at night in the semi-outdoor environment of CAST where the experiment was undertaken. The calibration procedure employed (re-calibrated for current temperature at the beginning of each night of experimentation) may not have been sufficient to track with the temperature drop over the roughly hour long data sweeps. This scatter is more readily apparent in the skewness and kurtosis distributions of figs. 3.25 to 3.28.

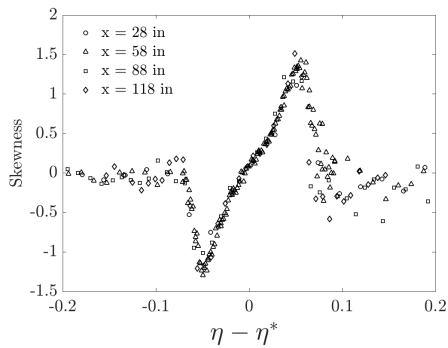


Figure 3.25: Distribution of skewness for $r = 0.4$.

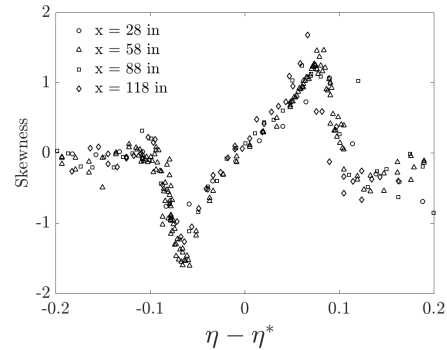


Figure 3.26: Distribution of skewness for $r = 0.2$.

The skewness factor is representative of the symmetry of the fluctuating quantities while the kurtosis is representative of the amplitude distribution with respect to the variance $\overline{u'^2}$. The u-component skewness factor curve for $r = 0.4$ (fig. 3.25) collapses nicely in similarity coordinates with an inflection in the mixing layer region, an indication of a high degree of homogeneity of turbulence in that region, but maintains significant scatter on the low-speed side. The kurtosis plots show the freestream value at approximately 3, which is consistent with the literature. The flat part of the mixing region is ~ 2.75 , which is quite a bit lower. It is generally accepted that a value of 3.5 in the mixing region is indicative of a fully turbulent region. The scatter on the low side can most likely be attributed to the hotwire calibration nearing its operational limits and not necessarily an increase in intermittency as would be implied with a higher kurtosis value. Absent pressure fluctuation distributions and absent data measured further downstream, the mixing layers tested herein cannot be conclusively labeled fully-developed, though seemingly trend that way beyond $x = 88$ inches.

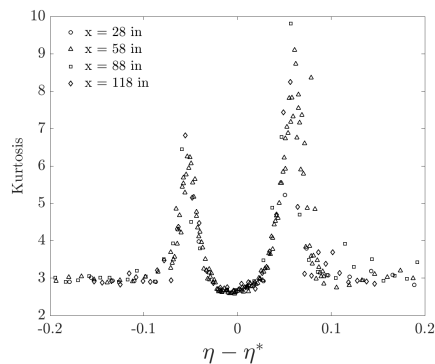


Figure 3.27: Distribution of kurtosis for $r = 0.4$.

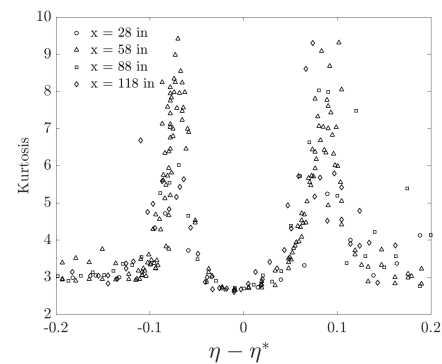


Figure 3.28: Distribution of kurtosis for $r = 0.2$.

Spectral analysis

The longitudinal u-component energy spectrum (see section 4.2 for definitions) along the centerlines of the various mixing layers (i.e. $\eta^* = 0.5$) are presented in figs. 3.29 to 3.31. A $-5/3$ region was clearly developed in every presented case, strongly suggestive of local isotropy in those regions. A coarse traverse at $x = 7$ inches for the dual-stream case with velocity ratio $r = 0.2$ was undertaken to see if this inertial cascade was present close to the fan outlet. At this downstream location, which is well within the region of freestream development where the effects of the individual fans are felt (see Chapter II), a $-5/3$ region, albeit small, is observed (see fig. 3.29a).

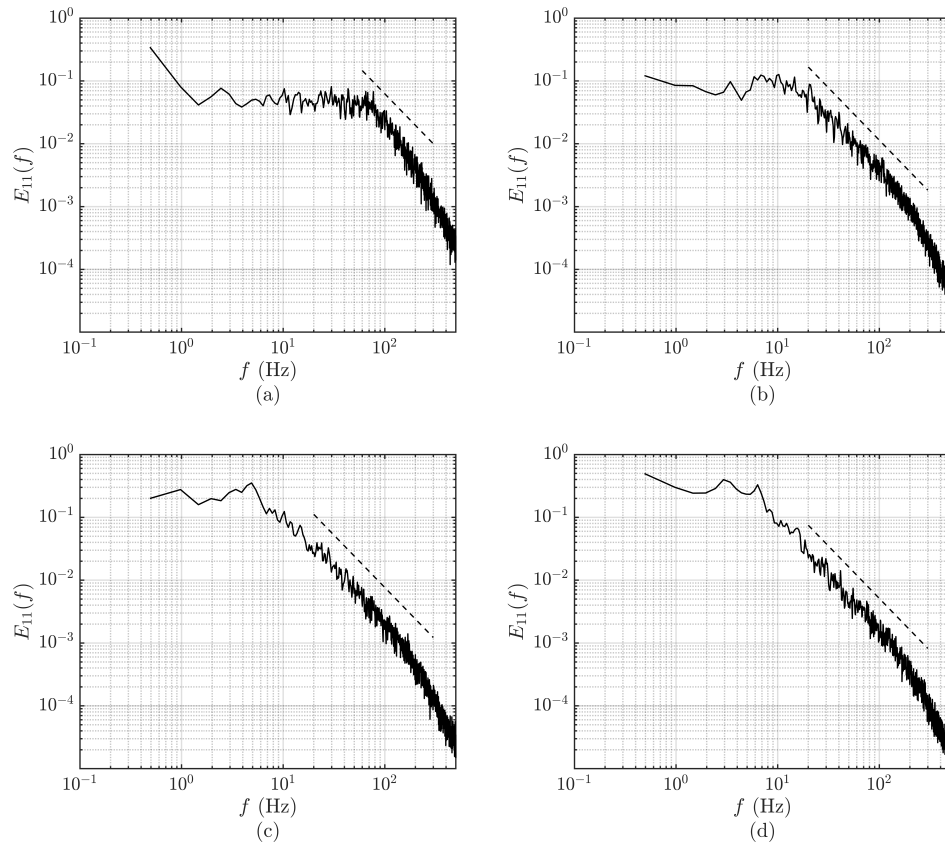


Figure 3.29: Energy spectrum for the dual-stream mixing layer, $r = 0.2$, along the centerline at distances of (a) $x = 7$ inches, (b) $x = 28$ inches, (c) $x = 88$ inches, (d) $x = 118$ inches from the fan array outlet plane. A reference line of slope $-5/3$ indicates a fully developed inertial cascade.

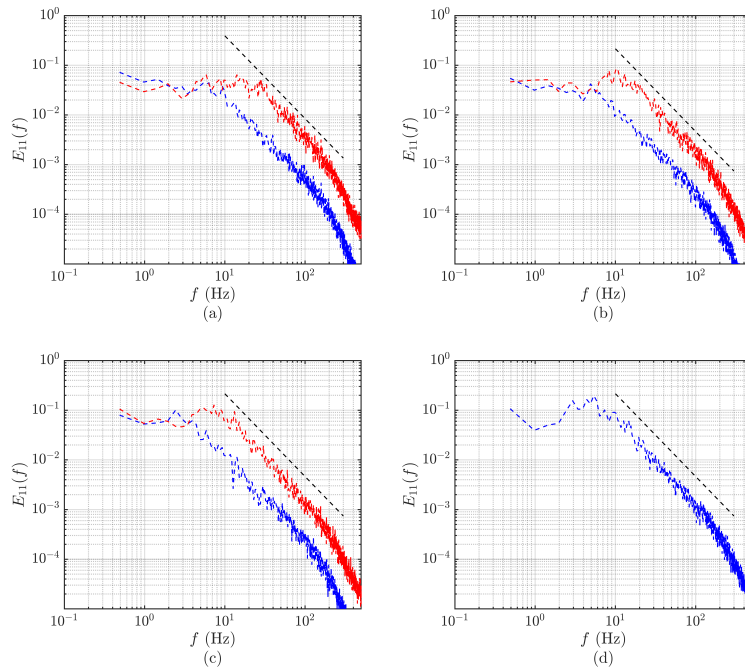


Figure 3.30: Energy spectrum for the triple-stream mixing layer, $ss = 4d$, along the centerline at distances of (a) $x = 28$ inches, (b) $x = 58$ inches, (c) $x = 88$ inches, (d) $x = 118$ inches from the fan array outlet plane. A reference line of slope $-5/3$ indicates a fully developed inertial cascade. Red denotes the upper mixing layer and blue denotes the lower mixing layer.

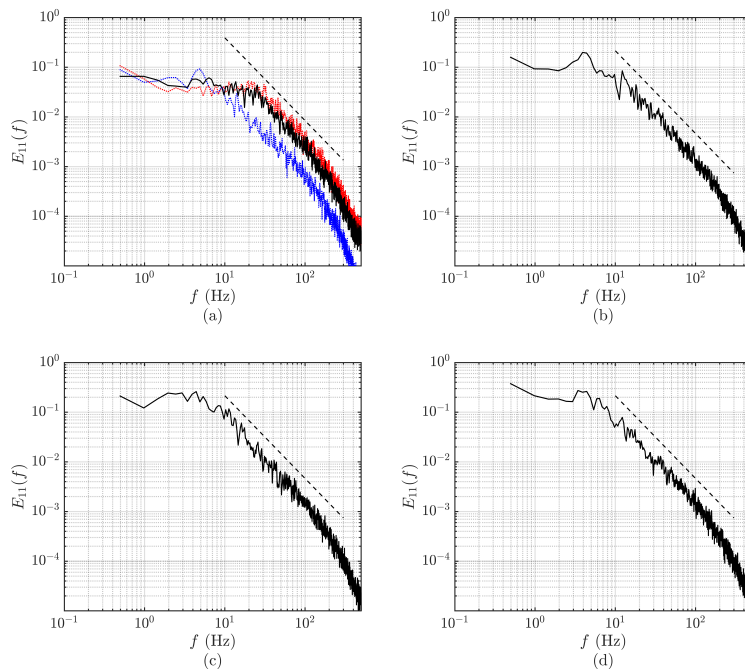


Figure 3.31: Energy spectrum for the triple-stream mixing layer, $ss = 2d$, along the centerline at distances of (a) $x = 28$ inches, (b) $x = 58$ inches, (c) $x = 88$ inches, (d) $x = 118$ inches from the fan array outlet plane. A reference line of slope $-5/3$ indicates a fully developed inertial cascade.

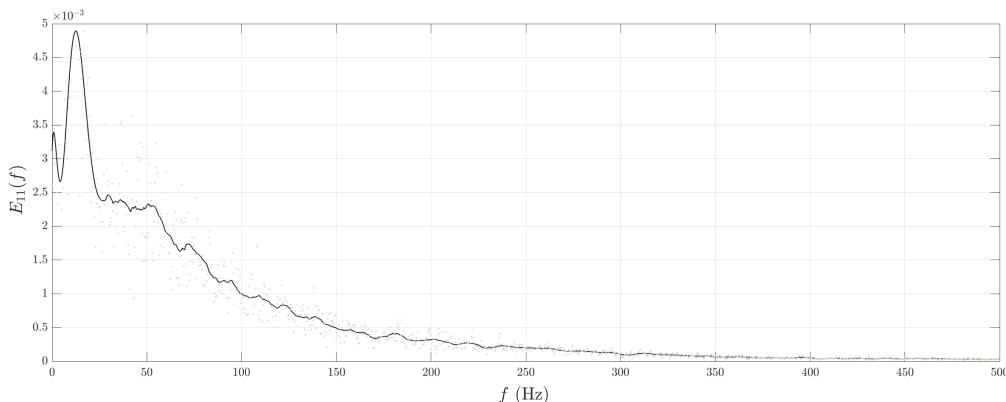


Figure 3.32: Energy spectrum for the dual-stream mixing layer, $r = 0.2$ along the high-speed stream edge at $\eta - \eta^* \sim -1/8$ at $x = 28$ inches distance downstream. A major peak at $f = 12.7$ Hz corresponds to an inverse wave number of 6.3 inches, roughly the non-uniform transverse distance between crests of the spatial wave-front developed from the non-uniform initial conditions of the discrete side-by-side modules.

Energy spectra for the velocity measurements taken just outside the outer edges of the mixing layer, where $\eta - \eta^* \sim \pm 1/8$ is the criteria used to identify the edge (as in Dimotakis and Brown, 1976), can be tracked throughout the flow evolution. Most notable in the earlier development of the mixing layer (e.g. at $x = 28$ inches) is a peak frequency corresponding to an inverse wave number of roughly the module width, an example given in fig. 3.32.

3.4 Fully-developed turbulence - local isotropy

A qualitative difference in the behavior of turbulent shear flows has been noted beyond a transition Reynolds number in outer scales of $Re_{\delta_\omega} \approx 1 - 2 \times 10^4$ (Dimotakis, 2000). This is not to be confused with the laminar/turbulent transition, but is a further transition in the flow observed in many different turbulent flows. It has been suggested somewhat recently by D'Ovidio and Coats (2013) that the underlying growth mechanism of the large structures seemingly changes pre- and post-transition from an amalgamation-event-driven growth mechanism pre-transition to an entrainment-based constant-growth mechanism post-transition. Leaving aside the details underpinning the growth of the large coherent structures, what has been well-established experimentally, numerically, and theoretically post-transition is the change in flow dynamics that manifests as a broader spectrum of eddies with sufficient scale separation to support a quasi-inviscid dynamical representation that

is only weakly dependent on Reynolds number. That is to say that post mixing-transition, a power-law regime of slope $\approx -5/3$ emerges in the energy spectrum and broadens with increasing Reynolds number.

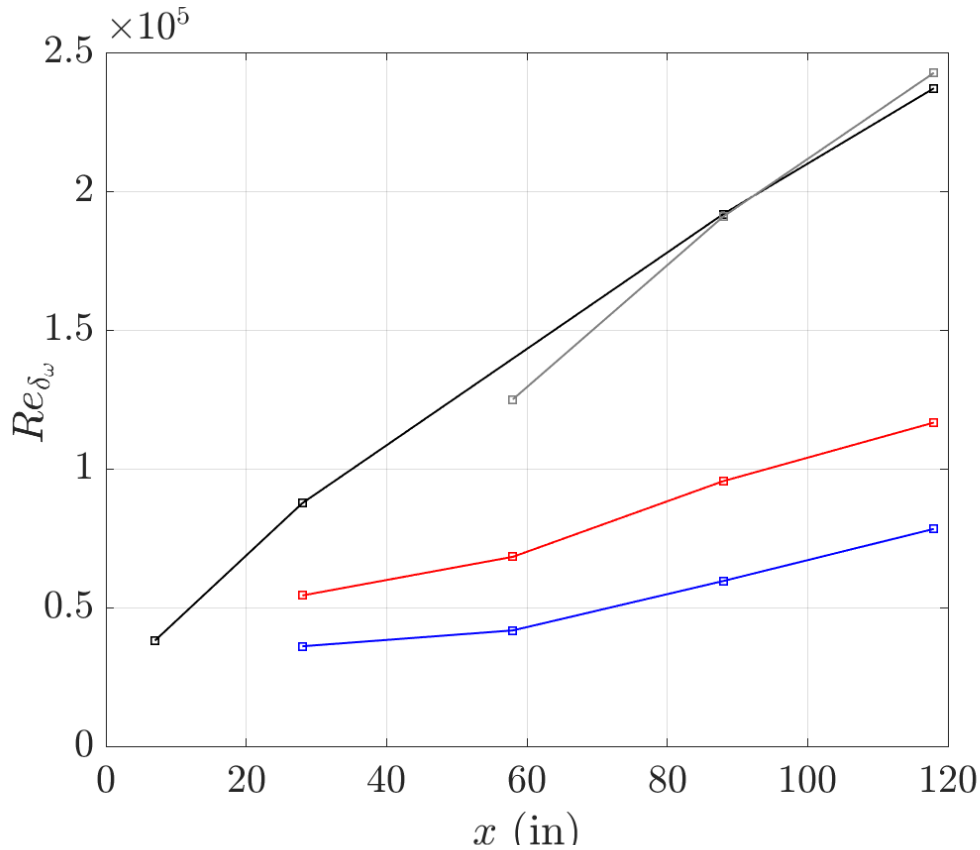


Figure 3.33: The Reynolds number as a function of downstream distance for fully-developed, non-merging mixing layers. The black line is the dual-stream case of $r = 0.2$, the gray line is the post-merged triple stream case with $ss = 2d$ and the red and blue lines are the upper and lower pre-merged mixing layers of the triple-stream case $ss = 4d$.

Because the vorticity thickness scales approximately linearly with downstream distance (i.e. $\delta_\omega(x)$), the local Reynolds number is expected to increase linearly with x . The Reynolds number plotted as a function of downstream distance is given in fig. 3.33. The Reynolds number is well above (oftentimes an order of magnitude higher than) the aforementioned mixing criteria for every data set within the testing domain between $x = 28$ inches and $x = 118$ inches for every mixing layer case presented herein. Even for the traverse taken near the fan outlet plane at $x = 7$ inches is the Reynolds number comfortably above the criteria ($Re_{\delta_\omega} = 4 \cdot 10^4$).

3.5 Summary

This chapter introduced the flow evolutions of dual- and triple-stream mixing layers initiated across a multi-source wind tunnel without the use of a splitterplate geometry. The dual-stream mixing layers were determined to behave principally the same as the canonical single-source splitterplate experiments found in the literature with a noted set of nonuniformities in the outer freestreams attributed to the module geometries that smooth with downstream development. Triple-stream shear layers of varying inter-shear spacings were explored to further elucidate merging characteristics of adjacent shear layers, as this is the primary mechanism of turbulent flowfield generation for nearly every flow modality of multi-source wind tunnels (not implementing flow manipulating geometries). Careful selection of velocity ratios allowed for comparison of post-merged triple-stream mixing layers with their dual-stream counterparts. The shear layer width was accounted for by the vorticity thickness based on the maximum slope of the velocity gradient. The growth of the shear layer was tracked through spanwise traversals at four select downstream locations for velocity ratios $r = 0.2$, $r = 0.4$ such that spreading diagrams could be drawn and virtual origins geometrically determined. When the triple-stream shear layers are initially separated so as to support the evolution of two distinct mixing layers (i.e. $ss = 4d$), the analysis for conventional mixing layers applies. Near-merging and when initialized with a separation distance that does not support two distinct mixing layers (i.e. $ss = 2d$), an augmented analysis based on the parameters of either of the two outermost streams is proposed. Post-merged triple-stream mixing layers recover dual-stream mixing layer type behavior (i.e. the shear layer growth rate appears to recover to the nominal value) with the exception that the shear layer width has necessarily grown by essentially the imposed separation at the array outlet plane. Every configuration tested was determined to be well-above the mixing criteria $Re_{\delta_\omega} > 1 - 2 \times 10^4$. Each of the fully-developed, non-merging mixing layers tested in this experimental campaign is plotted in fig. 3.34. When scaled by the vorticity thickness, non-merging mixing layers have mean velocity profiles that are self-similar even though significant tunnel-related effects were observed in the freestreams. This suggests that the freestream velocity differences, when calculated from values of $\xi = (y - y_{50})/\delta_\omega \sim \pm 1$, are nearly constant with downstream development.

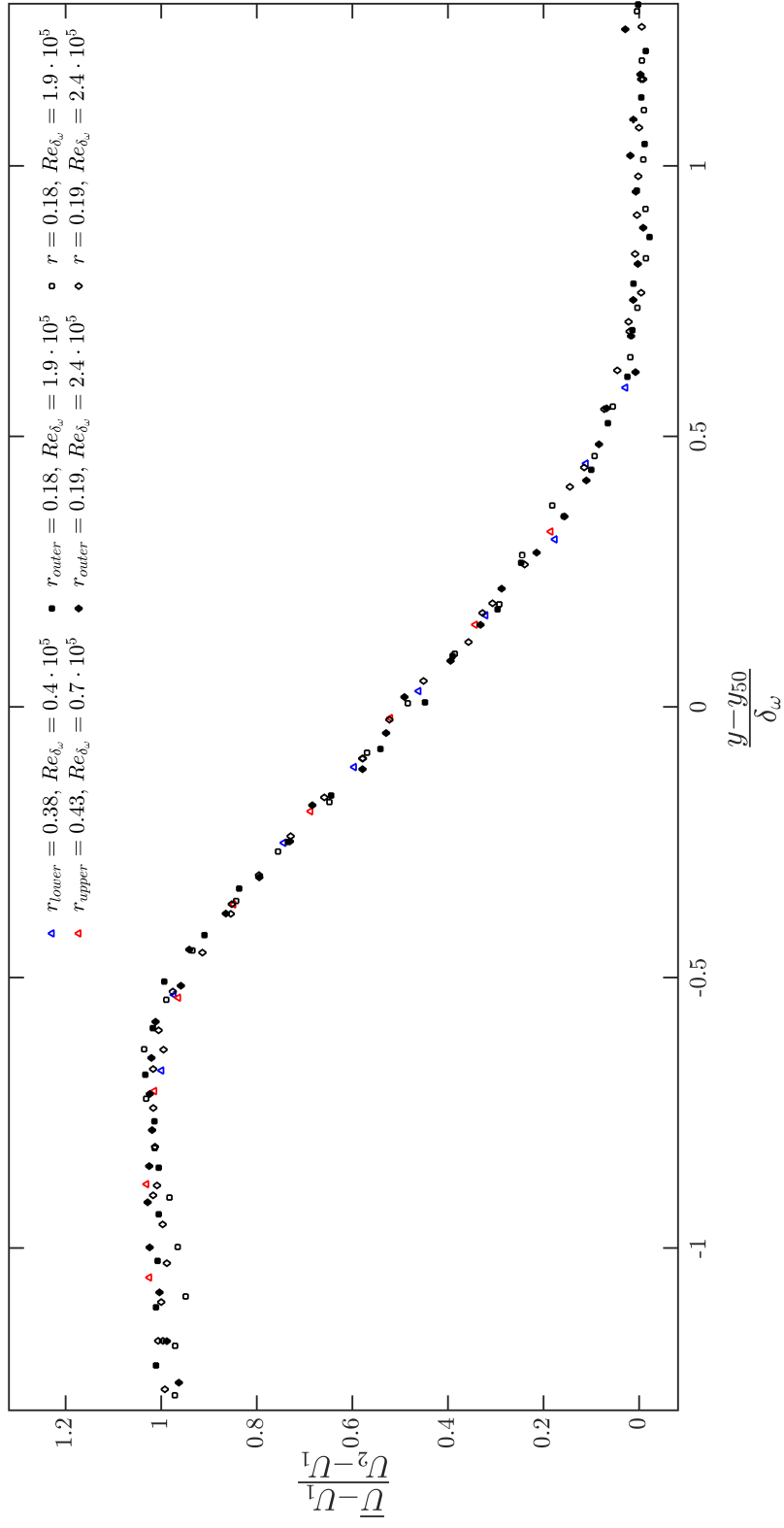


Figure 3.34: Profiles of the nondimensional mean velocity for each fully-developed, non-merging mixing layer.

*Chapter 4***THE CONTINUOUS-GUST AND QUASI-COHERENT
TURBULENT VELOCITY FIELD**

To account for the transient effects of gustiness, the random (or at least less-organized) nature of wind motions is leveraged to consider a stationary time series whose statistics can be regarded as constant and independent of the origin of time when averaged over a suitable time period (say, five minutes to an hour). With these statistics in hand, the task becomes one of simulation of suitable forcing spectra for the regions of interest during anticipated times-of-flight. That is to say that to experimentally simulate the continuous-gust turbulent velocity field a flyer is likely to experience far above, just above or at times, within the canopy layer, one must produce time records in a wind tunnel that exhibit the statistical characteristics and sequential behavior of the actual turbulence in the region during the times of flight. Because it is not currently possible to simulate the full range of relevant atmospheric motions for every stability condition in a laboratory setting, special emphasis is placed on representative energetic disturbances near the surface that overlap frequencies of note in the flyer response spectrum during the presence of a reasonably strong wind. An example of simulation of the gusty region just above the canopy top in the roughness sublayer was briefly mentioned in fig. 2.7 in the context of generation of unsteady flowfields. As will be seen, this unsteadiness calls into question the applicability of the following statistical analysis so unsteady flowfields initiated by the ‘breathing’ modality are omitted in this chapter and left to future careful study. The remaining two instances, however, will be considered in depth, namely the spectral overlap of atmospheric turbulence far above local effects in the inertial sublayer and the superimposed wake region within the canopy layer.

4.1 Turbulence-generation techniques in wind tunnels**Conventional wind tunnel turbulence-generation techniques**

Passive grid-generated turbulence remains the stalwart experimental technique to develop isotropic turbulence in a wind tunnel. The technique is considered passive insomuch as the grid acts as a geometric obstacle to the flow and is not itself vibrating, rotating, or otherwise adding mean momentum to the flow. Resulting turbulence energy decays according to the law of the so-called initial-period-of-decay that is

valid beyond the first 30 mesh lengths over a wide range of Reynolds numbers (e.g., see Loehrke and Nagib, 1972). The generated turbulence is insensitive to most grid design parameters other than solidity. Use of a contraction further showed improved isotropy (Comte-Bellot and Corrsin, 1966) and has become a staple element of closed-return wind tunnel design ever since. Passive grid-generated turbulence in conventional wind tunnels results in typical values of $Re_{\lambda_T} \sim 50 - 150$.

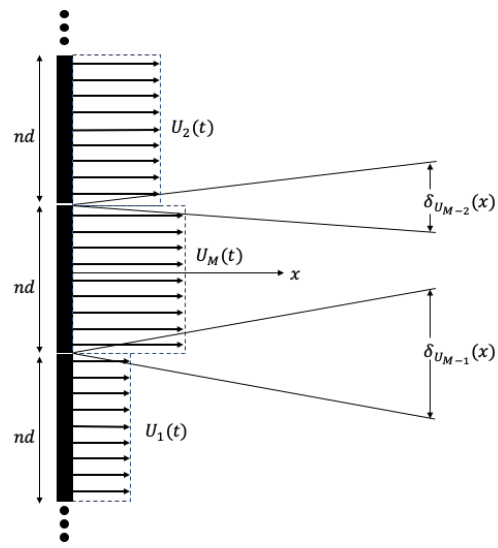
In light of the experimental findings of Sheih et al. (1971) in the ABL, a push to increase turbulence Reynolds numbers through active means was initiated by many researchers (e.g. Gad-el-Hak and Corrsin, 1974). Arguably the most successfully-implemented active turbulence generation technique in wind tunnels to-date is based on the grid design of Makita (1991), where $Re_{\lambda_T} \sim 400$ was achieved in a relatively small wind tunnel ($0.7 \times 0.7 \text{ m}^2$) with a mean velocity of 5 m/s. Roadman and Mohseni (2009, Table A1) gives a rather exhaustive list of wind- and water-tunnel-generated turbulence with both active and passive grids and a supplemental list of the various Makita-style active grids to-date is given by Hearst (2018, Table 1).

Turbulence-generation techniques using multi-source wind tunnels

Multi-source wind tunnels can generate active turbulence through shearing velocities initialized at the fan array exit plane through software-enabled reconfigurations alone¹. In the random-phase (R-P) mode, inlet conditions are initialized out-of-phase and driven sinusoidally such that velocity ratios of adjacent input increments are always changing in time and taking a pseudo-random value between zero and one. This reduces the prevalence of any specific shear-induced length scale to be encountered downstream in the measurement domain. In contrast, the quasi-grid (Q-G) configuration is presented as a static software assignment of alternating on-off patterns such that the velocity ratio at each on-off interface is always constant (and maximally one). A specific wake-like geometric length scale is introduced at the array exit plane accordingly and a shear-induced length scale may persist downstream in the measurement domain. Combinations of these techniques are also possible.

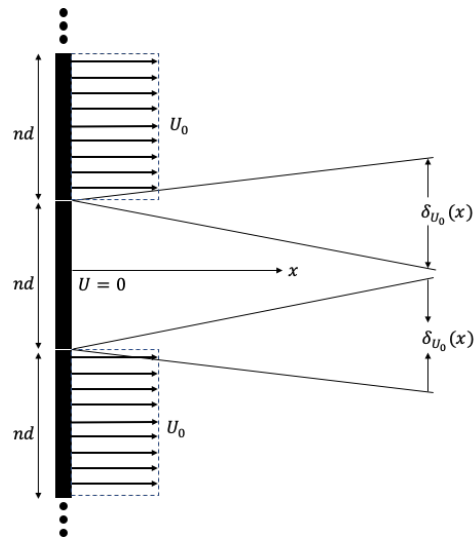
¹Of course any of the traditional geometric turbulence (hardware) augmentation techniques can be implemented instead-of or in-addition-to, but the effect of software augmentation alone on the inlet conditions is exclusively explored herein.

Random-phase (R-P) mode



$$(0 < \Delta U(t)/2\bar{U}(t) < 1)$$

Quasi-grid configuration



$$(\Delta U/2\bar{U} = C = 1, \text{ as drawn})$$

Figure 4.1: Conceptual drawing of shearing velocities initiated at the fan array exit plane.

4.2 Analysis techniques

Though a turbulent flow can vary in all three spatial dimensions in time, a one dimensional spectra is oftentimes used to describe the way in which waves, or eddies, exchange energy along the most practically measurable dimension of information. Time-based point measurements can be correlated to a time-lagged version of itself (autocorrelation) and subsequently Fourier-transformed into the frequency domain to generate a so-called one-dimensional energy spectra. Because measurements along a line cannot distinguish between wavenumber vectors aligned with the direction of measurement from those oblique to the direction of measurement, wavenumbers higher than a given wavenumber value $k/2\pi = f/\bar{u}$ contribute energy to that particular wavenumber in a process called aliasing. Thus, there presents a finite energy value at $k = 0$ proportional to an integral length scale L_{11} in a one-dimensional energy spectra when physically there should be no energy at this value. For a quasi-steady velocity field, the contribution from all frequencies to the one-dimensional energy spectrum sums to the total energy, given as a constant average value satisfying the condition:

$$\int_0^{\infty} E_{11}(f) df = \overline{u'^2} \quad (4.1)$$

where $E_{11}(f)$ describes the fluctuating energy of the u-component of motion per unit frequency at the frequency f . Because energy spans over a broad range of scales for atmospheric flows, it is customary to plot the abscissa of the spectra on a logarithmic scale. By using the relation

$$\int_0^{\infty} E_{11}(f) df = \int_0^{\infty} f \cdot E_{11}(f) d\ln(f) \quad (4.2)$$

spectra plotted as $fE_{11}(f)$ vs $\ln(f)$ preserves the relation that the area under the curve represents variance of energy, as in eq. (4.1), and further preserves its magnitude when converting from the frequency domain to the wavenumber domain when Taylor's hypothesis holds, since $fE_{11}(f) = kE_{11}(k)$. Where temporal wind records are characterized by a time-varying mean velocity, length scale statistics are omitted and left to future careful study. For the temporal wind records with rather steady mean velocities generated herein, Taylor's hypothesis is deemed reasonable, and the Taylor microscale, is calculated from:

$$\lambda_T^2 = \frac{\overline{u'^2} u'^2}{\left(\frac{\partial u}{\partial t}\right)^2} \quad (4.3)$$

The frequencies of interest

Given the inherent variability of the flow regimes that are candidates for simulation, it is useful to set functional limits ranged upon the frequencies of interest. Panofsky and McCormick (1954), using time series measured at $z = 100$ m at the Brookhaven National Laboratory site that would later be used to generate the spectrum of fig. 1.7, gives a conservative estimate that at frequencies on the order of about 1 Hz and greater, the spectral intensity does not depend on radiation intensity but is proportional to the square of the mean wind speed. The explicit threshold provided (a reduced frequency of $fz/\bar{u} < 0.6$) suggests convection may only play an important role in the production of eddies with periods of about 30 seconds and longer ($f \approx 0.03$ Hz and lower). As such, any forcing function with forcing frequencies less than $f_f = 0.05$ Hz will not be considered as a suitable candidate for mechanical-type turbulence simulation and are thus excluded. A further narrowing of frequencies of interest above canopies is possible if we are to consider, as an example, a canopy with average roughness element height of, say, 25 m within a 500 m neutrally-stratified boundary layer depth. The wind tunnel studies referenced in section 1.6 suggest longitudinal length scales ranging from order 10^0 m to 10^1 m based on $H = 25$ m. For nominal mean velocities of reasonably strong winds, then the frequencies of peak energy would fall within the range of $0.1 < f_p < 0.5$ Hz. Any forcing function initiated discretely in time intending to simulate an unsteady gusty environment will be limited to this range.

4.3 Experimental simulation results and discussion

Spectral results for the many candidate turbulent flowfields tested are provided in the dimensional frequency domain. Those with steady mean velocity are further analyzed in the wavenumber domain. This phase of experimentation focused on the great many combinations of flowfield inputs available through software augmentation, and as such one single-wire hotwire testing apparatus was fixed along the centerline at $x/d \sim 30$ ($x/nd = x/L \sim 0.8125, n = 36$), sampling at 2 kHz for either 32 or 64 seconds per experiment. Streamwise and spanwise traversals are set for future work, so no direct statement of homogeneity is provided at this time.

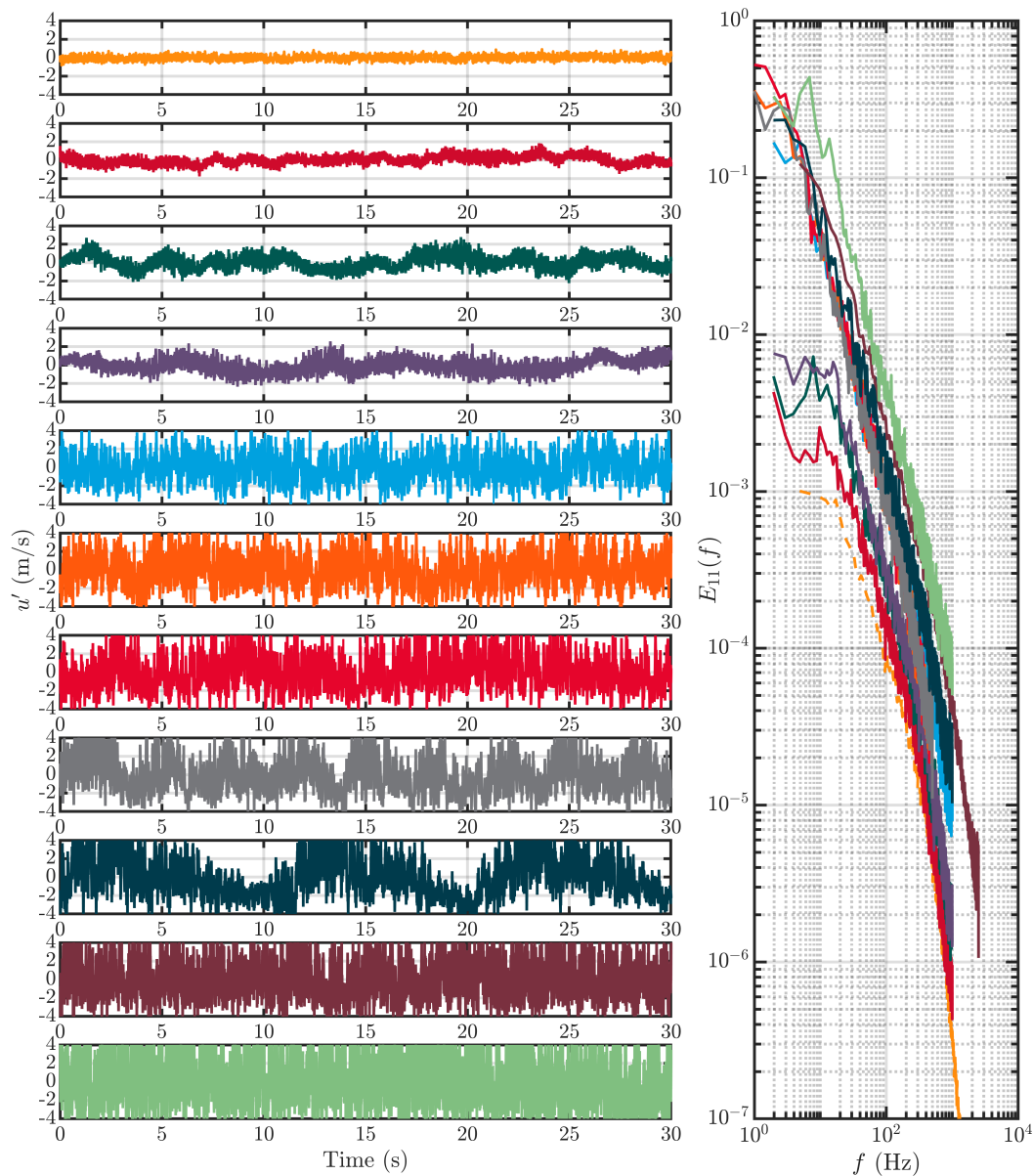


Figure 4.2: Fluctuating component time series and corresponding u -spectra in the frequency domain for the measured turbulent flowfields.

Results - random-phase and quasi-grid

Figure 4.3 showcases the u -spectra of a selection of measured flowfields with steady mean velocity profiles. The uniform turbulent flowfield generated when all fans are specified to the same input condition (i.e. the uniform flow modality) is considered to be the baseline flowfield and is drawn as dashed when included. The Taylor

microscale Reynolds number for this baseline case is $Re_{\lambda_T} = 135$, which falls within range of typical passive grid-generated wind tunnel turbulence, and decays with downstream evolution according to fig. A.5 and fig. A.10. A range of $500 \lesssim Re_{\lambda_T} \lesssim 900$ is achieved by activating the random-phase (R-P) mode to the baseline case, where the mean velocity is maintained at $\bar{u} = 8.1 \pm 0.3$ m/s, and the turbulence intensity increases from $TI = 5.4\%$, 8.3% , 9.6% for a commanded 30% , 50% , 90% allowable ranged fluctuation amplitude away from the prescribed mean velocity input, respectively. A near doubling of Re_{λ_T} is achieved by spatially partitioning the array into a so-called quasi-grid (Q-G) configuration. Intergrid spacing is initialized with $l_g = nd = 0.320$ m ($n = 4$) in each direction (i.e. adjacent 4×4 blocks of fans alternate on-off-on-off in a gridded manner), resulting in a ratio of deactivated module area to total fan array area, or effective solidity, of $\varphi = 69.1\%$.

Discussion - turbulence generation by shearing

Though the mechanisms of the generation of turbulence effect the nature of the spectra of a flowfield in the low-wavenumber regions, the phenomenological theory put forth by Kolmogorov (1941) presumes that the behavior of the scale motions over an intermediate range of scales in the inertial subrange smaller than the largest eddy length scale but larger than the dissipation length scale η is governed by a constant dissipation rate with a spectrum of the shape $E(k) = C_k \epsilon^{2/3} k^{-5/3}$, assumed universal, and well supported through myriad experimental results. This so-called $-5/3$ behavior, shorthand for $k^{-5/3}$ behavior, can be observed at-a-glance in the frequency domain in fig. 4.2b and wavenumber domain in fig. 4.3a in the candidate measured flowfields. A more rigorous analysis is undertaken by premultiplying the shapes of the u -spectra in ways that better highlight the nature of the distinct regions in the energy cascade. In fig. 4.3b, the u -spectra is premultiplied by dissipation scales and normalized by η to highlight collapse in the high wavenumber regions. This representation is useful in clearly separating the scales in the low-wavenumber domain, where it can be seen that the relative effect of increasing Re_{λ_T} dilates the $-5/3$ region through increased energy transport in the larger eddies of the flow.

The mechanism of generating the relatively large turbulent fluctuations in the flowfields presented herein is accomplished through high local shear rates at the fan array exit plane, particularly evident in the quasi-grid configuration, but also present in the random-phase mode. For turbulent shear flowfields with high local shear rates, the structure of the turbulence exhibits anisotropic tendencies in the direction of downstream evolution. It is useful to capture the principle effects of the mean

shear deformation on the large scale eddies due to the mean velocity gradient. This is accomplished by considering the ratio of the timescales of the small scale turbulent motions to the large eddy mean deformation timescale, as in Lee et al. (1990), which defines a dimensionless shear-rate parameter $S^* = Sq^2/\epsilon$, with $q^2 = u'^2$ and $S = \partial\bar{u}/\partial y$. When displayed in the compensated form of fig. 4.3c (i.e. premultiplied by $\epsilon^{-2/3}(kS^*)^{5/3}$ and plotted in the kS^* domain), the inertial subrange should present horizontally. In this representation it is most readily made apparent the increased subinertial range on account of the increased mean velocity gradients. The two groupings in fig. 4.3c correspond to the R-P mode (lower grouping) and Q-G configuration (upper grouping) and reflect the differences in velocity ratios between adjacent inlet conditions that generate the principle shear layers, as diagrammed in fig. 4.1.

With this picture in mind, the quasi-grid configuration essentially initializes single-stream mixing layers about every edge of the on-off static reconfigurations that evolve and merge with downstream development, likely introducing a spanwise peaked velocity distribution similar to that observed in the freestreams of the mixing layers of Chapter III. Unlike the planar mixing layers with imposed spanwise coherence along the width of the fan array apparatus however, the quasi-grid distribution is broken up along the width and height of the array (symmetrically in this case) and thus introduces three-dimensionality while still maintaining discrete wake-like geometric separations at flow initiation. This is what is meant by a quasi-coherent flow modality. The random-phase configuration, in contrast, allows for temporally-changing inlet conditions at whatever resolution selected. In this way, it is a perturbation technique applicable to any such mean velocity profile that was activated, in this case, at a per-fan basis of a uniform flow modality. Because any given ranged fan input command is phased randomly to its neighbors, velocity differences between adjacent fans are rarely maximum (as in the Q-G case) or zero (adjacent fans of the same velocity) but occupy values in-between according to a Gaussian-like distribution set through software. If the targeted mean velocity is selected to be center of the allowable range, then the bias toward the centered velocities allows for good mean velocity tracking with fluctuations that have no preferred frequency scale. This is what is meant by a pseudo-random flow modality that distributes energy broadly amongst the scales.

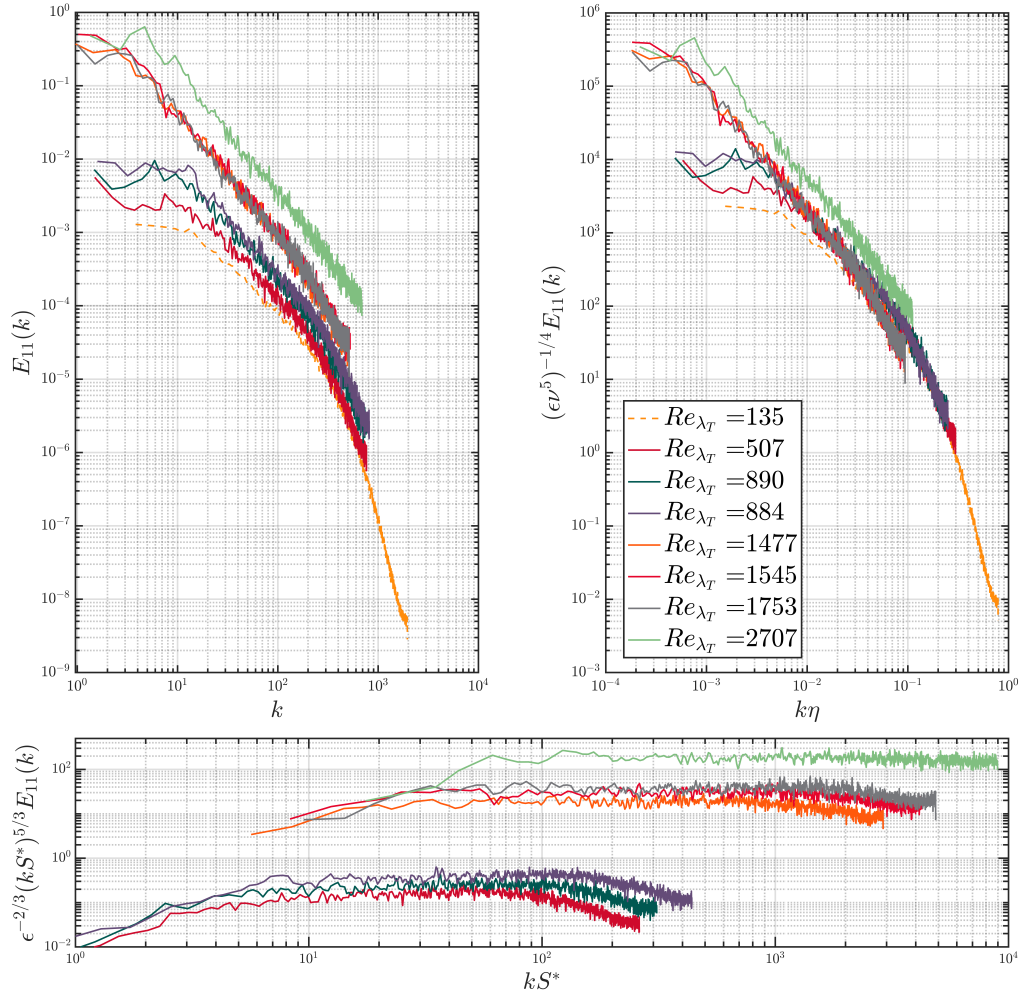


Figure 4.3: The longitudinal velocity (u) spectra with various scalings. The topmost-left is the dimensional u -spectra in the wavenumber domain. The topmost right u -spectra is compensated (pre-multiplied) using the dissipative (Kolmogorov) scales. The bottommost u -spectra is compensated (pre-multiplied) using inertial subrange scales. The Taylor Reynolds number ranges from $Re_{\lambda_T} = 135$ (the baseline uniform case, dashed, with $U = 8.0$ m/s, $TI = 2.7\%$) to $Re_{\lambda_T} = 2707$ (quasi-grid with $U = 9.1$ m/s, $TI = 26.9\%$).

4.4 Summary

In this chapter, turbulence generation techniques based on shearing velocities phased randomly (R-P) and distributed in a grid-like manner (Q-G) are explored in some depth. Based on the results of fig. 4.3 and fig. C.1, the R-P configuration appears to be a good candidate for the generation of pseudo-random atmospheric-like turbulence (of a relevant turbulence intensity) found in the ISL in the frequency range comprising the spectral overlap for flyers of interest. The quasi-grid (Q-G) configuration introduces static initial shear layer conditions (by virtue of forcing a geometric separation at the exit plane) that evolve shear layers into a superimposed three-dimensional wake-like flowfield. Though no statement on spatial structure can be provided at this time, significant increases in velocity fluctuations of the quasi-coherent flow modality at the single-point measurement location compared to the pseudo-random flow modality are noted, as is evident from the values of Re_{λ_T} which were reported as high as $Re_{\lambda_T} \sim 2700$ for the (Q-G) case and ranged from $500 \lesssim Re_{\lambda_T} \lesssim 900$ for the (R-P) case. It can be said that the quasi-coherent flow modality effectively increases u' at the likely expense of flow uniformity through the coarsening static reconfiguration of initial fan RPM distribution. Though no traversals have been reported, one can imagine a significant wave-like appearance to the velocity profiles along the transverse planes not unlike what is observed in the freestream of the mixing layers due to the module geometry funneling effect discussed in Chapter III. These flowfields at the single point measured behave locally isotropically and a general trend of increasing turbulence intensity within groupings is also observed to further dilate the subinertial range. The largest subinertial range is nearly two decades when $Re_{\lambda_T} \sim 2700$, thus confirming that turbulence generated from increased local mean velocity gradients is an effective technique to increase Re_{λ_T} . A more quantitative statistical analysis that promotes comparison of the many flow modalities so far introduced is undertaken next in Chapter V.

Chapter 5

SUMMARY OF RESULTS AND A WAY FORWARD

Four primary flow modalities of multi-source wind tunnels have been discussed throughout this dissertation. In Chapter II, extensive visualizations of the uniform flow modality are introduced and serve as a baseline of comparison for the generation techniques to follow. In Chapter III, the generation of mixing layers through software partitioning was explored and the basic structure of dual- and triple-stream shear layers initiated across multi-source wind tunnels without the use of a splitterplate was established. Chapter IV marked the exploration of pseudo-random and quasi-coherent flowfields through the random-phase (R-P) and quasi-grid (Q-G) turbulence generation techniques, respectively. The fundamental objective of this work, indeed, is the experimental simulation of atmospheric-like disturbances, both continuous and discrete, from the perspective of the flyer near the surface in the presence of a reasonably strong wind. The suitability of the flowfields generated by multi-source wind tunnels as representative environmental forcing spectra were discussed in some depth and can be summarized by their research potential as:

- **Uniform flow** - a ‘passive’ grid-like turbulence useful for the study of classical (isotropic) turbulence with nominal $Re_{\lambda_T} = 135$, representing the baseline ‘conventional’ wind tunnel flow modality
- **Shearing flow** - splitterplate-less mixing layer(s) with locally isotropic turbulence in the layer interior with Re_{δ_ω} ranging from 4×10^4 to 4×10^5 ; a candidate experimental discrete gust forcing function provided the shear layer dynamics are decoupled from the flyer response dynamics as the flyer passes through
- **Pseudo-random flow** - random fluctuations about a targeted mean velocity with varying deviation amplitude that result in $500 \lesssim Re_{\lambda_T} \lesssim 900$, a good candidate for environmental forcing experienced far above local effects in the inertial sublayer (ISL)
- **Quasi-coherent flow** - more information regarding the spatial structure of these flowfields is warranted but can preliminarily be considered as a ‘greater-

diameter' grid-like turbulence that generates a superimposed wake-like flow-field within the measurement domain with Re_{λ_T} routinely order 10^3 at relevant mean velocities, a principle development toward within-canopy type environmental forcing

Projecting forward, combinations of the above flow modalities may further unlock research potential (e.g. see appendix D for a preliminary overview of combining the shearing and pseudo-random flow modalities), but given the expansiveness of potential combinations afforded, candidate flowfields can only be systematically considered if an appropriate comparison framework is first established. Significant emphasis has been placed toward a spectral view, since the focus of testing narrows toward the energetic overlaps of the forcing spectrum and the natural modes of the flyers which can straightforwardly be analyzed through the energy spectrum. It is thus desirable for comparisons to be facilitated through a consistent spectral view for each of the flow modalities enabled through multi-source wind tunnels.

5.1 A framework for comparison

Though the flow types thus explored are markedly different, in any conceivable scenario of note, the flowfield encountered by the flyer is nearly always a high Reynolds number (high-Re) turbulent flowfield. It is this reality that enables a binding framework of comparison to be established. A quantitative definition of 'high-Re' is first given followed by a means with which to connect turbulence characteristics (i.e. representative length scales) to shearing velocity parameters, a useful scaling transformation considering that each of the flow modalities leverages shearing velocities of some kind at the array outlet to generate turbulent flowfields. A normalized spectral representation is then proposed as a quantitative metric to observe how the energy of the flowfield distributes amongst the frequency scales for the various flow modalities. Based on this spectral view, a few primary comparisons are discussed.

Fully-developed (post-transition) turbulence

The mixing transition criteria (Dimotakis, 2000) introduced in Chapter III, whereby the quality of the turbulence is observably different below and beyond, is restated here to serve as a quantitative definition for a sustained fully-developed turbulent flow field, or as a shorthand, a high-Re flow. For flowfields with appropriate outer scales, a high-Re flow must necessarily be, based on a bevy of experimental observation

for many different flow geometries,

$$Re = \frac{U\delta}{\nu} > 1 - 2 \times 10^4 \quad (5.1)$$

where U and δ are local values of the characteristic velocity that drive the turbulence in a flowfield of transverse extent, respectively. The Reynolds number for a region of the flowfield driven by a (constant) shearing velocity difference $\Delta U = U_2 - U_1$ across a transverse extent $\delta(x)$, as in the mixing layer cases, is defined then by

$$Re_{\Delta U} = \frac{\Delta U \cdot \delta(x)}{\nu} \quad (5.2)$$

For flow fields with no obvious or appropriate outer scales, the mixing transition criteria is defined by the Taylor microscale, λ_T , and the root mean square of the fluctuating velocity u' as:

$$Re_{\lambda_T} \equiv \frac{u'\lambda_T}{\nu} > 100 - 150 \quad (5.3)$$

Reynolds numbers exceeding these criteria are considered fully-developed, post-mixing-transition turbulent flow fields, or high-Re flows.

Indeed the notion of eddies of varying sizes within a turbulent flowfield is conceptualized from the picture of the turbulence cascade for fully-developed turbulence (stated generally as $Re_{\Delta U} \gg 1$ when derived). The three length scales of a turbulent velocity field describe eddies of the order of the shearing velocity transverse extent, eddies so small that viscosity dissipates energy as heat, and an intermediate range of eddies that transfers energy between the two, with each eddy convected by the local velocity vector. The dynamics of the energy-accepting larger scale eddies, denoted by extent λ_δ (which are of the order $\lambda_\delta \sim \delta$) are understood to essentially be inviscid. Thus, the rate at which these larger scale eddies acquire energy from the shearing velocity does not depend on viscosity, an idea first put forth by Taylor (1935). The energy is cascaded to smaller and smaller eddies under the influence of the strain field until they reach a small enough size for the effects of viscosity to dissipate the energy as heat. The smallest eddy scale, referred to as the Kolmogorov viscous scale, denoted λ_ν , acts as a limiting scale for the inviscid processes. Building on Taylor's ideas of inviscid scaling of larger eddies, Kolmogorov (1941) extended this rationale to eddies of size λ that are smaller than δ but still large enough such that their local eddy Reynolds number

$$Re_\lambda = \frac{u_\lambda \cdot \lambda}{\nu} \quad (5.4)$$

with a characteristic velocity u_λ associated with an eddy of extent λ is still larger than unity. Assuming that little to no energy is lost when transferring between ranges of inviscid eddies (i.e. the energy dissipation rate ε is constant), then

$$\varepsilon \sim \frac{u_\lambda^3}{\lambda} \approx \frac{\Delta U^3}{\delta} \quad (5.5)$$

is a useful approximation of an eddy of scale λ very nearly the size of the largest eddy δ . Plugging this approximation into eq. (5.4) and rearranging gives a relationship between the local eddy Reynolds number Re_λ and the turbulent shear flow Reynolds number as

$$Re_\lambda = Re_{\Delta U} \cdot \left(\frac{\lambda}{\delta}\right)^{4/3} \quad (5.6)$$

A threshold whereby viscosity can no longer be ignored would occur when the Reynolds number associated with a particular eddy is of order unity, i.e., $Re_\lambda = 1$. This occurs at eddies of scale λ_v whereby ?? gives under this condition

$$\frac{\lambda_v}{\delta} = Re_{\Delta U}^{-3/4} \quad (5.7)$$

The in-between characteristic length scale can further be defined for isotropic flow, whereby the dissipation rate ε and the volume-averaged velocity fluctuations u' are related by

$$\varepsilon = \frac{15\nu}{\lambda_T^2} u'^2 \quad (5.8)$$

where λ_T is the so-called Taylor microscale. With the ratio $u'^2/\Delta U^2$ constant for a fully developed turbulent flowfield due to a shearing velocity (see e.g. fig. 3.20 and fig. 3.21 to evaluate how well this assumption holds for multi-source-generated experimental shear layers), and assuming the dissipation rate ε scales with $\Delta U^3/\delta$ according to eq. (5.5), then Eq. eq. (5.8) can be rearranged to give a relationship between the length scale characteristic of the largest eddies δ , the length scale characteristic of the intermediate eddies λ_T and the Reynolds number defined for the region of the flowfield driven by a shearing velocity $Re_{\Delta U}$ as

$$\frac{\lambda_T}{\delta} = \gamma \cdot Re_{\Delta U}^{-1/2} \quad (5.9)$$

where γ is a constant of the flow.

The three length scales of a turbulent flowfield can then conveniently be expressed by the scaling relationships as follows

- The large eddy scale, $\lambda_\delta \sim \delta$

- The Taylor microscale, $\lambda_T \sim \delta \cdot Re_{\Delta U}^{-1/2}$
- The Kolmogorov scale, $\lambda_v \sim \delta \cdot Re_{\Delta U}^{-3/4}$

Moving amongst the scales

Each of these flow modalities as presented is united under the banner of high-Re flows and as such manifests a power-law regime of slope $\approx -5/3$ in the energy spectrum that should broaden with increasing Reynolds number. As will be made clear in subsequent analysis, it is useful to normalize eq. (4.1) by the total energy to give a fractional representation of the u-component energy per unit frequency at f as:

$$\int_0^{\infty} F_{11}(f) df = 1 \quad (5.10)$$

where $F_{11}(f) = E_{11}(f)/\overline{u'^2}$ and $F_{11}(f) \cdot df$ represents the fraction of the energy in the interval df at f . In this way, if the energy of the fluctuating components in the flow contains mostly large eddies, $F_{11}(f)$ will exist mainly in the region of low frequencies. If the energy of the fluctuating components in the flow contains mostly smaller eddies prone to dissipation, $F_{11}(f)$ will exist mainly in the region of high frequencies.

A useful comparison of the distribution of energy amongst the scales of various high-Re flows can be made through use of Raichlens criteria (Raichlen, 1967). In the normalized form of eq. (5.10), Raichlen proposed a demarcation of the particular frequency f_{50} at which exactly 50% of the energy of the fluctuating components is found above and below this value:

$$\int_0^{f_{50}} F_{11}(f) df + \int_{f_{50}}^{\infty} F_{11}(f) df = 0.5 + 0.5 \quad (5.11)$$

so that

$$\int_0^{f_{50}} F_{11}(f) df = 0.5 \quad (5.12)$$

Equation (5.12) is a useful criteria insomuch as this characteristic frequency has been observed to closely align with the transition from the large-scale energy region to the subinertial range (e.g., see Spencer, 1970, for the dual-stream mixing layer case) without reliance solely on sparsely collected data in the lower resolution region as $f \rightarrow 0$. Any such percentage can be targeted and found straightforwardly with numerical integration provided eq. (5.10) is (nearly) satisfied. A finite sampling

rate with data resolved according to Nyquist's criteria precludes characterizing energy contributions approaching infinity, though high frequency small eddy energy contributions are typically some four orders of magnitude or lesser than the large-scale energy accepting eddies found predominantly in the region $f < f_{50}$.

A criteria for the dissipative scales can likewise be determined. Hinze (1975) gives a spectral estimate of the Taylor microscale λ_{T_s} based on Taylor's hypothesis as

$$\frac{1}{\lambda_{T_s}^2} = \frac{2\pi^2}{U^2} \int_0^\infty f^2 F_{11}(f) df \quad (5.13)$$

Similar to the 50% criteria put forth to demarcate a 'beginning' of the inertial subrange, an estimate for the 'end' of the inertial subrange is made using the integral of eq. (5.13) as representation of the dissipative scale motion, so that

$$0.1 = \frac{2\pi^2 \lambda_{T_s}^2}{U^2} \int_0^{df_{10}} f^2 F_{11}(f) df \quad (5.14)$$

where df_{10} represents the dissipation frequency at which 90% of dissipative energy is found above this value (i.e. 10% is found below). If it is presumed that in some way the frequency df_{10} in eq. (5.14) demarcates frequencies above which energy contributes predominantly to dissipation processes for any given recorded observation (based on the notion that the Taylor microscale itself marks the length scale below which viscosity significantly affects the dynamics of the turbulent eddies), then a heuristic check of the validity of a fully-developed high-Re assumption can straightforwardly be made by looking for sufficient separation between energy-accepting and dissipative scales in the normalized spectral view. A [90% ←||→ 10%] demarcation at the frequency f_{90} can be used to mark an 'end' of a region where 90% of the total fluctuating energy resides. The [10% ←||→ 90%] demarcation at df_{10} is used to mark the 'start' of the dissipation contributing frequencies. Determination of these threshold frequencies partially reflects the choice of sampling frequency, as anything above the Nyquist frequency is susceptible to aliasing. If the two regions marked in this way are widely separated with no appreciable overlap, then an intermediate range of eddies is likely supported and statistical treatments that rely upon local isotropy are considered to be justified.

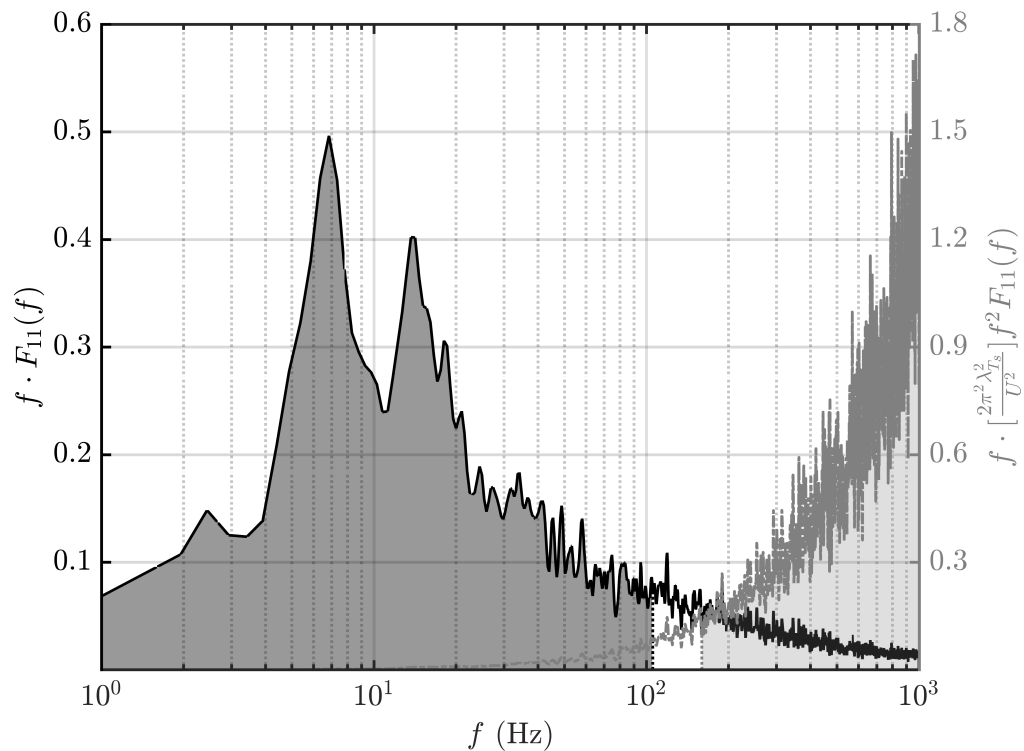


Figure 5.1: Normalized energy spectrum plotted in an area-preserved manner highlighting two separate and non-overlapping regions. The leftmost region demarcates the frequencies that contribute 90% of the total fluctuation energy (from $f \rightarrow 0$ to f_{90}) and the rightmost region reflects the frequencies that account for 90% of the energetic contribution to dissipative processes (from df_{10} to $f_s/2$, where f_s is the sampling rate).

Interpreting with caution

With these analysis techniques now established, comparisons between primary flow modalities can cautiously be made. Because shearing velocities initiated at the fan array outlet plane are the primary mechanism by which the turbulent flowfields evolve, greater focus has been placed on the nearly inviscid dynamics of the large energy-accepting eddies. However, as previously shown, advantages in analysis emerge when considering the cascade of energy through the intermediate range of eddies down to the dissipative scales. Canonical treatments used to fit a form of the energy spectrum based on the $-5/3$ behavior of the intermediate range, though useful, presume a single length scale attributed to the large energy-accepting eddies. Noticeable multi-scale behavior is present, for example, in the quasi-grid (Q-G)

initiated flowfield of fig. 5.1 and scaling techniques presuming a primary time or length scale are likely to miss (i.e. smooth) the discrete contributions of the forced (and not necessarily equal) intergrid spacings.

Further care must be exercised for instances when a frequency component with a period longer than the record length is present, as the presence of a ‘trend’ in the time series renders the data nonstationary. Trend removal is beyond the scope of discussion, but suffice to say that selection of relatively short record lengths ($T = 32\text{s}$ or 64s) and limitation of the range of forcing frequencies to $f_p > 0.05$ Hz eliminates all long-lasting trends except that of the purely sinusoidal flowfields of the ‘breathing’ modality (which have been omitted and left to future careful study). Flow-induced oscillations from the quasi-coherent evolutions of the coarsening grid-like RPM distributions, though in some cases discretely energetic, are not considered ‘trends’ in the sense previously described and are thus included when calculating $\overline{u'^2}$. This reflects the notion that natural shear layer evolutions discretely separated at initiation and their subsequent downstream mergings are considered fundamentally differently than are artificially forced input oscillations of a ‘breathing’ modality. The pseudo-random flows initiated by the random-phase (R-P) algorithm conceptually represent something sitting in-between the aforementioned, but the results in appendix C support that energy is added broadly across frequency scales with no preference toward any obvious (discrete) frequency thus contributing to u' and included in the calculation of $\overline{u'^2}$, when applicable.

It is perhaps a bit clearer now, with these cautions made explicit, the appeal of a statistical metric that does not presume a certain form of the correlation function(s) in the low-wavenumber regions. The spectral representation of the dissipative scales in eq. (5.13), unlike eq. (5.12), does assume a form, but its application is limited to the range of scales well-supported to behave universally with a constant dissipation rate and is merely used as a ‘sanity-check’ for the separation of scales assumed for high-Re flows. More central to this analysis are characteristic time and length scales associated with the various inviscid flow dynamics enabled through the multi-sourcedness of the fan array. In general, homogenous and isotropic assumptions are required to express measured Eulerian turbulence characteristics in some physically meaningful way. Of course an incompressible turbulent shear flow subjected to a mean deformation rate, as in the mixing layer case, is very much so anisotropic with a continuous production of turbulence due to the mean shear. Likewise Taylor’s

hypothesis regarding the spatial structure of turbulence essentially remaining unchanged when carried along by a mean velocity must be carefully considered when neither the main flow is uniform nor the level of turbulence low. The applicability of Kolmogorov's and Taylor's hypotheses for a shear flow were explored by Hinze (1975) and Lin (1953), respectively. Their findings can be summarized in terms of time scales present in the flow. When the time-scale of the changes of the statistical parameters are small compared to the time-scale of the turbulent fluctuations and when the main motion is steady (i.e. without 'trends'), averages taken with respect to time can be justified if the production of energy nearly compensates for its dissipation. According to Lin's criteria, Taylor's hypothesis is valid for shear flows when

$$f \gg \frac{1}{2\pi} \frac{\Delta U}{\delta_\omega} \quad (5.15)$$

providing further justification of the universality of the turbulence cascade beyond the inviscid region. What remains, then, is classification of the large energy-accepting regions which will be accomplished through use of the semi-arbitrary frequency threshold f_{50} . An estimate of the integral length scale in the longitudinal direction is calculated from

$$Lu_x = \frac{1}{2\pi} \frac{U_c}{f_{50}} \quad (5.16)$$

where U_c is the convective velocity of the initial shear layer(s) at the fan array outlet plane taken roughly equivalent to the average of the two outer streams (or wake/non-wake regions).

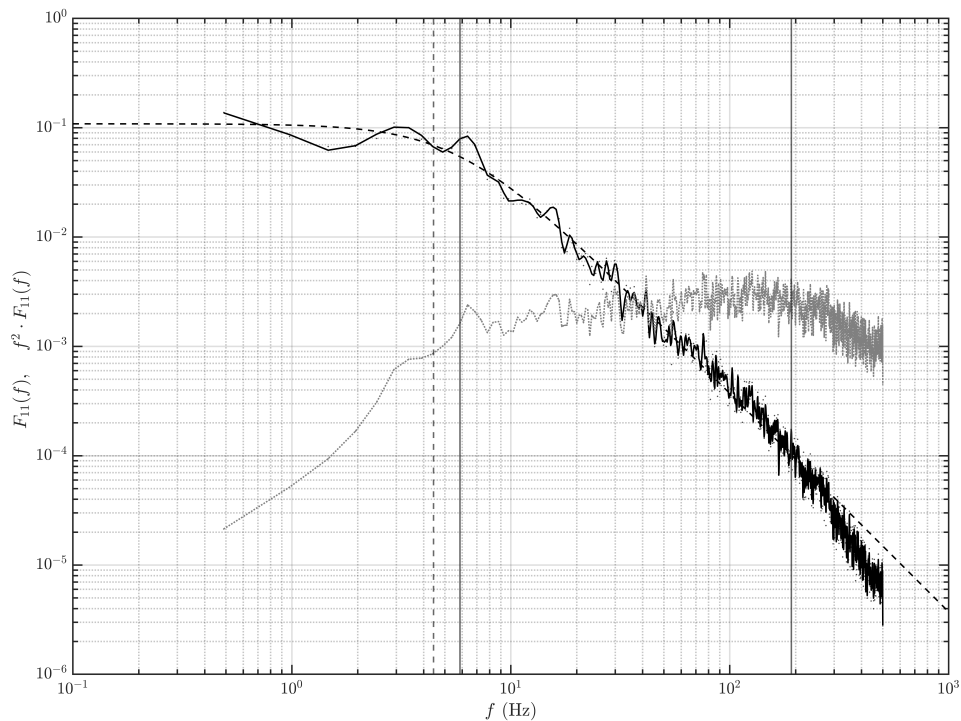


Figure 5.2: Normalized energy spectrum for $r = 0.2$ along the centerline at $x = 118$ inches. The dashed vertical line marks the frequency of validity according to Lin's criteria. The left-most solid vertical line marks the Raichlen criteria of f_{50} and gives a reasonable estimate of the beginning of the $-5/3$ roll-off. The right-most solid vertical line marks df_{10} and reasonably divides the frequency at which the slope steepens away in the dissipative range. The theoretical fit is of a form proposed by Dryden.

5.2 Comparisons

General behaviors amongst the modalities are now considered by comparing the statistical markers derived from the normalized spectral view. A representative example is provided in fig. 5.3 through comparison of the uniform flow modality, quasi-grid flow modality, and the centerline of a dual-stream mixing layer in the wavenumber domain.

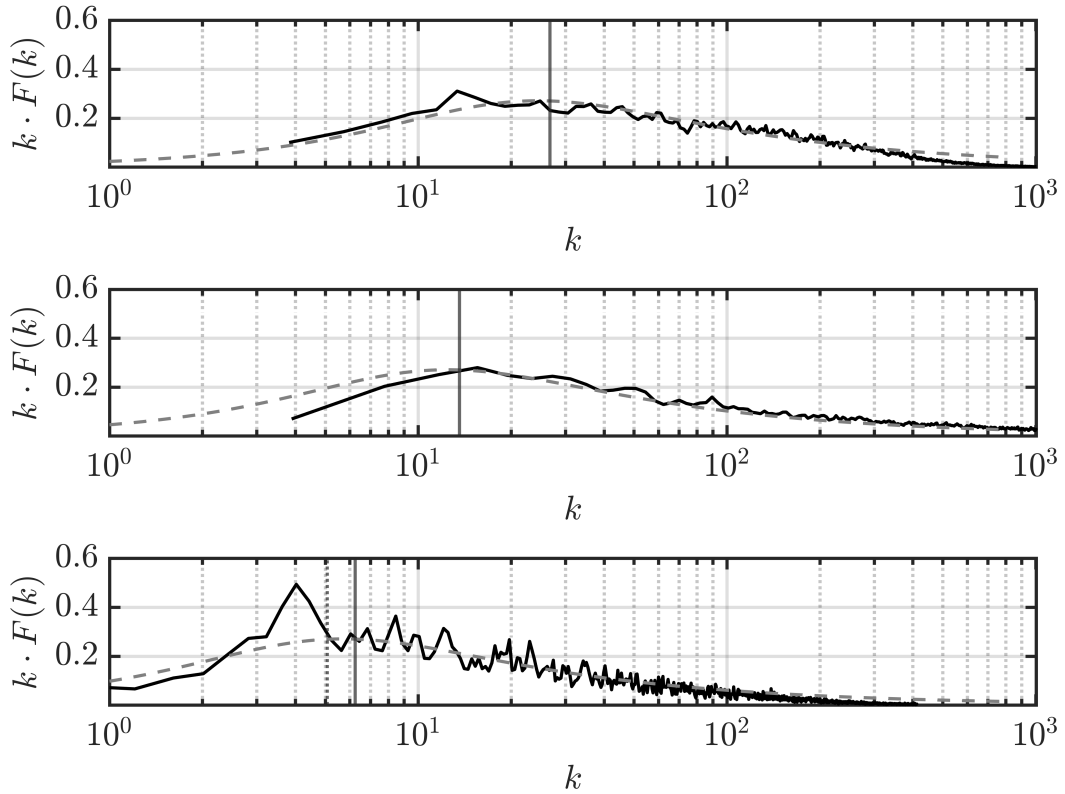


Figure 5.3: Normalized energy spectrum for the uniform flow modality (top), the quasi-grid modality (middle), and dual-stream shear layer $r = 0.2$ along the centerline (below), each at $x/L \sim 0.75$. The solid vertical line corresponds to the wavenumber based on f_{50} . The dashed vertical line of the dual shear layer normalized energy spectrum corresponds to Lin's criteria.

The areas under the F_{11} curves integrate to unity within 5%. Various theoretical forms of the function F_{11} have been proposed, with Kolmogorov's theory for isotropic homogenous turbulence describing the cascade of energy through the dissipative scales ubiquitously used and validated for a wide range of turbulent flows. The form proposed by von Kármán in eq. (1.11) is dashed when included and is expected to be a reasonable fit beyond the criteria of eq. (5.15). The solid vertical lines of fig. 5.3 correspond to $k_{50} = 2\pi f_{50}/U_c$. The maximum linear wavelength associated with the inverse wavenumber contributing 50% of the energy is then $\Lambda_x^u = 2\pi/k_{50}$.

Table 5.1: Summary of results tabulated using Raichlen’s criteria for three different flow modalities at approximately the same measurement location.

Type	x (in)	f_{50} (Hz)	Lu_x (in)	Λ_x^u (in)
Uniform	92	34	1.5	9.3
Quasi-coherent	92	17	2.9	18.2
Dual-stream ML	88	8	6.3	39.6

With the baseline uniform flow modality statistically established in table 5.1, it is clear that the effect of coarsening the RPM distribution of the fan array outlet plane into a quasi-grid and dual-stream mixing layer shifts energy into lower wavenumbers accordingly. A module related funneling effect was discussed in detail in section 2.2 and appendix B. For the uniform flow modality, Λ_x^u is 9.3 in. (0.235 m), corresponding to the distance between module-center peaks (i.e. $3d$, $d = 0.080$ m) of the velocity profile (see fig. 2.5). Aside from this funneling effect, there is no significant ΔU at the fan array outlet plane and a canonical form of the energy spectrum yields a good fit. The module funneling effect was also noted in the outer freestreams of the mixing layers and is likely present in some form in the quasi-grid configuration (though traverses have yet been carried through to confirm).

Along the centerline interior of the dual-stream mixing layer, the dominant wavelength is expected to be the streamwise coherent structure spacing Λ_x . Using the estimate from k_{50} , values for $\Lambda_x^u/\delta_\omega$ can be calculated based on the previously presented results of Chapter III. Table 5.2 shows that the estimate of the streamwise spacing normalized by the vorticity thickness is well within the range $3.1 < \Lambda_x/\delta_\omega < 5.0$ reported in the literature for dual-stream mixing layers (Dimotakis and Brown, 1976), further lending credence to the utility of the 50% energy threshold. Interestingly, the average of f_{50} for the upper and lower triple-stream mixing layer initially separated by $ss = 4d$ and allowed to evolve is essentially the value of f_{50} calculated for the $r = 0.2$ dual-stream mixing layer, suggestive that the separated triple-stream mixing layers are energetically similar (when normalized) and redistribute energy upon merging centered about the average of their previous respective characteristic frequencies. The R-P modality appears, at first take, to be the obvious perturbation candidate when uniformity is to be maintained but significant ‘roughening’ of the flow is enabled through static reconfiguration (i.e. ‘coarsening’) of the RPM input distribution and this yields significant increases in the fluctuating energy. Further traverse-based testing is warranted for the quasi-coherent flow types in light of the comparison framework.

Table 5.2: Summary of results tabulated using Raichlen’s criteria for a dual-stream and triple-stream mixing layer.

r	x (in)	f_{50} (Hz)	Lu_x (in)	$\Lambda_x^u/\delta_\omega$
0.16	28	19	2.4	3.6
0.18	58	-	-	-
0.19	88	8	6.3	3.7
0.19	118	6	7.9	3.5
r_{upper}	x (in)	f_{50} (Hz)	Lu_x (in)	$\Lambda_x^u/\delta_\omega$
0.34	28	28	2.1	3.3
0.43	58	18	3.2	3.5
0.48	88	11	5.2	4.1
-	118	9	6.6	-
r_{lower}	x (in)	f_{50} (Hz)	Lu_x (in)	$\Lambda_x^u/\delta_\omega$
0.34	28	9	3.3	4.1
0.43	58	8	3.4	3.0
0.48	88	5	5.7	4.0
-	118	3	8.5	-

5.3 Concluding remarks

The qualitative behavior of the turbulence is observably different when fully-developed post-mixing-transition. For all the flow modalities thus far presented, the high-Re number criteria ($Re_\delta \approx 10^4$, $Re_{\lambda_T} \approx 10^2$) has been met. This serves, then, as a necessary minimum requirement in the development of multi-source wind tunnels with intended use as environmental simulators for flyers near the surface. Characteristics of the evolving flowfields can further be tuned through the introduction of perturbation techniques applied as initial conditions.

The uniform flow modality (i.e. all fan units set to produce nominally the same initial velocity condition) develops a well-mixed (within 2% of the mean) turbulent flowfield beyond $x/L \sim 0.5$ with $Re_{\lambda_T} = 135$ and serves as a basis of comparison for all other flow modalities discussed herein. Both initialized dual-stream and triple-stream mixing layers at flight-relevant freestream velocity differences are explored and found to principally behave like the mixing layers developed in a more conventional splitterplate experiment. The Reynolds number Re_{δ_ω} based on the velocity difference ΔU and vorticity thickness δ_ω (both outer scale parameters) is shown to linearly increase with downstream development as the vorticity thickness increases commensurately. The spectral analysis along the centerline confirms local isotropy for every tested case. Statements of the *suitability* of these mixing layers as experimental forcing functions for discrete gust testing can only be made with the

(approximate) flyer dynamics known. That is to say that the coupling/non-coupling of dynamics (length scales, frequency scales, etc.) between the environment and the flyer is determined by the flyer dynamics in relation to the generated shear layers. At least qualitatively the ‘right’ kind of mixing layer (i.e. fully-developed at relevant freestream velocities) is created within the testing envelope of the multi-source wind tunnel that serves as a candidate flow modality to be used in discrete gust experiments for full-scale dynamic vehicle testing.

The random-phase perturbation technique proves useful in increasing Re_{λ_T} upwards of nearly sevenfold with only a slight further-loss-of-uniformity (to within 3.7% of the mean). Significant increases in Re_{λ_T} are made through a static-reconfiguring of the discrete source fan-units into a so called quasi-grid flow modality. The highest recorded Taylor microscale Reynolds number was found to be $Re_{\lambda_T} = 2700$, likely accompanied by a non-negligible loss of uniformity at the fixed measurement location, though traverses were not undertaken during this campaign so no direct statement of homogeneity is put forth. Each flow modality is shown through the presence of a -5/3 slope power law region to be locally isotropic at relevant freestream velocities with an inertial subrange that dilates further as Re_{λ_T} increases.

5.4 Looking forward - research potential

Development of a multi-source wind-generating apparatus that produces relevant mean velocities and appropriate high-Re flowfields in an ample (and open) test envelope primes its use as an environmental flow simulator for near surface flowfields. Further to the point, appropriate and useful (i.e. machine-learning-capable¹) free-flight full-scale autonomous (manmade and/or natural) vehicle testing is made possible. For a brief overview of two-such facilities (CAST at Caltech and a temporary takeover of the 25ft Space Simulator at JPL to assist in the forward flight characterization of the Mars helicopter Ingenuity), see appendix A.4.

It is thought that the development of a large and open multi-source wind tunnel test facility further provides significant research potential toward the more fundamental understanding of the development of turbulence through shearing velocities. In time, with higher resolution traverses and flow visualization techniques further developed, questions surrounding the treatment of flowfields post-mixing transition may be better understood. For instance, in the case of the mixing layer, significant controversy still remains as to whether the initialized quasi-2D coherent structures

¹‘crash and learn’, as davidkremers says.

that grow pre-transition from pairing events continue to do so two-dimensionally post-mixing-transition. Numerical discrepancies at high-Re center squarely upon this matter (e.g., cf. McMullan et al., 2015; Suryanarayanan and Narasimha, 2017). The artifice of the wake of the splitterplate in the development of mixing layers is obviated (or at least reduced in a spanwise-coherence sense) through replacement of the splitterplate geometry with a software-based static reconfiguration of many discrete source fans and, because the testing domain is open-air, influences from artificial solid boundaries occur significantly further downstream.

Moreover, it is believed that some of the significant freestream nonuniformities that result from the multi-source module design can be reduced with careful software calibration, conventional flow-manipulator introduction, or by simply shifting testing further downstream, provided the envelope allows for it. Further solace is found in the consideration that local isotropy is observed in each primary flow modality, so that the details of the largely inviscid dynamics of the low wavenumber range eddies do not fundamentally alter the cascade of energy in the inertial subrange down to the dissipative scales.

BIBLIOGRAPHY

- Abramovich, Genrikh Naumovich et al. (1984). “The theory of turbulent jets”. In: *Moscow Izdatel Nauka*.
- Amir, Mohammad and Ian P Castro (2011). “Turbulence in rough-wall boundary layers: universality issues”. In: *Experiments in fluids* 51.2, pp. 313–326.
- Bernal, Luis Paulino (1981). *The coherent structure of turbulent mixing layers. I. Similarity of the primary vortex structure. II. Secondary streamwise vortex structure*. California Institute of Technology.
- Böhm, Margi et al. (2013). “Turbulence structure within and above a canopy of bluff elements”. In: *Boundary-layer meteorology* 146.3, pp. 393–419.
- Breidenthal, R (1980). “Response of plane shear layers and wakes to strong three-dimensional disturbances”. In: *The Physics of Fluids* 23.10, pp. 1929–1934.
- Brown, Garry L and Anatol Roshko (1974). “On density effects and large structure in turbulent mixing layers”. In: *Journal of Fluid Mechanics* 64.4, pp. 775–816.
- (2012). “Turbulent shear layers and wakes”. In: *Journal of Turbulence* 13, N51.
- Brunet, Yves, JJ Finnigan, and MR Raupach (1994). “A wind tunnel study of air flow in waving wheat: single-point velocity statistics”. In: *Boundary-Layer Meteorology* 70.1, pp. 95–132.
- Castro, Ian P, Hong Cheng, and Ryan Reynolds (2006). “Turbulence over urban-type roughness: deductions from wind-tunnel measurements”. In: *Boundary-Layer Meteorology* 118.1, pp. 109–131.
- Christen, Andreas (2005). “Atmospheric turbulence and surface energy exchange in urban environments: results from the Basel Urban Boundary Layer Experiment (BUBBLE)”. PhD thesis. University of Basel.
- Christen, Andreas, Eva van Gorsel, and Roland Vogt (2007). “Coherent structures in urban roughness sublayer turbulence”. In: *International Journal of Climatology: A Journal of the Royal Meteorological Society* 27.14, pp. 1955–1968.
- Cionco, Ronald M (1965). “A mathematical model for air flow in a vegetative canopy”. In: *Journal of Applied Meteorology and Climatology* 4.4, pp. 517–522.
- Coccal, O et al. (2007). “Structure of turbulent flow over regular arrays of cubical roughness”. In: *Journal of Fluid Mechanics* 589, pp. 375–409.
- Comte-Bellot, Geneviève and Stanley Corrsin (1966). “The use of a contraction to improve the isotropy of grid-generated turbulence”. In: *Journal of Fluid Mechanics* 25.4, pp. 657–682.

- D'Ovidio, A and CM Coats (2013). "Organized large structure in the post-transition mixing layer. Part 1. Experimental evidence". In: *Journal of fluid mechanics* 737, pp. 466–498.
- Davenport, Alan G (1961). "The spectrum of horizontal gustiness near the ground in high winds". In: *Quarterly Journal of the Royal Meteorological Society* 87.372, pp. 194–211.
- Davidson, MJ et al. (1996). "Wind tunnel simulations of plume dispersion through groups of obstacles". In: *Atmospheric Environment* 30.22, pp. 3715–3731.
- Diederich, Franklin W and Joseph A Drischler (1957). "Effect of spanwise variations in gust intensity on the lift due to atmospheric turbulence". In: *NACA-TN-3920*.
- Dimotakis, Paul E (2000). "The mixing transition in turbulent flows". In: *Journal of Fluid Mechanics* 409, pp. 69–98.
- Dimotakis, Paul E and Garry L Brown (1976). "The mixing layer at high Reynolds number: large-structure dynamics and entrainment". In: *Journal of Fluid Mechanics* 78.3, pp. 535–560.
- Dziomba, B and HE Fiedler (1985). "Effect of initial conditions on two-dimensional free shear layers". In: *Journal of Fluid Mechanics* 152, pp. 419–442.
- Etkin, Bernard (1981). "Turbulent wind and its effect on flight". In: *Journal of Aircraft* 18.5, pp. 327–345.
- Fiedler, HE and H-H Fernholz (1990). "On management and control of turbulent shear flows". In: *Progress in Aerospace Sciences* 27.4, pp. 305–387.
- Fiedler, Heinrich E. (1998). "Control of Free Turbulent Shear Flows". In: *Flow Control: Fundamentals and Practices*. Ed. by Mohamed Gad-el-Hak and Andrew Pollard. Berlin, Heidelberg: Springer Berlin Heidelberg, pp. 335–429. ISBN: 978-3-540-69672-8.
- Finnigan, John (2000). "Turbulence in plant canopies". In: *Annual review of fluid mechanics* 32.1, pp. 519–571.
- Finnigan, John J, Roger H Shaw, and Edward G Patton (2009). "Turbulence structure above a vegetation canopy". In: *Journal of Fluid Mechanics* 637, pp. 387–424.
- Florens, Emma, Olivier Eiff, and Frédéric Moulin (2013). "Defining the roughness sublayer and its turbulence statistics". In: *Experiments in fluids* 54.4, pp. 1–15.
- Foken, Thomas (2006). "50 years of the Monin–Obukhov similarity theory". In: *Boundary-Layer Meteorology* 119.3, pp. 431–447.
- Gad-el-Hak, Mohamed and Stanley Corrsin (1974). "Measurements of the nearly isotropic turbulence behind a uniform jet grid". In: *Journal of Fluid Mechanics* 62.1, pp. 115–143.
- Gaonkar, Gopal H (2008). "Review of turbulence modeling and related applications to some problems of helicopter flight dynamics". In: *Journal of the American Helicopter Society* 53.1, pp. 87–107.

- Görtler, von H (1942). “Berechnung von Aufgaben der freien Turbulenz auf Grund eines neuen Näherungsansatzes.” In: *ZAMM-Journal of Applied Mathematics and Mechanics/Zeitschrift für Angewandte Mathematik und Mechanik* 22.5, pp. 244–254.
- Greenblatt, David (2016). “Unsteady low-speed wind tunnels”. In: *AIAA Journal* 54.6, pp. 1817–1830.
- Guala, Michele, M Metzger, and Beverley J McKeon (2011). “Interactions within the turbulent boundary layer at high Reynolds number”. In: *Journal of Fluid Mechanics* 666, pp. 573–604.
- Harman, Ian N and John J Finnigan (2007). “A simple unified theory for flow in the canopy and roughness sublayer”. In: *Boundary-layer meteorology* 123.2, pp. 339–363.
- Hearst, R Jason (2018). “The use of active grids in experimental facilities”. In: *iTi Conference on Turbulence*. Springer, pp. 173–178.
- Hinze, J.O. (1975). *Turbulence*. McGraw-Hill classic textbook reissue series. McGraw-Hill. ISBN: 9780070290372.
- Ho, Chih-Ming and Patrick Huerre (1984). “Perturbed free shear layers”. In: *Annual review of fluid mechanics* 16.1, pp. 365–422.
- Hutchins, N and Ivan Marusic (2007). “Evidence of very long meandering features in the logarithmic region of turbulent boundary layers”. In: *Journal of Fluid Mechanics* 579, pp. 1–28.
- Jakosky, Bruce M and Roger J Phillips (2001). “Mars’ volatile and climate history”. In: *nature* 412.6843, pp. 237–244.
- Jiménez, Javier (2004). “Turbulent flows over rough walls”. In: *Annu. Rev. Fluid Mech.* 36, pp. 173–196.
- Kaimal, Jagadish Chandran and John J Finnigan (1994). *Atmospheric boundary layer flows: their structure and measurement*. Oxford university press.
- Kármán, Theodore von (1931). *Mechanical similitude and turbulence*. 611. National Advisory Committee for Aeronautics.
- (1948). “Progress in the statistical theory of turbulence”. In: *Proceedings of the National Academy of Sciences of the United States of America* 34.11, p. 530.
- Kármán, Theodore von and Leslie Howarth (1938). “On the statistical theory of isotropic turbulence”. In: *Proceedings of the Royal Society of London. Series A-Mathematical and Physical Sciences* 164.917, pp. 192–215.
- Koepp, N, HE Fiedler, and J-H Kim (1991). “The spatially accelerated mixing layer in a tailored pressure gradient”. In: *European Journal of Mechanics B Fluids* 10.4, pp. 349–376.

- Kolmogorov, Andrey Nikolaevich (1941). “The local structure of turbulence in incompressible viscous fluid for very large Reynolds numbers”. In: *Cr Acad. Sci. URSS* 30, pp. 301–305.
- Lee, Moon Joo, John Kim, and Parviz Moin (1990). “Structure of turbulence at high shear rate”. In: *Journal of Fluid Mechanics* 216, pp. 561–583.
- Liepmann, Hans Wolfgang and John Laufer (1947). “Investigations of free turbulent mixing”. In: *NACA-TN-1257*.
- Lin, Chia-Chiao (1953). “On Taylor’s hypothesis and the acceleration terms in the Navier-Stokes equation”. In: *Quarterly of Applied Mathematics* 10.4, pp. 295–306.
- Loehrke, RI and Hassan M Nagib (1972). *Experiments on management of free-stream turbulence*.
- Lumley, J. L. (June 1964). “Passage of a turbulent stream through honeycomb of large length-to-diameter ratio”. In: *Journal of Basic Engineering* 86.2, pp. 218–220.
- Lumley, J.L. et al. (1964). *The Structure of Atmospheric Turbulence*. Interscience monographs and texts in physics and astronomy. Interscience Publishers. ISBN: 9780470553657.
- Macdonald, RW (2000). “Modelling the mean velocity profile in the urban canopy layer”. In: *Boundary-Layer Meteorology* 97.1, pp. 25–45.
- Makita, Hideharu (1991). “Realization of a large-scale turbulence field in a small wind tunnel”. In: *Fluid Dynamics Research* 8.1-4, p. 53.
- McMullan, William A, S Gao, and Christopher M Coats (2015). “Organised large structure in the post-transition mixing layer. Part 2. Large-eddy simulation”. In: *Journal of Fluid Mechanics* 762, pp. 302–343.
- Mehta, RD (1991). “Effect of velocity ratio on plane mixing layer development: Influence of the splitter plate wake”. In: *Experiments in fluids* 10.4, pp. 194–204.
- NASA et al. (2016). *Sol 1419*. <https://www.flickr.com/photos/seandoran/28297558424/>, Last accessed on 2021-07-26.
- Oke, Tim R (2006). “Towards better scientific communication in urban climate”. In: *Theoretical and Applied Climatology* 84.1, pp. 179–190.
- Oke, Timothy R et al. (2017). *Urban Climates*. Cambridge University Press.
- Oster, D and I Wygnanski (1982). “The forced mixing layer between parallel streams”. In: *Journal of Fluid Mechanics* 123, pp. 91–130.
- Oster, D, I Wygnanski, et al. (1977). “Some preliminary observations on the effect of initial conditions on the structure of the two-dimensional turbulent mixing layer”. In: *Turbulence in Internal Flows* (ed. SNB Murthy), pp. 67–87.

- Ozono, Shigehira and Hiroshi Ikeda (2018). “Realization of both high-intensity and large-scale turbulence using a multi-fan wind tunnel”. In: *Experiments in Fluids* 59.12, pp. 1–12.
- Panofsky, Hans A (1984). “Atmospheric turbulence”. In: *Models and methods for engineering applications*. 397.
- Panofsky, Hans A and Robert A McCormick (1954). “Properties of spectra of atmospheric turbulence at 100 metres”. In: *Quarterly Journal of the Royal Meteorological Society* 80.346, pp. 546–564.
- Perret, Laurent et al. (2019). “The atmospheric boundary layer over urban-like terrain: influence of the plan density on roughness sublayer dynamics”. In: *Boundary-Layer Meteorology* 170.2, pp. 205–234.
- Poggi, Davide et al. (2004). “The effect of vegetation density on canopy sub-layer turbulence”. In: *Boundary-Layer Meteorology* 111.3, pp. 565–587.
- Pond, S, RW Stewart, and RW Burling (1963). “Turbulence spectra in the wind over waves”. In: *Journal of the Atmospheric Sciences* 20.4, pp. 319–324.
- Prandtl, Ludwig (1932). “Meteorologische anwendung der stromungslehre”. In: *Beitr. Phys. Atmosph* 19.
- Raichlen, Fredric (1967). “Some turbulence measurements in water”. In: *Journal of the Engineering Mechanics Division* 93.2, pp. 73–98.
- Raupach, Michael R, John J Finnigan, and Yves Brunet (1996). “Coherent eddies and turbulence in vegetation canopies: the mixing-layer analogy”. In: *Boundary-layer meteorology 25th anniversary volume, 1970–1995*. Springer, pp. 351–382.
- Renn, Peter (2018). *Real time probe based motion capture flow characterizations*. Senior Thesis, ME 90. California Institute of Technology.
- Reynolds, Ryan T and Ian P Castro (2008). “Measurements in an urban-type boundary layer”. In: *Experiments in Fluids* 45.1, pp. 141–156.
- Roadman, Jason and Kamran Mohseni (2009). “Gust characterization and generation for wind tunnel testing of micro aerial vehicles”. In: *47th AIAA aerospace sciences meeting including the new horizons forum and aerospace exposition*, p. 1290.
- Roth, Matthias (2000). “Review of atmospheric turbulence over cities”. In: *Quarterly Journal of the Royal Meteorological Society* 126.564, pp. 941–990.
- Sabin, Cullen Milo (1965). “An analytical and experimental study of the plane, incompressible, turbulent free-shear layer with arbitrary velocity ratio and pressure gradient”. In:
- Saiy, M and SJ Peerless (1978). “Measurement of turbulence quantities in a two-stream mixing layer”. In: *Journal of Fluid Mechanics* 89.4, pp. 709–722.
- Schofield, JT et al. (1997). “The Mars Pathfinder atmospheric structure investigation/meteorology (ASI/MET) experiment”. In: *Science* 278.5344, pp. 1752–1758.

- Shaw, Roger H et al. (1995). “A wind tunnel study of air flow in waving wheat: two-point velocity statistics”. In: *Boundary-Layer Meteorology* 76.4, pp. 349–376.
- Sheih, Ching-Ming, H Tennekes, and JL Lumley (1971). “Airborne Hot-Wire Measurements of the Small-Scale Structure of Atmospheric Turbulence”. In: *The Physics of Fluids* 14.2, pp. 201–215.
- Smith, David E et al. (2001). “Mars Orbiter Laser Altimeter: Experiment summary after the first year of global mapping of Mars”. In: *Journal of Geophysical Research: Planets* 106.E10, pp. 23689–23722.
- Spencer, BW (1970). “Statistical investigation of turbulent velocity and pressure fields in a two-stream mixing layer”. PhD thesis. University of Illinois at Urbana-Champaign.
- Spencer, BW and BG Jones (1971). “Statistical investigation of pressure and velocity fields in the turbulent two-stream mixing layer”. In: *AIAA Journal*.
- Stathopoulos, Ted and Charalambos C Baniotopoulos (2007). *Wind effects on buildings and design of wind-sensitive structures*. Vol. 493. Springer Science & Business Media.
- Stull, Roland B (1988). *An introduction to boundary layer meteorology*. Vol. 13. Springer Science & Business Media.
- Suryanarayanan, Saikishan and Roddam Narasimha (2017). “Insights into the growth rate of spatially evolving plane turbulent free-shear layers from 2D vortex-gas simulations”. In: *Physics of Fluids* 29.2, p. 020708.
- Sutton, O.G. (1953). *Micrometeorology*. McGraw-Hill.
- Taylor, Geoffrey Ingram (1935). “Statistical theory of turbulence”. In: *Proceedings of the Royal Society of London. Series A-Mathematical and Physical Sciences* 151.873, pp. 421–444.
- Tennekes, Hendrik, John Leask Lumley, Jonh L Lumley, et al. (1972). *A first course in turbulence*. MIT press.
- Turner, D Bruce (1964). “A diffusion model for an urban area”. In: *Journal of Applied Meteorology and Climatology* 3.1, pp. 83–91.
- Van der Hoven, Isaac (1957). “Power spectrum of horizontal wind speed in the frequency range from 0.0007 to 900 cycles per hour”. In: *Journal of Atmospheric Sciences* 14.2, pp. 160–164.
- Veismann, Marcel et al. (2021). “Low-density multi-fan wind tunnel design and testing for the Ingenuity Mars Helicopter”. In: *Experiments in Fluids* 62.9, pp. 1–22.
- Watkins, Simon et al. (2010). “On low altitude flight through the atmospheric boundary layer”. In: *International Journal of Micro Air Vehicles* 2.2, pp. 55–68.

- Wieringa, Jon (1992). “Updating the Davenport roughness classification”. In: *Journal of Wind Engineering and Industrial Aerodynamics* 41.1-3, pp. 357–368.
- Witte, Brandon M, Robert F Singler, and Sean CC Bailey (2017). “Development of an unmanned aerial vehicle for the measurement of turbulence in the atmospheric boundary layer”. In: *Atmosphere* 8.10, p. 195.
- Wynanski, I et al. (1979). “On the perseverance of a quasi-two-dimensional eddy-structure in a turbulent mixing layer”. In: *Journal of Fluid Mechanics* 93.2, pp. 325–335.
- Yeung, Alton et al. (2018). “Measuring low-altitude wind gusts using the unmanned aerial vehicle GustAV”. In: *Journal of Unmanned Vehicle Systems* 6.4, pp. 235–248.
- Yoder, Dennis A, James R DeBonis, and Nicholas J Georgiadis (2015). “Modeling of turbulent free shear flows”. In: *Computers & fluids* 117, pp. 212–232.

Appendix A

FAN ARRAY WIND TUNNELS

Appendix A is adapted from:

C. Dougherty, M. Veismann, A. Stefan-Zavala, P. Renn, M. Gharib. “The design and characterization of fan array wind tunnels.” Awaiting submission to: *Measurement Science and Technology*

C.D participated in the conception of the project, performed certain experiments, prepared certain data, and wrote the manuscript.

The fan array wind tunnel (FAWT) is a multi-source wind tunnel capable of generating a host of spatiotemporally-varying flowfields via software interfacing, offering a versatile, configurable alternative to traditional wind tunnel design and testing. By utilizing an array of DC-powered off-the-shelf cooling fans (in place of one singular drive section), greater flow control and decreased mixing lengths are achieved. The open-loop design of FAWT provide a substantially large useable test section area when compared with its effective footprint. This, in turn, allows FAWT to be implemented in confined spaces that otherwise could not accommodate wind tunnel testing. The fan array itself is fully and individually software addressable, which translates to the capability of generating a variety of traditional and non-traditional spatially- and temporally- varying flows. Some representative examples with implementation are given in table A.1.

A.1 Design Intent

FAWT seeks to accommodate both traditional static aerodynamic testing as well as dynamically controlled free flight investigations subject to configurable flow patterns, though any application that requires spatiotemporally-varying flows can be accommodated. This new wind tunnel class, at its core, provides a paradigm shift in the field of multi-source wind tunnels by incorporating a wide variety of flow conditions in a space-efficient and scalable package. By generating flow patterns not dependent upon obstacle geometries (which result in major pressure losses), an open loop tunnel concept can be implemented, maximizing test section size in a limited space environment. Additionally, FAWT methodology encourages appro-

appropriate interfacing between computer modeling and experimentation by providing an input-output domain familiar to both. Discrete fan units, uniquely addressable, provide source input of nearly endless combination, limited only by the top-end speed and responsiveness of each source-unit.

A.2 Schematic Overview

An overall diagrammatic view of FAWT design is presented in this section in order to categorize and generalize the various forms that can be built. The unifying concept between any FAWT implementation is the number of fan units per given array dimension. In this sense, a fan unit is akin to a pixel comprising an image (or array), such that fan arrays are labeled similar to pixel resolutions as *number x number*. The value that will be most useful throughout, however, is the ratio of the smallest flow-producing hardware dimension d to the overall fan array dimension, either height h or width L . In this way, particularly for square arrays, it is immediately clear how finely the array is divided. For example, a 10 x 10 fan array would have a $d/h = d/L = 1/10 = 0.1$.

The FAWT can be divided into 2 main systems:

- Hardware
 - Fan Unit
 - Power Distribution System (PDS)
 - Micro-controller
- Software
 - Network Architecture
 - (External Control)

Hardware

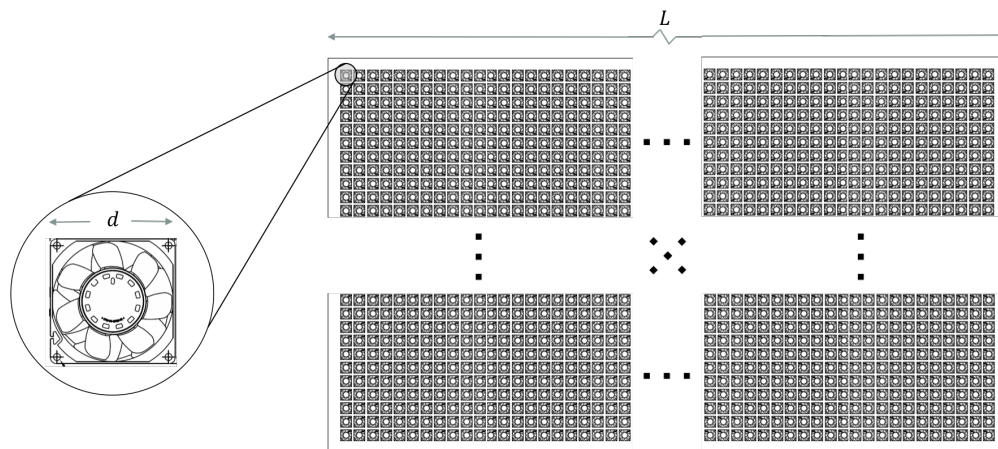
Fan Unit:

The fan unit is the primary hardware component comprising FAWT. The size, electrical requirements, and total number of fans can be selected based on a number of considerations, including desired performance (i.e. resolution and speed), available space/infrastructure, and/or cost. Depending on the desired use case, a number of configurations can be built with the smallest spatial building block being the fan unit size itself. The FAWT implementations presented herein each use a PWM-capable

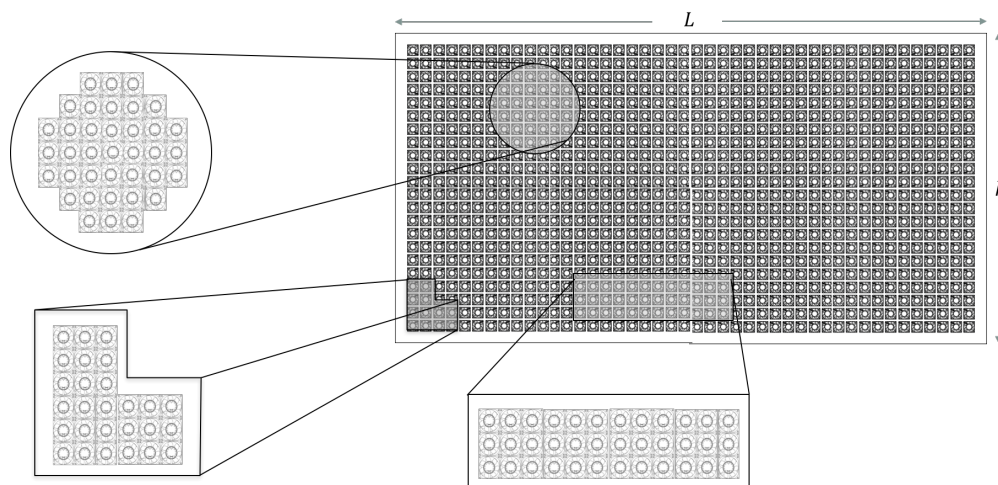
fan unit¹ with tachometer rpm feedback configured in a square array geometry, unless otherwise noted.

Table A.1: Fan RPM distributions for example implementations for FAWT.

Flow Type	Implementation
Uniform flow	Assign same RPM to all fans
Shear flow	Assign desirable gradient of RPM to all fans
Vortex flow	Introduce transverse velocities using side arrays
Gusting flow	Accelerate/decelerate fan RPMs



(a) Exploded view highlighting a fan unit of outer case dimension d , the smallest building block of the array.



(b) Various examples of how the fan units can be grouped into "modules" to build up an array with overall dimensions $L \times h$.

Figure A.1: Annotated hardware overview of FAWT.

¹PWM-capable fan unit: 4-wire DC cooling fan with PWM signal control and tachometer feedback through a built-in hall effect sensor.

Power Distribution System (PDS):

In place of a single-drive system, FAWT typically employs a multi-layered power design approach. The power distribution system (PDS) consists of the cascading assortment of electrical hardware necessary to step down source power (typically from the wall of a building) to the specified fan unit power requirements. For relatively small implementations, power can be supplied directly to the fan units using a modified computer power supply. For larger builds, a distributed power bus/bank is preferable. Although a seemingly simple consideration, the electrical power required to generate reasonable flow speeds can be considerable.

Micro-controller:

A PWM capable micro-controller is utilized to set the duty cycle (%) of a given set of fans. The micro-controller can also be used to read in the tachometer signal from the built-in hall effect sensor in the fan unit. Most micro-controller boards have limited digital output pins, typically < 50, such that a network of boards is required for builds with fan unit numbers greater than this amount.

Software

The control software, in the simplest sense, interfaces with the PWM-capable digital pins of the micro-controllers. The user can send a series of coordinated duty cycle inputs that cause the fans to spin to a desired RPM, which can be read back through the micro-controller accessing the tachometer signal of the fans. More integrated software implementations can use this tachometer feedback for closed-loop control.

Network Architecture:

For FAWT implementations with a sizable number of fan units, it is often required to develop a network architecture to handle the simultaneous pipeline of data to and from the micro-controller boards. This is effectively done through a Local Area Network (LAN) that terminates into a router, from which each micro-controller board and ultimately each fan unit is uniquely software-addressable. This provides operational control and feedback to single fan units, groups of fans, and/or the entirety of the fan array depending on the desired level of distinction.

External Control:

Since the control input to the fan array is a user-defined matrix data structure accessed through a network, virtually any external source or software can be used to control the array. This is useful in implementations where it is desirable to have feedback automation mapped by some measured quantity, recorded by a DAQ for instance.

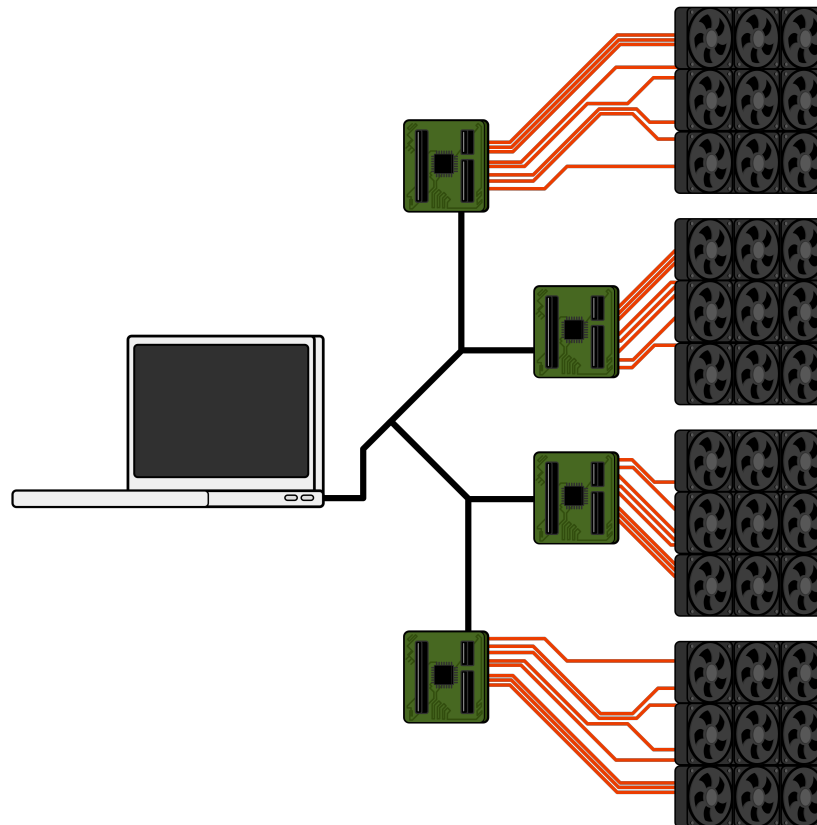


Figure A.2: Flow of information from module to micro-controller to computer through a network.

A.3 Flow Quality

The Effect of Measurement Location

The typical fan units used in FAWT have non-negligible hub geometries where the internal fan circuitry is housed. To determine the effect of the hub geometry on the development of the flow, three measurement locations relative to the face of the fan unit were identified (see fig. A.3) and the development of a uniform flow modality was measured at various downstream locations.

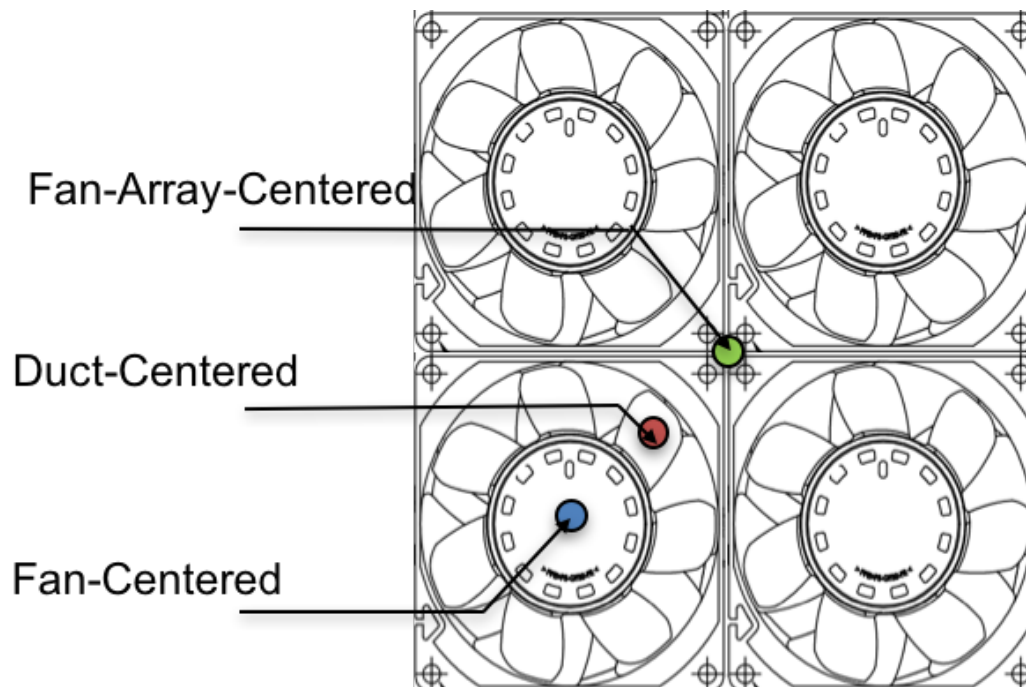


Figure A.3: Three identifiable regions of the simplest square array configuration. The “fan-centered” and “fan-array-centered” locations represent a stagnation condition whereas the “duct-centered” represents an accelerated inlet condition.

The inlet condition at the face of the fan unit ultimately dictates the initial flow development, which varies depending on the measurement location relative to the fan unit geometry when close to the fan source. This is clearly showcased in Figure A.4. As velocities are increased, the initial deviation from the desired reference velocity increases as well, though the effect of the fan unit geometry is no longer observed beyond $x/L \approx 0.5$. The initial flow development is considered simply to highlight the expected flow evolution of FAWT from source to measurement apparatus. The effect of the individual fan geometry in the formation of a uniform flow diminishes quickly and can effectively be ignored when measuring sufficiently far downstream, as will most frequently be the case. These results are included for completeness and to further give context to subsequent analysis. In the following section, the useable testing volume relative to the fan array and fan unit dimensions is established.

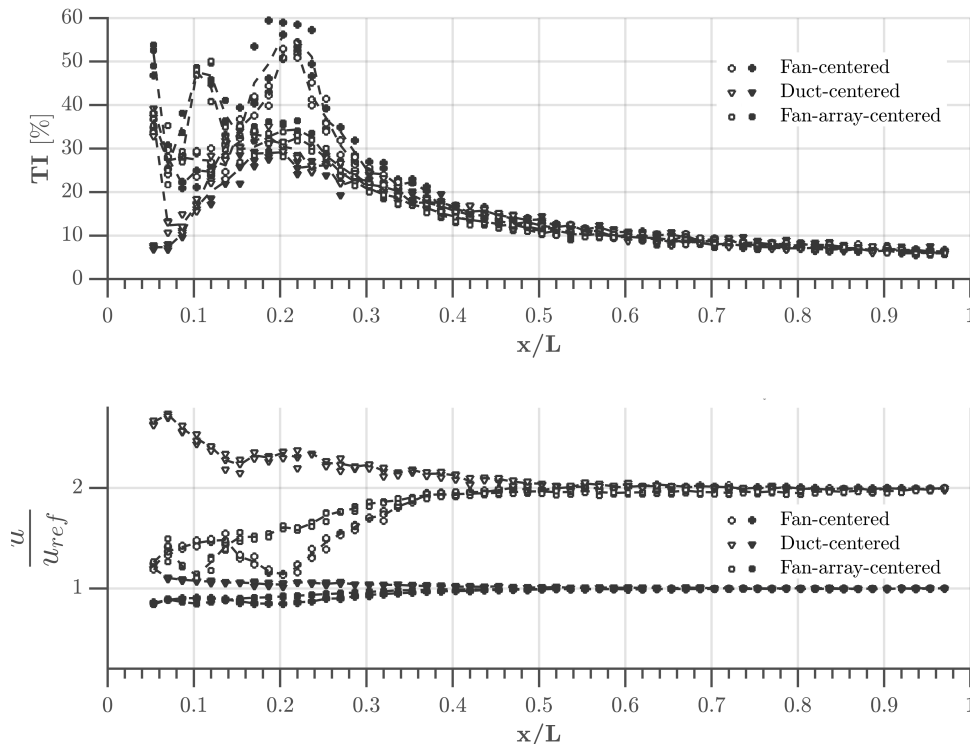


Figure A.4: The downstream convergence of the measured values of turbulence and freestream velocity indicate that the flow has fully mixed and is invariant to the measurement location beyond $x/L \approx 0.5$.

Useable Test Section

Configurations:

Unlike a traditional wind tunnel, the test section of the FAWT oftentimes occupies the volume *immediately* downstream of the source fan(s) and associated flow manipulators. It is important to quantify how the flow evolves spatially through this test section in the primary two implementations of FAWT: **enclosed** and **non-enclosed**.

- **enclosed:** An optically-clear enclosure is sometimes included to further confine the flow and provide adequate mounting structure for quantitative flow diagnostics. The boundary condition of the *enclosed*-configuration is the canonical boundary layer of a flat plate.
- **non-enclosed:** Uninhibited dynamical free flight testing is achieved by removing any test section enclosure to allow for flyers to plunge, translate, and otherwise interact with FAWT in realistic simulated flight scenarios. In this *non-enclosed*-configuration, the boundary condition is a shear layer formation that grows due to entrainment as the flow evolves downstream.

Effective Size:

It is important that proper mixing occurs prior to encountering the test apparatus to ensure flow uniformity through the extent of the test setup. In general and irrespective of the configuration chosen, FAWT deliver a useable test section that is $\sim 80\%$ of the array outer dimension at $x/L \approx 0.5$. The 20% spatial margin is most clearly seen in spanwise velocity cross sections, as in fig. B.3. Values are considered approximate simply because the downstream development of the flows generated from FAWT vary slightly from build-to-build (e.g. due to differences in room geometry, distance from floor, available air reservoir, etc.), though the core development of the flow remains largely unaffected, as is demonstrated in the centerline analysis of the following section.

Turbulence Decay

Turbulence decay is a useful measure of the downstream development of the core region of the flow. Since turbulence is generated at the scale of the source fan, normalization of the downstream location by the primary dimension of the fan-unit, d , is used instead. The centerline turbulence decay for a variety of fan-unit and fan-array sizes is given in Figure A.5, with configuration noted. The homogeneous, exponential downstream decay of turbulence for the cohort of FAWT sizes and configurations tested highlights the centerline invariance of the flow with respect to the boundary condition. Thus, it is reasonable to predict downstream centerline characteristics of a steady uniform flow by simply considering the fan-unit size itself. The relatively short mixing lengths contribute to the compactness and utility of FAWT. The spread of data observed in the 92 mm fan is on account of the various flow manipulator configurations tested in that particular implementation, the primary subject of the subsequent section. Flow conditioning is first explored from the point-of-view of the traditional low-speed wind tunnel design process and then expounded to include some more modern considerations.

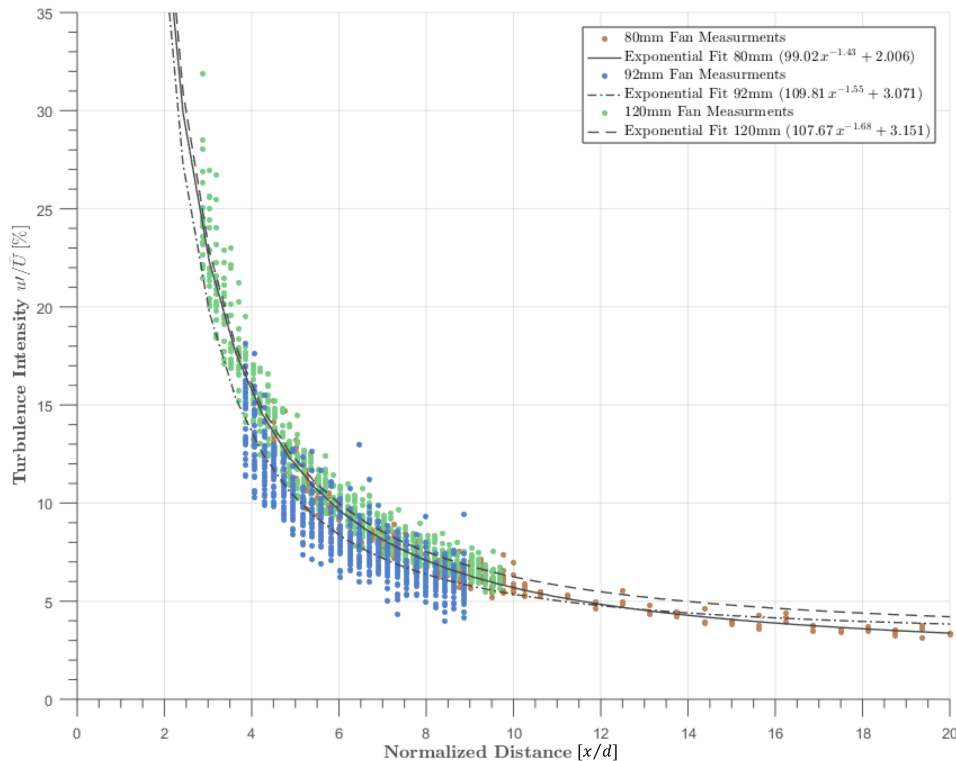


Figure A.5: Centerline homogeneous turbulence decay for three different sized fan units configured into arrays. The $d = 0.080$ m fan unit corresponds to a 36×36 dual-layer array, the $d = 0.092$ m fan unit corresponds to a 11×11 single-layer array, and the $d = 0.120$ m fan unit corresponds to a 10×10 single-layer array.

Flow Manipulator Configurations

Due to the geometry of FAWT, installation of flow manipulators can be thought of as extensions or inserts immediately downstream of the main fan array. For a given test section size, spanwise turbulence initializes in smaller length scales by virtue of utilizing many small source fans in place of one large one. Though not a requisite, all fan units of a given array presented herein are identically manufactured and thus rotate in the same sense. To determine the influence of single and/or combinations of flow manipulators on the turbulence properties of fan array wind tunnels, a specially designed enclosure extension was installed on a representative FAWT (11×11 , $d/L = 0.09$) and hot-wire measurements were recorded. A diagrammatic view of the flow manipulator placements is given in fig. A.6.

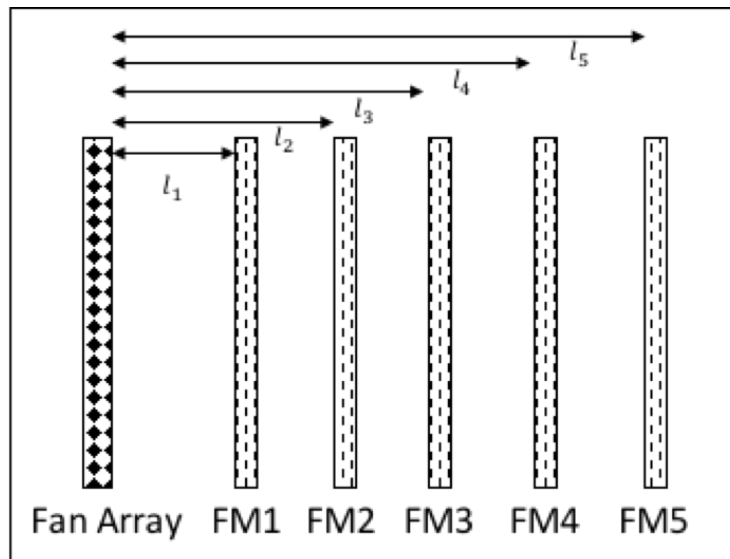


Figure A.6: Diagram view of flow manipulator (FM) placement at set downstream locations ($l_{1,2,\dots,5}$) relative to the fan array.

Honeycomb + Auxiliary Manipulators:

The influence of honeycomb on eliminating transverse velocities is well documented for single-source wind tunnels. To understand the effect of honeycomb on FAWT, an analysis similar to J. L. Lumley (1964) is undertaken. A comparison of downstream development of turbulence intensity with and without a honeycomb is given in fig. A.7. Because flow variability is oftentimes prioritized over flow quality for FAWT builds, it is recommended that the honeycomb be implemented flush against the array as the primary flow manipulator with auxiliary manipulator(s) slotted downstream of that, as necessary, to further reduce turbulence. From a convenience stand-point (especially for larger builds), placing the honeycomb flush to the array provides the support and access to mounting structure necessary for secure installation, regardless of configuration.

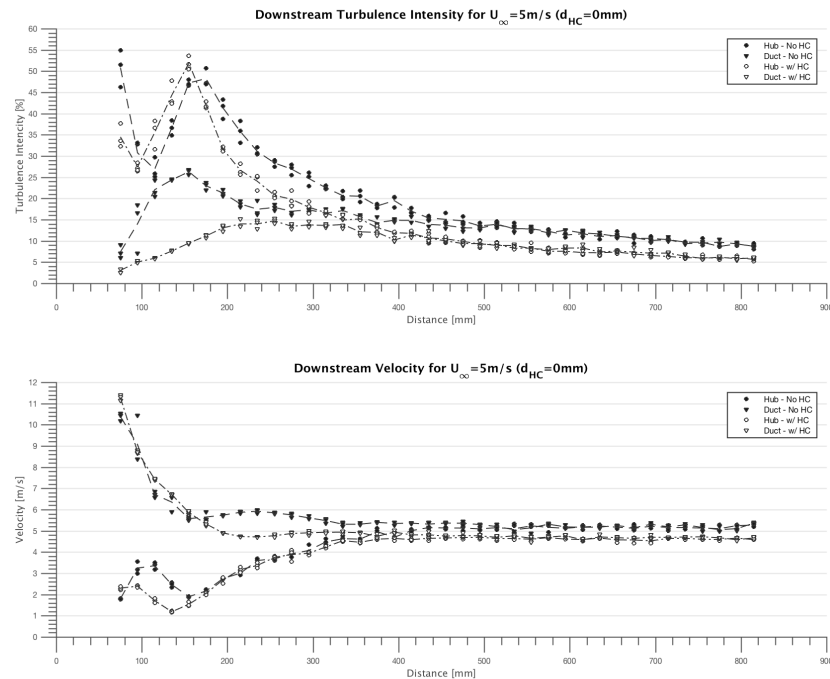


Figure A.7: Effect of honeycomb on downstream development of uniform flow.

A summary of viable flow manipulator configurations is presented in table A.2 to aid in the selection of auxiliary manipulators for a desired turbulence intensity. Representative trends are showcased graphically in fig. A.8 for the addition of auxiliary manipulators, in particular the addition of perforated plates and/or screens downstream of the honeycomb. A reference configuration of a fan array with no flow manipulators is denoted as “REF”. The majority of the configurations tested slot a honeycomb into “FM1” while auxiliary flow manipulators are typically installed further downstream. The typical order tested is honeycomb (HC) followed by perforated plate(s) (PP) followed by screen(s) (S).

Table A.2: Flow manipulator configurations. *honeycomb*: HC, *perforated plate*: PP, *screen*: S.

Config.	<i>FM1</i>	<i>FM2</i>	<i>FM3</i>	<i>FM4</i>	<i>FM5</i>
E	HC	PP	PP	S	S
L	HC	PP	PP	S	-
K	HC	PP	S	-	-
H	HC	PP	PP	-	-
G	HC	PP	-	-	-
J	HC	-	-	-	-
REF	-	-	-	-	-

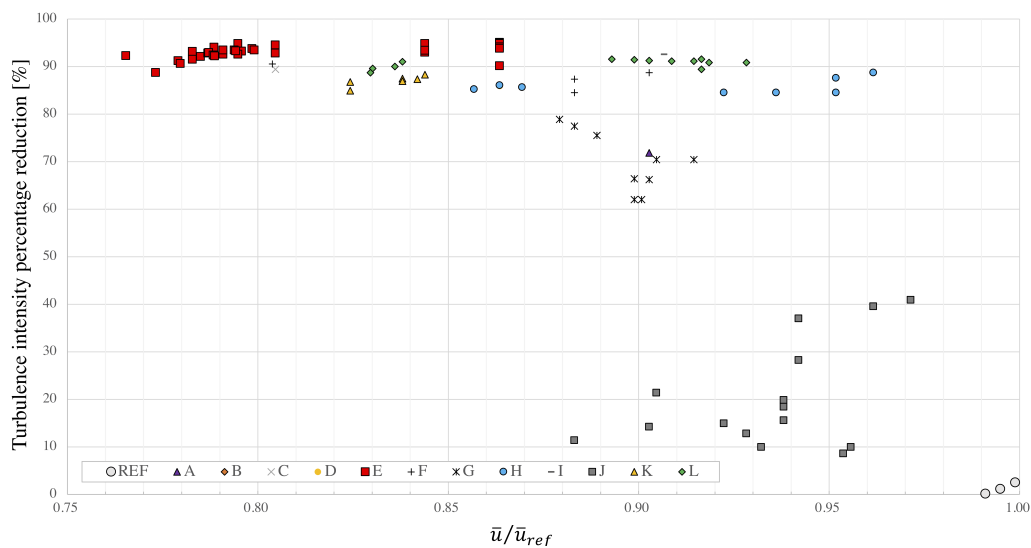


Figure A.8: Effectiveness of various flow manipulator configurations at reducing turbulence intensity.

Ideally, turbulence intensity is reduced while maintaining freestream velocity. Therefore, it is desirable to select a flow manipulator configuration tending toward the upper right portion of fig. A.8. Some viable configurations are highlighted in table A.3.

Table A.3: Turbulence intensity and velocity reduction for various flow manipulator configurations. Dimensional units for $l_{1,2,\dots,5}$ are in inches.

Config.	l_1	l_2	l_3	l_4	l_5	TI %	\bar{u}/\bar{u}_{ref}
E	2	6	7	13	21	0.35	0.86
L	2	6	7	13	-	0.60	0.89
K	9	13	15	-	-	0.83	0.84
H	2	6	7	-	-	0.99	0.86
G	2	6	-	-	-	2.25	0.91
J	2	-	-	-	-	5.10	0.94
REF	-	-	-	-	-	7.11	1.00

Flow Variety

The primary utility of FAWT is in the multifariousness of flow generation. As previously discussed, this subclass of wind tunnel implementation is primed to be utilized for free-flight dynamic stability and controllability testing of flyers of interest, though statically-mounted testing is obviously possible, as are other more traditional use cases. It is vitally important to understand the capabilities of fan array flow generation prior to fully exploring strategies for the aerodynamic testing of free-flying flyers. A hierarchical overview of the types of flows able to be generated by FAWT is given in fig. A.9.

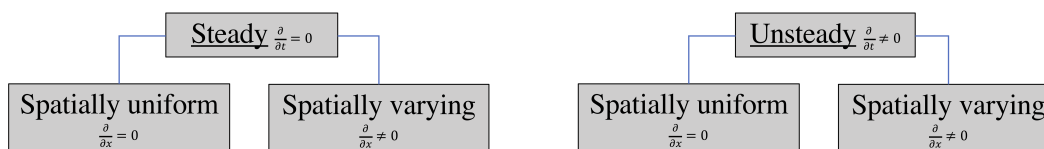


Figure A.9: Types of flows able to be generated by FAWT.

Table A.4: Description of techniques and analysis for flow characterization.

Measurement Device	Technique	Description of Analysis
Hot-wire anemometer	manually traversed	coarse spatial interpolation, fast temporal averaging
Five-hole pitot system	(semi-) manually traversed	fine spatial interpolation, slow temporal averaging
Particle Image Velocimetry	position laser sheet at ROI	ensemble average of 15 Hz double-pulse image sets

The measurement devices, techniques, and analyses utilized in the subsequent example datasets is summarized in Table A.4. For steady flows (both uniform and non-uniform), single-point and rake measurement apparatuses are sufficient to properly capture flow evolution. Particle image velocimetry (PIV) is able to visualize steady flowfields, discretely oscillatory flow behavior (when phase-averaged), and instantaneous snapshots of unsteady behavior while continuous measurements of unsteady flows prove more challenging for current technologies. As such, discussion and visualizations below deal solely with steady flows.

Steady Flows

The majority of effort in flow characterization thus far has been applied toward steady flows. Since the test envelope for FAWT begins immediately downstream of the source fans and/or flow-manipulators, the streamwise development is typically the first section of interest. For first insights, a vertical centerline streamwise 2D plane is measured. For both uniform and non-uniform flows, this viewpoint allows for quick apprehension of the spatial limits of the flow generated as well as a general sense of the downstream development. After analyzing the streamwise plane, a set of suitable downstream locations are selected based on the type of experiment to be run. At this point, the data for 2D spanwise planes of interest are acquired to help visualize the horizontal (and vertical) extent of the generated flow.

Flow Type #1: Steady, spatially-uniform

This is the default use case of conventional wind tunnels. In subsonic flight regimes, this flow modality well-simulates the motion through the inviscid free atmosphere or through the homogeneously turbulent inertial sublayer depending on the level of turbulence intensity. It is desired to condition the flow to acceptable levels of uniformity across the test section through flow manipulation. In each FAWT build at Caltech and JPL, honeycomb is used to eliminate the fan swirl. In cases where freestream turbulence intensities should better match background turbulence of the ABL, grids and screens are excluded. Grids and screens may also be excluded as a matter of convenience on larger builds where they may not be practical to install. When further flow manipulation is required, a filing cabinet style enclosure is attached to the array. All implementations are considered open-circuit, open-jet wind tunnels beyond the mixing region. Two streamwise planar example datasets acquired on different resolution FAWT using a five-hole probe system were shown in section 2.2 (see fig. 2.4 and fig. 2.6). Turbulence intensity distributions from traverses using a standard single hotwire are given in fig. A.10.

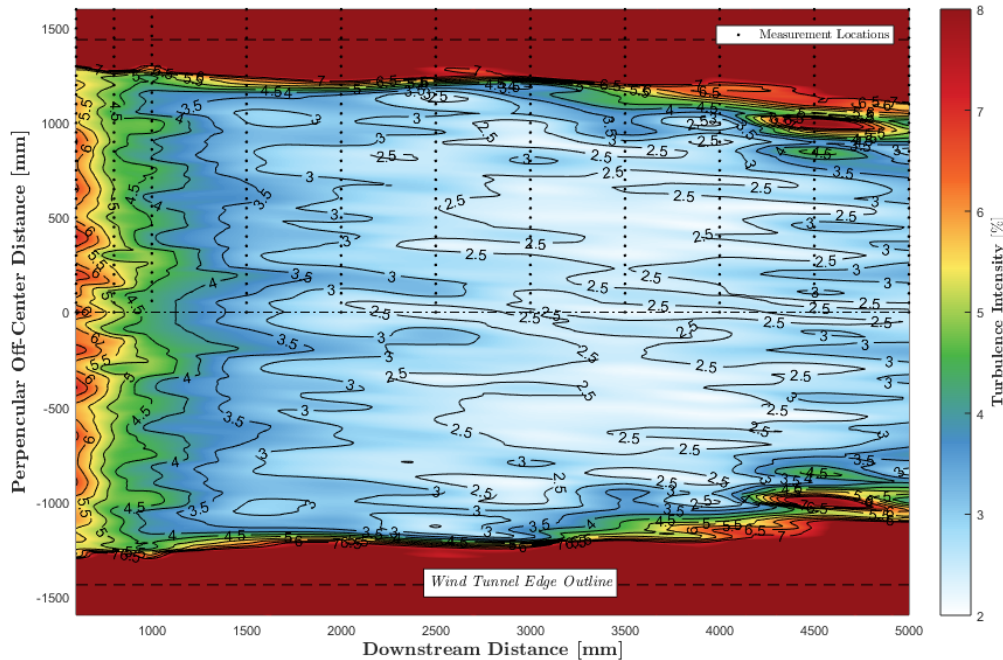


Figure A.10: The turbulence intensity distribution of a $d/L = 0.03$ resolution dual-layer array at nominal freestream velocities.

Flow Type #2: Steady, non-uniform (irrotational)

A steady non-uniform input distribution may or may not generate flowfields that are irrotational. For the cases where there are no inflection points in the mean velocity profile, a time-averaged measurement technique alone is justified. Extracting velocity profiles along lines of interest from these datasets is straightforward. This is oftentimes useful to enhance intuition of spatially-varying flows that are not immediately obvious from a contour plot alone. An illustrative example is a vertical gradient shear flow. Figure A.11 showcases the streamwise velocity contour plot alongside the spatial evolution of velocity profiles. For flow patterns that are rather non-uniform and directionally variant, probe-based techniques may not be suitable and two-dimensional particle image velocimetry (2D-PIV) can be utilized instead if the space permits. The primary example dataset is a steady vortex generation from an enclosed configuration FAWT with side fan units installed, shown in fig. A.12.

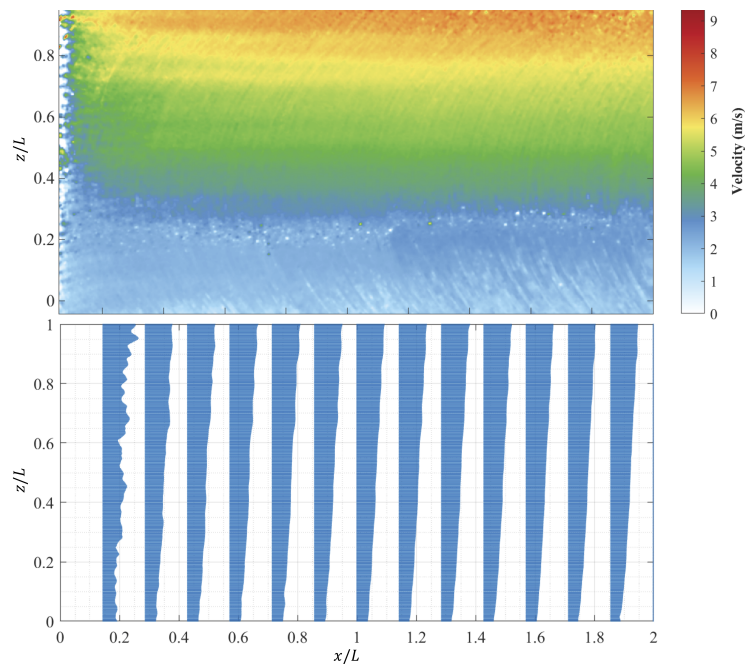


Figure A.11: Spatial development of a gentle vertical gradient shear flow. Contour shear velocity profiles (above) with corresponding velocity profiles (below) for a centerline streamwise measurement plane of a $d/L = 0.03$ resolution array. The maximum velocity is 7.5 m/s incremented piecewise per fan down to the idle velocities of the fan units, 2 m/s.

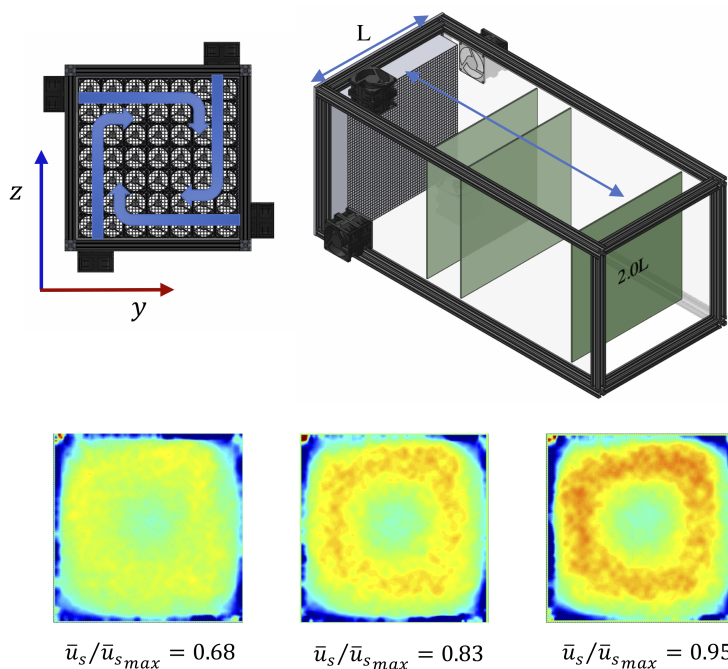


Figure A.12: Spanwise vorticity plots derived from particle image velocimetry measurements at $x/L = 2.0$ with varying side fan velocities \bar{u}_s .

A.4 Main facilities with FAWT implementations

The 25-ft Space Simulator at JPL

A specially designed FAWT was developed for integration into the Jet Propulsion Laboratory (JPL) 25-ft Space Simulator during an experimental campaign in 2018 to enable forward flight simulation of Ingenuity on Mars. Significant sub-scale testing of the fan units was completed prior to full-scale implementation to ensure performance under low-density conditions at relevant velocities to simulate desired Ingenuity flight characteristics. These tests were necessary to investigate forward flight vehicle dynamics and inform flight controller gain settings in a simulated non-terrestrial environment well-before (successfully) tackling Martian flight conditions for the very first time on April 19, 2021, marking the first ever powered controlled extraterrestrial flight by an aircraft. For details on this particular build, the reader is referred to Veismann et al. (2021).

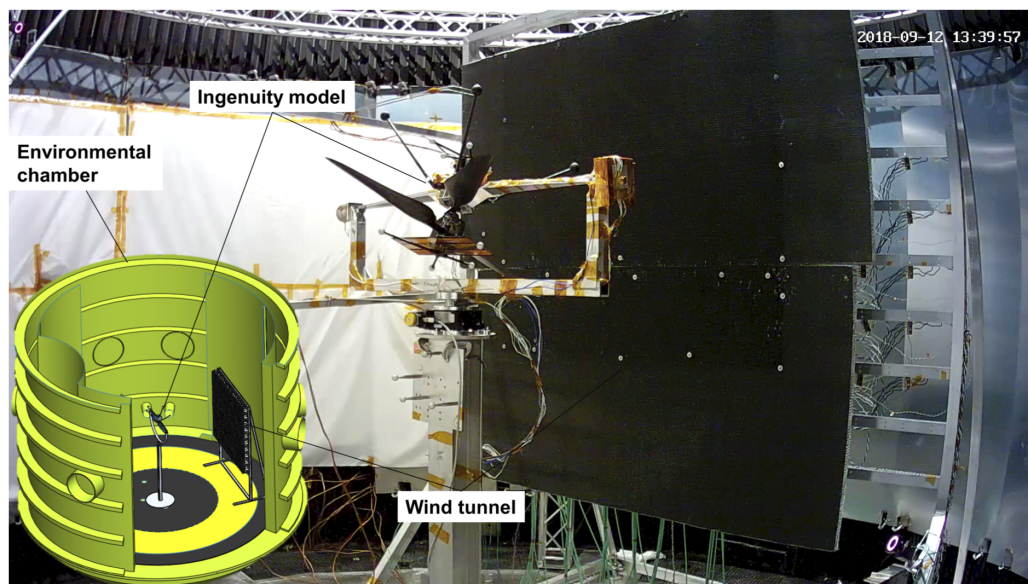


Figure A.13: FAWT within the 25-ft Space Simulator chamber at the Jet Propulsion Laboratory (JPL). A full-scale model of Ingenuity is seen fix-mounted (upside-down) in front of a bank of $21 \times 21 \times 2 = 882$ individual fan units stacked in two layers with a metallic honeycomb affixed to the outlet plane.

CAST at Caltech

At the Center for Autonomous Systems and Technologies (CAST) at Caltech, considerable effort has been made to better understand and further define the role of autonomous flyers, crawlers, rollers as extensive and extensible tools to humanity. Vital to the success of this goal is creating the proper contextual environment from which both humans and machines can explore, iterate, and otherwise learn.

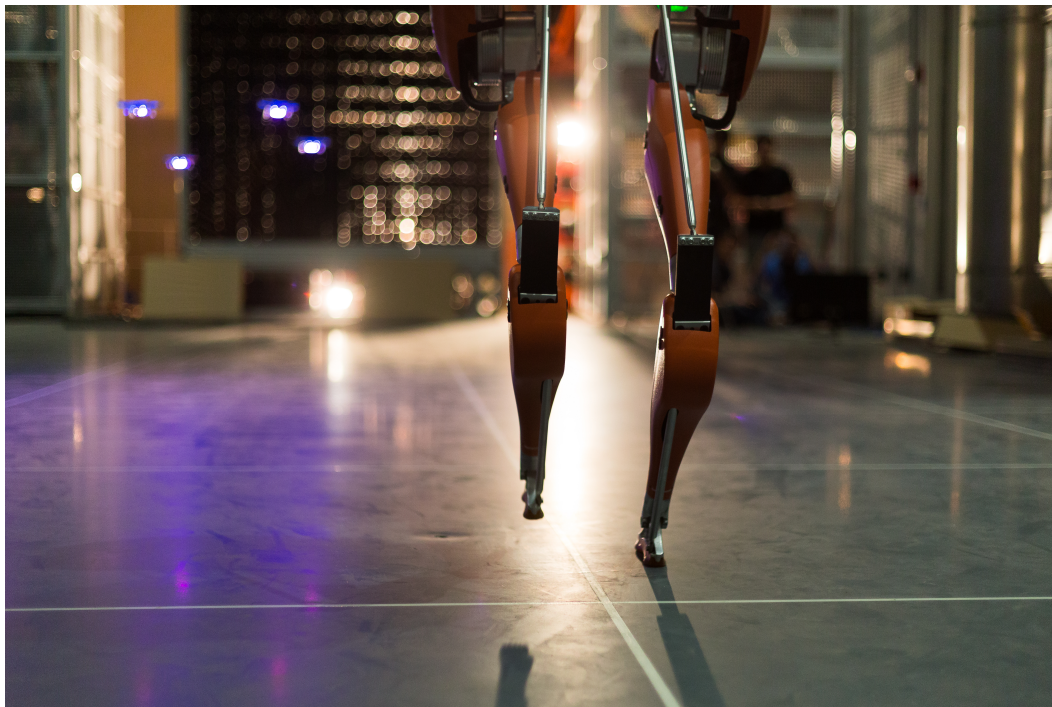


Figure A.14: A bipedal walker in the foreground interacting with a flock of flyers in the surround against the backdrop of the CAST fan array.

The Aerodrome within CAST is home to the first real weather fan array wind tunnel, an open-air and continuously measurable flight environment geared toward the emerging fields related to (hybridized) autonomous flyers. The four-story tall flight arena is outfitted with two U-shaped tiers of infrared motion capture cameras able to identify objects of interest with up to 100 micron resolution.



Figure A.15: FAWT within the Aerodrome in CAST.

*Appendix B***CONSIDERATIONS FOR FLOW DEVELOPMENT OF A
MODULE WITH NON-NEGLIGIBLE INLET GEOMETRY**

The FAWT in the Aerodrome within CAST at Caltech, unlike any of the other builds mentioned throughout this dissertation, uses a series of modules with inlet geometry to build up a bigger array. The open air wind tunnel is comprised of a 12×12 grid of slightly diverging ducts that feed air to a 3×3 fan distribution per duct, totaling 36×36 total fan units. When viewed from a perspective downstream of the array looking back, the array appears as any other FAWT, however, flow visualizations show that the influence of each 3×3 module is noticeable an appreciable distance downstream. The flow evolution of an isolated module sheds some light on the funneling influence and subsequent core convergence associated with the divergent inlet geometry, shown in fig. B.1. Immediately downstream of the outlet, spanwise (z - y plane) visualization of the module shows the annular flow output of the nine total fans, just as in the 3×3 array presented in fig. 2.4. Differences in the flow evolution emerge for a constant commanded RPM fan distribution, however, with increasing distance downstream compared to builds without the module inlet geometry on account of the difference in boundary conditions at the fan intake. Namely, the useable uniform core region converges much more quickly than in fig. 2.4. The area of the core region of the flow for both builds is $\sim L \times L$ at $x/L = 0.5$. Beyond $x/L > 0.5$ (where the effect of each individual has mixed into a bulk flow), the core area reduces from a square cross section to a circular cross section as fluid is entrained. At $x/L = 4.23$ the 3×3 module has a cross sectional area of approximately $0.45 \cdot (L \times L)$ compared to the build without inlet geometry that has a cross sectional area of approximately $0.75 \cdot (L \times L)$ at the same downstream location at comparable flow speeds. The core convergence of a single module is made more readily apparent when velocities below a certain threshold are subtracted away, as in the visualization of fig. B.2.

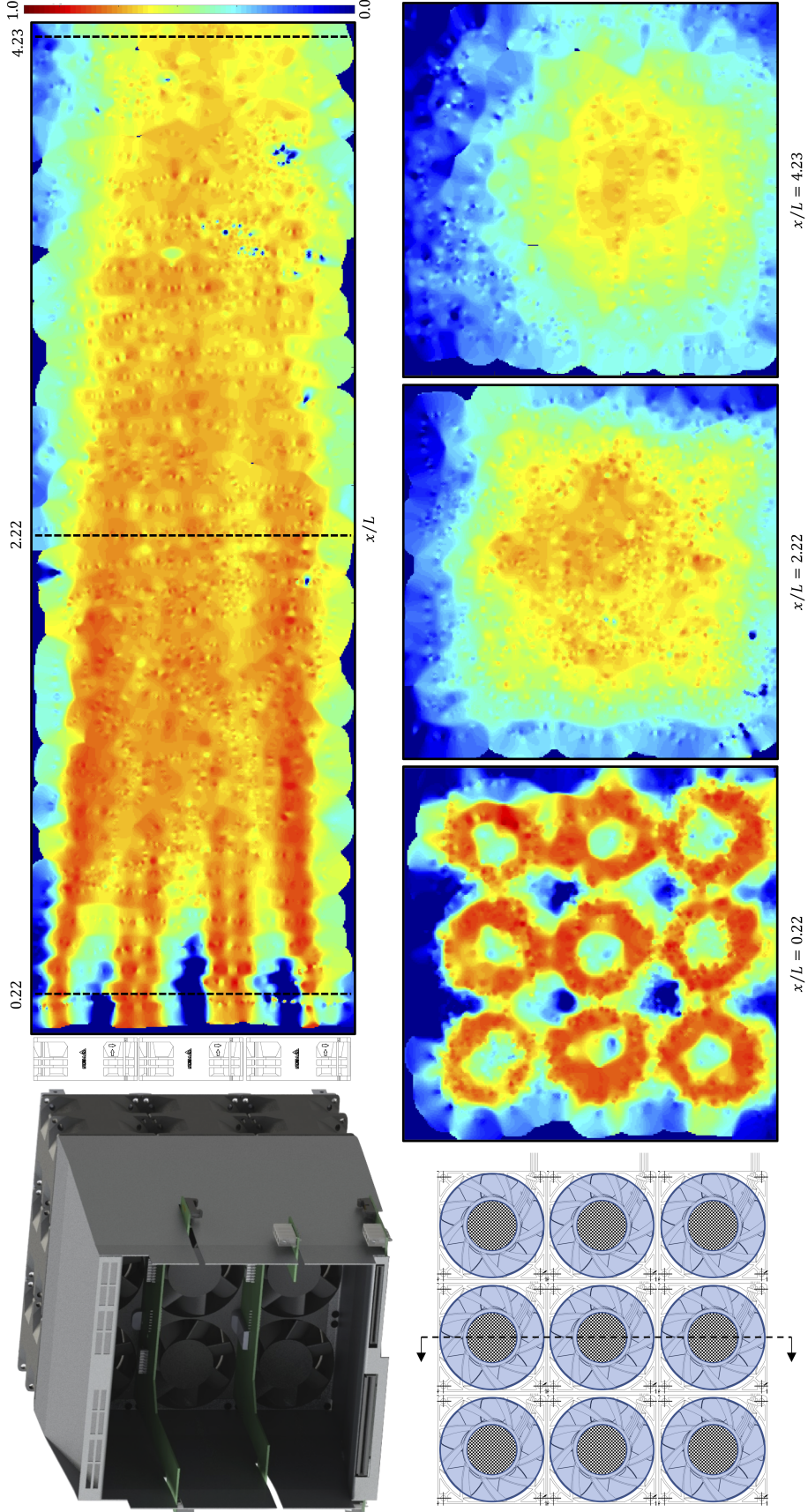


Figure B.1: Development of a steady uniform flow measured for a $d/L = 0.33$ resolution array ($d = 0.080$ m) with a diverging duct mounting structure at fan unit intake. The streamwise (x - z plane) cut corresponds to the centerline ($y = 0$) and the positions of the spanwise (z - y plane) distributions are dashed for all three locations. The core flow homogenizes first from discrete source units to a nearly uniform square cross section of size $\sim L \times L$ and then spatially reduces with downstream distance as the core flow smooths to a rounder cross-section as the boundary shear layers entrain and grow. The colorbar corresponds to \bar{u}/\bar{u}_{max} .

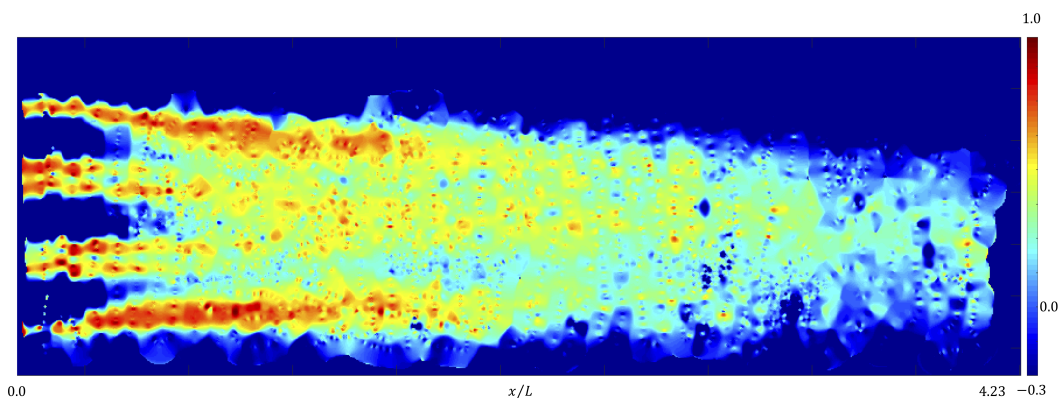


Figure B.2: Streamwise (x - z plane) visualization of a $d/L = 0.33$ resolution array ($d = 0.080$ m) with a diverging duct highlighting the core convergence of a single 3×3 module for a commanded constant RPM input condition. The colorbar corresponds to $\Delta\bar{u}_T/\bar{u}_{max}$, where $\Delta\bar{u}_T$ is the difference between the mean velocity \bar{u} and a certain threshold value \bar{u}_T .

With a diverging duct geometry installed upstream, each of the eight fan units encircling the center fan unit of a given module have at least one boundary condition adjacent to a solid surface. The corner fan units each have two boundaries along a surface whereas the center fan intakes free from any surface. These differences in boundary conditions create a funneling preference to the center fan that steepens the velocity profile away from a rounded flat top to that resembling more of a parabolic shape. When modules with parabolic-like velocity profiles are installed adjacent to one another, a peak-and-valley distribution remains for a greater distance downstream, as seen in fig. B.3.

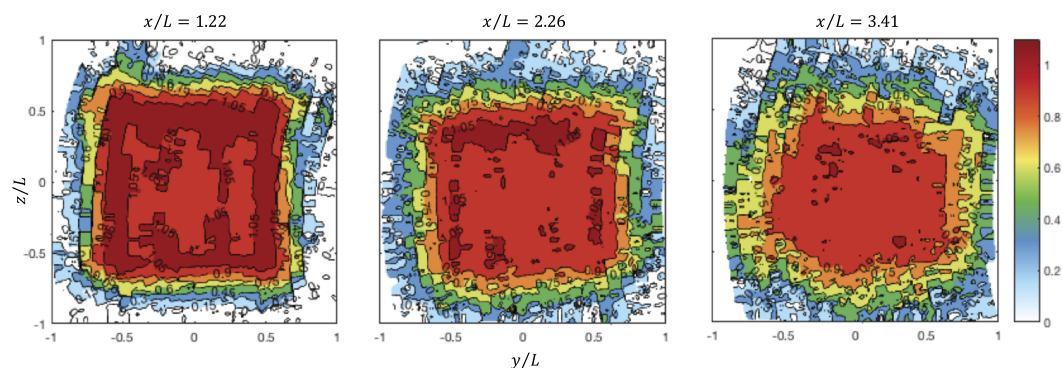


Figure B.3: Spanwise (z - y plane) visualization of a $d/L = 0.11$ resolution array ($d = 0.080$ m) comprised of nine total (3×3) modules assembled into a 9×9 array. The colorbar corresponds to $\bar{u}/\bar{u}_{0,0}$, where $\bar{u}_{0,0}$ is the center velocity at $z/L = y/L = 0$.

Appendix C

TURBULENCE ON-DEMAND (TOD)

A technique to increase turbulence intensity without significant changes to the mean velocity profile (i.e. increased background turbulence decoupled from a targeted mean) is briefly presented. With the receptivity of the flow to commanded discrete forcing frequencies for uniform flow modalities established in section 2.1, pseudo-random perturbation algorithms can be developed. Collectively referred herein as turbulence on-demand (TOD) are the techniques for the tailoring of specific turbulence parameters through software interfacing alone. This is not unlike the toolset available to the numericist in simulated environments¹, but manifested in experimental domains to the extent possible with existing hardware. A couple salient features of TOD are enumerated below.

C.1 Fluctuations about a desired mean - random-phase (R-P) mode

A straightforward consequence of having individual and separate control of each fan unit (particularly in the stacked dual-unit design) allows for prescript and ranged fluctuations about a desired mean. This effectively decouples the turbulence intensity from the mean (which is not possible through geometric means). The algorithm is straightforward and is quickly described as follows:

- assign allowable deviation percentage from the desired mean
- assign “phase” or starting point within the allowable range to be randomly distributed spatially across the fan units
- activate fans and allow them to cycle within the range allotted

¹A form of the Navier-Stokes equations common in forced incompressible flow simulations is $\frac{\partial u}{\partial t} + (u \cdot \nabla)u = -\frac{1}{\rho}\nabla p + \nu\nabla^2 u + f$. Similarly, the effect of environmental disturbances can be explored with suitable forcing functions developed in the experimental domain.

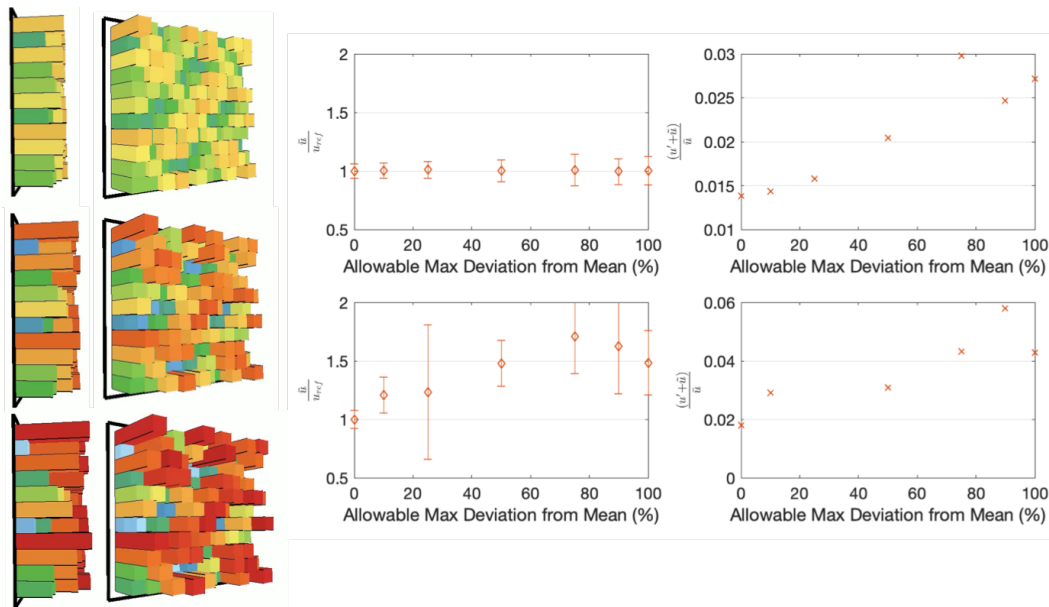


Figure C.1: Example of varying turbulence intensity about a desired mean. The above row shows the effect when the algorithm is active compared to the bottom row where it is initialized as spatially random but not active.

Because the respective fan inputs are pseudo-randomly-phased relative to each other, this flow augmentation is called the random-phase mode (R-P), after Ozono and Ikeda (2018). For reference, a spatially random but static implementation is shown in the bottom row of fig. C.1, which is unable to maintain a targeted mean². The top row presents results when the R-P algorithm is active. Pictorials along the left of fig. C.1 are snapshot representations of select ranged deviation percentages corresponding to 30%, 50% and 90% (top moving down), respectively. The target nondimensional mean of $\bar{u}_{target}/\bar{u}_{actual} = 1$ is maintained through the sweep of deviation percentage increases (top leftmost plot) with a corresponding increase in velocity fluctuations as deviation percentage increases (top rightmost plot). This effect can further be exploited in the dual-unit abstraction, as an extra array layer is available for dual-unit builds, as is explored in the next section. By decoupling the mean velocity from the fluctuations, input energy can be distributed broadly amongst the frequency scales, opening up new parameter spaces to explore for a given desired mean profile. Though a uniform flow profile was used as an example, R-P algorithms can be activated for any such steady (non-uniform) mean profile.

²Though not desirable in this particular implementation, the ability to create bulk-flow unsteadiness without introducing input unsteadiness should prove advantageous for future experimentation.

C.2 TOD Considerations: single vs. dual-layer FAWT

There exist two primary implementations of FAWT technologies. Dual-layer FAWT provide an additional stacked layer of fan units, oftentimes rotating in the opposite sense. The extra layer can be solely reserved to prescribe fluctuations or used to enhance velocity throughput when coupled to the main layer. Figure C.2 compares the ability of a single and dual-layer FAWT to track a targeted mean velocity over a range of allowable percentage deviation. The dual-layer FAWT cannot track \bar{u}_{target} as accurately as the single layer FAWT, due in large part to the unmodeled complex nonlinear internal flow interactions of the counter-rotating stacked fan units which further deviate the desired output from the commanded inputs based on the simplified mathematical treatment presented in section 2.1. The corresponding increase in turbulence intensity for the dual-layer, however, is substantive and provides a greater range of amplitudinal perturbation potential. For these reasons, dual-layer FAWT are preferable for most applications requiring various turbulent fluctuations.

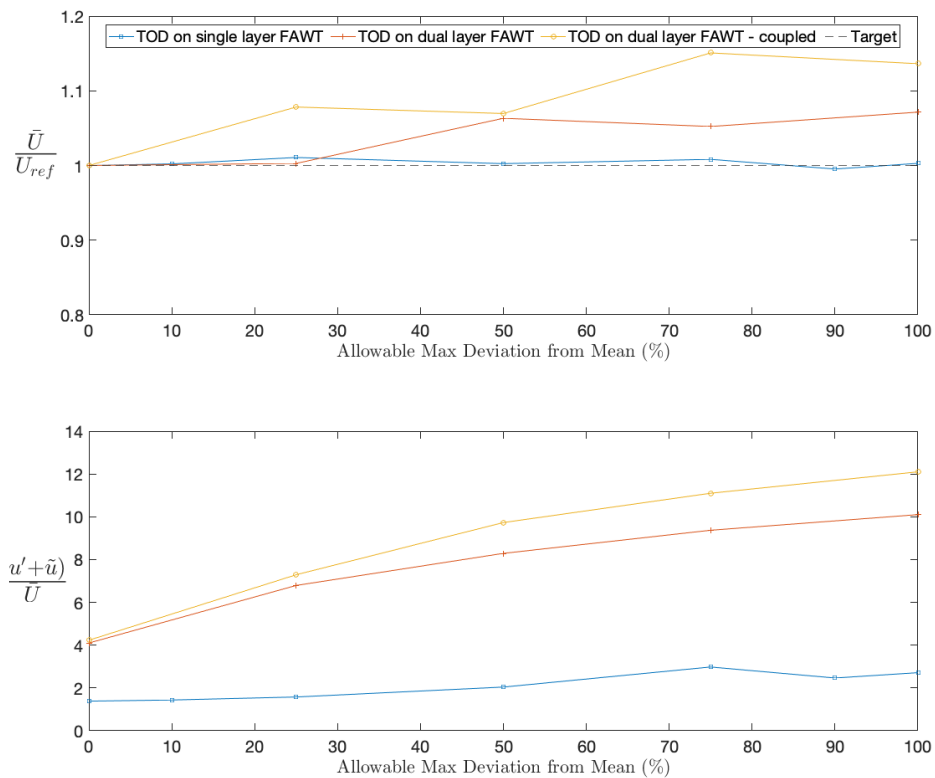


Figure C.2: Comparisons of the TOD algorithm on a single- and dual-layer FAWT.

Due to the nonlinear acceleration/deceleration profiles of the fan units tested herein, the mean velocity of the flowfield in the breathing modality increases with increasing allowable deviation. When decoupled (i.e. one layer used for a desired mean profile and the other for disturbance), a maximum deviation from the mean of 7% is recorded. When both layers are coupled with the TOD algorithm active, this trend worsens with maximum deviations from the mean approaching 11.5%. With algorithmic optimization, this undoubtedly can be improved.

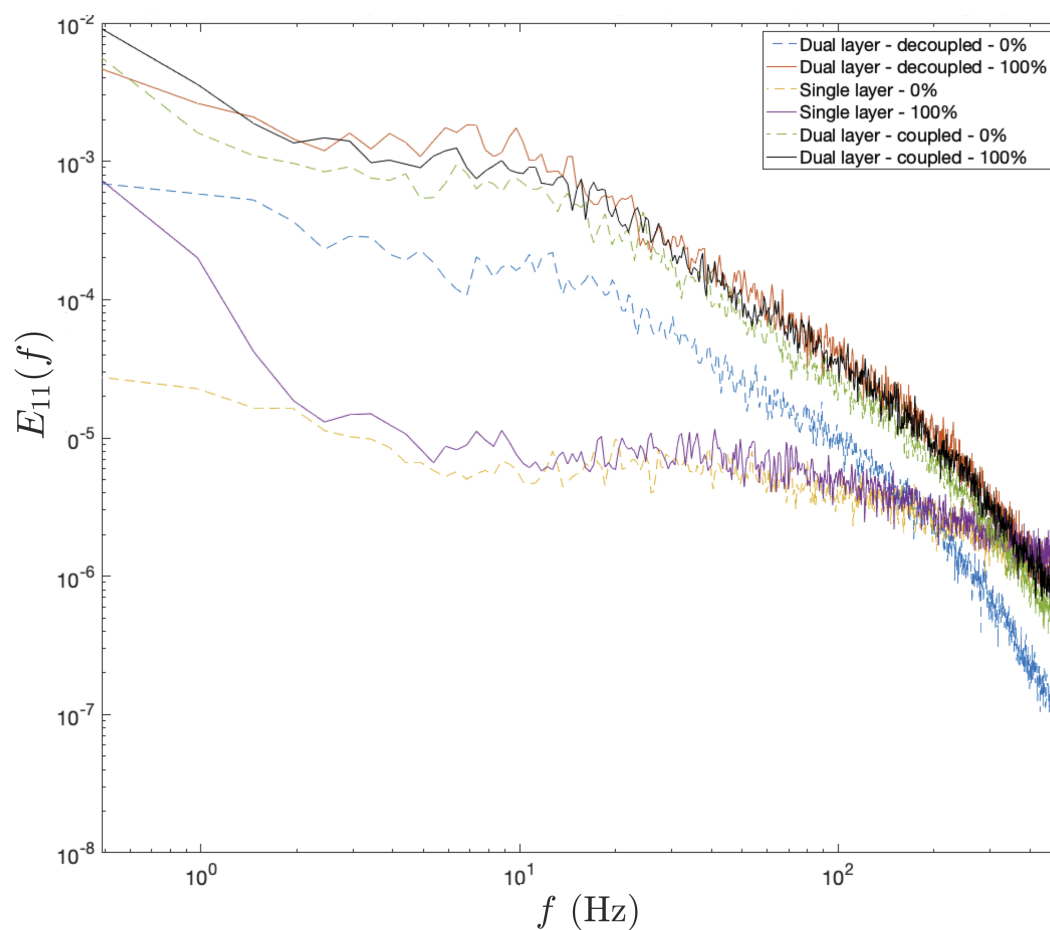


Figure C.3: Comparisons of the energy spectra of the TOD algorithm implemented on a single- and dual-layer FAWT.

One particular advantage of the dual-layer implementations is made evident when comparing energy spectra. Single layer arrays are overall less energetic and flatter responding compared to the dual-layer arrays when the TOD algorithm is active. For the single layer arrays, energy is added only in the lower frequency region and not broadly distributed. A *coupled* dual-layer is in many ways analogous to a single

layer FAWT, and little change is observed in the energy spectra beyond energetic content being added to the low frequency region. A marked difference is observed, however, when the two layers of the dual-layer are decoupled, with one layer devoted to the mean profile (in this case, a uniform flow) and the other to disturbances about the desired mean. The trend is made readily apparent in fig. C.4. TOD algorithms effectively add energy to the flow broadly in the decoupled dual-layer FAWT implementation without dramatically affecting the nature of that turbulence. In this sense, turbulent fluctuations can be dialed up or down through software without principally changing the flowfield.

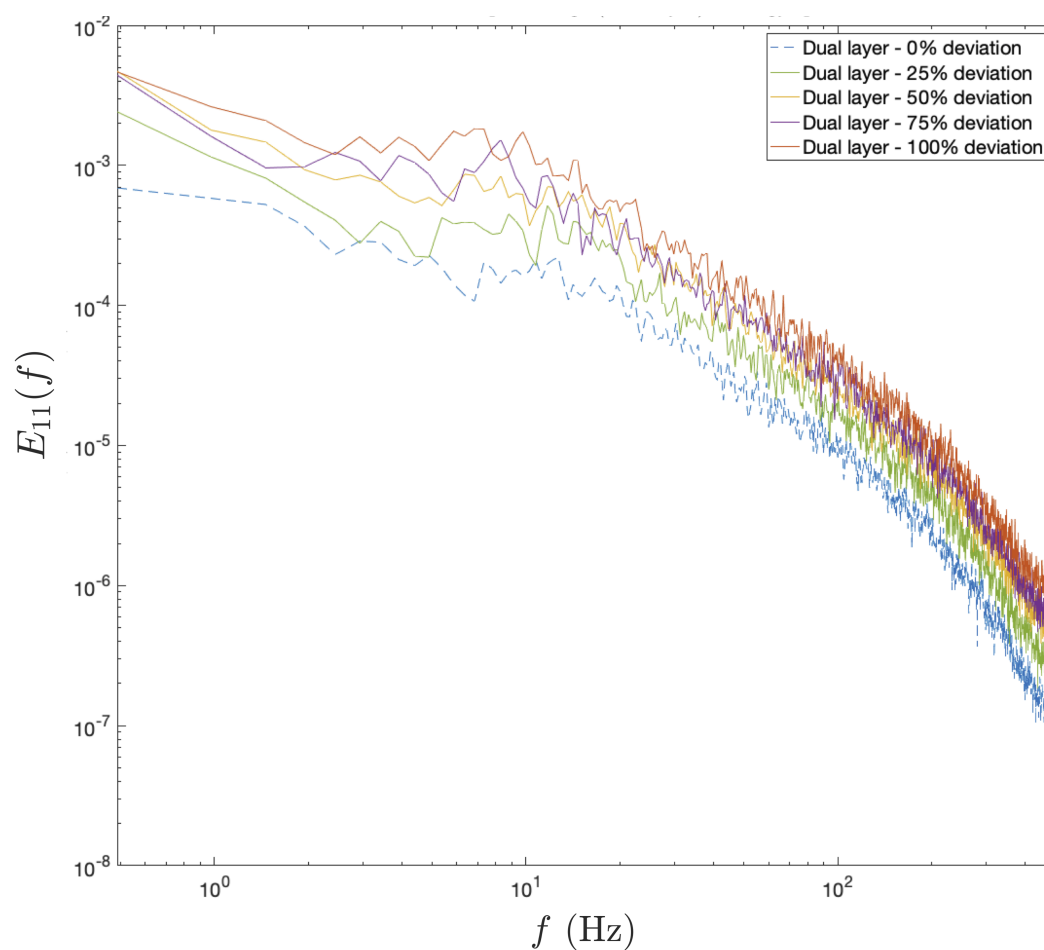


Figure C.4: The energy spectra for the TOD algorithm applied to the backmost layer of a decoupled dual-layer fan array showcases that the increase of the total fluctuation energy is broadly distributed across all relevant scales as the maximum allowed percentage deviation range in the TOD algorithm is consistently increased.

Appendix D

A COMBINATION OF FLOW MODALITIES: A DISCUSSION OF THE APPLICATION OF PERTURBATION TECHNIQUES

D.1 The application of software-enabled perturbation techniques

The relative magnitudes of the ratio of the fluctuating velocities to the mean velocities (i.e. the turbulence intensity) will nominally vary with altitude in an atmospheric boundary layer (e.g., see Stull, 1988) and a prevailing wind flowing over and around the built-up environment will generate a whole host of wakes, mixing layers, and combinations thereof. These realities motivate the development of software-enabled perturbation techniques that can both increase the standard deviation of the fluctuating velocities about a desired mean as well as initiate, evolve, and combine flowfields in representative ways. Stated summarily, the perturbation strategy is achieved through three primary tactics:

- Randomize initial velocity conditions and play those through activated dynamic-ranging algorithms
- Statically-reconfigure (combine) the individual discrete fan units into a coarser representation and allow the flow to naturally evolve
- A combination of the two aforementioned

The random-phase (R-P) perturbation technique discussed in appendix C can actively dial the turbulence intensity higher through a prescriptable range that is limited amplitudinally by the available percentage-deviation to the maximum velocity output from the targeted mean. This perturbation technique distributes energy broadly amongst all the scales, particularly when ranged symmetrically (recall fig. C.1 and fig. C.4) and was shown in Chapter IV that a near doubling of the turbulence intensity corresponded to a nearly sevenfold increase of Re_{λ_T} for a mean velocity that stayed within 4% of the targeted mean velocity. Also showcased in Chapter IV was the static reconfiguration of the fan array into a so called quasi-grid. Significant increases of Re_{λ_T} were noted. Turbulence initializes from the principal shear layers generated at the fan outlet plane, diagrammed in fig. 4.1. In the following section a

combination of techniques is explored, whereby within a coarser planar segment of statically-reconfigured fan units, dynamic-ranging algorithms are activated.

A discussion by way of example - a perturbed triple-stream mixing layer

The triple-stream mixing layer introduced in Chapter III is an exemplar flow modality candidate to leverage the aforementioned perturbation tactics. Since the mixing layers generated herein are implemented with virtually no boundary structure beyond the source-fan housing (i.e. "splitterplateless"), traditional boundary layer augmentation techniques are not an available option. Instead attempts to control the flowfield with the fluid medium itself are undertaken. One could argue that the static-reconfiguration of source fans through software is a pseudo-manipulation of boundary conditions, as it introduces a geometrically relevant length scale, but that discussion is left for another time. In either case, it is emphasized that no additional geometries are added to the multi-source configuration¹.

A brief overview of the behavior of perturbed free shear layers

Because mixing layers are susceptible to inviscid instabilities, they are good candidates for flow manipulation. By flow manipulation, two notions are implied in line with the two primary perturbation techniques. In the parlance of H. Fiedler and Fernholz (1990) a flow can be influenced 1) by the design choices of the wind tunnel flow management system (honeycombs, screens, static-reconfigurations, etc.) and 2) by flow control (dynamic-ranging algorithms), which is a process to manipulate certain characteristics of a flow to achieve "improvements" of a specified technical outcome.

Supported by a plethora of experimental evidence, the coherent structures of a conventionally-generated mixing layer are most receptive to periodic oscillations just downstream of the splitterplate edge (e.g., see Oster and Wygnanski, 1982), where mixing is initiated. In a similar manner, perturbations initiated through software-means in multi-source wind tunnels affect the local neighborhood of flow development where mixing is initiated. Ho and Huerre (1984) summarize some conditions to effectively manipulate the development of mixing layers. Amplitudinal fluctuations as small as $u'/U \sim 10^{-7}$ are enough to influence the behavior of the

¹In particular, no splitterplate geometry is added to divide the mixing layer, no turbulence-generating grids are added to increase freestream turbulence, and no loudspeaker or vibrating ribbon is added to periodically oscillate the flow. All the desired effects are attempted through software means alone. There is no reason (beyond convenience and principle) why any or all of the aforementioned elements could not be integrated into these kinds of experiments.

coherent structures if activated at the proper forcing frequency. First and foremost, the imposed fluctuation should be spatially coherent along the span. Secondly, vortex formation² can be controlled through careful selection of the forcing frequency. For example, in the range of $(1/2)f_n < f_f < 2f_n$, the vortices are found to form at the forcing frequency. The higher the initial energy at the forcing frequency in this range, the greater the suppression of the growth of the subharmonic $f_n/2$, which plays an important roll in vortex pairing. As such, the forcing frequency has a stabilizing effect in that the coherent structures stay distinct for longer.

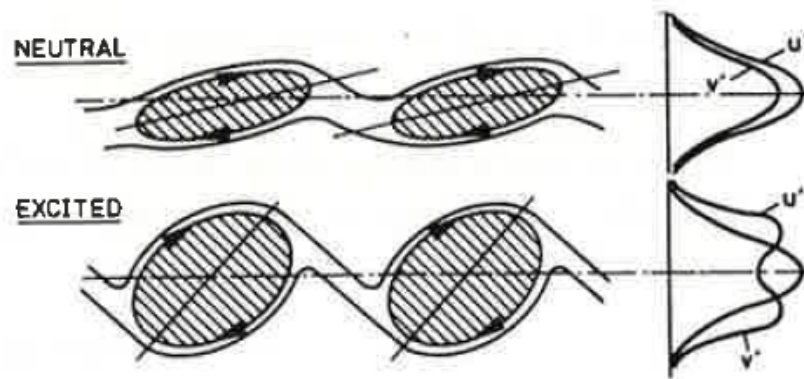


Figure D.1: The stabilizing effect on coherent structures through forcing, from Koepp et al. (1991).

When excited and stabilized, the ratio of the major axes of the coherent structures approach unity and the longitudinal velocity component along the streamwise direction is largely reduced. The spreading rate of the mixing layers can thus be increased by promoting vortex amalgamations or reduced by suppressing the subharmonic. The effect hinges primarily on the selection of the forcing frequency and secondarily on its amplitude. At very low forcing frequencies far from the natural frequency (i.e. $f_f \ll f_n$), larger perturbations on the order of 10^{-2} are necessary to effect similar behavior. At such low frequencies, mode competition becomes more evident, with the forced wave dominating the flow evolution.

The behavior of perturbed mixing layers can thus be summarized as follows:

- Coherent structures are generated upon initiation of the mixing layer and grow with downstream development; in virtually every situation, the expectation is

²this is synonymous to the location of the first vortex rollup. In an excited shear layer, this occurs at the particular harmonic of the forcing frequency that is nearest but less than the natural frequency.

that the coherent structures exist quasi-two-dimensionally if they are initiated with spanwise coherence

- Manipulation of these turbulent shear flows are possible by manipulation of the coherent structures themselves
- Introducing forcing frequencies where the flow is most receptive is the best way to manipulate the coherent structures
- Changes in freestream turbulence may also affect the spreading rate of the mixing layer by encouraging the onset of mixing, but are observed to be secondary (less-effective) to manipulation of the coherent structures

Perturbation strategy for triple-stream mixing layers

These experiments, considered in its entirety, consist of a plant (the base flowfield) a measuring system (hotwire traverse in this case) and a controller (the software algorithms commanding the fan actuators). Open-loop control is employed throughout, though efforts are underway for closed-loop control for future studies. The processes triggered by the control of the fan actuators is intrinsically nonlinear, but the controllability of the flow is governed by the stability characteristics of the fluid medium, namely the temporal and spatial growth behavior of initial perturbations. The receptivity of the flow to external forcing can be expected to occur where the flow is locally and/or globally unstable, shown to occur where mixing is initiated in the case of the mixing layer.

With the above discussion in mind, the triple-stream mixing layer perturbation strategy acts to potentially influence the subsequent development of the merged dual-stream mixing layer in three primary ways:

- By encouraging amalgamations of a different kind by bringing two mixing layers into proximity of one another; these may act as superpositions if the natural frequencies are (near-)matched or mode competition may become evident
- By stabilizing/destabilizing the coherent structures with selection of perturbation frequency and amplitude at the fan outlet plane, the spreading rate can be augmented

- By increasing the energy content broadly in the freestream; if the scales of these random motions are of the order of the shear layer width, then quasi-steady bulk-flow behaviors like "snaking" may occur

Preliminary results and discussion

Fan arrays were shown to behave as low-pass filters (see Chapter II) frequency-limited to $f_f \lesssim 2$ Hz for the apparatus used herein. Greater-amplitude perturbations of at least order 10^{-2} are to be used, then, since the natural frequencies of the triple-stream mixing layers estimated from $f_c \sim f_{50} = U_c/\Lambda_x^u$ are greater than half the forcing frequency (see table 5.2). Perturbed triple-stream mixing layer experiments are currently being undertaken, but some tentative conclusions can be drawn for the completed datasets at $x = 88$ inches for the $ss = 4d$ case, shown in fig. D.2. Because the perturbation tactics require velocity margin above and below a targeted mean velocity, freestream velocities must be sufficiently far from the operational maximum and minimum velocity of the fan array wind tunnel to be effective. In the triple-stream mixing layer cases presented herein, ranged fluctuations, when applied everywhere through software, are not expected to be effective on the lower segment side (as those freestream velocities are near the idle velocity of the fan units). As such, the mean velocity profiles are collapsed upon the lower mixing layer parameters (which are not expected to change much) to highlight the qualitative effects of the upper mixing layer development due to implemented perturbation techniques.

The perturbation tactics are employed either at every planar segment (i.e. across the whole fan array) or on selected planar segments with the remainder segments left to baseline initial conditions. For instance, the random-phased ranged-fluctuation algorithm activated over a 60% amplitudinal range (an order 10^1 perturbation) is implemented across all three planar segments in one such experiment, but then is implemented on select planar segments (e.g. across only the center segment, subscripted as 'c', or the upper segment, subscripted as 'u') in other experiments. The same is true for the presented sinusoidal perturbations initiated at forcing frequencies of $f_f < 2$ Hz.

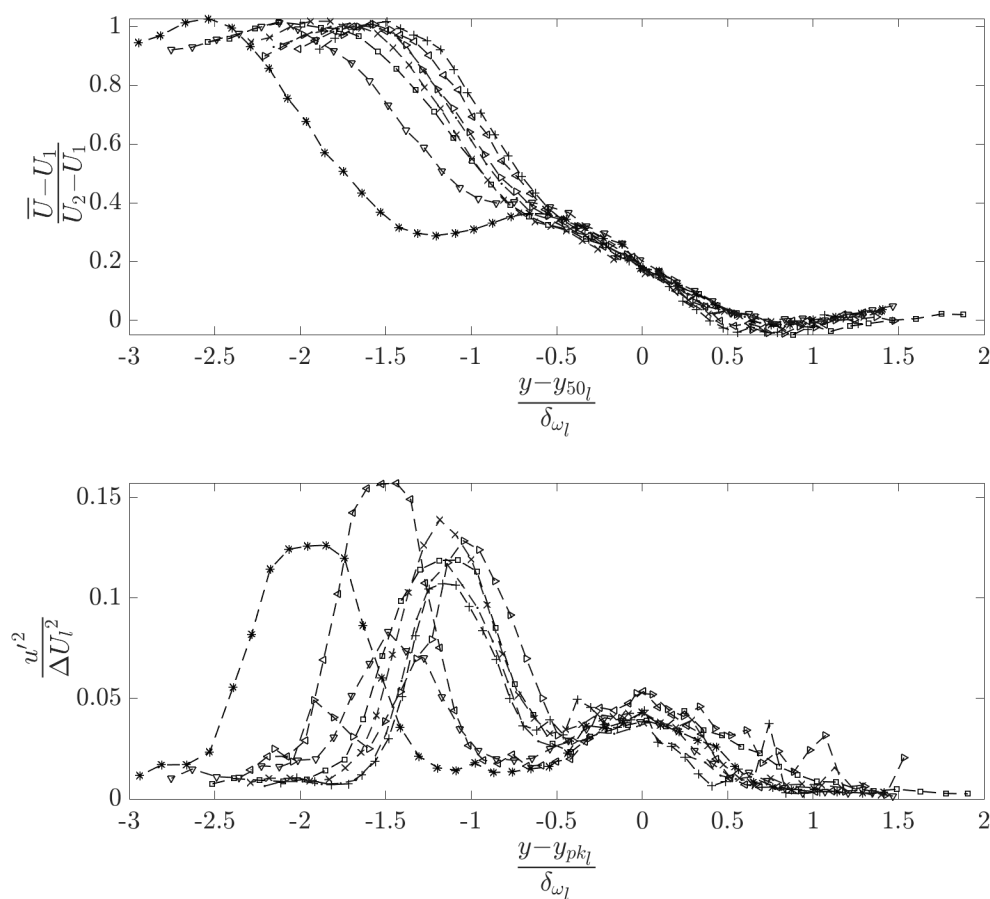


Figure D.2: Mean velocity profile (above) and fluctuating velocity profile (below) for the perturbed triple-stream mixing layer with initial separation of $ss = 4d$. The baseline (non-perturbed case) is denoted by the (\square) marker. Random-phase perturbations are denoted by ($*$) when applied to the whole array, ($+$) the center segment, and the (\triangleleft) upper segment. Sinusoidal periodic perturbations of $f_f = 1$ Hz is applied to the whole array (\cdot) and the upper segment (\triangleright), $f_f = 2$ Hz is applied to the whole array (\times) and the upper segment (∇).

Immediately evident in the mean velocity profiles are changes in the separation distance between the upper mixing layer and lower mixing layer, seen as a ‘fanning-out’ relative to the baseline configuration (denoted by the (\square) marker). The relative maximum-slope thickness, at first glance, also appears to change, suggesting the spreading rates are augmented. The fluctuating velocity distributions, when pinned at the peak u'^2 location for the lower mixing layer, show movement of the upper mixing layer fluctuating velocity peaks relative to the baseline case. Differences in behavior in the mean velocity profiles elucidated by this rather limited analysis is

observed in the random-phase case applied over the whole array (*) and the periodic sinusoidal perturbation of $f_f = 2$ Hz applied only to the high-speed stream of the upper mixing layer (∇). An effective movement of the peak centerline location of the upper mixing layer toward the high-speed stream in the case of the random-phase perturbation applied solely to the upper segment (\Leftarrow) is clearly showcased in the fluctuating velocity distribution. These particular cases warrant further careful study. Traverses at the remaining downstream locations scheduled for near-future experimentation will allow calculation of the spreading rate and x-wire hotwire measurements will help determine the lateral fluctuating velocity evolution, which is likely to increase³ when the mixing layers are excited and/or near merging.

³Subsequent increases of mixing layer thickness deducible from mean velocity measurements is most likely due to increased lateral momentum transport on account of the increased lateral fluctuating velocity components though no direct experimental evidence can be provided from single-wire hotwire traverses. An estimate of the mean transport of turbulence energy for two-dimensional flow is given in the form $-\frac{\partial}{\partial y} \frac{1}{2} (\overline{u'^2 v'} + \overline{v'^3} + \overline{v' w'^2})$.